



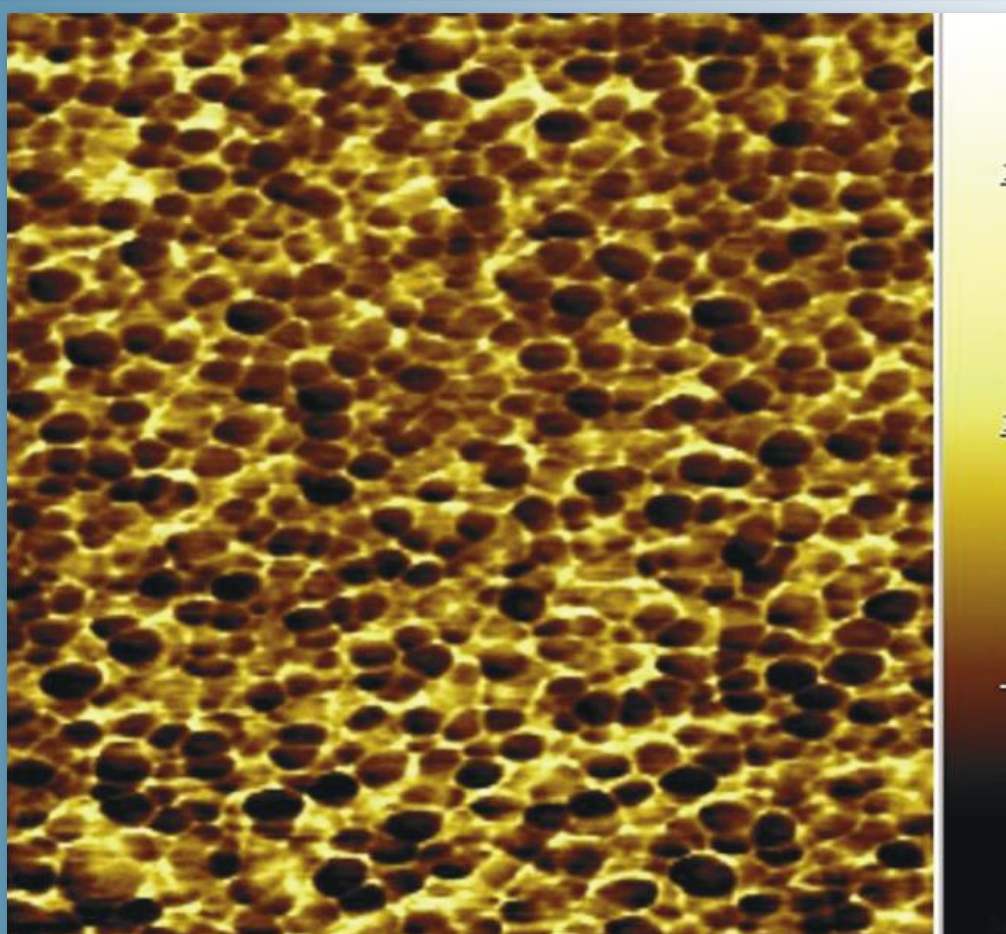
ISSN 1028-8546

Volume XIX, Number 2
Section: En
July, 2013

Azerbaijan Journal of Physics

Fizika

www.physics.gov.az



G.M. Abdullayev Institute of Physics
Azerbaijan National Academy of Sciences
Department of Physical, Mathematical and Technical Sciences

Azerbaijan Journal of Physics

FIZIKA

*G.M.Abdullayev Institute of Physics
Azerbaijan National Academy of Sciences
Department of Physical, Mathematical and Technical Sciences*

HONORARY EDITORS

Arif PASHAYEV

EDITORS-IN-CHIEF

Nazim MAMEDOV

Chingiz QAJAR

SENIOR EDITOR

Talat MEHDIYEV

INTERNATIONAL REVIEW BOARD

Ivan Scherbakov, Russia
Kerim Allahverdiyev, Turkey
Mehmet Öndr Yetiş, Turkey
Gennadii Jablonskii, Buelorussia
Rafael Imamov, Russia
Vladimir Man'ko, Russia
Eldar Salayev, Azerbaijan
Dieter Hochheimer, USA
Victor L'vov, Israel
Vyacheslav Tuzlukov, South Korea
Majid Ebrahim-Zadeh, Spain

Firudin Hashimzadeh, Azerbaijan
Anatoly Boreysho, Russia
Mikhail Khalin, Russia
Hasan Bidadi, Tebriz, East Azerbaijan, Iran
Natiq Atakishiyev, Mexico
Maksud Aliyev, Azerbaijan
Bahram Askerov, Azerbaijan
Arif Hashimov, Azerbaijan
Vali Huseynov, Azerbaijan
Javad Abidinov, Azerbaijan
Bagadur Tagiyev, Azerbaijan

Tayar Djafarov, Azerbaijan
Talat Mehdiyev, Azerbaijan
Emil Guseynov, Azerbaijan
Ayaz Baramov, Azerbaijan
Tofiq Mammadov, Azerbaijan
Salima Mehdiyeva, Azerbaijan
Shakir Nagiyev, Azerbaijan
Rauf Guseynov, Azerbaijan
Almuk Abbasov, Azerbaijan
Iskender Djafarov, Azerbaijan
Yusif Asadov, Azerbaijan

TECHNICAL EDITORIAL BOARD

Senior secretary Elmira Akhundova, Nazli Guseynova, Sakina Aliyeva,
Nigar Akhundova, Elshana Aleskerova

PUBLISHING OFFICE

33 H.Javid ave, AZ-1143, Baku
ANAS, G.M.Abdullayev Institute of Physics

Tel.: (99412) 439-51-63, 439-32-23
Fax: (99412) 447-04-56
E-mail: jophphysics@gmail.com
Internet: www.physics.gov.az

It is authorized for printing:

Published at "SƏRQ-QƏRB"
17 Ashug Alessger str., Baku
Typographer : Aziz Gulaliyev

Sent for printing on: __.__. 201__
Printing approved on: __.__. 201__
Physical binding: _____
Number of copies: _____ 200
Order: _____

DEVIATIONS FROM PLASMA STABILIZATION AGAINST THE ONSET OF SPACE-CHARGE EFFECT IN A GAS DISCHARGE STRUCTURE WITH SEMICONDUCTOR CATHODE

M. ÖZER^{1*}, E. KOÇ¹ AND B. G. SALAMOV^{1,2}

¹*Physics Department, Faculty of Arts and Sciences,
Gazi University, Beşevler 06500 Ankara, Turkey*

²*National Academy of Science, G.M.Abdullayev Institute of Physics,
AZ-1143 Baku, Azerbaijan*

* metinoz@gazi.edu.tr

In this study, the relationship of uniform plasma distribution to a space-charge effect was experimentally demonstrated at microgaps (45-525 μm), in *GaAs* cathode and neon environment. We discussed that, when the onset of space-charge arise as a dominant effect, the deviations from plasma stabilization lead to the field perturbation of gas space. Experimental observation of the onset of space-charge effect is determined at the reduced values of E/p . In this case, the photon-induced secondary electron emissions reached the high values. However, the aspect of uniform plasma distribution is obtained at the enhanced values of E/p when the space-charge effect isn't important.

Keywords: semiconductor cathodes, secondary electron emission, space-charge effect, electrical breakdown, discharge stabilization

PACS: 52.25.Jm; 52.80.-s; 51.50.+v

1. INTRODUCTION.

A prevalent interest in space-charge effect originated from positive ions for microplasma is based on the relation between plasma stabilization and its existence. Under a certain conditions of discharge plasma such a correlation leads to the various oscillation structures the appearing in discharge current when the space-charge densely occupies the gas space. So, knowledge of space-charge effect in various discharge regimes including Townsend and glow discharge have recently gained an important meaningful for plasma devices required to the conditions of homogeneous operation. A considerable attention is related to the continuousness of the field uniform of these devices used in extensive applications including semiconductor devices, plasma display panels and microelectromechanical systems (MEMS) [1-4].

Field distortion on the basis of space-charge is studied at the wide scale of pd (where p is pressure, and d is discharge gap) in the various discharge plasma. Ref [5] determined that the number of ions reaches a constant value in the vicinity of cathode. They presented that at the enhanced values of pd Townsend discharge can occur as an unstable formation with respect to the onset of space-charge. Ref [6] presented that, when the density of ions is dominant than that of electrons, at the subnormal regime the spatiotemporal structures exists due to ions. Common considerations for plasma stabilization reveal that the movement of ion-beams plays an important role [7, 8].

However, the mechanisms responsible for the onset of discharge plasma are importantly decisive with respect to the evaluation of space-charge effect. At the enhanced values of E/p (where E is electric field), the discharge plasma can develop from a uniform field with the contribution of secondary electron emission (*SEE*) from cathode, and the electrical field in such discharges is in relation to a homogeneous distribution due to the small space-charge effect. At the reduced values of E/p , the discharge plasma initiates at nearly unimportant *SEE* levels or ignites in a typical photoionization structure, and mostly this case leads to the onset of space-charge effect. So, the evaluation of first conditions of evolution of

discharge plasma becomes important for plasma stabilization. Note that in present study E/p ratio is roughly in the range of 30-800 V/cm \times Torr for neon plasma.

In plasma stabilization, the semiconductor cathodes with high resistivity in discharge plasma play an important role with respect to the annihilation of the space-charge effect. A discharge system consisted of semiconductor cathode is a semiconductor gas discharge structure (*SGDS*), which is commonly used in microdischarge applications including *IR* converter [9] and *UV* light source [10]. In *SGSD* the space-charge effect is annihilated by semiconductor cathode to some extent, which becomes important to obtain a uniform plasma distribution.

In this study we present the main processes affecting the uniform structure of field distribution due to the space-charge effect in *SGDS*. For this purpose, we calculated *SEE* coefficients in the onset of discharge plasma. The results emphasize that the typical losses from uniform plasma distribution is due to the space-charge construction. Importantly, the conditions of onset of space-charge effect are in relation to the development of collision processes at the high scale of pd in Paschen curves. In particular, when the space-charge effect dominantly appears in the discharge system, the fluctuations in the discharge current are highly observed at the high values of pd .

2. EXPERIMENTAL.

Fig. 1 shows experimental apparatus of discharge system with a semiconductor cathode in parallel-plane geometry. Semiconductor material (7) consisted of semi-insulating n-type *GaAs* with high resistivity ($\rho \cong 10^8 \Omega \times \text{cm}$), which is a direct semiconductor with bandgap of 1.35 eV at room temperature, is used in experiments. The thickness and the diameter of *Cr*-doped *GaAs* cathode are 1 and 36 mm, respectively. The anode covered with a conductive *SnO₂* (10) consists of a glass disk (11) with a 2 mm thickness and a 36 mm diameter. The cathode external surface is covered with a roughly 40 nm high

conductive Ni-layer (6) that is transparent to visible light with nearly 10% transmission. The SnO_2 and the Ni electrodes were connected to an external circuit consisted of a DC voltage source (up to 2500 V) and a series resistor R_1 (=10 kV) to measure the current in the circuit. An insulator slab (9) that consists of the spacer with a circular aperture (8) is placed between the semiconductor and the glass plates.

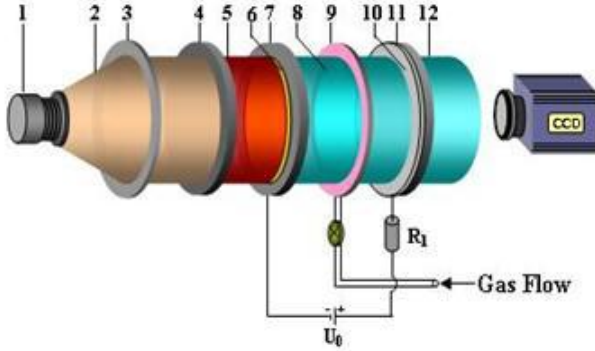


Fig. 1. SGDS with semiconductor cathode: 1-light source, 2-incident light beam, 3-lens, 4-Si filter, 5-IR light beam, 6-semi-transparent Ni contact, 7-semiconductor cathode, 8-discharge gap, 9-insulating mica foil, 10-semi-transparent conductive SnO_2 contact, 11-flat glass disk, 12-visible light beam.

The size of d (45–525 μm) and p (15–760 Torr) were chosen to obtain the broad left and right-hand branches of the breakdown curves. The interelectrode distance between the glass and the semiconductor cathode plates is filled with neon gas. Before neon gas was filled the system, the cell was evacuated up to $p = 1 \times 10^{-6}$ Torr. The gas pressure of discharge system was adjusted by a needle valve between the discharge chamber and the mechanical pump. The diameter D of the circular discharge gap of the insulator layer is in the range of 18 mm. The current–voltage characteristics (CVCs) and the radiation–voltage characteristics are recorded by varying of the applied voltage in the range of 5 V s^{-1} . The values of breakdown voltage V_{br} are determined from CVCs. In the present paper, when the semiconductor cathode absorbs the incident radiation, we investigate the space-charge effect in discharge system with the semiconductor cathode. An incandescent lamp (1) with a Si filter (4) uniformly illuminates the photocathode, and when the photocathode absorbs IR light, the increases in its photoconductivity arise. An optical arrangement (3) is performed to provide a spatial homogeneous illumination on the cathode. The experiments were performed at room temperature in GaAs cathode.

3. RESULTS AND DISCUSSION.

The condition of onset of discharge plasma depending on γ levels is shown in Fig. 2 with respect to E/p value. We observed that, when the value of E/p increases, the electrons released by semiconductor cathode reach the rather high emission levels. So, at the enhanced values of E/p , the onset of the ionization avalanche is in relation to the cathode emission behavior. This state is required to the evaluation of mechanism

leading to an increase of γ levels. The concept of low-pressure discharge is affected with the secondary electrons emitted by the cathode to burn gas. In the presence of ions, which predominantly are responsible for the cathode emission at these values of E/p as the effect or number of processes including collision-induced excitation states (long and short lifetime) can be negligible in gas space, the development of discharge draws a structure corresponding to Townsend discharge. But, the ions that reach the high enough energies lead to the high γ levels when they hit the cathode. In this case, the space-charge effect remains at the low levels, and field distribution does not distortion.

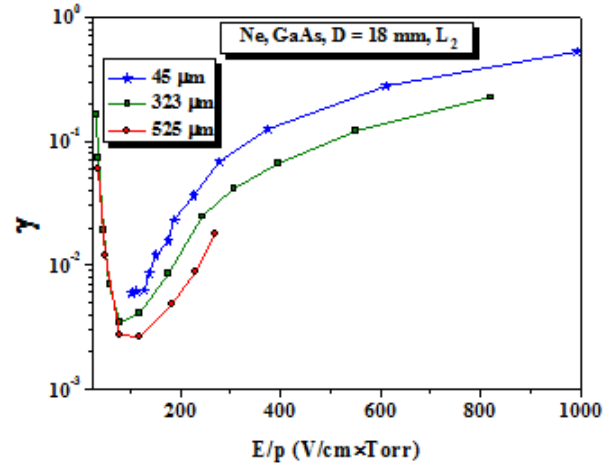


Fig. 2 γ coefficients obtained from neon environment for GaAs cathode under L_2 illumination intensity.

A typical peculiarity, which is the increase of collision processes in gas space, leads to the development of collision-induced excitation at the reduced values of E/p . Such a case expresses the presence of formations induced from photon, the effect of which mainly causes two processes: firstly, the process appears the ionization due to photoionization, i.e., the interaction of neutral atom and photon leads to the formation of ions, which corresponds to the equal energy than first ionization potential of atom. Later, if the multiphoton isn't process with effect for the ionization, the photons of gas space remarkable provide the electron emission from the cathode with a photoemission processes. Such a case is observed from Fig. 2 at the reduced values of E/p . The result indicates that the number of electrons emitted by cathode begins to increase at the values of $E/p \approx 100$ V/Torr \times cm. So, the photoemission process is importantly responsible for an increase of γ levels at the reduced values of E/p . However, while the photons lead to the electron emission from cathode, the space-charge effect becomes important due to the accumulation of ion beams in gas space. In particular, this case is accompanied by a time lag in breakdown curves.

The main relation between the electron emission to photon and the breakdown evolution corresponds to the high values at the scale of pd . The increases at scales of pd for the given a discharge gap lead to a growth of collision frequency and a decrease in mean free path in gas space. Therefore, while the photoionization process dominates with the increasing at scales of pd , the

increment of field with the time lags in breakdown evolution reveals a growth of the electrons emitted by semiconductor cathode. Comparison of photoemission process and different cathodes at various pd values in gas space emphasizes that the electron emission due to photon-cathode interactions becomes important with the increasing of pd scale. So, the present results are in a good agreement with respect to the growth of electron levels emitted photon-cathode interactions with the increasing at scales of pd in comparison with [11].

After discharge plasma is established in parallel-plane geometry, the amount of space-charge plays a decisive role with respect to a change in uniform of field distributed in gas space. From Fig 3, one can see that the influence of space-charge accumulating in discharge gap becomes important for plasma stabilization. The result obtained from experiments indicates that the increase of discharge gap leads to the important perturbations in field distribution as of low-current values. But, the space-charge effect in the low currents can be negligible, and therefore the uniform plasma distribution is consistently obtained at these values of discharge current. So, for unsteady-state current structures such an observation includes the field fluctuations due to the accumulation of space-charge with the increasing of discharge gap (at 525 μm). However, comparison of uniform plasma and discharge gap implies that the increase of field is important for the linear trends of discharge current when the applied voltage is increased. In particular, the ions in high fields hit the cathode to create the secondary electrons as they approach the cathode at the high enough velocities. This means that the onset of discharge plasma begins from a uniform field. In this case, we obtained that the values of electrons emitted by cathode reach at the high enough levels. But, with the increase of discharge gap our consideration is that the high density of ion beams occupies the gas space at the reduced values of E/p , and therefore the movement of the ion-beams moved towards cathode leads to the loss of the uniform distribution via field fluctuations in discharge gap.

For the characterization of the movement of ions in gas space, existing results shows their velocities at the values of E/p . The authors [12, 13] in studies associated with the ion velocity determined that their velocity at the reduced values of E/p importantly falls. This case emerges the importance of ions approaching the cathode. The ion beams approaching towards cathode at the low velocity values distorts the homogeneous distribution of field. However, it should be mentioned that there is the serious relation between space-charge effect and Townsend instabilities obtained from low-current plasmas.

Usually, the small space charge effect is in relation to the homogenous structure of Townsend discharge [14]. Minor distortion of field originated from this space-charge doesn't lead to the loss of steady-state structure in

discharge plasma. But, when the space-charge effect dominates, for low-current microplasmas the losses in the homogenous structure of discharge plasma take places due to field distortion.

The spatiotemporal inhomogeneities based on space-charge effect can be observed in discharge mode including subnormal glow as well as low-current plasma [5, 6]. The determinations that are made at the right-hand branches of breakdown curves show in further increasing in collision frequency between atoms, and the growth in collision processes leads to the accumulation of space-charge in plasma volume. It is obtained that at low pressures lateral constriction leads to the field fluctuations for spatiotemporal structure [15].

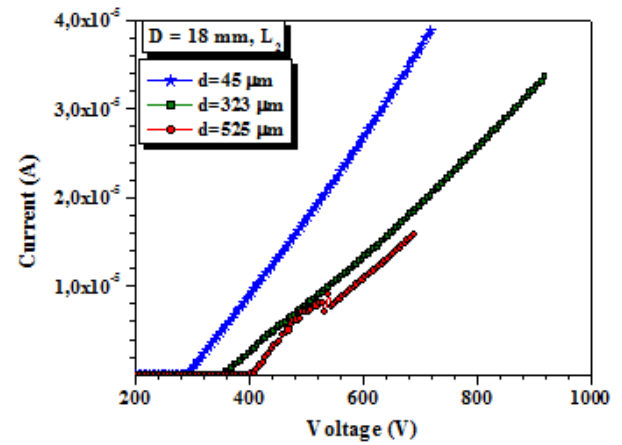


Fig. 3 CVCs obtained from several discharge gaps in neon plasma environment at $p = 66$ Torr under L_2 illumination intensity.

4. CONCLUSION.

In this study, we presented the relation between plasma stabilization and the space-charge effect in neon environment and GaAs cathode. We demonstrated the possible of the onset of space-charge effect when the scale of pd is increased at a given d value. In particular, this case corresponds to the fluctuations in discharge current when the collision processes develop in gas space. At the high values of pd , the onset of discharge plasma is in relation to photoionization structure or volume ionization processes. The result is that, when the space-charge accumulates in the discharge volume, the homogenous distribution of field losses, and therefore the deviations from discharge plasma are observed at the high values of pd .

ACKNOWLEDGMENT: This work is supported by the Gazi University BAP research projects 05/2011-39, 05/2011-73, 05/2012-26 and 05/2012-64.

- [1]. S. S. Yang, S. M. Lee, F. Iza, and J. K. Lee 2006 J. Phys. D: Appl. Phys. 39, 2775.
- [2]. C.-H. Chen, J. A. Yeh, and P.-J. Wang 2006 J. Micromech. Microeng. 16, 1366.
- [3]. L. Schwaederlé, M.K. Kulsreshath, L. J. Overzet, P. Lefauchaux, T. Tillocher, and R. Dussart, 2012 J. Phys. D: Appl. Phys. 45, 065201.

- [4]. *E. Koç, S. Karaköse and B.G. Salamov* 2013 Phys. Status Solidi A
- [5]. *I. D. Kaganovich, M. A Fedotov and L. D. Tsengin* 1994 Tech. Phy. 39 241.
- [6]. *V. I. Kolobov and A. Fiala* 1994 Phy Rev E 50 3018.
- [7]. *B. M. Jelenković and A. V. Phelps* 1999 J. Appl. Phys. 85 7089.
- [8]. *V. P. Nagorny* 1999 J. Appl. Phys. 101 023302.
- [9]. *B. G. Salamov*, 2004 J. Phys. D: Appl. Phys. 37, 2496.
- [10]. *B. G. Salamov, Y. Öztekin Çiftci, and K. Çolakoglu*, 2004 IEEE Trans. Plasma Sci. 32, 2093.
- [11]. *A. V. Phelps and Z. Lj. Petrović*, 1999 Plasma Sources Sci. Technol. 8, R21.
- [12]. *V. Lisovskiy, J.-P. Booth, K. Landry, D. Douai, V. Cassagne, and V. Yegorenkov* 2006 J. Phys. D: Appl. Phys. 39, 660.
- [13]. *V.A. Lisovskiy and V.D. Yegorenkov* 1998 J. Phys. D: Appl. Phys. 31, 3349.
- [14]. *M. S. Mokrov and Yu. P. Raizer* 2008 Plasma Sources Sci. Technol. 17 035031.
- [15]. *R. R. Arslanbekov and V. I. Kolobov* 2003 J. Phys. D: Appl. Phys. 36 2986.

THE EFFICIENT PLASMA LIGHT SOURCE ON THE BASIS
OF NANOPOROUS ZEOLITEK. KOSEOGLU¹, B.G. SALAMOV^{1,2*} AND T.G. MAMMADOV²¹Physics Department, Faculty of Sciences, Gazi University, Beşevler 06500 Ankara, Turkey²National Academy of Science, G.M.Abdullayev Institute of Physics, AZ-1143 Baku, Azerbaijan

* bala@gazi.edu.tr

The stabilization of glow microdischarges (GMD) in a *dc* air plasma is studied experimentally functions of pressure p (18-760 Torr), interelectrode distances d (50-250 μm), and diameter D (9-22 mm) of the cathode areas in the gas discharge system (GDS) with nanoporous zeolite cathode for the first time. Comparison of current and discharge light emission (DLE) from GDS are used for the determination of the stabilization under low- and atmospheric pressure GMD conditions. It is found that the gas DLE inside the nanoporous zeolites develop from the surface if the amplitude of the applied voltage reaches given threshold. Moreover, uniform DLE can be generated in air up to atmosphere pressure. The effect of various diameters on the zeolite cathode area to the discharge is considered as well. It is also shown that breakdown voltage U_B is reduced significantly at atmospheric pressure when nanoporous zeolite cathode with large emitting area is used. Due to the very small electrode gap width we can describe the behaviour of the charged particles in the electric field of our system with the dc Townsend breakdown theory, depending on the pressure range.

Keywords: zeolite cathode, discharge light emission, atmosphere pressure, breakdown voltage, plasma light source**PACS:** 52.25.Jm; 52.80.-s; 51.50.+v

1. INTRODUCTION.

There is growing interest in non-thermal plasma processing techniques optimized for atmospheric pressure applications due to their significant industrial advantages. At atmospheric pressure, thin film deposition at very high rates is possible, and costintensive vacuum technology can be avoided. Many approaches have been proposed in the last 15 years to overcome the problems of generating and sustaining a stable, uniform and homogeneous non-thermal atmospheric pressure (AP) plasma [1,2].

There are two approaches based on the Paschen similarity law ($pd=\text{const}$), which scale down the electrode dimensions in the micrometre range in order to ignite discharges at atmospheric pressure, at moderate voltages, working in the Paschen minima of the different gases. Many authors use a microhollow-cathode-array in order to generate atmospheric pressure glow discharges. Recently, we suggested the use a planar gas discharge system (GDS) with semiconductor cathode as alternative large emitting area UV plasma source [3]. Such an idea has already been tried by using micro-hollow-cathode discharge (MHCD) geometries driven by continuous or pulsed dc power supplies. However, there is an inherent difficulty in large-scale integration due to the requirement of series resistors to balance all microdischarges, although parallel operation of multiple discharges in some schemes has been successful in MHCDs. This problem can be significantly avoided by using the semiconductor GDS with multichannels spacer. It is known [3] that if one of the electrodes is made in the form of a photocathode plate with a resistivity greater than $10^6 \Omega\text{cm}$ in a planar discharge cell, the gas discharge current can be distributed over the whole area of the electrodes, causing light emission by the of gas discharge (GDLE). The uniformity of the GDLE depends on the resistivity distribution of the photo-cathode plate, and the GDLE intensity is proportional to the discharge current. Such systems have reached a certain degree of technical perfection and at present they are adequate for different purposes of the registration of IR images [4]. Current density in the

converter is controlled locally to focus of optical IR pattern to a photosensitive semiconductor, which gives an image converted to visible radiation by means of discharge. But since the GDS with semiconductor cathode cannot effectively operate at atmospheric pressure, therefore we are used for the first time an insulating nanoporous zeolite which is an improvable advanced material instead of the semiconductor. Operating efficiently of the system will be based on the use of zeolite cathode, which is a good absorber of gas molecules in their nanoporous. Thus, this system differs from the wellknown planar GDS with GaAs cathode [5] in that the emitting surface of the cathode facing to the gas discharge was nanoporous zeolite cathode (ZC). The electrode dimensions, especially the electrode gap width d in the micrometer range, are small enough to generate sufficiently high electric field strengths to ignite atmospheric pressure glow discharges applying *dc* voltages (less than 1.5 kV). With this last type of plasma source plasma can be generated in air at atmospheric pressure. For these reasons, it is important to know the relation between the geometrical parameters and the discharge characteristics from the viewpoint of the cell optimization.

Deliberate modification of electrode surfaces with zeolites has evoked considerable interest. The attractive zeolite characteristics that are liable to affect the electron transfer reactions at an electrode-solution interphase are (a) the size and shape selectivity due to the rigid structure made of pores and channels of molecular dimensions; (b) the cation-exchange capacity arising from the charge compensation of the negatively charged aluminosilicate lattice by mobile extra framework cations; and (c) the catalytic properties of both intrinsic and extrinsic sites of the microporous materials. This has led to the design, preparation, and use of various zeolite-modified electrodes.

The zeolite frameworks are formed by chains of Si and Al anionites. The framework has a negative charge because of its structure and this charge is compensated by water molecules and cations of alkali and alkali-earth

metals Ca, K, Na, Mg weakly connected with it. Water can be removed by heating or evacuation of the zeolite, which has no effect on a rigid framework, its structure is virtually unchanged. The zeolite pores have the right forms. Connecting between each other through “windows” (0.26-0.27 nm), they form the perforated channel chain. That’s why the zeolites can be considered as the object on which besides well-known phenomena (adsorption, ion-exchange phenomena), investigate the electron porous emission, electron multiplication and gas discharge in pores, dielectric and electric properties at pore saturation by different gases and liquids.

The high emissive characteristics of nanotubes and pores provide the basis for a new class of electron emitters with extremely low supply voltage and power consumption [6,7]. Investigations into the emissive properties of different nanomaterials indicate that they are promising as field emitters. The unique emissive characteristics of carbon nanotubes render them effective electrode coatings in gas discharge devices. Field-emission-cathode gas-discharge luminescent lamps are widely used for the background illumination of liquid crystal screens.

2. EXPERIMENTAL.

The behaviour of the current-voltage characteristic (CVC) of the discharge cell with zeolite cathode is determined by the type of the discharge. Therefore CVCs of the zeolite plate were taken at different residual pressures and the *GDLE* from the pores was simultaneously detected. Natural zeolite was taken as a porous object. Zeolites are nonstoichiometric compounds, the compositions of which vary over wide limits and produce a series of solid solutions. Zeolites are aqueous aluminosilicates in which an infinite aluminosilicate frame is produced by $[\text{SiO}_4]^{4-}$ and $[\text{AlO}_4]^{5-}$ tetrahedra having common vertices. These tetrahedra have communicating cavities occupied by large ions and water molecules [8]. Clinoptilolite is the most abundant of the natural zeolites [9], but composition and purity vary widely among the many deposits found throughout the world. For our study we used $(\text{Ca}, \text{K}_2, \text{Na}_2, \text{Mg})_4\text{Al}_8\text{Si}_{40}\text{O}_{96} \times 24\text{H}_2\text{O}$ the clinoptilolite from Western Turkey deposit in Gordes Manisa. This natural zeolitic material contains on average 90-95% of the clinoptilolite zeolitic mineral [10,11]. Clinoptilolite belongs to a class of zeolite minerals having the clear-cut structural topology of heulandite (HEU) and the ratio of $\text{Si}/\text{Al} > 4.0$. The structural topology of the HEU tetrahedral lattice is well understood.

The experiments were carried out with a cathode plate made of a clinoptilolite type zeolite [12]. The ZC used in this work is plates having a diameter D of 22 mm and a thickness of 2 mm. The pressure in the chamber was monitored by a digital manometer attached to a pumping system and was kept at a certain constant value during the whole course of measurement. The entire experimental study of this work was performed in ambient air from 10^{-2} Torr pressures and the measurements were carried out at room temperature. The setup used here is similar to that applied earlier [13,14], where a GDED with a *GaAs* photodetector was studied at room temperature.

3. RESULTS AND DISCUSSION.

The CVCs of the *GDS* at atmospheric pressure were investigated. Fig. 1 gives typical CVCs for the discharge cell with different D of the ZC. Due to the very small d we can describe the behaviour of the charged particles in the electric field of our *GDS* with the dc Townsend breakdown theory, depending on the pressure range. At this point, we assume that a *homogeneous stationary* Townsend discharge [15] is established in the *GDS*. From the physical point of view, the most important feature of this kind of gas discharge is that space charge effects inside the gap are small and do not cause a distortion in the electric field between the electrodes. Another characteristic property is the homogeneous distribution of the current density perpendicular to the current flow. The *DLE* from the discharge is also homogeneous, while the wavelength of the *DLE* depends on the filled gas. The *DLE* intensity is proportional to discharge current. A local change of a ZC resistance leads to a local change of the current and the *DLE* [16].

Hence, the principle of operation of the *GDS* is based on some specific properties of the Townsend discharge. The voltage drop at the discharge gap for Townsend discharge mode is independent of the current. Therefore, the slope of the CVC provides the resistance of the ZC. Then, the specific conductivity can be computed from the resistance and the geometric dimensions. We notice that the current density in the *GDS* in the investigated parameter range does not exceed the limiting current for the existence of the Townsend discharge at given experimental conditions [4]. We remark that the feeding voltage V_0 is the sum of the voltage drops at the gas gap and at the zeolite component. One of the characteristic features of the Townsend discharge is the constancy of the voltage drop V_B at the discharge domain while current varies.

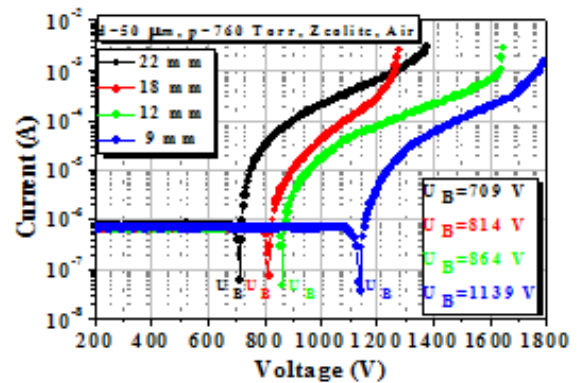


Fig. 1. The CVC of the discharge system with ZC at atmospheric pressure for the different values of D .

The range of the stationary operation and current depends on D of the active electrode area [17]. Considering this figure for the *GDS* with a ZC at different D of the electrode areas one can note the following: (a) the increment of D of the ZC areas leads to a decrease in U_B values for air (i.e. $U_B = 1139$ V for 9 mm and $U_B = 709$ V for 22 mm); (b) the current values rise abruptly at smaller values of D (e.g., $D = 9$ -18 mm) for AP; (c) the range of stable operation and current depend on the D of the electrode area. It is also found that the slopes of

current curves depend on the D . $GDLE$ inside the porous zeolites develop from the surface if the amplitude of the applied voltage reaches given threshold. Discharge inside the pores of ZC framework is produced by dc power supply and produce relatively cold microplasmas with high level of non-equilibrium with no instabilities. It is found that the gas in ZC pores ionizes and, accordingly, the number of electrons in the pores grows. It is shown that such a ZC in a planar gas discharge cell considerably reduces the ignition voltage of the GDS .

Strictly speaking, the most suitable interelectrode distance is $d = 50 \mu\text{m}$ up to the AP . This situation indicates that the better stabilization of dc glow discharges at AP can be obtained for ZC in GDS . Thus, it is possible to produce gas discharges up to AP by means of GDS at moderate voltages so that wide areas of plasma applications become feasible under those conditions. For further step, the physical processes determining the stable function of an ionization system and spatial stabilization of the discharge can be taken into account as a result of the distributed resistance of the ZC. Because, stabilization effect is closely related to the CVC results obtained for different ZC diameters. Therefore, representative plots of CVC s in cases of different cathode D at AP are shown in Fig. 1.

It can be seen that the CVC s have a smooth current increase, but they are completely different from the CVC s of the GDS with $GaAs$ semiconductor cathode (for comparison see Fig. 2 in [3]). Fig. 1 also show that with a change in the D the U_B changes and the form of the CVC s is reproducible, expect for minor differences in the values of the current. Our previous works [18] commented on the physical properties of microdischarges generated inside the porous zeolite by dc driven discharges. The detailed description of the discharge properties with respect to the effect of the pore size, discharge power, and gas mixture can be found in [19]. The results showed that the microplasmas inside the ceramic foam formed only for the specific discharge power and pore size of the ceramics. At small voltages, a surface barrier discharge on the surface of the ceramics may only be observed. With the increase of the applied voltage, however, the surface discharges transits into capillary microdischarges inside the ceramics, which onset voltage increases with the decreasing pore size. Upon the transition to microdischarges, the amplitude of the current pulses increases extremely, as well as the corresponding discharge current and power. The increase of the discharge current is larger for the bigger pore size, due to the increase of the radius of the discharge channel and volume of the generated microplasma.

The current dependence on pressure for GDS with ZC at $U_0 = 1000 \text{ V}$ is shown in Fig. 2. With a change in the residual gas pressure up to AP the current changes. In a running experiment, the pressure p and the conductivity of the porous ZC and semiconductor cathode are fixed, and the supply voltage U_0 is slowly increased from 0 V , thereby increasing the voltage drop at the gas layer. As soon as U_0 reaches the critical voltage for breakdown in the gas, homogeneous ignition of the discharge takes place. The value of the critical voltage and residual pressure are determined by the so-called Paschen curve [20].

Fig. 2 shows detailed information regarding the CVC of the cell with respect to pressure when a dc voltage of a high enough magnitude is applied to the system. The voltage value from U_B to feeding voltage U_0 applied to the electrodes is the potential drop across the ZC cathode, whereas the value from 0 to U_B is mainly the potential drop at the discharge gap. The optimal operation value of d is found as $50 \mu\text{m}$ for air-filled GDS . However, the atmospheric pressure is much more compatible and optimal for planar gas discharge cell with ZC, as shown in the values of current and DLE in Figs. 2 and 3, respectively. In addition, discharge currents and DLE intensities in GDS with ZC are much larger and intensive compared to the air-filled cell with $GaAs$ cathode. In the GDS with $GaAs$ cathode, DLE satisfies the optimal and effective conditions at lower pressures (15-350 Torr), i.e., the current and DLE intensities in this media are high.

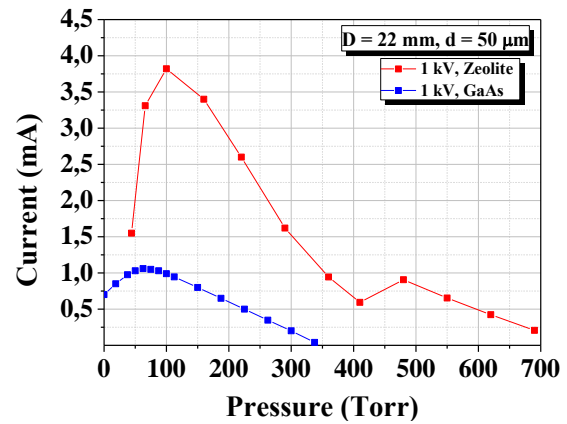


Fig. 2. Current dependence on pressure for discharge system with ZC and $GaAs$ cathode under strong illumination.

However, the situation of current and DLE intensities becomes vice versa near the AP . In other words, while an instant decrease in the DLE intensities from the GDS with $GaAs$ cathode is observed, higher DLE intensities are obtained from cell with ZC, conversely. Moreover, maximum DLE intensity values are very different in GDS with $GaAs$ cathode, whereas these values are the almost the same in system with ZC near the AP , as shown Fig. 2. This situation proves that one should prefer to use ZC at AP s rather than $GaAs$ cathode since the DLE values are better. It can be also stated that the better stabilization of dc glow discharges at AP s can be obtained for GDS with ZC.

Fig. 3 shows the same behaviour of the DLE in a gas discharge cell with the semiconductor and ZC. For a thin discharge gap of the cell the proportionality between the gas brightness and the current density, j , can be observed in a broad range of j . Note that when the feeding voltage is higher than 750 V , the curve for ZC in Fig. 3 represents the saturation of the DLE intensity, which is related to the maximal limit of the photomultiplier. Moreover, the shape of the CVC and the DLE intensity in a system depend on the voltage increment of the power supply [13]. The dependence of the intensity of the $GDLE$ and ignition of discharges associated with all nanopores of ZC on the electric field strength is shown in Fig. 3. We have observed a significant increase of the discharge brightness in

the discharge gap with ZC compared to that of the main traditional discharge gap with *GaAs* semiconductor cathode [3]. It is seen that the gain G increases exponentially with feeding voltage. Such dependence is in accordance with the literature data for gain measurements in gas electron multipliers [21] and reflects the existence of the avalanche electron multiplication mechanism. One can see that in this case there is a significant increase in the output brightness, which takes place thanks to initiation of a self-sustained discharge in the multichannels. At fixed feeding voltage U_0 the brightness is proportional to the current density of the gap and seems to behave linearly to the current range covered here. The maximum gain achieved in the present work is 50 for the pressure of 45÷50 Torr and the feeding voltage $U_0 = 900$ V.

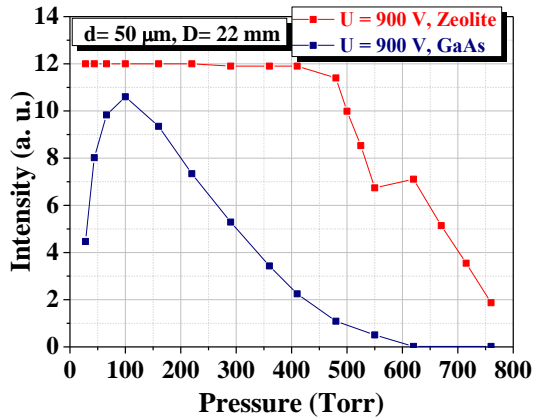


Fig. 3. DLE dependence on pressure for discharge system with ZC and *GaAs* cathode under strong illumination.

The filamentation was primarily due to the formation of a space charge of positive ions in the discharge gap, which changed the discharge from the Townsend to the glow type [22,23]. The intensity of *DLE* in the system with ZC exceeds the intensity of the *DLE* in the system with *GaAs* cathode. In earlier publication [22], we showed that the use of metallic patched concentrators with an area of $S = 5 \times 10^{-4} \text{ cm}^2$ and a density of 400 cm^{-2} leads to a five-fold increase in the gas light intensity. In this case the local intensity of *DLE* exceeds the intensity of uniform *DLE* in the system without metallic patched concentrators as many times as the working area of the photocathode exceeds the total area of the current concentrators.

The obtained electrical characteristics of *GDS* with a ZC and the comparison of the discharge patterns show that the system possesses a noticeably larger discharge light amplification or gain G . Electrons entering the pores of the ZC in the discharge gap are multiplied in the electric field by the avalanche mechanism, so that a rather small current in the discharge gap without pores becomes a much larger current in the gap with ZC. Since the current is concentrated in the pores of ZC, the source of the loss of resolution i.e., electron scattering with the flight between the discharge electrodes disappears [24]. Thus, the *GDS* with ZC shows good technical performance. The *DLE* of the latter is observed from the backside of the structure. Thus, it is experimentally demonstrated that gas discharge gap with ZC can be used for generating and sustaining a stable, uniform and homogeneous non-thermal atmospheric pressure plasma.

4. CONCLUSION.

By analysing the current and optical emission from a plasma discharge, more complete information can be obtained about the possibility of varying the intensity of the light emitted by a *GDS* with ZC, especially with its working as plasma light source with the prolonged working time. Specific geometry of the zeolite channels structure and the strong electric field in the nanopores provide an efficient electron multiplication and related excitation of gas atoms. The use of gas discharge gap with nanoporous ZC leads to increase in the *GDLE* intensity. In a system with ZC, the total intensity of *GDLE* exceeds the intensity of uniform *GDLE* in the *GDS* with *GaAs* photocathode. This device may find an application in for generating and sustaining stable, uniform and homogeneous non-thermal atmospheric pressure plasma.

Thus, it is experimentally demonstrated that *GDS* with ZC can operate as an effective light intensifier up to *AP* with gain values of 40÷50 observed. We also believe that on the basis of the outlined principles, by using dielectric spacer of proper design with a large number of multichannels and a single-hole microcapillary discharge plate (i.e. suggested in [25]) it is possible to build ultrafast and rather sensitive large emitting area plasma light source with internal image amplification.

ACKNOWLEDGMENTS. This work is supported by Gazi University BAP research Projects 05/2012-26, 05/2012-64 and 05/2012-55.

- [1]. T. Yokoyama, M. Kogoma, T. Moriwaki and S. Okazaki 1990 J. Phys. D: Appl. Phys. 23 1125.
- [2]. F. Massines, A. Rabehi, P. Decomps, R.B. Gadri, P. Segur and C. Mayoux 1998 J. Appl. Phys. 83 2950.
- [3]. B.G. Salomov, Y. Çiftci, K. Çolakoglu 2004 IEEE Transactions on Plasma Science 32 2093.
- [4]. H. Willebrand, Y. Astrov, L. Portsel, S. Teperick and T. Gauselmann 1995 Infrared Phys&Technol. 36 809.
- [5]. B.G. Salomov, M. Özer, M. Kasap and S. Altındal 1999 J. Phys. D: Appl. Phys. 32 682-687.
- [6]. A.V. Eletsii 1997 Usp. Fiz. Nauk 167 945 [1997 Phys. Usp. 40 899].
- [7]. Yu.V. Gulyaev, L.A. Chernozatonskii 1995 J. Vac. Sci. Technol. B 13 435.
- [8]. G. Gottardi and E. Galli 1985 Natural Zeolites (Berlin: Springer).
- [9]. C. Senaratne, J. Zhang, M.D. Baker, C.A. Bessel, D.R. Rolison 1996 J. Phys. Chem. 100 5849.

- [10]. *A. Giaya, R.W. Thompson, R. Denkwicz* 2000 Microporous Mesoporous Mater. 40 205.
- [11]. *Ch. Baerlocher, W.M. Meier and D.H. Olson* 2001 Atlas of Zeolite Framework Types (Amsterdam: Elsevier).
- [12]. *G. Vitale, L. Bull, R.E. Morris, A.K. Cheetham, B.H. Toby, C.G. Coe and J.E. MacDougall* 1995 J.Phys. Chem. B 99 16087.
- [13]. *B.G. Salamon, S. Büyükkakış, M. Özer, K. Çolakoglu* 1998 Eur. Phys. J. Appl. Phys. 2 275.
- [14]. *V.I. Orbukh, N.N. Lebedeva, S. Ozturk, B.G. Salamon* 2013 Superlattices and Microstructures 54 16-25.
- [15]. *B.G. Salamon, Ş. Ellialtıoglu, B. Akinoglu, N.N. Lebedeva* 1996 J. Phys. D: Appl. Phys. 29 628.
- [16]. *B.G. Salamon, K. Colakoglu and S. Altındal* 1995 Infrared Phys. & Technol. 36 661.
- [17]. *H.Y. Kurt and B.G. Salamon* 2003 J. Phys. D: Appl. Phys. 36 1987.
- [18]. *V.I. Orbukh, N.N. Lebedeva, S. Ozturk, S. Uğur, B.G. Salamon* 2012 J. Optoelectron. Adv. Mater. 4 205.
- [19]. *K. Hensel, V. Martisovits, Z. Machala, M. Janda, M. Lestinsky, P. Tardiveau, A. Mizuno* 2007 Plasma Process. Polym. 4 682-693.
- [20]. *Y.P. Raizer* 1991 Gas Discharge Physics (Berlin: Springer).
- [21]. *H. Sakurai, T. Tamura, S. Gunji, and M. Noma* 1996 Nucl. Instrum. Methods Phys. Res. A 374 341.
- [22]. *K. Aktas, S. Acar, B.G. Salamon* 2011 Plasma Sources Sci. Technol. 20 045010.
- [23]. *B.G. Salamon, M. Kasap and N.N. Lebedeva* 2000 J. Phys. D: Appl. Phys. 33 2192.
- [24]. *A.V. Phelps, B.M. Jelenkovic* 1987 Phys Rev.A 36 5327.
- [25]. *L.M. Portsel, V.M. Marchenko and H.G. Purwins* 2005 J. Appl. Phys. 97 076101.

THE CHARGE TRANSPORT IN THE NANOPOROUS NATURAL ZEOLITE

K. KOSEOGLU¹, I. KARADUMAN¹, S. ACAR^{1*} AND B.G. SALAMOV^{1,2}¹Physics Department, Faculty of Sciences, Gazi University, Beşevler 06500 Ankara, Turkey²National Academy of Science, G.M.Abdullayev Institute of Physics, AZ-1143 Baku, Azerbaijan

*sacar@gazi.edu.tr

We present the electrical characterization of a natural zeolite plate and charge transport is studied functions of pressure (4-760 Torr), temperatures (295-435 K) and diameter D (5-25 mm) of the cathode areas in the gas discharge electronic devices (GDED) with nanoporous zeolite cathode (NZC) for the first time. There are not enough investigations devoted to conductivity of zeolites in a dc voltage mode. Comparison of current from GDED is used for the determination of the stabilization under low- and atmospheric pressure (AP) glow microdischarges conditions. It is found that the gas in zeolite pores ionizes and, accordingly, the number of electrons in the pores grows. Moreover, we established that in the studied temperature range, resistance R of NZC decreases from 7.31×10^{10} to $7.19 \times 10^8 \Omega$ as temperature increases from 295 to 435 K. In this range, there exists only one linear region representing the activation energy E_a value as 0.309 eV. The experimentally obtained electronic and ionic conductivities and their interactions are discussed. It is of importance to have knowledge in peculiarities of operation of GDED. It can be supposed that cheap natural zeolite will be effective in low-power GDED.

Keywords: nanoporous natural zeolite, charge transport, activation energy, electronic conductivity, temperature dependence

PACS numbers: 72.20.i; 72.50.Ht; 52.80.-s; 51.50.+v

1. INTRODUCTION

Clinoptilolite has received the greatest attention in literature on the ion conducting properties of zeolites, perhaps due to early reports revealing a high frequency relaxation in these materials, or because of the wealth of crystallographic knowledge pertaining to the zeolite structure, i.e., aluminium framework sites, cation positions, etc. [1,2]. Electrically conducting zeolite-like frameworks are largely unstudied as electronic materials, but may offer new avenues in energy applications, ranging from electrical energy storage to catalysis. Zeolite materials are characterized by the presence of nanoscale channels and pores delineated by their crystalline framework. Here, we present a clinoptilolite with framework composition $(\text{Ca}, \text{K}_2, \text{Na}_2, \text{Mg})_4 \text{Al}_8 \text{Si}_{40} \text{O}_{96} \times 24\text{H}_2\text{O}$, that suggested can be exhibits mixed conductivity -ionic and electronic. Certainly, if the focus of the electron transfer was the intrazeolite surface, then the prospects for product and transition state shape selectivity would be good.

A variety of experimental techniques, such as, dc conductivity studies [3], the monofrequency dielectric method [4,5] and impedance spectroscopy [6], have been employed for the assessment of conduction parameters in zeolitic structures. The measurement of accurate and meaningful conductivity values, especially in such polycrystalline materials, is a quite hazardous procedure, in as much as the usual polarization effects at the electrode-solid electrolyte interface obscure a correct assessment. Interfacial problems in dc conductivity measurements may be overcome by using reversible electrodes (e.g. molten sodium and solid solution electrodes). Pure bulk dc conductivity values can also be extracted from ac data, and in some favorable cases, it is possible to obtain information about electrode capacitance, intergranular resistances, capacitances, and the amount of electronic conductivity present. In case where the monofrequency technique is used for the measurement of the pellets resistance, the accuracy depends the more on the selection of the working frequency the lower the temperature is. In the somewhat

more complicated but reliable impedance spectroscopy method the effective resistance and the reactance of the material is measured over a wide frequency range, and the impedance spectra are discussed in terms of equivalent-circuit diagrams [7].

For many common nonmetallic materials, the measured conductivity σ_{ac} is usually expressed in the form

$$\sigma_{ac}(\omega, T) = \sigma_0 + \sigma'(\omega) \quad (1)$$

where σ_0 is the steady state conductivity and $\sigma'(\omega)$ the purely dispersive component of the ac conductivity. Based on the Nernst-Einstein theory, σ_0 shows a temperature dependence of the Arrhenius type (more precisely an Eyring-type law)

$$\sigma_0 T = \left(\frac{Nq^2}{\lambda k_\beta} \right) \exp \left(\frac{\Delta S}{k_\beta} \right) \exp \left(-\frac{E_{dc}}{Tk_\beta} \right) \quad (2)$$

where N , q are the number and electric charge of the mobile ions respectively, ΔS is the entropy of activation and λ a factor related to the specific jump process. E_{dc} is the dc activation energy which is generally expressed as $E_{dc} = E_d + E_m$, where E_d is the energy required for the creation of a defect charge carrier ($E_d \ll$ in zeolites) and E_m the energy required for ion migration from its trapping site. A plot of $\ln(T\sigma_0)$ as a function of the inverse of the absolute temperature should yield a straight line having a slope of $-E_{dc}/k_\beta$. The approximation of temperature independent dc activation energy has been experimentally confirmed in a wide range of zeolitic structures, which show a linear temperature dependence of σ in the Arrhenius diagrams. Conduction phenomena in natural and synthetic zeolite structures are ionic bulk processes ascribed to the highly mobile groups of the charge-balancing cations in a diffusion rate process, throughout sequences of successful jumps (configurational tunnelling) between localised trapping sites [8].

The zeolite frameworks are formed by chains of *Si* and *Al* anionites. The framework has a negative charge because of its structure and this charge is compensated by water molecules and cations of alkali and alkali-earth metals (Na^+ , K^+ , NH_4^+ , Ca^{2+}) weakly connected with it. Water can be removed by heating or evacuation of the zeolite, which has no effect on a rigid framework, its structure is virtually unchanged. The zeolites can be considered as the object on which besides wellknown phenomena (adsorption, ion-exchange phenomena), investigate the electron porous emission, electron multiplication and gas discharge in pores, dielectric and electric properties at pore saturation by different gases and liquids [9]. In earlier study we used the gas discharge electronic devices (GDED) with *GaAs* cathode which is cannot effectively operate at atmospheric pressure (AP), so an insulating nanoporous zeolite is used to understand conduction mechanism for the first time in this study. Operating efficiently of the system will be based on the use of zeolite cathode (ZC), which is a good absorber of gas molecules in their nanoporous. Thus, this system differs from the wellknown planar GDED with *GaAs* cathode [10] in that the emitting surface of the cathode facing to the gas discharge was nanoporous ZC. Therefore, the question of the possibility of penetrating of the ion conductivity zeolites on direct current and application of nanoporous zeolites in a GDED is open for discussion.

In this work, we report for the first time to our knowledge, direct observations of the steady-state or/and continuously falling currents at dc voltage mode in a wide range of pressure up to the AP and in ambient air microdischarges and that is not a trivial characteristic of ionic conduction in the nanopores natural zeolite (NZ). The current-voltage characteristics (CVC) of the zeolite plate were taken at different residual pressures, temperatures and the gas discharge light emission (GDLE) from the pores was simultaneously detected. It is found that, when such a zeolite plate used as a cathode in a planar gas-discharge cell, in the natural zeolite another mechanism of conductivity due to electron multiplication in the pores is possible also and the ignition voltage of the discharge uniformly distributed over the electrode surface considerably drops.

2. EXPERIMENTA

Natural zeolite (clinoptilolite) was taken as a large-diameter NZC. Zeolites are nonstoichiometric compounds, the compositions of which vary over wide limits and produce a series of solid solutions [9]. The thickness is 1 mm and the diameter D of clinoptilolite zeolite plate is 22 mm which is the most suitable D for reduce the U_B . The setup used here is similar to that applied earlier [11], where a GDED with a *GaAs* photodetector was studied at room temperature. The GDLE intensity from the cell was detected by photomultiplier head (ELSEC 9010). The photomultiplier tube of the unit (Thorn-EMI 9235 QA) has a high sensitivity in the UV-blue region of the spectrum which coincides with the GDLE from the cell. Electrical peripherals consist of a Digital Multimeter (Keithley 199) and a DC Power Supply (Stanford PS 323, 2500V). The electrical circuit is

interfaced to PC by data acquisition card. The resistivity of zeolite was measured by two-point probe method with a Keithley 2400 sourcemeters at room temperature.

When determining the breakdown voltage U_B , the growth rate of the discharge voltage does not exceed 1 V/s. Besides, the feeding voltage U_0 or the rate of feeding voltage can be changed easily in the experiments. Therefore, these two quantities are used as the main control parameters. Other parameters like gas pressure p and discharge gap thickness d remain fixed or changed discontinuously in a wide range. In a running experiment, the pressure p and the conductivity of the natural zeolite cathode are fixed and the U_0 is slowly increased from 0 V thereby increasing the voltage drop at the gas layer. As soon as U_0 reaches the critical voltage for breakdown in the gas, homogeneous ignition of the discharge takes place. The value of the critical voltage is determined by the so-called Paschen curve [5].

3. RESULTS AND DISCUSSION

Insert in Fig. 1 presents the CVC of the parallel-plane geometry with respect to D of the zeolite electrode areas. The range of the stationary operation and current depends on D of the active electrode area [11]. Considering this figure for the system with a NZC at different D , of the electrode areas, one can note the following: (a) the increment of D of the NZC areas leads to a decrease in U_B values for air (i.e. $U_B = 1139$ V for 9 mm and $U_B = 709$ V for 22 mm); (b) the current values rise abruptly at smaller values of the D (e.g., $D = 9$ -18 mm) for AP; (c) the range of stable operation and current depend on the D of the electrode area. It is also found that the slopes of current curves depend on the D . GDLE inside the microporous zeolites develop from the surface if the amplitude of the applied voltage reaches given threshold. Discharge inside the micropores of zeolite framework is produced by dc power supply and produce relatively cold microplasmas with high level of non-equilibrium with no instabilities. It is found that the gas in zeolite pores ionizes and, accordingly, the number of electrons in the pores grows. It is shown that such a zeolite plate used as a NZ in a planar gas discharge cell considerably reduces the ignition voltage of the GDED.

Strictly speaking, the most suitable interelectrode distance is $d = 50$ μm up to the AP. This situation indicates that the better stabilization of dc glow discharges at AP can be obtained for NZC in GDED. Thus, it is possible to produce gas discharges up to AP by means of GDED at moderate voltages so that wide areas of plasma applications become feasible under those conditions. For further step, the physical processes determining the stable function of an ionization system and spatial stabilization of the discharge can be taken into account as a result of the distributed resistance of the NZC. Because, stabilization effect is closely related to the CVC results obtained for different NZC diameters. Therefore, representative plots of CVCs in cases of different cathode D at AP are shown in insert of Fig. 1. Our previous works [9] commented on the physical properties of microdischarges generated inside the porous zeolite by dc driven discharges. The detailed description of the discharge properties with respect to the effect of the pore

size, discharge power, and gas mixture can be found in [12]. The results showed that the microplasmas inside the ceramic foam formed only for the specific discharge power and pore size of the ceramics. At small voltages, a surface barrier discharge on the surface of the ceramics may only be observed. With the increase of the applied voltage, however, the surface discharge transits into capillary microdischarges inside the ceramics, which onset voltage increases with the decreasing pore size. Upon the transition to microdischarges, the amplitude of the current pulses increases extremely, as well as the corresponding discharge current and power. The increase of the discharge current is larger for the bigger pore size, due to the increase of the radius of the discharge channel and volume of the generated microplasma.

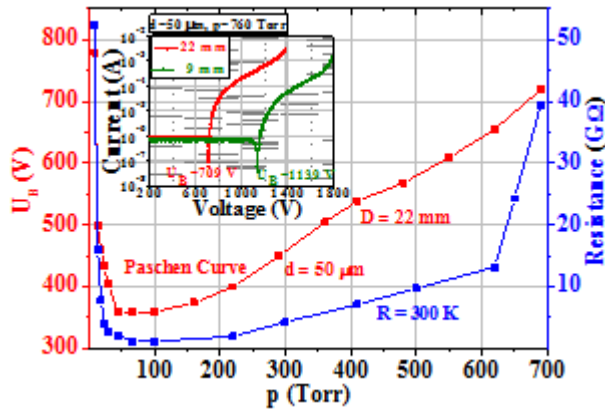


Fig. 1. Pressure dependence of U_B (i.e. Paschen curve) and zeolite resistance in the GDED at room temperature.

The breakdown voltage (U_B) is an essential experimental parameter that is very useful for the understanding of microplasma discharges. It provides essential information separating the gas state from the plasma discharge state. The U_B of a gas discharge and the corresponding breakdown value depend on the gas type, the material of the cathode, the pressure, and the discharge gap width (see Fig. 1). A combination of gas and electrode surface processes is important to the left of pd_{min} . The 'left-side' of the Paschen curve exists in a running experiment. It is also obvious that Paschen curve for $D=22$ mm have almost similar behaviour with resistance change curve.

At the same time, the electrical resistance R measurements were carried out on clinoptilolite sample in the temperature range of 295-435 K. Fig. 2 shows the variation of the R as a function of temperature for the NZC sample with 1 mm thickness. An increased interaction between water and the mobile charge balancing cations, an increase in the protonic conduction contribution, and/or an increase in cation mobility with increasing temperature are thought to be the possible factors responsible for the conductivity increase. Room temperature resistivity ρ was determined as $7.31 \times 10^{10} \Omega \text{cm}$. In the studied temperature range, it was observed that the R of NZC decreases from 7.31×10^{10} to $7.19 \times 10^8 \Omega$ as temperature increases from 295 to 435 K. The experimental data of resistivity - temperature dependence can be analyzed and calculated based on.

$$\rho(T) \propto \exp(E_a / k_B T) \quad (3)$$

$$\rho = \rho_0 \exp(-E_a / k_B T) \quad (4)$$

where ρ_0 the pre-exponential factor and E_a is the resistivity activation energy. E_a value was found from the linear fit the $\ln \rho - 1000/T$ graph. In this range, there exists only one linear region representing the activation energy E_a value as 0.309 eV.

The magnitude of the ionic conductivity and its temperature dependence expressed by the corresponding activation energy E , is a complex quantity determined by a number of factors; the electrostatic interaction (coulombic factor) between the negatively charged framework and the mobile cations, as well as sterical effects caused by the relative size of the ions and the narrowest points in the cations' conduction path play a critical role. Related effects are expected to be effectively demonstrated in zeolites since the group contains members with a gradation of channel sizes and shapes, and with charge balancing ions of different ionic radii. Their sizes directly affect the cation-lattice coulombic interaction. An additional contribution arises from the intercationic repulsions, which has to be considered, especially for large ions and high ionic concentrations (low $\text{SiO}_2/\text{Al}_2\text{O}_3$ ratio). Molecular adsorption results to a much more complex behaviour [13].

Experimentally obtained temperature dependences of the resistance of clinoptilolite samples is shown in Fig. 2. As it can be seen from Fig. 2 when the temperature increases the resistance of the zeolite sample decrease exponentially. The increase in temperature leads to a change in the concentration and mobility of water molecules and exchanged cations as result of structural relaxation and dissociation of water. A sharp decrease in the resistance observed in the low temperature range (295 - 435 K). At room temperature for the clinoptilolite samples containing monovalent cations resistance decreases more than two times, at the same time for the samples with divalent cations resistance decreases - almost an order of magnitude. The experimental results can be explained as follows. In a bulk crystal with ionic conductivity, ion migration is possible at availability of defects sublattice or vacancies under the influence of an electric field. Ion transitions which cause conductivity at dc are the main way along the walls of the channels and cavities. Ion mobility in clinoptilolite depends on the energy of their connection with the host lattice.

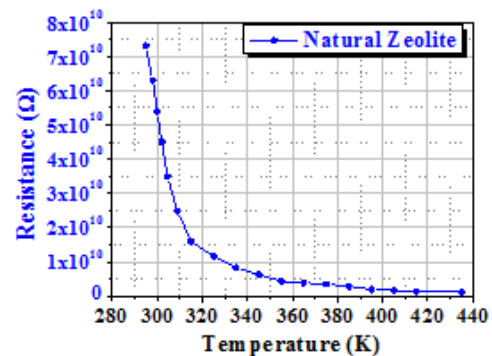


Fig. 2. Temperature dependence of measured electrical resistance for zeolite.

During conductivity involves only those ions, which under the influence of the thermal motion ripped from their localized centers and are more in the free state. These ions must overcome some potential barrier that keeps ion [14], therefore their number is insignificant. Ions have to move from vacancy to vacancy, i.e., from one potential well to another. Water molecules and impurities can be adsorbed on vacancies (lattice defects). First of all at adsorption the deepest potential wells will be filled. Then the vacancies for movement of ions will be less with deep wells. As the temperature increase the number of vacancies becomes less that leads to reduce activation energy of exchanged cations at sufficiently high temperatures. It seems from this point the zeolite framework can take up to 90% of the water. For existence of ionic conductivity must be free ions, the occurrence of which may be due to dissociation and external influences. It is possible in the case when ion energy is not less than the difference energy between the bound and free state of the ion. In addition, at some distance should be a new center for localization of ion. At constant strength of electric field the ion will move on these localized centers. In the high-temperature range the conductivity is due to mainly loosely coupled with a framework exchange cations, having a greater concentration and mobility [15].

Even a single cation jump process in the sublattice of the interstitial sites, induces small adjustments in the equilibrium configuration of the interacting particles. In the zeolites case, where the electrical conductivity and the diffusion process occur by the same mechanism, the specific ionic conductivity σ (S cm^{-1}) and diffusion coefficient D (cm^2/s), are related by the Nernst-Einstein law

$$\sigma T = (nq^2/k_B f) D \quad (5)$$

where n is the concentration of diffusing particles (cm^{-3}) and f a geometrical factor which accounts for the non-random migration mechanism (geometrical correlation factor or *Haven ratio*). In conformity with the observation of highly correlated ionic motions, Schoonheydt [16] adjusted the above relation by introducing a supplementary ionic conduction correlation factor f_i ($f^* = f/f_i$). For the benefit of the succeeding discussion it would be useful to mention that the diffusion coefficient is proportional to the product of the vacant sites concentration and the jump probability.

The conductivity of zeolites is strongly affected by their composition, a situation which is to be expected by the general expression, widely used for liquid electrolytes,

$$\sigma = \sum_i n_i q_i \mu_i \quad (6)$$

relating σ with the mobility of the carriers μ_i , of species i , their charge q_i and concentration n_i . The concentration, and sequentially σ , is expected to be inversely proportional to the $\text{SiO}_2/\text{Al}_2\text{O}_3$ ratio [17]. The rise of the silicon content signifies a decreased number of negative charges per unit volume of the NZ framework and a greater average distance between them. Even with the assumption that all the exchangeable cations are potential

conductivity carriers, fewer effective charge carriers will lead to a decline of the conductivity. In addition, the corresponding elongation in the distance of the extraframework cationic sites increases the mean length of the cation jumps responsible for conduction, and thus reduces the values of the ionic conductivity [18].

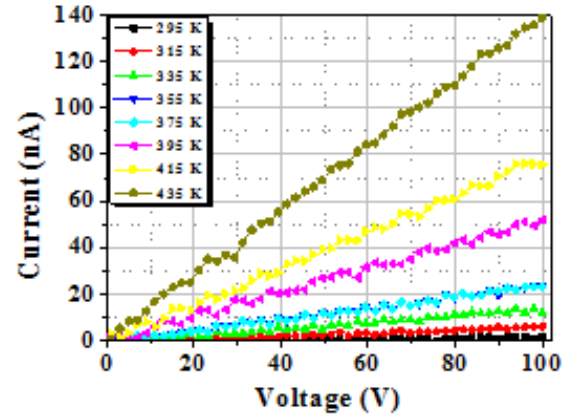


Fig. 3. CVC of a gas discharge cell according to different temperature.

The experimental results of temperature dependence of the CVCs in the clinoptilolite samples are shown in Fig. 3. By decreasing the aluminum content, the conductivity values (at a constant temperature) display a dramatic reduction, of about five orders of magnitude around 523 K. The conductivities of the relatively Al-rich Y zeolite are substantially greater than those of the dealuminated zeolite DY, which has far fewer ions per unit cell contributing to the ion conductance [19].

In [20] authors indicate that a common feature of the conductivity in both liquid and solid electrolytes is the fact that Eq.6 can be applied only for low cation concentrations, since σ passes through a maximum before it decreases as the carriers density is increased [21] and the intercationic repulsions make a significant contribution. The location of the maximum on the curve of σ versus n appears to be determined by the zeolite structural configuration, the nature and size of the ionic particles, and hydration conditions.

4. CONCLUSION

The temperature dependence of the current in an GDED with NZ on control parameters (p , D) is investigated in air. Our results shows that the spatial distribution of the emitted lights in air corresponds to the stationary regimes up to AP. Influence of porous zeolite structure on electrical conductivity of clinoptilolite samples are investigated in the temperature range 295-435 K. Discovered an increase in temperature dependence of conductivity, which satisfactorily explains the exponential law. It is also observed that the R of NZC decreases nearly 100 fold as temperature increases and in this range, there exists only one linear region representing the activation energy E_a value as 0.309 eV. It is shown that U_B is reduced significantly at AP when the D of NZC is increased. It is also obvious that Paschen curve for $D = 22$ mm have almost similar behaviour with resistance change

curve. It is established that the effect of various D on the clinoptilolite cathode area to the discharge are provided stable, homogeneous, nonthermal and controllable operation with a large emitting area operating at AP for developing miniature field-portable instruments.

ACKNOWLEDGMENT: This work is supported by the Gazi University BAP research projects **05/2011-28, 05/2012-37**.

-
- [1]. A. Adboulaye, J.V. Zanchetta, F.D. Renzo, J.C. Giuntini, J. Vanderschueren, G. Chabanis 2000 Microporous Mesoporous Mater. **34** 317.
 - [2]. A. Nicolas, S. Devautour-Vinot, G. Maurin, J.C. Giuntini, F.J. Henn 2007 J. Phys. Chem. C **111** 4722.
 - [3]. K.V. Topchieva, I. F. Moskovskaya and V.Ya. Stetsenko 1963 Russ. J. Chem. **7** 1020.
 - [4]. D.C. Freeman and D.N. Stamires 1961 Chem. Phys. **35** 799.
 - [5]. N. Petranovic, M. Susic 1991 J.Chem. Soc. Faraday I **75** 2083.
 - [6]. N. Knudsen, E. Krogh Andersen, I.G. Krogh Andersen, P. Norby and E. Skou 1993 Solid State Ionics **61** 153.
 - [7]. P. Kurzweil, W. Maunz and C. Plog 1995 Sensors and Actuators B **25** 653.
 - [8]. G.T. Kerr 1973 Adv. Chem. Series **121** 219.
 - [9]. V.I. Orbukh, N.N. Lebedeva, S. Ozturk, Ş. Uğur and B.G. Salamov 2012 Optoelectron. Adv. Mat. **6** (11) 947.
 - [10]. Salamov B G, Özer M, Kasap M and Altındal S 1999 J. Phys. D: Appl. Phys. **32** 682–687
 - [11]. K. Aktas, S. Acar and B.G. Salamov 2011 Plasma Sources Sci. Technol. **20** 045010.
 - [12]. K. Hensel, V. Martisovits, Z. Machala, M. Janda, M. Lestinsky, P. Tardiveau, A. Mizuno 2007 Plasma Process. Polym. **4** 682.
 - [13]. W.M. Butler, C.L. Angell, W. McAllister and W.M. Risen 1977 J. Phys. Chem. **81** 2061.
 - [14]. Yu.M. Poplavko 1980 Dielectric Physics (Kiev: Visha Shkola) p 398.
 - [15]. L.P. Karatsuba, V.A. Yevdokimova, S.V. Lankin 2007 Perspect. Mater. **N 5** 340-342.
 - [16]. R.A. Schoonheydt 1980 J. Physique C **6-216** 41.
 - [17]. F.J.Jansen and R.A.Schoonheydt 1973 J. Chem. Soc. Faraday Trans. I **69** 1338.
 - [18]. G. Kelemen and W. Lortz 1992 J. Mater. Sci. **27** 6036.
 - [19]. P. Nischwitz, P. Amels and F. Fetting 1994 Solid State Ionics **73** 105.
 - [20]. S.D. Mikhailenko, S. Kaliaguine and E. Ghali 1997 Microporous Mater. **11** 37.
 - [21]. N.H. Mogensen and E. Skou 1995 Solid State Ionics **77** 51.

ON FEATURES OF POTENTIAL DISTRIBUTION IN AVALANCHE PHOTODIODES WITH DEEPLY BURIED PIXELS

Z.Y.SADYGOV^{1,2}, X.I.ABDULLAYEV³, F.I.AHMADOV^{2,4}, E.A.JAFAROVA¹,
A.A.DOVLATOV¹, R.C.MADATOV^{3,4}, R.M.MUXTAROV³, A.Z.SADYGOV^{2,4},
N.A.SAFAROV¹

¹ G.M.Abdullayev Institute of Physics of ANAS, AZ-1143, Baku, Azerbaijan.

² Joint Institute of Nuclear Research, 141980, Dubna, Russia.

³ Azerbaijan National Academy of Aviation, AZ-1045, Baku, Bina, Azerbaijan.

⁴ Institute of Radiation Problems ANAS, AZ-1143, Baku, Azerbaijan.

The shape of potential distribution in micro-pixel avalanche photodiodes (MAPD) with deeply buried pixels is investigated. It was found that the electrons created in the photosensitive part of the device are collected to the corresponding n^+ -pixel and multiplied in the avalanche region. At the same time the holes generated in the semiconductor substrate, passes through the gaps between the n^+ -pixels, and therefore they are not amplified. This results in improvement the both signal/noise ratio and radiation resistance of the device.

Key words: micropixel avalanche photodiode; silicon photomultiplier; avalanche multiplication of charge; potential distribution.

PACS: 07.77.-n; 07.77.-Ka; 29.40 Wk; 85.30 De; 85.60 Dw

The possibility of using a semiconductor analog of vacuum photomultipliers – the micro-pixel avalanche photodiodes (MAPD) in the medical and nuclear physics apparatus is widely discussed in last years [1, 2]. Pixels in these structures operate in Geiger mode, and therefore the device has high gain of signal ($\sim 10^6$), and higher detection efficiency of the photons ($\sim 60\%$) compared with the conventional photomultiplier. Two different designs of MAPD are best known at the present which are proposed in [3, 4]. The first structure comprises a silicon substrate, on which surface is formed a matrix of individual p-n-junctions (surface pixels). Each pixel is connected to the common metal bus by the individual conductive film resistance. Overall conductive bus and individual film resistors are located between the pixels.

The second structure contains no conductive bus or the individual film resistors, no another elements on the photosensitive surface. The matrix of pixels consist separated n^+ - regions deeply buried into the epitaxial silicon layer of p-type conductivity, growing on the surface of n-type conductivity silicon substrate. This allows creating a device with a high pixels density for a wide range of dynamic linearity of the photoresponse [5]. For understanding the operation and optimization of operating parameters MAPD such as photon detection efficiency, the gain of the photoelectron, radiation resistance, and others it is necessary to know the nature of the potential distribution and the shape of the trajectory of the charge carriers in such MAPD. This work is devoted to solving these problems.

To determine the shape of the potential distribution consider the cross-section of the MAPD-3N sample shown in Fig. 1. This sample is produced in collaboration with the Zecotek Photonics Inc. Company. It comprises a silicon substrate of n-type conductivity on which surface are sequentially formed heavily doped n^+ - layer with the impurity concentration $N_{dw} > 10^{18} \text{ cm}^{-3}$, first epitaxial layer of p-type conductivity with the impurity concentration $N_{a,1} = 1,85 \cdot 10^{15} \text{ cm}^{-3}$, heavily doped n^+ - region (pixels) with the impurity concentration $N_{dp} > 10^{18} \text{ cm}^{-3}$, the second layer of epitaxial p-type conductivity with the

impurity concentration $N_{a,2} = N_{a,1} = N_a = 1,85 \cdot 10^{15} \text{ cm}^{-3}$ and the heavily doped p^+ - layer with the impurity concentration $N_{as} > 10^{18} \text{ cm}^{-3}$. Both p-type epitaxial layers have the same thickness of 4μ . The highly doped n^+ -regions are located symmetrically between the epitaxial layers (see Fig. 1a) and have thickness of 0.6μ .

For accurate describing of the potential distribution in MAPD it is necessary to use a three-dimensional Poisson equation with taking into account the form of n^+ -regions. However, the symmetry of the MAPD structure allows us to understand the characteristics of the potential distribution in the structure described with one-dimensional Poisson equation. This case is discussed below more detailed.

As can be seen from Figure 1, the main part of the device consists of alternating regions of n^+ -p - n^+ -p- p^+ (section "a") and the n^+ -p-p- p^+ (section "b"). Due to the high concentration of impurities in n^+ -, p^+ - layers and n^+ -regions (pixels) depletion of these areas will not be considered, i.e. it is assumed that the depletion occurs only in the epitaxial p-type layers.

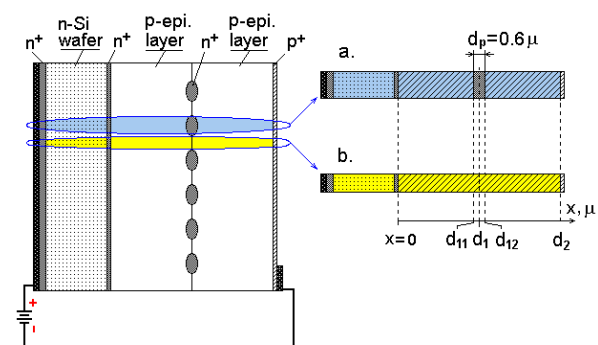


Fig.1. Cross-section of the MAPD-3N structure with deeply buried pixels.

First consider the section "a" (Fig. 1a). At low values of the potential on the device the depletion is arisen at the boundary of the first epitaxial layer and substrate (more precisely, with its n^+ - layer), because both p-type epitaxial layers have a common contact with each

other (here they act as a single p- type conductivity layer) and form n⁺-p - junction. The potential distribution is described by $U(x) = \frac{qN_a(W-x)^2}{2\varepsilon_s\Box}$ being a solution of the one-dimensional Poisson equation

$$\frac{d^2U}{dx^2} = \frac{qN_a}{\varepsilon_s} \quad (1)$$

with the boundary conditions $U(x = W) = 0$ and $dU/dx(x = W) = 0$, where q -electron charge, W -thickness of the depletion region at a given potential U , \Box_s – dielectric constant of silicon, N_a - the concentration of acceptor impurities.

In our case, $N_a = 1,85 \cdot 10^{15} \text{ cm}^{-3}$ and the depletion region reaches the boundary of n⁺ - pixel at a potential $U = \Delta U_1 = \frac{qN_a d_{11}^2}{2\varepsilon_s\Box} = 19,3 \text{ V}$. Its width W becomes $W_{I\max} = d_{11} = d_1 - (d_p/2) = 4 - 0,3 = 3,7 \text{ }\Box$. Here d_1 - thickness of the first epitaxial layer, d_p - the thickness of n⁺- region (pixel).

At further increasing of the applied potential $U \geq \Delta U_1 = 19,3 \text{ V}$ the p-n⁺ - junction located on the boundary of the first epitaxial layer with n⁺ - pixel opens, and then the second p- type conductivity epitaxial layer begins to deplete. Because the p-n⁺-junction between the first epitaxial layer and n⁺ - pixel is biased in the forward direction, therefore further increasing the potential drop on the first epitaxial layer stops.

At the value of potential $U = \Delta U_1 + \Delta U_2 = 19,3 + 19,3 = 38,6 \text{ V}$ the depletion in the second epitaxial layer reaches the boundary of p⁺- layer and the width of the depletion in the second epitaxial layer becomes equal its maximum value: $W_{2\max} = d_2 - d_{12} = d_2 - (d_1 + (d_p/2)) = 8 - 4 - 0,3 = 3,7 \mu$. Here, $\Delta U_2 = \frac{qN_a(d_2 - d_{12})^2}{2\varepsilon_s\Box}$ - potential difference in the second epitaxial layer. Thus, at this voltage U both epitaxial p-type layers are completely depleted.

As noted above the p-n⁺ - junction between the first epitaxial layer and the n⁺ - pixel is positive biased while the p-n⁺ - junction between the n⁺-pixel and the second epitaxial layer is negative biased. Therefore increasing of the potential over 38.6 V, all voltage exceeding this value drops by only on the second epitaxial layer. It can be said that the n⁺ - pixel shields further increasing of the field in the first epitaxial layer. Excess voltage is linearly distributed in the second epitaxial layer, similar to a conventional capacitor with dielectric layer of $d_o = d_2 - d_{12} = 3,7 \mu$ thickness.

As it is follow from the discussions above, if the bias voltage $U_b > (\Delta U_1 + \Delta U_2) = 38,6 \text{ V}$, for description of the potential distribution in the "a" section (Fig. 1) it is necessary to solve the equation (1) for three regions with the appropriate boundary conditions.

Solution of the equation (1) for the first epitaxial layer with the boundary conditions $U(x = d_{11}) = U_{01} = U_b - \Delta U_1$, $\frac{dU}{dx}(x = d_{11}) = 0$ is expressed as

$$U_1(x) = \frac{qN_a(d_{11}-x)^2}{2\varepsilon_s\Box} + U_{01}, \quad 0 \leq x \leq d_{11} \quad (2)$$

In the range of $d_{11} \leq x \leq d_{12}$ the n⁺- region is not depleted, and therefore here

$$U_2(x) = \text{const} = U_{01}, \quad d_{11} \leq x \leq d_{12} \quad (3)$$

Solution of the equation (1) for the second epitaxial layer with the boundary conditions $U(x = d_2) = 0$, $\frac{dU}{dx}(x = d_2) = -\frac{U_{01} - \Delta U_2}{d_2 - d_{12}}$ is described as:

$$U_3(x) = \frac{qN_a(x-d_{12})^2}{2\varepsilon_s\Box} - \frac{qN_a(d_2-d_{12})}{\varepsilon_s\Box}(x-d_{12}) - \frac{U_{01}-\Delta U_2}{d_2-d_{12}}(x-d_{12}) + U_{01}, \quad d_{12} \leq x \leq d_2, \quad d_{12} = d_{11} + d_p \quad (4)$$

Using the equations (2) - (4), we can construct the potential distribution in the "a" section of the MAPD-3N sample (Fig. 1a).

The potential distribution in the section "b" of the MAPD-3N sample (fig.1.b) with the boundary conditions

$$U(x = d_2) = 0 \text{ and } \frac{dU}{dx}(x = d_2) = -\frac{U_b - \Delta U_3}{d_2},$$

if $U_b > \Delta U_3 = \frac{qN_a d_2^2}{2\varepsilon_s\Box}$,

where ΔU_3 - potential difference required for full depletion of both epitaxial layers with total thickness d_2 , is given by:

$$U(x) = \frac{qN_a(d_2-x)^2}{2\varepsilon_s\Box} + \frac{U_b - \Delta U_3}{d_2} \cdot (d_2 - x) \quad (5)$$

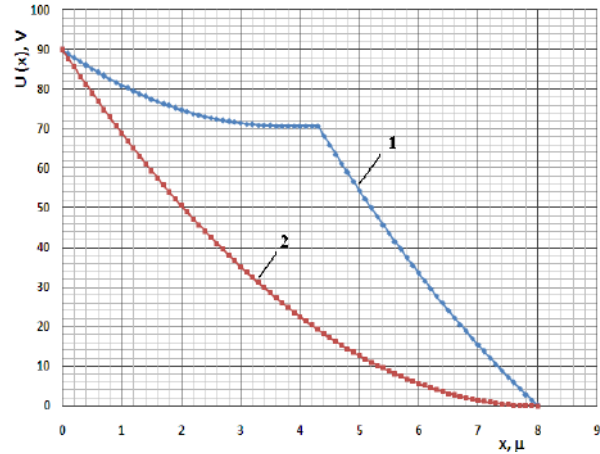


Fig. 2. The potential distribution in the MAPD-3N sample: 1 - the potential distribution in the section "a", 2 - the potential distribution in the section "b".

Fig. 2 shows the potential distribution in the sections "a" and "b" of the MAPD-3N sample at $U_b = 90 \text{ V}$. It is evident that the potential distribution in the section "a", containing n⁺ - pixels differs greatly from the potential distribution in the section "b", and in all points with the same coordinate "x" the value of potential in the section "a" significantly higher than the corresponding value in section "b". It provides a strong electric field around n⁺-

pixels with convex shape of equipotential surfaces from the second epitaxial layer side (see Fig. 3).

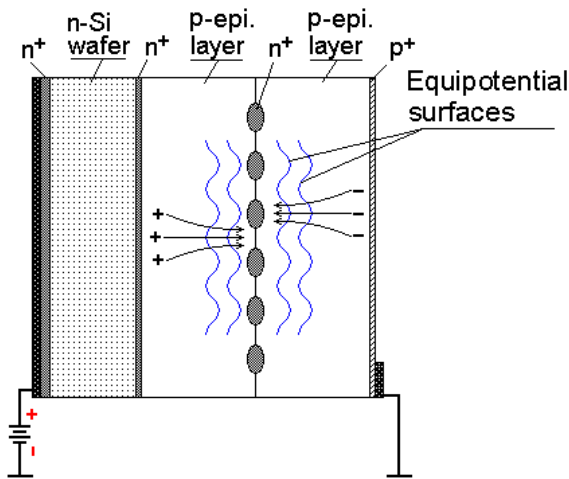


Fig. 3. Shape of equipotential surfaces and the trajectory of the charge carriers in MAPD with deeply buried pixels.

The convex shape of the equipotential surfaces provides unique properties of MAPD with deeply buried pixels among the known analogues. Conventional designs of avalanche photodetectors and also MAPD with surface pixels [6,7] have a planar structure, and thus the charge carriers of dark generation in the semiconductor substrate

enter the avalanche region of device and multiply here creating additional noise. However in MAPD with deeply buried pixels the hole current generated in the substrate and first epitaxial layer passes through the gaps between the n^+ -pixels, and therefore it is not amplified. Only electrons created in the second epitaxial layer (the photosensitive thickness) undergo the multiplication. Due to a strong electric field around the corresponding n^+ -pixels the electrons are collected and accelerated causing avalanche process.

This means that increasing of the dark generation current in MAPD with deeply buried pixels caused by radiation-induced defects has slight effect on the main operating parameters of the device. This offers a good opportunity to create new MAPD with improved radiation hardness.

Thereby, it is shown that due to deep location of pixels in MAPD, a strong electric field around n^+ -pixel with equipotential surfaces of the convex shape from the photosensitive surface is created. This leads to the fact that the hole current generated in the substrate and first epitaxial layer passes through the gaps between the n^+ -pixels and not amplified. The preferential conditions for multiplication are created for photoelectrons generated in the photosensitive part of device. Therefore, this structure has improved signal/noise ratio and high radiation resistance.

- [1]. N. Anfimov, I. Chirikov-Zorin, A. Dovlatov, et al. Beam test of Shashlyk EM calorimeter prototypes readout by novel MAPD with super high linearity // Nucl. Instr. and Meth. A. 2010. V. 617, P.78-80.
- [2]. Z. Sadygov, et al. Three advanced designs of micro-pixel avalanche photodiodes: Their present status, maximum possibilities and limitations // 2006. Nucl. Instr. and Meth. A. V. 567, P. 70-73.
- [3]. Z.Y. Sadygov Patent Russia № 2102820, priority 10.10.1996.
- [4]. Z.Y. Sadygov Patent Russia № 2316848, priority 01.06.2006.
- [5]. Z.Y. Sadygov, A.G. Olshevsky, A.A. Dovlatov et al. Micropixel avalanche photodiode with wide range of linearity // JTF letters. 2010. V.36, rel. 11, p. 83-89.
- [6]. N. Dinu, et al. Characteristics of a prototype matrix of Silicon Photo Multipliers (SiPM). // JINST, 4, P03016, 2009, P 1-9.
- [7]. http://sales.hamamatsu.com/info/eul/MPPC/PDF/S11829_S11830-3344MF_eng.pdf

SYNTHESIS OF CARBON ENCAPSULATED MAGNETIC NANOSTRUCTURES BY USING CASPIAN HEAVY OIL

S.H.ABDULLAYEVA^{1,2}, N.N.MUSAYEVA^{1,2*}, R.B.JABBAROV^{1,2},
A. A.EL-GENDY³, A.LEONHARDT³

¹*G.M. Abdullayev Institute of Physics, Azerbaijan NAS, Baku, Azerbaijan*

²*Research & Development Center for Hi-Technologies, MCIT, Baku, Azerbaijan*

³*Institute of Solid State and Materials Research, IFW Dresden, Germany*

E-mail: nmusayeva@physics.ab.az

Magnetite nanoparticles and nanorods have been obtained by high pressure hydrothermal method using Caspian oil as additional carbon source. Obtained magnetite nanostructures can be applied in industry and medicine.

Keywords: magnetite, oil, water, SEM

PACs: 75.20.{g, 75.75.+a, 75.20.En, 75.30.Cr, 75.50.Bb

Water pollution is the first global problem of the World. Many industries are responsible for water pollution, for they dump their unwanted waste into our water systems. To name a few, the garbage they dump are sewage, waste water, industrial waste, oils, marine waste, medical waste and nuclear waste. As a result, harmful substances such as; asbestos, lead, mercury, nitrates, phosphates, sulfur, oils, petrochemicals, fertilizers, pesticides, dangerous drugs and litter contaminate our water systems.

In addition to industrial dumping, many individuals also contribute to the problem by disposing their household waste improperly; this includes harmful chemicals and medications deposited into drains.

Eventually, all living things suffer; we will be unable to rely on water from our water systems and/or we will contract serious diseases and illnesses from the water we use for drinking and bathing. Imperative that we take the necessary steps to help clean and preserve our waters.

Magnetite, which is one of the two common naturally occurring iron oxides (Fe_3O_4) is the most magnetic of all the naturally occurring minerals on Earth [1].

Magnetite powder efficiently removes arsenic(III) and arsenic(V) from water, the efficiency of which increases ~200 times when the magnetite particle size decreases from 300 to 12 nm.[2] Arsenic-contaminated drinking water is a major problem around the world, which can be solved using magnetite as a sorbent.

Several methods such as arc discharge [3], high temperature heat treatment [4], ion beam sputtering [5], chemical vapor deposition (CVD) [6-8] have been developed for synthesizing carbon encapsulated metal (or metal compound) nanoparticles.

There are some works, which present promising results using oil (aromatic heavy oil [9,10], turpentine oil [11] for synthesizing carbon encapsulated iron nanoparticles.

Gas chromatographic analysis shows that Caspian oil is a combination of different long-chained hydrocarbons with 84 ± 2 % carbon, 11% H, and little amounts of N, S and O_2 .

We have used high pressure hydrothermal method for synthesizing Carbon coated magnetite (Fe_3O_4) nanowires by decomposition of ferrocene ($\text{Fe}(\text{C}_5\text{H}_5)_2$) under solvothermal conditions using Caspian oil as

additional carbon source.

Ferrocene is placed inside a stainless steel high pressure vessel. Afterwards the Caspian oil is added. Subsequently the vessel is closed and the bomb head fixed tightly. By flushing with Ar for 15 to 30 minutes the air is replaced in order to obtain an oxygen free atmosphere. The vessel is heated up to 450 °C maintaining the temperature for a certain reaction time. After the synthesis the vessel is cooled down naturally. The product is then filtrated and washed with n-decane several times.

Brownish-black powdery products were obtained. These samples were analyzed using X-ray diffractometry (XRD) and scanning electron microscopy (SEM). The magnetic properties of the samples were determined by the alternating gradient magnetometry (AGM) measurements.

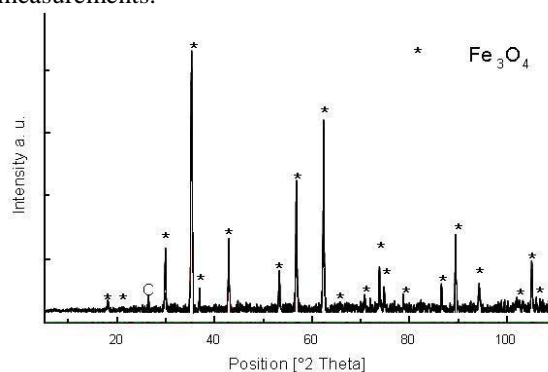


Fig.1. X-ray diffraction pattern of the carbon encapsulated magnetite nanoparticles and nanorods by using $\text{CoK}\alpha$ radiation.

In air as well as in argon the iron ions were partially oxidized since magnetite was detected by XRD analysis which is displayed in the X-ray diffractogram (Fig.1).

According to SEM investigation samples consists of particles in the nanometer range. These nanostructures are covered with carbon which can be seen in Fig. 2. Evidence for carbon can also be found in the XRD results (see Fig.1).

The samples show ferromagnetic behaviour which is also expected for nanosized magnetite (Fig.3). The saturation magnetization allows determining the exact content of Fe_3O_4 in the investigated samples which amount between 29 and 77 wt%.

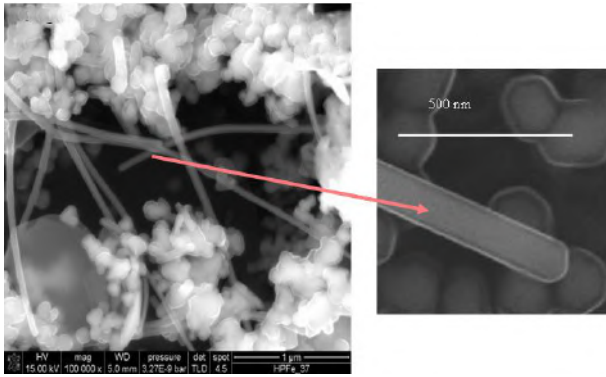
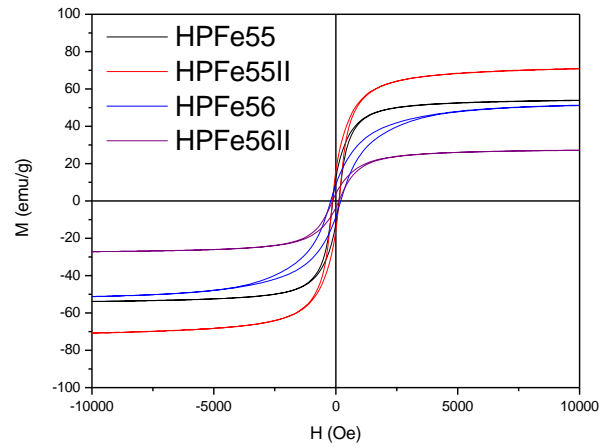


Fig.2. SEM image of the carbon encapsulated magnetite nanoparticles and nanorods (left), detail of the sample (right)



No.	H_c (Oe)	M_s (emu/g)	Fe_3O_4 ratio wt%
HPFe55	128	54	59
HPFe55II	140	71	77
HPFe56	204	51	55
HPFe56II	129	27	29

Fig.3. Magnetization curves of the samples at room temperature

-
- | | |
|--|--|
| <p>[1] <i>R.J.Harrison</i>; Dunin-Borkowski, RE; Putnis, A. Proceedings of the National Academy of Sciences, 2002, 99 (26): 16556–16561.</p> <p>[2] <i>J.T. Mayo et al.</i> Sci. Technol. Adv.Mater.2007; 8, 71</p> <p>[3] <i>J.Jiao, S.Seraphin.</i>//J/Appl. Phys. 83 (1998) 2442</p> <p>[4] <i>P.J.F.Harris, S.C.Tang.</i>//Chem.Phys. Lett. 293 (1998) 53</p> <p>[5] <i>T.Hayashi, S.Hirono, M.Tomita, S.Umemura.</i> //Nature 381 (1996) 772</p> <p>[6] <i>Z.-J.Liu, Z.Yuan, W.Zhou, Z.Xu, L.-M.Peng</i> Chem.Vap.Deposition 7 (2001) 24</p> <p>[7] <i>A.K.Sinha, D.W.Hwang, L.-P.Hwang.</i>// Chem.Phys.</p> | <p>Lett. 332 (2000) 455</p> <p>[8] <i>A.A.El-Gendy, E.M.Ibrahim, S.Khavrus, Y.Krupskaya, S.Hampel, A.Leonhardt, B.Büchner, R.Klingeler</i> Carbon 47 (2009) 2821-2828.</p> <p>[9] <i>J.Huo, H.Song, X.Chen.</i> // Carbon 42 (2004) 3177-3182</p> <p>[10] <i>J.Huo, H.Song, X.Chen, W.Lian</i> // Carbon 44 (2006) 2849-2867</p> <p>[11] <i>R.Afre, T.Soga, T.Jimbo, M.Kumar, Y.Ando, M.Sharon, P.Somani, M.Umeno.</i> // Microporous and mesoporous Materials, 96 2006) 184-190</p> |
|--|--|

NANOSTRUCTURE MATERIALS AND THEIR APPLICATIONS

S.H.ABDULLAYEVA^{1,2}, R.B.JABBAROV^{1,2*}, N.N.MUSAYEVA^{1,2}¹*G.M. Abdullayev Institute of Physics, Azerbaijan NAS, Baku, Azerbaijan*²*Research & Development Center for Hi-Technologies, MCIT, Baku, Azerbaijan**E-mail: rjabbarov@physics.ab.az*

Nanostructures have been described as 'novel materials whose size of elemental structure has been engineered at the nanometer scale'. Materials in the nanometer size range commonly exhibit fundamentally new behavior. Moreover, intervention in the properties of materials at the nanoscale enables the creation of materials and devices with enhanced or completely new characteristics and functionalities. Syntheses of phosphors for Light Emitting Diodes (LEDs) of various host matrices by different preparative methods are very important and are needed in phosphor industry. The present paper discusses the synthesis of nanophosphors applicable in Phosphor coated LEDs (PLED) for lighting applications and Carbon nanotubes (CNT) to prepare polymer/CNT nanocomposites. We report electropotential parameters of obtained phosphor converted white LED and SEM analyze of Carbon Nanotube.

Keywords: Light Emitting Diodes, nanophosphor, carbon nanotube.

PACs:75.50Tt

INTRODUCTION:

Materials in the nanometer size range commonly exhibit fundamentally new behavior. Moreover, intervention in the properties of materials at the nanoscale enables the creation of materials and devices with enhanced or completely new characteristics and functionalities. The field of nanoscience and nanotechnology is interdisciplinary in nature and it is being perused by physicists, chemists, materials scientists, biologists, engineers, computer scientists etc. Nanomaterials may be classified on the basis of dimensionality and modulation. Some special nanostructures like nanotubes, nanoporous materials, zeolites, core-shell structures have also come up with their novel characteristics. A number of methods have been used for the synthesis with the physical and chemical methods (Sputtering, Ion beam, Condensed phase, Combustion, Sol-gel) of nanostructure with various degrees of success and many direct and indirect techniques (AFM, TEM, SEM, XRD, AES, Raman, AS, PL and PLE) are employed for their characterization. The fact, which makes the nanostructures interesting, is that the properties become size dependent in nanometer range because of surface effect and quantum confinement effect. The geometric structure, chemical bonds, ionization potential, electronic properties, optical properties, mechanical strength, thermal properties, magnetic properties etc. are all affected by particle sizes in nanometer range. Importance of nanotechnology is growing day by day. Many more applications may be possible with the novel and peculiar properties of nanostructures. Dictated by the demands of miniaturization, increasing efforts are being made to synthesize, understand and apply the materials with reduced dimensions. The interest in nanomaterials is growing at a dramatic rate due to realization that reduced dimensions in nanometer regime can alter and improve the properties of materials.

REASONS FOR NOVEL PROPERTIES

Nanomaterials exhibit properties often superior to those of conventional coarse-grained materials and in addition, the properties can be tailored by controlling the

size. The changes in the properties of nanomaterials are driven mainly by three factors:

1) Increase in surface area to volume ratio: Atoms and molecules at surface or interface have different environment and bonding configuration, therefore these exhibit different characteristics. In micron size particles, the fraction of surface atoms is less than 10^{-8} and so they cause little effect. As size is reduced, relative number of atoms on surface increases inversely as particle size. For small sizes of the order of few 100 nm, the fraction of surface atoms is large and therefore influences the properties by greater amount making the properties size dependent.

2) Quantum size effect: When the size of the particle is comparable to phase coherent length of electrons, the energy spectrum is quantized into discrete levels. The effect is observable for particle sizes of the order of few 10 nm. In case of metals the continuous energy levels are discretized with energy spacing E_f/N , where E_f is Fermi energy and N is number of electrons present. The discretization in energy levels is experienced when their spacing exceeds the thermal energy. Quantum size effect is more pronounced in semiconductor nanoparticles because of moderate forbidden energy gap. Quantum size effect makes the energy states at the edges of valence and conduction bands forbidden, increasing the effective band gap, which affects the electronics and optical properties.

3) Lattice contraction: At very small sizes of the order of a few nm, lattice parameters may be reduced because of inward interatomic forces. Structural phase change, such as from cubic to hexagonal, has also been observed in this size range.

Intervention in the properties of materials at the nanoscale enables the creation of materials and devices with enhanced or completely new characteristics and functionalities. Therefore these find wide applications in various devices and improved performance is achievable and with the help of these materials certain new novel devices have also become possible.

SYNTHESIS/ COMBUSTION METHOD

It is a great challenge to synthesize particles of nanometer dimensions with narrow size distribution and purity. A variety of methods are used to obtain

nanostructured material. In principle, any method capable of producing very fine grain sized polycrystalline material can be utilized to produce nanocrystalline materials. Currently there are two approaches: reducing the size, also known as top down approach and building up by self-assembly or bottom up approach to obtain nanosize materials. In top down process larger materials are reduced to smaller dimensions of the order of nanometers and in bottom-up approach the materials are build-up to nanometer size. The commonly used methods can be categorized as physical and chemical methods.

Syntheses of phosphors for Light Emitting Diodes (LEDs) of various host matrices by different preparative methods are very import and need of the day for the phosphor industry. Nano phosphors are preferred over micron size phosphors in a number of applications not only due to their particle size but also better optical properties. Some of the techniques such as solid state diffusion, flame and laser pyrolysis and sol-gel process are being employed to manufacture. The main advantages of nanophosphors in potential applications such as solid state lighting, medical, security, displays, remote thermometry and thermoluminescence radiation dosimetry. The present paper discusses the synthesis of nanophosphor coated LEDs (PLED) for lighting applications and special nanomaterials as carbon nanotube.

Rare-earth-doped phosphors are known to emit at distinct and different wavelengths in the electromagnetic spectrum and have been widely used in color cathode ray tubes (CRT), tri-phosphor fluorescent lamps, X-ray intensifying screens and newly developed vacuum mercury-free lamps, as well as various types of displays such as plasma display panels, field emission displays and projection TVs. Recently, breakthroughs in inorganic light emitting diodes (LEDs) technology are significantly catalyzing the development of energy-efficient solid-state lighting (SSL) with long lifetime. Solid-state lighting technology has now already penetrated in a variety of specialty applications, in effect; LEDs have completely changed the “world of luminance”, for example automobile brake lights, traffic signals, liquid crystal displays and mobile backlights, flashlights and all manner of architectural spotlights. Selection of host lattice and suitable activators/ coactivators, doping process and physics of nanophosphors such as quantum confinement, quantum size, surface area, surface morphology, band gap variation, and shift in excitation are some of the parameters one has to study before selecting and synthesizing nanophosphors.

Combustion method, also known as “self-propagating high-temperature synthesis” (SHS), is yet another wet-chemical method which does not require further calcinations and repeated heating. It is an exothermic reaction and occurs with the evolution of heat and light. Such a high temperature leads to formation and crystallization of phosphor materials. For any combustion, fuel and oxidizer are required. When the mixture of fuel and oxidizer are ignited, combustion takes place. Later in the mid-1990s, several research groups began to investigate the use of combustion synthesis for oxide phosphor preparation and found it to be a technique of interest for phosphor synthesis in general. Materials for example phosphors prepared by the conventional solid

state reactions (SSR) which require a long reaction time of 2-6 h in a high temperature range of 1200-1600°C. Furthermore, high calcination temperature are also required to induce sintering and aggregation of particles. Milling process was also required in SSR resulting in a reduction of the particle size and a decrease in the luminescent properties. However, by using combustion synthesis, phosphor powders can be prepared in a simpler, safer, more energy saving way and within a shorter time. Combustion synthesis can produce more homogeneous products compared to the SSR method due to good mixing of starting materials and relatively low reaction temperature. As it is a high-temperature process, only thermodynamically stable phases can be prepared. At the same time, rapid heating and cooling rates provide the potential for the production of metastable materials with new and unique properties. The advantages of the combustion synthesis are the following: simple usage of equipment, high purity products, stabilization of metastable phases, and the formation of products with nearly any size and shape. There are four stages to describe the combustion synthesis.

Stage I: Composition of raw materials

The stoichiometric quantities of raw materials were calculated and weighed by using high precision mass balance.

Stage II: Mixing

The two solutions were mixed together and stirred using a magnetic bar for several hours at 75°C to obtain a viscous gel solution.

Stage III: Combustion synthesis

The mixed viscous gel obtained continues for combustion reaction. White combustion ash was obtained in 3-5 min by combusting the precursor gel at a temperature of 500°C.

Stage IV: Calcination step

The final synthesis is done by heating the combustion ash at 950°C -1100°C in a weak reductive atmosphere for 2h.

The combustion method has been successfully used in the preparation of a large number of technologically useful oxide (refractory oxides, magnetic, dielectric, semiconducting, insulators, catalysts, sensors, phosphors, etc.) and nonoxide (carbides, borides, silicides, nitrides, etc.) materials. In recent years, there has been tremendous interest in the combustion synthesis of materials because it is simple, fast, energetically economic and yields high purity products compared to the conventional routes used to prepare these materials. By combustion method we have successfully obtained YAG:Ce³⁺ and SrAl₂O₄:Eu²⁺ nanophosphors for p-LED application [1-3].

REQUIREMENTS OF LED PHOSPHORS/ COLOR COORDINATES/ GAMUT AND COLOR TEMPERATURE

The basic requirements of LED phosphors are as follows: 1) their excitation spectra should overlap well with emission spectra of LED (420-490 nm blue LED) or (360-400 nm near UV LED), 2) their emission spectra should lie in the green and red (500-650 nm) region for blue LED and RBG region for near UV LED, 3) they should not absorb the visible light emission from blue LED or those from other phosphors, 4) they should

exhibit high quantum efficiency, 5) light emission should not saturate at very high excitation density of LED chips (200 W cm^{-2} which is 3 times higher than FL), 6) LED phosphors must withstand temperatures up to 150°C without significant reduction in luminescence efficiency. So phosphors with very high thermal quenching temperature are desired, 7) their color rendering index (CRI) should be > 80 , and finally 8) their chemical and physical stabilities during LED manufacturing are important.

The color purity of a phosphor depends on the spectral energy distribution of the emission. Generally the color purity can be determined by measuring its x,y coordinates on a standard CIE color chart [4]. The color gamut of a phosphor is represented as an area in the CIE 1931 chromaticity diagram with the curved edge representing the monochromatic colors. Gamut areas typically have triangular shapes because most color reproduction is done with three primaries. Color temperature is a simplified way to characterize the spectral properties of emissions from phosphors. In reality the color of spectral energy distribution is determined by how much each point on the spectral curve contributes to the total output; the color temperature of most color TVs is in the 6,500 to 9,500 K range. Higher color temperatures are due to higher brightness and color saturation. [4]

SPECIAL NANOMATERIALS

With the advancement in technology, it has become possible to synthesize and characterize certain new types of materials having very small dimensions and novel characteristics. Nanomaterials are made by arranging the atom regularly at nanometer scale. This has given rise to certain special materials like fullerenes, carbon nanotubes, nanoporous materials, dendrimers, aerogels, zeolites, core-shell structure etc.

Carbon Nanotubes (CNTs):

These can be considered as cylinders made of graphite sheets, mostly closed at ends. The thickness of sheet is just the atomic size of carbon atom and area about a few square micrometers. It is also possible that many concentric cylinders may form as a nanotube. Such nanotubes are termed as multiwall carbon nanotube (MWCNT). The distance between their walls is 0.334nm. These are more common; however under certain conditions it is possible to obtain single wall carbon nanotube (SWCNT) [5]. CNT have a great technological application in electronics, optoelectronics, drug delivery etc.

Figure 1 demonstrate SEM picture of MWCNTs obtained by Aerosol CVD method.

APPLICATION: High brightness and performance acceptable LED based street lamps have been identified as one of the solutions for next generation energy saving lighting source in city lighting, especially in road lighting applications which provide suitable illumination for safety driving at night. Traditional street lamps require extremely high power to generate light (250 W typically). A current top-performance 250 W high pressure-sodium (HPS) lamp has a system efficacy of $\sim 60 \text{ lm/W}$. Due to the operation principle limitation of the bulb used, the

system efficacy will decrease to $\sim 45 \text{ lm/W}$ when the operation power consumption is 120 W. This limitation forces the dimming of HPS at midnight or other idle periods in order to save energy. However, LED street lamp has an advantage of constant system efficacy ($> 67 \text{ lm/W}$) under many driving system power consumption levels due to its operation principle. Thus in the desired lighting area, LED street lamp can provide various illumination levels efficiently based on different requirements with less power consumption [6,7,8].

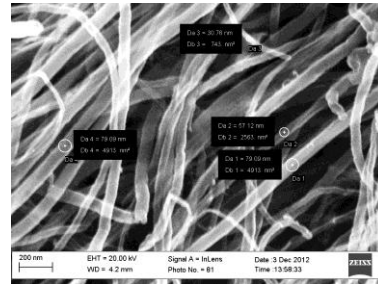


Fig. 1. SEM results of MWCNTs obtained by Aerosol CVD method

OUR R&D RESULTS~100W, 10000LM LED EMITTER METAL PLATE WHITE LED OUTDOOR LAMP.

The emission spectra of YAG:Ce^{3+} nanophosphor and CIE 1931 chromaticity diagram of obtained white light are presented in Figure 2. The electro-optical parameters of obtained white LED lamp are: Lumen output $\sim 10000 \text{ Lm}$; working voltage $\sim 30\text{-}36\text{V}$, working current $\sim 2.8\text{-}3.0\text{A}$, Color temperature $\sim (6000\text{-}6500\text{K})$ & $(3000\text{-}3300\text{K})$.

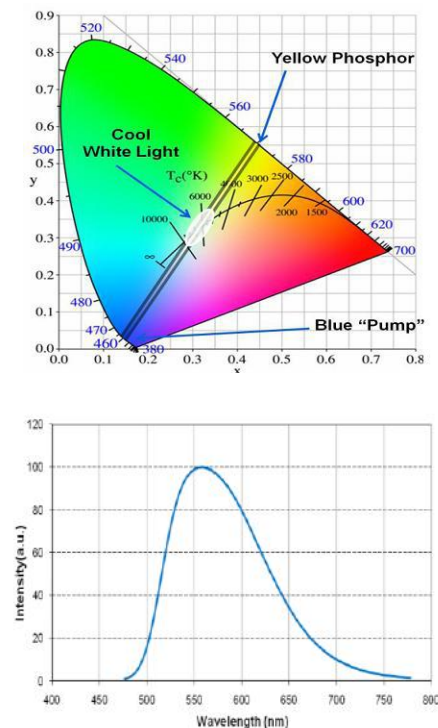


Fig.2. a) Emission spectra of YAG:Ce^{3+} nanophosphor and b) CIE 1931 chromaticity diagram

High efficiency of white is achieved using the wavelength of blue LED chips ranging from 455nm to 470nm. It can be used in combination with other color phosphor products. High brightness white LEDs using this

phosphor can be used for applications in display backlighting, camera flashes, signage, decoration, LED displays, projectors, automotive, general lighting, and a variety of high power applications.

-
- [1] *R.B. Jabbarov, S.H. Abdullayeva, N.N. Musayeva, C.A. Sultanov, S. Ozcelik.* Phosphor converted white LED street lamp.LED &LED lighting conference, 27-30 September-2012, Turkey, Istanbul, p.31.
 - [2] *S. Mammadova, H.Streit, T. Orucov, Ch. Sultanov.* Preparation and optical properties of $\text{SrAl}_2\text{O}_4\text{:Eu}^{2+}$ nanophosphor. Azerbaijan Journal of Fisics, Fizika, 2012, vol. XVII, n.4, section: En.
 - [3] *D. Jia, Y. Wang, X. Guo, K. Li, Y. K. Zou, and W.Jiac,* “Synthesis and Characterization of YAG:Ce^{3+} LED Nanophosphors,” J. Electrochem. Soc.,154 [1] J1–J4 (2007).
 - [4] *W.M.Yen, S. Shionoya and H. Yamamoto,* 2007. Phosphor Handbook, CRC Press, Boca Raton, FL (USA).
 - [5] *M. I. Mishchenko, W. J. Wiscombe, J. W. Hovenier and L. D.Travis,* 2000. in: Light Scattering by Nonspherical Particles: Theory, Measurements and Applications, ed. M. I. Mishchenko, J. W. Hovenier and L. D. Travis, Academic Press, San Diego.
 - [6] *B. Krause, M. Ritschel, Ch. Töschner, S. Oswald, W. Gruner, A. Leonhardt, P. Pötschke.* Composites Science and Technology 70 (2010) 151–160
 - [7] *Y. Liu, D. L. Ding, C. H. Leung, Y. K. Ho and M. Lu.,* Optical Design of a High Brightness LED Street Lamp. Proc. of SPIE-OSA-IEEE Asia Communications and Photonics, SPIE Vol. 7635, 763508 · © 2009 SPIE-OSA-IEEE
 - [8] *S. Ye, F. Xiao, Y.X. Pan, Y.Y. Ma, Q.Y. Zhang.,* Phosphors in phosphor-converted white light-emitting diodes: Recent advances in materials, techniques and properties. Materials Science and Engineering R 71 (2010) 1–34
 - [9] *Dongdong JIA.* Nanophosphors for White Light LEDs. Chem. Eng. Comm., 194:1666–1687, 2007

LOW-TEMPERATURE STUDY OF THERMALLY STIMULATED CURRENTS IN LAYERED-STRUCTURED $\text{Ti}_4\text{GaIn}_3\text{S}_8$ CRYSTALS

SERDAR DELICE^{*1}, MEHMET ISIK² AND NIZAMI HASANLI¹

¹*Department of Physics, Middle East Technical University, 06531 Ankara, Turkey*

²*Department of Electrical and Electronics Engineering, Atilim University, 06836 Ankara, Turkey*

** Corresponding author. Tel.: +90-312-210-50-54; fax: +90-312-210-50-99*

E-mail address: sdelice@metu.edu.tr (S. Delice)

Thermally stimulated current measurements were carried out on $\text{Ti}_4\text{GaIn}_3\text{S}_8$ single crystals in the temperature range of 10–300 K with a constant heating rate of 1.0 K/s. The characterization of trapping centers was accomplished by the measurements of current flowing along the c -axis of crystals. The analyses of the glow curves using various methods, such as curve fitting, initial rise, peak shape and differential analysis methods, were in good agreement with each other and revealed two trapping centers in $\text{Ti}_4\text{GaIn}_3\text{S}_8$ with activation energies of 17 and 260 meV. Attempt-to-escape frequencies were calculated as 1.0×10^1 and $8.2 \times 10^4 \text{ s}^{-1}$. Their capture cross sections have been determined as 1.1×10^{-24} and $3.5 \times 10^{-21} \text{ cm}^2$. The good agreement between the experimental results and the theoretical predictions of the model that assumes slow retrapping have confirmed that retrapping is negligible in these centers.

Keywords: Semiconductors, Chalcogenides, Electrical properties, Defects

PACs: 71.55.-i; 72.80.Jc; 72.20.Jv

1. INTRODUCTION

In present-day industry, there are many application areas of ternary and quaternary layered-structured semiconductors like memory switching elements, emission modulators and nonlinear optical transducers in nonlinear optics and optoelectronics [1]. $\text{Ti}_4\text{GaIn}_3\text{S}_8$ single crystals owing to high photosensitivity in the visible range of spectra and high birefringence in conjunction with a wide transparency range of 0.5–16 μm have great potential for optoelectronic devices [2]. The quaternary compound, $\text{Ti}_4\text{GaIn}_3\text{S}_8$, showing the properties of the layered thallium dichalcogenides group is created replacing a quarter of indium ions by gallium ones in TlInS_2 [3]. The lattice of $\text{Ti}_4\text{GaIn}_3\text{S}_8$, whose each successive layer is rotated by a right angle with respect to the previous one, consists of strictly periodic two-dimensional layers arranged parallel to the (001) plane. The bonding type between Ti and S atoms is interlayer while the type of bonding between Ga(In) and S atoms is an intralayer.

Previously, optical and photoelectrical characterizations of TlInS_2 crystals were accomplished in Refs. [4–11]. The basic absorption edges are formed by indirect and direct transitions with $E_{\text{gi}} = 2.28 \text{ eV}$ and $E_{\text{gd}} = 2.33 \text{ eV}$ [11]. Two broad emission bands centered at 515 and 816 nm related to donor-acceptor pair recombination were observed in photoluminescence (PL) study [12]. Recently, transmission and reflection measurements of $\text{Ti}_4\text{GaIn}_3\text{S}_8$ crystals were carried out in the wavelength region 400–1100 nm [13]. The presence of both optical indirect and direct transitions in order of 2.32 and 2.52 eV was revealed analyzing the room temperature absorption data. The variation rate of the indirect band gap with temperature was computed as $\gamma = -6.0 \times 10^{-4} \text{ eV/K}$ from the analysis of the transmission measurements data obtained in the temperature range of 10–300 K. PL spectra in the temperature range of 26–130 K was also studied and two emission bands were obtained in the wavelength region of 500–780 nm [14]. Radiative transitions from the donor levels located at 30 and 10 meV below the bottom of the conduction band to the

acceptor levels located at 810 and 190 meV above the top of the valence band, respectively, were proposed to be responsible for the observed bands.

Defects and impurities can be decisive factors for the performance of semiconductor materials used in today's technology. In the electronic devices, defects/impurities can result with nonradiative recombination centers which lower the internal quantum efficiency or even cause light generation impossible. Furthermore, in these devices, defects/impurities introduce scattering centers lowering carrier mobility, accordingly hindering high-frequency operation. Impurities are also known as effective phenomena for electrical and optical properties of materials. Therefore, many experimental techniques, used to get valuable information about the trapping centers created due to the presence of defects and/or impurities in semiconductors, have been used for years in order to create high-quality devices. Thermally stimulated current (TSC) is one of these significant experimental methods. The main purpose of this paper is to characterize the defects in $\text{Ti}_4\text{GaIn}_3\text{S}_8$ crystals by performing TSC experiments in a wide temperature range of 10–300 K.

2. EXPERIMENTAL DETAILS

Single crystals of $\text{Ti}_4\text{GaIn}_3\text{S}_8$ were grown by Bridgman method. The resulting ingot appears yellow-green in color; the freshly cleaved surfaces are mirror-like. Since there is no fracture or crack on the surface of the obtained sample, further burnishing and cleaning treatments were not required. The single crystals obtained were not subjected to the additional annealing. Electrical contacts were made on the sample surface with silver paste according to sandwich geometry. The electrical conductivity of the studied samples was n-type as determined by the hot probe method.

The TSC measurements were performed in the temperature range of 10–300 K using an Advanced Research Systems closed-cycle helium cryostat. Constant heating rate was achieved by a Lake-Shore 331

temperature controller. A Keithley 228A voltage/current source and a Keithley 6485 picoammeter were used for the TSC measurements. The nominal instrumental sensitivities of temperature and current measurement devices were about 10 mK and 2 pA, respectively. At low enough temperatures, when the probability of thermal release is negligible, a light-emitting diode generating light at a maximum peak of 2.6 eV was used to excite the charge carriers. When the illumination time is increased in a controlled way, it was observed that after nearly 600 s illumination, the traps are filled completely. So the illumination time was chosen as 600 s for TSC measurements. Throughout the excitation process, bias voltage of $V_1 = 1$ V is applied to the sample at the initial low temperature. When the excitation was turned off and an expectation time (300 s) has elapsed, the bias voltage of $V_2 = 100$ V was applied to the sample and the temperature was increased at a constant rate of 1.0 K/s. Whole measurement system was controlled by a computer using software written in LabViewTM graphical development environment.

3. RESULTS AND DISCUSSION

Figure 1 shows the TSC curves of $\text{Ti}_4\text{GaIn}_3\text{S}_8$ crystal measured in the 10–300 K temperature range. As seen from the figure, there exist two peaks with peak maximum temperatures (T_m) of 41 and 223 K. Experimental TSC glow curves of the $\text{Ti}_4\text{GaIn}_3\text{S}_8$ crystals have been analyzed using curve fitting, initial rise, peak shape and differential analysis methods.

Curve fitting method is based on the fitting of the TSC glow curve using a software program under the light of the analytical expression giving the temperature dependence of the TSC current. For slow retrapping case, this current is given by [15]

$$I = n_0 \nu \exp \left\{ -\frac{E_t}{kT} - \int_{T_0}^T \frac{\nu}{\beta} \exp(-E_t/kT) dT \right\}, \quad (1)$$

where n_0 is initial trap concentration, ν is attempt-to-escape frequency, β is heating rate and E_t is activation energy of the trapping center. The details of the curve fitting method were reported in our previous papers [16, 17]. When the curves in the low and high temperature ranges were fitted under the case of slow retrapping, a successful fitting results were obtained as represented with solid curves in Fig. 1. Since the temperature ranges of the observed TSC curves do not overlap, we have performed the curve fitting method on these curves separately. Activation energies of the trapping centers were found as 17 and 260 meV (Table 1). Attempt-to-escape frequencies of the trapping centers were calculated using the results of the curve fitting method and expression

$$\nu = \frac{\exp(t_m) t_m^3 \beta k}{(t_m + 2) E_t}, \quad \text{where} \quad t_m = \frac{E_t}{kT_m}.$$

Then capture cross section (S_t) of the trap can be calculated by the expression

$$S_t = \frac{\nu}{N_c \nu_{th}},$$

where $N_c = 2(2\pi m_e^* kT/h^2)^{3/2}$ is the effective density of states in the conduction band and ν_{th} is thermal velocity of a free electron. The capture cross sections of the trap levels were calculated using the effective mass $m_e^* = 0.16m_0$ reported for $\text{Ti}_4\text{GaIn}_3\text{S}_8$ [18] (see Table 1).

Table 1. The activation energy (E_t), capture cross section (S_t) and attempt-to-escape frequency (ν) of traps for two TSC peaks of $\text{Ti}_4\text{GaIn}_3\text{S}_8$ crystal.

Peak	T_m (K)	E_t (meV)				S_t (cm ²)	ν (s ⁻¹)
		Curve fitting method	Initial rise method	Peak shape method	Differential analysis method		
A	41	17	17	20	17	1.1×10^{-23}	1.0×10^1
B	223	260	260	270	258	3.5×10^{-21}	8.2×10^4

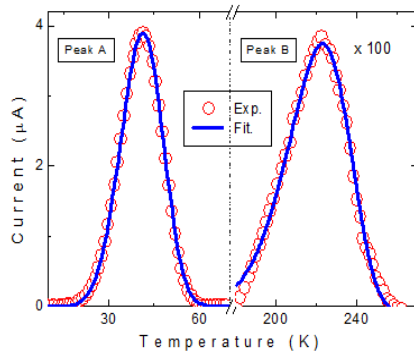


Fig. 1. Experimental TSC spectrum of $\text{Ti}_4\text{GaIn}_3\text{S}_8$ crystal with heating rate of 1.0 K/s.

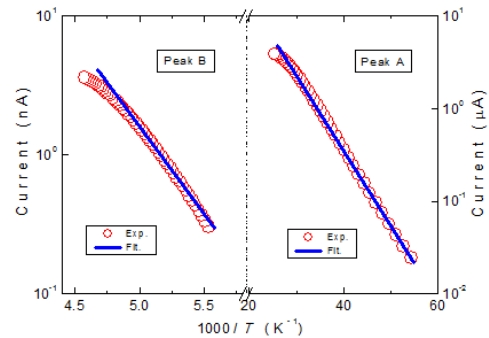


Fig. 2. Thermally stimulated current versus $1000/T$ for B- and A-peaks in the TSC spectrum of $\text{Ti}_4\text{GaIn}_3\text{S}_8$ crystals.

We have also used the initial rise method, which is independent of the recombination kinetics, to obtain the activation energies of the traps. The current is proportional to the $\exp(-E_t/kT)$ when the traps begin to empty as the temperature is increased [15]. When the initial portion of the TSC curve is analyzed, the plot of $\ln(I)$ as a function of $1/T$ gives a straight line with a slope of $(-E_t/k)$. The plots for TSC peaks of $\text{Ti}_4\text{GaIn}_3\text{S}_8$ crystal are given in Fig. 2. The activation energies of the observed traps calculated using initial rise method are 17 and 260 meV (Table 1).

Another useful method to calculate E_t values is the peak shape method [15]. In this method, low (T_l) and high (T_h) temperatures of the curve corresponding to half of the peak maximum intensity are used and the activation energy of revealed trap level is computed from the average value of following equations,

$$\begin{aligned} E_\tau &= [1.51 + 3.0(\mu_g - 0.42)]kT_{\max}^2 / \tau - \\ &- [1.58 + 4.2(\mu_g - 0.42)]2kT_{\max} \\ E_\delta &= [0.976 + 7.3(\mu_g - 0.42)]kT_{\max}^2 / \delta \\ E_w &= [2.52 + 10.2(\mu_g - 0.42)]kT_{\max}^2 / w - 2kT_{\max} \end{aligned}$$

where $\tau = T_m - T_l$, $\delta = T_h - T_m$, $w = T_h - T_l$ and $\mu_g = \delta/w$. The activation energies of the levels were obtained as $E_{tA} = 20$ meV and $E_{tB} = 270$ meV. These values are consistent with those calculated from above mentioned techniques (Table 1).

Thermally stimulated current of a discrete set of traps with trapping level E_t is described by the equation (1). If we assume v to be independent of T and then take the natural logarithm of both side and differentiate with respect to the temperature we obtain [19]

$$\frac{d(\ln I)}{dT} = \frac{E_t}{kT^2} - \frac{v_t}{\beta} \exp(-E_t/kT). \quad (2)$$

Since the current is maximum at $T = T_m$, the equation (2) yields

$$\frac{E_t}{kT_m^2} = \frac{v_t}{\beta} \exp(-E_t/kT_m). \quad (3)$$

Using the equation (3), the second derivative of the $\ln(I)$ can be written at the peak maximum temperature as

$$\left[\frac{d^2(\ln I)}{dT^2} \right]_m = -\frac{E_t}{kT_m^3} \left(2 + \frac{E_t}{kT_m} \right) = \alpha_m. \quad (4)$$

Activation energies of the traps associated with the observed peaks can be calculated from the slope of the tangent (α_m) at $T = T_m$ of the first derivative of the TSC curve. When the graphs of the first derivatives of the currents were plotted, it was revealed that the derivatives are equal to zero at $T_m = 41$ and 223 K with tangential slopes of $\alpha_m = -2.05 \times 10^{-2}$ and -4.16×10^{-3} , respectively (Fig. 3). The activation energies of the traps corresponding to these α_m values are found from equation (4) as $E_{tA} = 17$ meV and $E_{tB} = 258$ meV (Table 1). These values show a good agreement with the results obtained using the abovementioned methods.

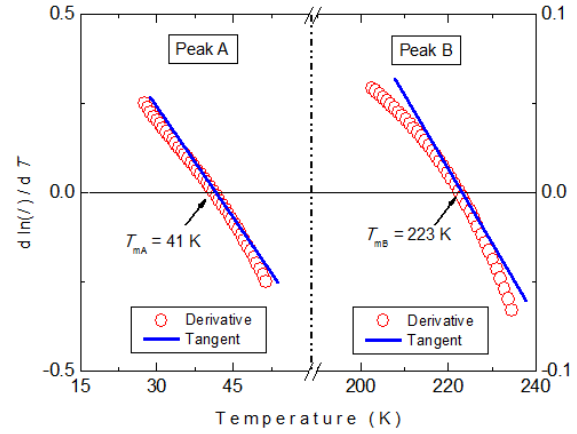


Fig. 3. Derivatives of the thermally stimulated currents.

4. CONCLUSIONS

Thermally stimulated current measurements in the temperature range of 10–300 K were studied in $\text{Ti}_4\text{GaIn}_3\text{S}_8$ single crystals. The TSC spectra, analyzed by various methods, revealed the presence of two trapping centres with activation energies of 17 and 260 meV. As the crystals studied are not intentionally doped, the observed levels are thought to exist due to the presence of defects created during the growth of crystals and/or unintentional impurities. The capture cross sections of the observed traps were calculated as 1.1×10^{-23} and $3.5 \times 10^{-21} \text{ cm}^2$. The retrapping process was negligible in the TSC measurements, since the analyses of the experimental data under the theoretical predictions owing to slow retrapping model were agreeable for the observed traps.

- [1]. A.M. Panich, J. Phys.: Condens. Matter. 20, 293202 (2008).
- [2]. K.R. Allakhverdiev, Solid State Commun. 111, 253 (1999).
- [3]. D. Muller and H. Hahn, Z. Anorg. Allg. Chem. 438, 258 (1978).
- [4]. H. Uchiki, D. Kanazawa, N. Mamedov and S. Iida, J. Lumin. 664, 87 (2000).
- [5]. Y. Shim, N. Uneme, S. Abdullayeva, N. Mamedov and N. Yamamoto, J. Phys. Chem. Solids, 66, 2116 (2005).
- [6]. Y. Shim, W. Okada and N. Mamedov, Thin Solid Films, 509, 137 (2006).
- [7]. Y. Shim, Y. Nishimoto, W. Okada, K. Wakita and N. Mamedov, Phys. Stat. Sol. (c) 5, 1121 (2008).
- [8]. N. Mamedov, Y. Shim and N. Yamamoto, Jpn. J. Appl. Phys. 41, 7254 (2002).

- [9]. *N. Mamedov, Y. Shim, H. Toyota, K. Wakita, N. Yamamoto and S. Iida*, Phys. Stat. Sol. (a) 203, 2873 (2006).
- [10]. *S.R. Samedov, O. Baykan and A. Gulubayov*, Int. J. Infrared Millimet. Waves 25, 735 (2004).
- [11]. *M. Halias, A. Anagnostopulos, K. Kambas and J. Spyridelis*, Physica B 160, 154 (1989); Mater. Res. Bull. 27, 25 (1992).
- [12]. *A. Aydinli, N.M. Gasanly, I. Yilmaz and A. Serpenguzel*, Semicond. Sci. Technol. 14, 599 (1999).
- [13]. *K. Goksen and N.M. Gasanly*, J. Phys. Chem. Sol. 69, 2385 (2008).
- [14]. *K. Goksen and N.M. Gasanly*, Cryst. Res. Technol. 43, 514 (2008).
- [15]. *R. Chen and Y. Kirsh*, Analysis of Thermally Stimulated Processes, Pergamon Press, 1981.
- [16]. *N.M. Gasanly, H. Ozkan and N.A.P. Mogaddam*, Semicond. Sci. Technol. 21, 1250 (2006).
- [17]. *M. Isik, K. Goksen, N.M. Gasanly and H. Ozkan*, J. Korean Phys. Soc. 52, 367 (2008).
- [18]. *A. Qasrawi and N.M. Gasanly*, Cryst. Res. Technol. 41, 174 (2006).
- [19]. *M. Castagne, J. Bonnafé, J. Romestan and J. P. Fillard*, J.Phys. C: Solid St. Phys. 13, 5555 (1980).

QUENCHING OF SHORT CIRCUIT CURRENT AND EXCITON DECAY IN CuGaSe₂ SINGLE CRYSTALS

I.KASUMOGLU, I.A.MAMEDOVA

*G.M.Abdullayev Institute of Physics, Azerbaijan National Academy of Sciences,
Baku, AZ 1143, Azerbaijan,
e-mail: gasimoglu@yahoo.com*

The influence of γ -radiation on short circuit current in CuGaSe₂ has been investigated at 77 K temperature. Quenching of short circuit current has been observed in short-wave and long-wave ranges of spectra and exciton decay in γ -irradiated CuGaSe₂ sample, connected with redistribution of electronic traps also has been observed.

Keywords: Short circuit current, γ -irradiation, p-CuGaSe₂, low-resistance

PACS : 61.80.Ed

1. INTRODUCTION

CuGaSe₂ single crystal is the representative of A^IB^{III}C^{VI}₂ ternary compounds group being isoelectronic analogue of A^{II}B^{VI}₂ group compounds. With a small exception, all compounds of A^IB^{III}C^{VI}₂ are p-type conducting. Some of these compounds have birefringence that is of interest for nonlinear optics [1]. Properties of these compounds vary over a wide range that is why they represent interest for practical application. Electrical, optical and luminescent properties have been investigated [2-4].

2. RESULTS AND DISCUSSION

This paper deals with investigation results of influence of γ -irradiation on short-circuit current in CuGaSe₂ at 77K.

CuGaSe₂ single crystal has been grown by method of chemical transport reactions. CuGaSe₂ is p-type conductivity and is low-resistant ($\rho=10^3$ Ohm·cm). It was used as ohmic contacts. The measurements carried out in vacuum cryorefrigerator. Values of signals were measured by high-sensitive electrometrical voltmeter B7-30. Registration was carried out by method of comparison of spectra before and after radiation.

The spectral dependence of short circuit current in not irradiated CuGaSe₂ has complex character in the range 200÷1000 nm is shown in Fig.1.

Quenching of current is observed in short-wave and long-wave ranges of spectra. In some of A^{II}B^{VI}₂ semiconductors excitation by photons with the energy smaller than band gap energy has two effects: excitation and also quenching of a background current. At the such excitation several interband electronic transitions and local centres are realized. Generation of basic carriers bring to overlapping of several impurity photoeffect bands (margins).

In the impurity part of spectra generation of nonbasic carriers, optical change of charge of various types of recombination centers and optical quenching of photocurrent occurs. In the result of combination of impurity effects, short-wave quenching can appear, therefore spectral dependence of short circuit current of ionized processes has view, characteristic for resonance transitions, which observed on spectra of initial (not irradiated) sample [5]. It is known, that sometimes in ternary compounds defects play determining role in change of electrical and optical parameters, caused by deep levels in the band gap [6]. That

is why investigation of change of a charging condition after treatment by γ -radiation is of interest.

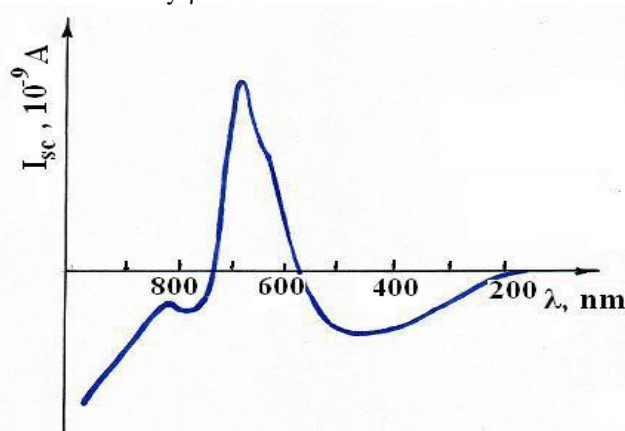


Fig.1 Spectral dependence of short circuit current in nonirradiated CuGaSe₂ at 77 K

The impurity quenching mechanism is well explained, if to use the scheme of two-leveled recombination centers model [7]. It is known, that impurity levels (donors and acceptors) exist in CuGaSe₂ [8-9]. Electrical properties of CuGaSe₂ single crystals strongly depend on donor and acceptor states concentration, due to existence of slow (r) and fast (s) recombination centers in investigated samples. Maximum of negative peak of short-wave quenching corresponds to 2,8 eV. Decrease of conductivity by the effect of monochromatic light is connect with carrier mobility change, due to their dispersion on phonons and on traps filled by electrons, concentration of which increases after γ -irradiation. Capture of electrons brings to increase of the charge value of centers, hence, to increase of dispersion [10]. Mobility of independent, charged, disseminating centers is described by inversely proportional dependence with concentration of centers. At defined light intensities the rise of captured carriers concentration is slowed down: in spectrum it corresponds to 550 nm and then negative increase is stopped, whereas free carriers concentration increases bringing to decrease of negative effect and transition to a positive site of spectra [7].

Spectra of CuGaSe₂ γ -irradiated by 18 R/s dose during 5 and 10 minutes are vary. In spectra of current of sample irradiated during 5 minutes, two lines in

long-wave range (780nm, 820 nm) are observed, but in the case of irradiation during 10 minutes, energy distance between these lines increased (735 nm, 840 nm) (Fig. 2 and Fig.3).

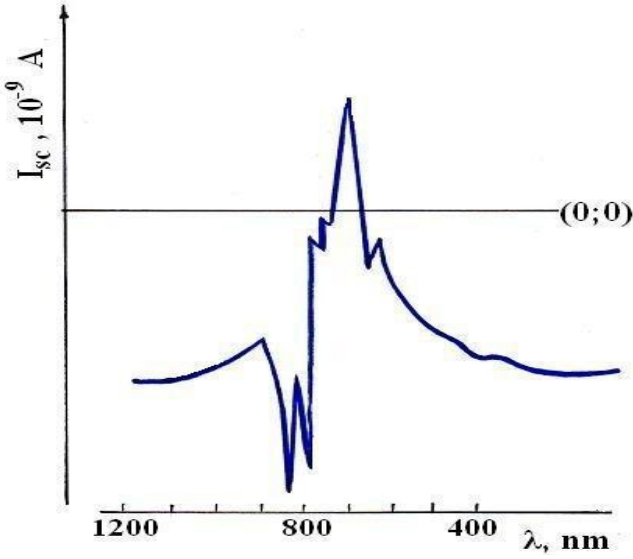


Fig.2 Spectral dependence of short circuit current in γ -irradiated CuGaSe₂ at 77 K (duration of an irradiation was 5 minutes)

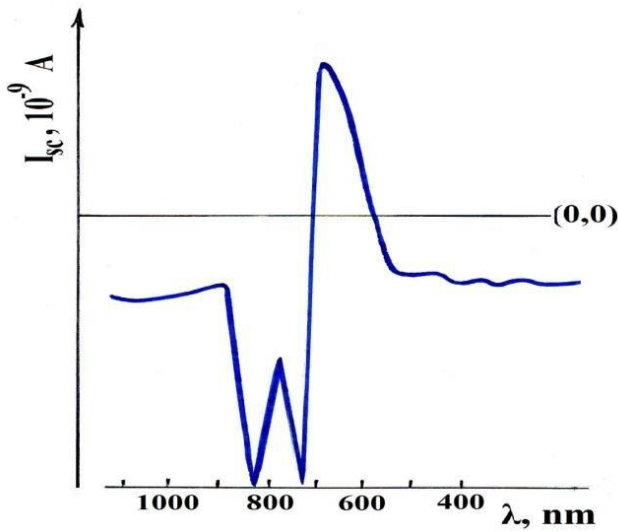


Fig.3 Spectral dependence of short circuit current in γ -irradiated CuGaSe₂ at 77 K (duration of an irradiation was 10 minutes)

Spectral dependence of short circuit current of γ -irradiated CuGaSe₂ during 15 minutes by 18 R/s dose, is shown in Fig.4. As it is shown from Fig.4, the spectrum almost is completely displaced downwards, only the small part of the spectrum remains in the positive site from zero line and quenching of current in short-wave site of spectrum is deepened and widened, maximum of this negative peak is corresponds to 2,5 eV.

At $\lambda=720$ nm, that corresponds to exciton position [11-13], sharp recession of short circuit current is observed. We assume that exciton decay takes place. For the benefit of such conclusion work [14] testifies. Increase of recession of short circuit current after treatment by γ -irradiation, maybe connected by redistribution of traps: trap concentration

taking place in thermal balance with conduction band, decreases and deep traps playing a role of dispersion and recombination centers are formed, concentration of which increases after treatment by γ -radiation. The excitonic decays plays main role in formation of photovoltaic spectra. Excitons of not high energies turn out from states located near the valence band top and bottom of conduction band. In this case, as CuGaSe₂ single crystals are p-type crystals, then excitons locate near the valence band. The deep quenching observed at short wavelength site of spectra shows that slow "r" and rapid "s" centers are exists in these samples, which by using this fact one can explain the influence of the excitation on the processes taken place in energy bands in these samples.

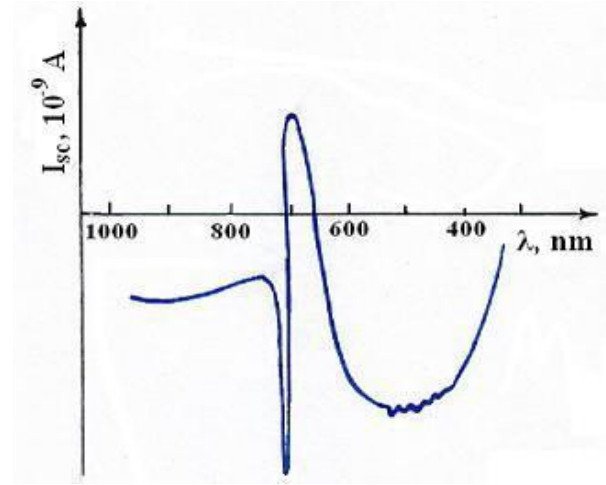


Fig.4 Spectral dependence of short circuit current in γ -irradiated CuGaSe₂ at 77 K (duration of an irradiation was 15 minutes)

Observing of excitons show the polarization of these crystals. So deep maxima are also observed in the spectra of the samples treated by polarized light. From experimental results one can assume that increasing of concentration of donor and acceptor impurities after irradiation plays main role, that is why after irradiation the conductivity come to own conductivity despite the conductivity history. If the ϵ_0 static dielectric constant is high, but mass determined by equation (1) is small,

$$\frac{1}{\mu} = \frac{1}{m_e^*} + \frac{1}{m_h^*} \quad (1)$$

then potential energy of attraction

$$V = -\frac{e^2}{\epsilon_0 r} \quad (2)$$

must be small concerning to kinetic energy connected with relative motion of electrons and holes:

$$T = \frac{p_r^2}{2\mu} \quad (3)$$

where, p_r^2 - impulse of electrons concerning holes

$$r = r_e - r_h \quad (4)$$

In these cases, which are fulfilled for more of semiconductors, a series of bind states (excitons) are formed, which break up after an irradiation [15].

3. CONCLUSION

One can assume that radiation defects play a main role of barriers. At illumination by monochromatic light from

impurity and own range, capture of basic carriers by slow recombination centers localized in the range of recombination barriers takes place.

So properties of ternary compounds can be ruled, by changing the height of barriers by the means of external influences.

-
- [1]. *H. Harhn, G.Frank*, Lanoqold chem., 1953, Bd 271, 163
 - [2]. *S.Tanaka, S.Kawami, H.Kobayashi, H.Susakura* J.Phys.Chem .Solids 38 (1977) 680
 - [3]. *C.Paorisi, N. Romeo, G.Sberveglies amd I.Torricone*: J.Luminescence 15 (1977) 101
 - [4]. *A.V.Mudrui, I.V.Bodnar, I.A.Victorov, V.F.Gremenok, A.L.Patuk and I.A.Shakin* ICTMC-11, Salford, 8-12 September, 1977
 - [5]. *I.V.Potikevich, A.V.Lyubchenko, L.A.Boroyko*, FTP {Russian, Semiconductors) V.5, N.10, p.1992-1994, 1977
 - [6]. *I.Kasumoglu, I.A.Mamedova, G.S.Mekhtiev, M.A.Aliev /Xeberler*, Transactions NAS of Azerbaijan, V.XXX, (2) p.56-58, 2010
 - [7]. *L.G.Paritskiy and S.M.Rivkin*, FTP {Russian, Semiconductors), V.1,N5, p.718, 1967
 - [8]. *T.K.Kasumov, M.A.Aliev, F.I.Mamedov* Photoconductivity in CuGaSe₂ single crystals AS Azerbaijan Nakhchivan Science centre №90, p.7-8, 1982
 - [9]. *G.Masse and N.Lahlou* J.Appl.Phys. 51(9) pp.4981-4984, 1980
 - [10]. *G.G.Chemersyuk and V.V.Serdyuk* FTP {Russian, Semiconductors), V.1, №3, p.339, 1967
 - [11]. *Masamu Susaki, Takeshi Miyoushi, Hiromichi Hopinaka and Nobuyaki Yamamoto*, Appl.Physics, v.17, N , pp 1955-1959, 1978
 - [12]. *T.K Kasumov, I.G.Kasumov*, Reports of As of Azerbaijan. v.XLVI, №3, p.19-22, 1985
 - [13]. *I.P.Ponomaryov, A.Yu.Serov, I.V.Bodnar* , FTP {Russian, Semiconductors) v.49, N.1, p.23-26, 2007
 - [14]. *A.N.Pikhtin, V.A.Potapov, M.Yunis*, FTP {Russian, Semiconductors) v.22, N.6, 1988
 - [15]. *J. Fillips* Optical spectra in solid states. Trans. "Mir", 174 p, 1988.

STUDY OF EFFECT OF ANNEALING ON THE FILM STRUCTURE

 $Bi_2Te_{2,7}Se_{0,3}<Lu>$

I.T.MAMEDOVA, N.R.MEMMEDOV, N.M.ABDULLAYEV

G.M. Abdullayev Institute of Physics of the National Academy

of Sciences of Azerbaijan G.M.Abdullaev

H. Cavid pr., 33., Baki, Az-1143

email:ilaha_mamedova@physics.ab.az

Research on AFM polycrystalline thin films of $Bi_2Te_{2,7}Se_{0,3}<Lu>$ thickness of 30-40 nm, obtained by thermal spraying on the glass showed that the optimum annealing temperature of 230°C, for 30 minutes resulting in the maximum crystallite sizes averaging from 36 to 33 nm, and increase the size of fine grains to the smoothing of surface roughness as well as the ordering of the film structure.

Keywords: substrate, dislocation, crystallite unit, the surface energy.

PACs: 546.471.2.539.23

INTRODUCTION

Many of the tasks that the practice puts the developers of thermoelectric devices can be solved with the use of film thermocouples and film thermopile.

As shown in the study of semiconductors $A^V B^VI$ small blocks single-crystal structures revealed a marked increase in the thermoelectric figure of merit due to scattering of carriers to interconnect borders. This additional scattering mechanism can not operate by changing the block size, the degree of disorientation, as well as varying the grade of the dopant [1].

Was of interest displayed by the X-ray and "meping" study doping (lutetium) Lu films of $Bi_2Te_{2,7}Se_{0,3}$ of Bi_2Te_3 - Bi_2Se_3 obtained by thermal spraying [2]. This is a continuation of research initiated in [3,5].

EXPERIMENTAL

By the "hot wall" series of films of $Bi_2Te_{2,7}Se_{0,3}<Lu>$, p-type conductivity was obtained by sublimation of the synthesized compounds on the installation VUP-4 in a vacuum pressure of about 10^{-4} Pa. The substrate temperature was about 200 °C, at a rate of deposition of thin layers of ~ 2 nm / s [5]. Film samples with thickness from 30 to 40 nm, manufactured of dissection $(90Bi_2Te_3-10Bi_2Se_3)_{1-x}Lu_x$ ($x=0.15$) in preheated, NaCl crystals and glass substrates. Films were annealed in a vacuum to remove the elastic stress fields for 30 min. at a temperature of 230 °C followed by lowering the temperature of 10 °C / min. [4]. Structural studies of the films by X - ray diffractometer Bruker D8 Advance Research and surface topography of the films $Bi_2Te_{2,7}Se_{0,3}<Lu>$ with an atomic force microscope brands AIST-NT (Tokyo Instr., Japan). mode, scanning of the incident beam when the latter is in the plane normal direction or in the profile to the film. Also, with this microscope, the surface morphology of the films was studied [5].

EXPERIMENTAL RESULTS

On the radiograph obtained from the polycrystalline film $Bi_2Te_{2,7}Se_{0,3}<Lu>$, (Fig.1.a, b) after annealing, is consistent with data [2], based on a hexagonal lattice polycrystal Bi_2Te_3 ($a = 0,43835$, $c = 3,0487$ nm;

p.gr.D53d, R3m, Z = 3). The composition of the annealed film $Bi_2Te_{2,7}Se_{0,3}<Lu>$, forms isostructural on the basis of the hexagonal structure of chalcogenide bismuth telluride.

Consequently, during the annealing of the films up to 230 °C is not any real structural rearrangements, the formation of new phases, the X-ray observed increase in the size of the microparticles, a polycrystalline structure of $Bi_2Te_{2,7}Se_{0,3}<Lu>$. Calculations d_{exp} spacings shows that annealing the film at a temperature of up to 230 °C is hardened structure.

Upon receipt of the polycrystalline films $Bi_2Te_{2,7}Se_{0,3}<Lu>$, unannealed films on the surface are observed protyazhennnye dislocation lines (Fig. 2. a) annealing in vacuum at T = 230 °C for 30 minutes produced a vertically directed small and medium blocks.

Annealing leads to a restructuring of dislocation fracture (Fig. 2a). Further increase of the annealing temperature to 230 °C leads to formation of additional cracks and transverse dislocation, ie cracks dislocation network whose segments are oriented to each other (Fig. 2, b).

Transparencies of $Bi_2Te_{2,7}Se_{0,3}<Lu>$, doped lutetium 30 nm thick annealed at 230 °C is observed nano polycrystalline form. Blocks maximum crystallite size up to 36 nm are oriented to the substrate plane. As part of the films, clusters do not occur.

The histogram AFM (bottom figure) is an illustration of non-annealed surface roughness of the film $Bi_2Te_{2,7}Se_{0,3}<Lu>$ which is 36.41 nm,

The histogram AFM (Fig. 2.b) is an illustration of the annealed film $Bi_2Te_{2,7}Se_{0,3}<Lu>$ at 230 °C, where the roughness of the film is 33.20 nm.

The maximum length blocks crystallite grain structure composes 33.20 nm, and the thickness of the block may decrease from 30 to 60 nm pottverzhdaetsya studies [5, 6].

DISCUSSION

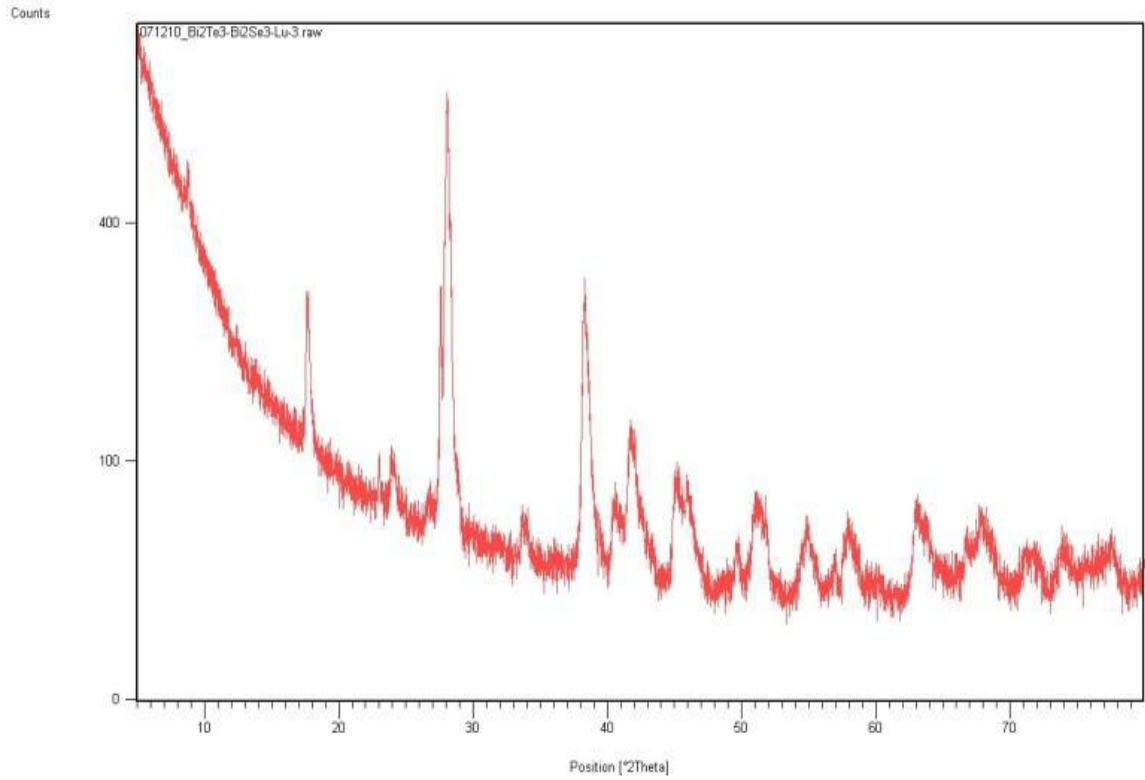
One of the reasons for the formation of dislocations should be considered as non-uniform appearance of thermal deformations in the surface and deep layers of the polycrystalline film by thermal spraying.

Reticular cracks in the films after annealing can be explained by the formation of a new model of the crystal

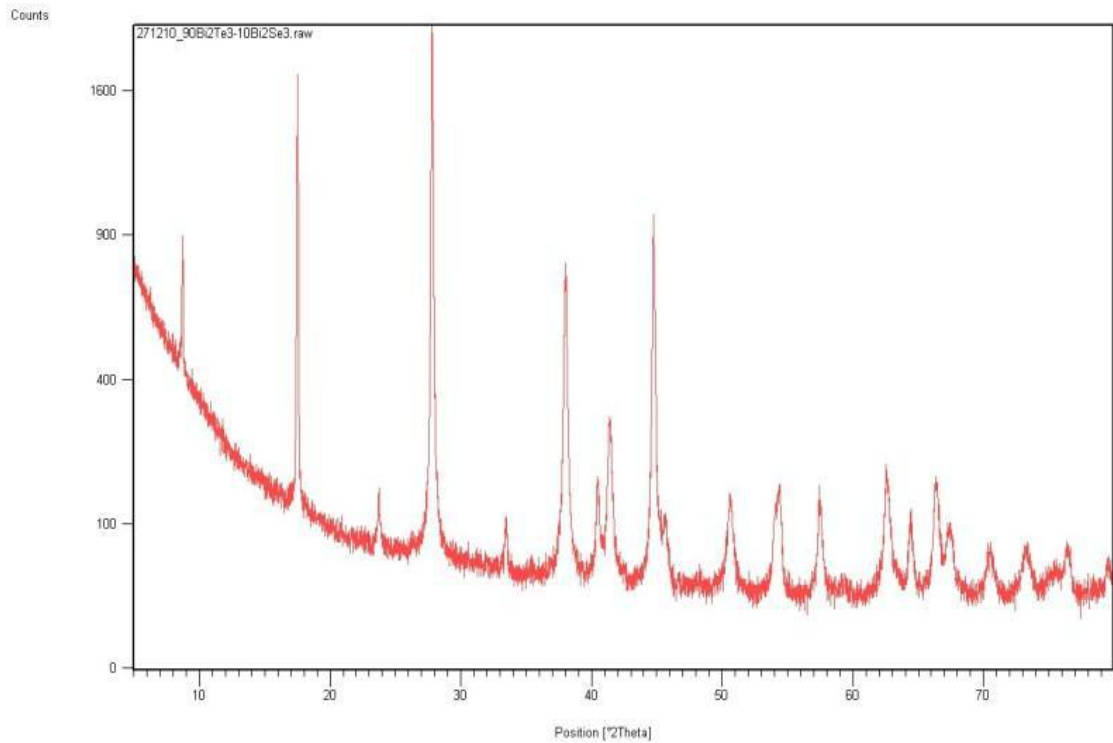
surface with relatively low energy consumption. For example, when recording the ratio Griffiths often take as a first approximation, that an extension of the current in the bulk of the cavity δA_s work expended by increasing the surface is equal to the increment of the surface energy

$$\delta A_s = \gamma \delta S.$$

Here S-cavity surface area, γ - surface energy.



a)



b)

Fig. 1. X-ray diffraction pattern at (a) - starting film $Bi_2Te_{2.7}Se_{0.3}<Lu>$, (b) - and the film annealed at 230°C.

Image absorption coefficient can be observed in the vicinity of large defects, inclusions, pores, dislocations and microcracks. [7]

Directly after film deposition oriented had a fine grain structure with a grain size up to 36 nm. Annealing to 230 ° C leads to the formation of the polycrystalline structure type (0001) // (0001) films $Bi_2Te_{2.7}Se_{0.3}<Lu>$, a large number of medium grain size up to 33 nm, fusion of fine grains into blocks.

This growth can be attributed to the different conditions of deposition dimensional films Thickness of up to 100 nm and different lengths of time annealing [1].

The increase in value of the RMS roughness and grain size of the film obviously connected with the process of crystallization and homogenization of the blocks. Formation of a new phase (diffusion reaction) does not occur, annealed films result in further improvement of the structure.

As a result of deposition on substrates grew ensemble nanostructure increase a deposition time and annealing temperature increase in small blocks, and their diameters to reduce disorientation.

CONCLUSION

Thus, research on AFM polycrystalline thin films of $Bi_2Te_{2.7}Se_{0.3}<Lu>$, thickness of 30-40 nm, obtained by thermal spraying on the glass showed that the optimum annealing temperature of 230 °C, for 30 minutes to homogenization leads crystallite size units from 36 to 33 nm, and increase the size of small grains, to smoothing of surface roughness as well as the ordering of the film structure.

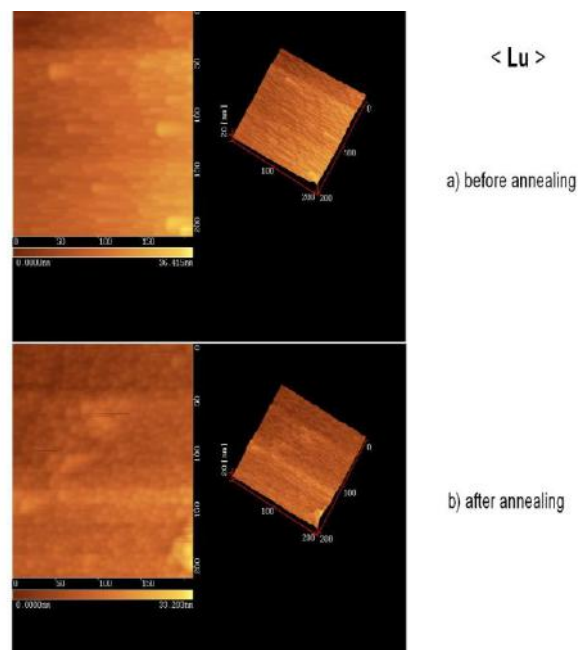


Fig. 2. Painting surface (a) - starting film $Bi_2Te_{2.7}Se_{0.3}<Lu>$, (b) - the film annealed at 230°C.

Studies have been conducted with the support of the development of science at the President of the Azerbaijan Republic in the framework of a pilot project EIF-2010 - 1 (1) - 40/01 - 22.

- [1]. Н.С. Лидоренко. Плёночные термоэлементы: физика и применение. М., Наука, с. 9, 1985.
- [2]. С.И. Мехтиева, Н.М. Абдуллаев, Н.Р. Меммедов, Р.И. Султанов. НАНАзербайджана, Известия, XXVII, № 2, с. 93, 2007.
- [3]. С.И. Мехтиева, Н.З. Джалилов, Н.Р. Меммедов, В.З. Зейналов. «Микроструктура плёнок $Bi_2Te_3-Bi_2Se_3$, легированных Tb». Azərbaycan Milli Elmlər Akademiyası, Xəbərlər. cild XXVII, № 2, с. 148, 2007.
- [4]. Б.М. Гольцман, В.А. Кудинов, И.А. Смирнов. Полупроводниковые Термоэлектрические материалы на основе Bi_2Te_3 . М., Наука, с.302 1972.
- [5]. Н.М. Абдуллаев, С.И. Мехтиева, Н.Р. Меммедов, М.А. Рамазанов, А.М. Керимова. Исследование влияния отжига на структуру плёнок $Bi_2Te_3-Bi_2Se_3$, ФТП, , том 44, выпуск 6, с.853, 2010.
- [6]. А.М. Керимова, Н.А. Абдуллаев, Н.М. Абдуллаев, С.И. Мехдиева, Н.Т. Меммедов. «Mapping» vasitəsilə $Bi_2Te_{2.7}Se_{0.3}$ bircinsliyinin tədqiqi Fizika vol.XVIII, № 4 section: Az с.10-13, 2012.
- [7]. А.Байдуллаева, М.Б. Булах, А.И. Власенко, А.В. Ломовцев, П.Е. Мозоль. ФТП, том 38, вып.1, 29, 2004.

THE PRESSURE DEPENDENCE OF THE PHONON SPECTRA OF ORTHORHOMBIC *GeSe* AND THE SECOND ORDER STRUCTURAL PHASE TRANSITION FROM SIMPLE - TO BASE- CENTERED ORTHORHOMBIC LATTICE

F.M. HASHIMZADE¹, D.A. HUSEINOVA¹, Z.A. JAHANGIRLI^{1,2,*},
B.H. MEHDIYEV¹, G.S. ORUDZHEV^{1,2}

¹ *G.M. Abdullayev Institute of Physics, National Academy of Sciences of Azerbaijan,
AZ 1143, Baku, Azerbaijan*

² *Azerbaijan Technical University,
Gusein Javid Avenue, 25, AZ 1073, Baku, Azerbaijan*

*Corresponding author: cahanzakir@yahoo.com

The IR- and Raman-active phonon frequencies of orthorhombic *GeSe*, were calculated as a function of hydrostatic pressure using the method of density functional theory in the ABINIT software package. Comparison with the published results of theoretical calculations and experimental data of the pressure dependence of Raman-active phonons has been carried out. Our calculations show that at a pressure of about 29 *GPa* the crystal structure of *GeSe* undergoes a continuous transition from simple orthorhombic to base-centered orthorhombic lattice.

Key words: *GeSe*, phonon spectra, Birch-Murnaghan, DFPT, Raman spectra

PACS: 62.50.+p; 64.30.+t; 68.65.+g

1. INTRODUCTION

Modern microelectronics based on the use of thin films grown on different substrates. The mismatch of the lattice constants results in a compressive or tensile stress in thin films. Furthermore biaxial and hydrostatic stresses a rise due to the difference of thermal expansion coefficients of the substrate and film. Under the influence of the applied pressure structural lattice parameters and electronic properties of crystals are substantially modified, and this should be considered in the development of various devices. Therefore, the study of influence of pressure on the structural, elastic and electronic parameters of the compounds is of great interest.

Earlier the pressure dependences of some of the phonon frequencies of the *GeSe* compound have been investigated in [1,2], which also conducted experimental studies of the pressure dependences of the structural parameters and a low-frequency Raman-active shear mode A_g .

As a result of their research, the authors concluded that the density functional theory adequately describes not only the equilibrium structure and vibrational properties of highly anisotropic compound *GeSe*, but also effectively predicts details of pressure-induced changes of the lattice parameters and atomic positions therein.

The authors carried out a theoretical calculation of the pressure dependence of the interlayer shear mode A_g in the approximation of the rigid layer. Their results show that this approximation gives a poor description of the pressure dependence of the interlayer mode.

The effect of hydrostatic pressure on the Raman spectra of this compound has been also studied empirically in [3]. The pressure dependence of Raman spectra *GeSe* has been studied up to a pressure 7 *kbar*, and a large difference between the pressure coefficients of the low-frequency interlayer and intralayer modes of

lattice vibrations was found.

Thus, the study of changes of interlayer and intralayer bonds in layered crystals, depending on the pressure requires more detailed study

In this paper we report a more detailed calculation of the effect of pressure on the IR - and Raman-active phonons.

2. CRYSTAL STRUCTURE AND THE METHOD OF CALCULATION

It is known that the following four compounds from A^4B^4 group (*GeS*, *GeSe*, *SnS*, *SnSe*) have an orthorhombic lattice structure. The crystal structure is layered. Space group symmetry is $P_{nma} (D_{2h}^{16})$ [4]. The positions of the atoms, in fractional coordinates, in the structure are follows: both atoms are at $4c$ as $\pm(x; 1/4; z)$ and $\pm(1/2 - x; 3/4; 1/2 + z)$.

The unit cell of the crystal contains eight atoms arranged in two layers, each consisting of four atomic planes in sequence: the cation-anion-anion-cation.

In this work, the calculations were performed from first-principles using density functional theory (*DFT – LDA*) on the basis of plane waves and pseudopotentials, implemented in a software package ABINIT [5].

In our calculations the exchange-correlation interaction was described in the local density approximation [6]. As a norm conserving pseudopotentials were used Hartvigsen-Goedekker-Hutter (HGH) pseudopotentials[7].

In the expansion of the wave function plane waves with a maximum kinetic energy up to 40 Hartree have been considered, which provides a good convergence of the total energy. Integration in the Brillouin zone (ZB) has been performed by using a partition of $4 \times 4 \times 4$ with a shift from the origin according to the Monkhorst-Pack scheme [8].

The lattice parameters and the equilibrium position of the atoms in the unit cell were determined from the condition of minimization of Hellmann-Feynman forces acting on the atoms. Minimization process was carried out until the force modules become less than 10^{-7} *Hartree/Bohr*. Then, interatomic force constants in the configuration space were calculated by the Fourier transform using ANADDB routine in the ABINIT software package [5]. These force constants were subsequently used to calculate the phonon modes at a number of arbitrary points of ZB.

Group-theoretical analysis predicts the presence of 12 Raman-active modes and 7 IR-active modes. In the Raman spectra the active modes are A_g, B_{1g}, B_{2g} and B_{3g} , while in the IR spectra the modes appear with symmetry B_{1u}, B_{1u}, B_{3u} . A_u mode is not active in the IR and Raman phonon spectra.

To obtain correct vibrational spectra of the crystals the calculations must be based on the equilibrium values of the lattice constant and the coordinates of the atoms therein. Therefore, it is necessary to perform an

optimization of the structural parameters. For optimization of the crystal structure under normal conditions and under pressure BFGS algorithm was used to minimize for given stress tensor components S_{ij} .

The theoretical values of the structural parameters for GeSe at zero pressure and temperature are given in Table 1.

Considering the fact that the use of the LDA approximation usually leads to a small underestimation of the lattice parameters, the optimized and the experimental values of the lattice parameters are in a good agreement. This procedure was repeated for several magnitudes of pressure. At each pressure, before the calculations of phonon frequencies the structures were completely relaxed. The results are presented in Figures 1 and 2. For comparison, these figures show the experimental results [1]. Figure 3 shows the pressure dependence of the phonon frequencies of the Brillouin zone center. Unfortunately, experimental pressure dependence of the phonon frequencies is known only for one mode A_g . This comparison is shown in Figure 4.

Table 1. Structural parameters for *GeSe* at zero pressure and temperature.

Parameters	$a(\text{\AA})$	$b(\text{\AA})$	$c(\text{\AA})$	x_A	z_A	x_B	z_B
Theory	4.305	3.76	10.568	0.1109	0.1173	0.4942	0.8550
Experi- ment	4.388 ^a	3.833 ^a	10.825 ^a	0.1115 ^a	0.1211 ^a	0.502 ^a	0.8534 ^a
	4.38 ^b	3.82 ^b	10.79 ^b	0.106 ^b	0.121 ^b	0.503 ^b	0.852 ^b
	4.381 ^c	3.834 ^c	10.847 ^c	0.110 ^c	0.124 ^c	0.504 ^c	0.844 ^c

^aRef.[4], ^bRef.[9], ^cRef.[2]

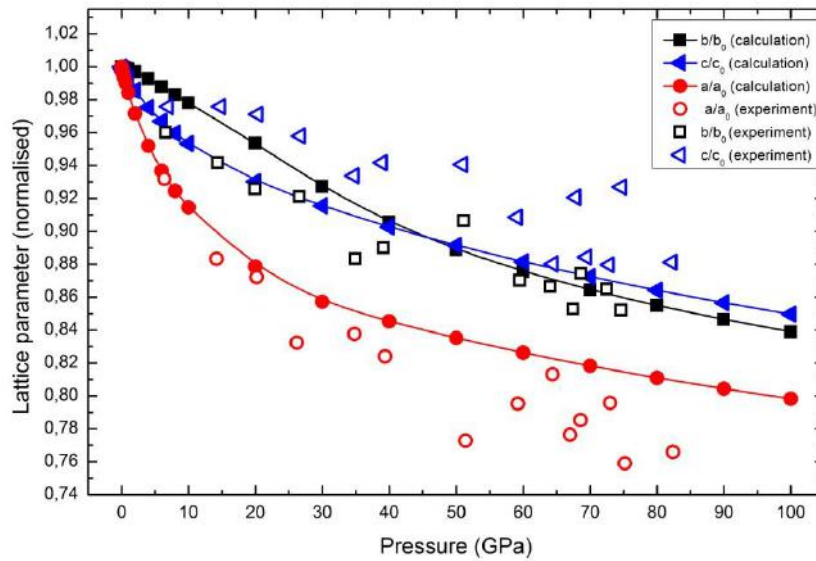


Fig. 1. Normalized lattice parameters of *GeSe* as a function of hydrostatic pressure. Solid symbols correspond to the calculated values and open symbols correspond to experimental data extracted from Ref.[10]. The solid lines correspond to the best fit to the calculated data.

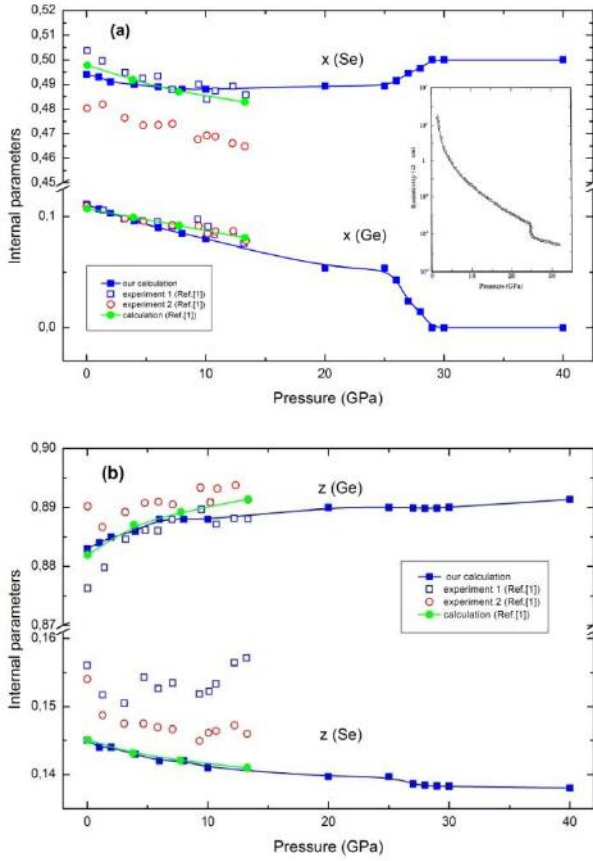


Fig. 2 (a) and (b). Pressure dependence of internal parameters. The inset of Fig. 2(a) shows the plot of electrical resistivity of $GeSe$ as a function of pressure extracted from Ref. [10]

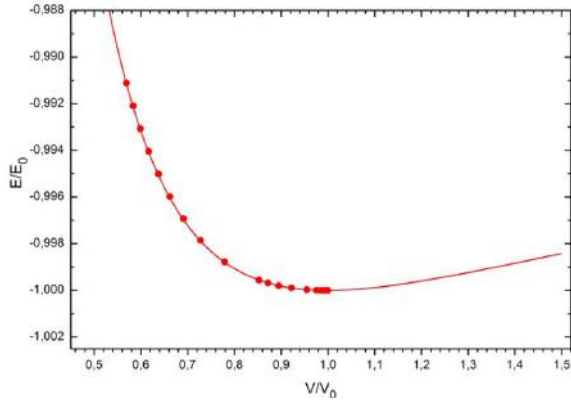


Fig. 3. Birch-Murnaghan equation of state.

3. DISCUSSION

It can be seen from Figures 4 that the theoretical dependence of the frequency of the phonon mode A_g matches quite well with the experimental results. Note, however, that our results are related to zero temperature and therefore the frequency is slightly higher than the frequency experimentally measured at room temperature. In addition, we compared the pressure coefficients for several modes, experimentally investigated in [3] at low pressures.

For low-frequency A_g mode with a frequency of 39 cm^{-1} we obtained a good agreement, namely, the experimental value of baric coefficient is 7, while the theory predicts 6.5. For mode with the frequency 174 cm^{-1} the experimental value is 2.9, and the theoretical value is 2. However, with the modes of A_g with frequency of 188 cm^{-1} and B_{3g} with frequency of 151 cm^{-1} , we observed, in contrast to the experimental situation, a negative value for baric coefficient. At present we do not have a convincing explanation of this difference.

Fig.3 shows the Birch-Murnaghan equation of state, constructed for bulk modulus of 40.78 and the pressure derivative modulus of 5.26. The points on the curve are the values of the dimensionless total energy theoretically calculated by the LDF method. These results agree with the experimental values of [2]. We calculated the bulk modulus of elasticity in two different ways. First, just by optimizing the cell parameters we obtained the value of 40.7 GPa . Second, by using the calculated independent elastic modulus, we obtained the value of 36.8 GPa . Both values are in a reasonable agreement with the experimental value of 379 kbar found in [2].

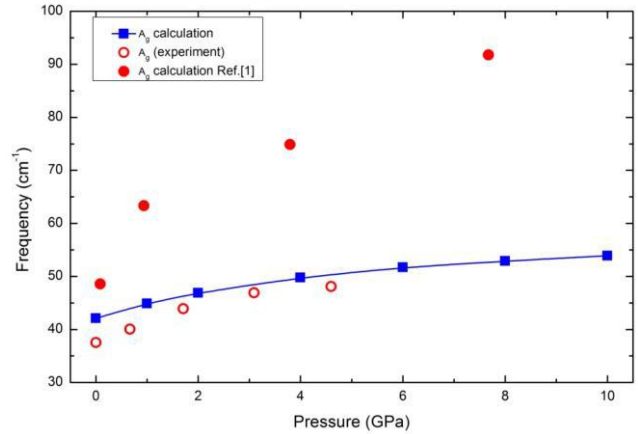


Fig. 4. The hydrostatic pressure dependence of the A_g shear phonon mode.

Calculations show that at a pressure of about 29 GPa crystal structure undergoes a transition from a simple orthorhombic to base-centered orthorhombic. Apparently, this phase transition explains the jump in electrical resistance $GeSe$ observed at 250 $kbar$ in the experiment [10].

Fig.2 (a) shows the change in the internal parameters $x(Ge)$, $x(Se)$ with pressure. The sharp change in the $x(Ge)$, $x(Se)$ near 29 GPa correlates with a sharp drop in the resistance at 250 $kbar$ (See inset in Fig.2(a)). The difference in the pressure is attributed to the effect of the temperature. Our calculations refer to zero temperature, while the experiments were carried out at room temperature. Raising the temperature, naturally, increases compressibility, which leads to a phase transition at slightly lower pressures.

4. CONCLUSION

The vibrational spectra of *GeSe* under pressure were calculated with ab initio technique and compared to the experimental results of [1,2,3] and the theoretical results of [1,2]. Our results for the phonon modes can be used to interpret further IK experiments in future research. The results are consistent with Raman experiments of [1,2,3]. Our calculations predict a

possibility of a phase transition at about 29 *GPa* from orthorhombic $P_{nma} (D_{2h}^{16})$ to $C_{mcm} (D_{2h}^{17})$: both atoms are at $4c$ as $\pm (0, 1/4, z)$. Suggested that the jump of conductivity *GeSe* at a pressure of 25 *GPa* is associated, with this phase transition.

-
- [1]. H. C. Hsueh, H. Vass, S. J. Clark, G. J. Ackland, and J. Crain, High-pressure effects in the layered semiconductor germanium selenide, *Phys.Rev. B* **51**, 1995, p.16750-16760.
 - [2]. H.C. Hsueh and J.Crain, Compression Mechanisms in Highly Anisotropic Semiconductors, *Phys. Stat. Sol. (b)* **211**, 1999, p.365-371.
 - [3]. H. R. Chandrasekhar, R. G. Humphreys and M. Cardona, Pressure dependence of the Raman spectra of the IV-VI layer compounds GeS and GeSe, *Phys.Rev. B* **16**, 1977, p. 2981-2983.
 - [4]. H. Wiedemeier, H. G. Schnering, Refinement of the structures of GeS, GeSe, SnS and SnSe, *Z. Kristallogr.* **148**, 1978, p. 295-303.
 - [5]. X. Gonze, J. M. Beuken, R. Caracas, F. Detraux, M. Fuchs, M. Rignanese, L. Sindic, M. Verstraete, G. Zerah, F. Jallet, First-principles computation of material properties: the ABINIT software project Original Research Article Computational Materials Science, Volume 25, Issue 3, November 2002, p. 478-492
 - [6]. S. Goedecker, M. Teter, J. Hutter, Separable dual-space Gaussian pseudopotentials, *Phys. Rev. B* **54**, 1996, p.1703–1710.
 - [7]. C. Hartwigsen, S. Goedecker, J. Hutter, Relativistic separable dual-space Gaussian pseudopotentials from H to Rn, *Phys. Rev. B* **58**, 1998, p.3641-3662.
 - [8]. H. Monkhorst, J. Pack, Special points for Brillouin-zone integrations, *Phys. Rev. B* **13**, 1976, p.5188-5192.
 - [9]. J. Okazaki, The Crystal Structure of Germanium Selenide GeSe, *Phys.Soc.Jap.* **13**, 1958, p.1151-1155.
 - [10]. A. Onodera, I. Sakamoto, Y. Fujii, N. Mori, S. Sugai, Structural and electrical properties of GeSe and GeTe at high pressure, *Phys. Rev. B* **56**, 1997, p. 7935-7941.

P-V-T DEPENDENCES IN THE FLUID OF THE CARBON DIOXIDE AND CALCULATION OF OIL COMPONENTS PROPERTIES

E.E. RAMAZANOVA¹, M.M. ASADOV², E.N. ALIYEV¹

¹*Scientific-Research Institute Geotechnological Problems of Oil,
Gas and Chemistry, Baku*

²*Institute of Chemical Problems,
National Academy of Sciences of Azerbaijan, Baku
E-mail address: mirasadov@gmail.com*

Experimentally studied P-V-T dependences of carbon dioxide near the critical point are needed to determine the quantitative ratio of phases. Based on the experimental and theoretical data we have developed modified equations for calculation of critical properties of systems containing oil components. These modified equations to estimate physical-chemical properties can be used for calculation of critical properties and for other natural hydrocarbons.

Keywords: fluid CO₂; solubility; fluid extraction; PVT dependencies; calculation of critical parameters

PACS: 93.85.Tf; 82.60.-s; 05.70.Jk; 82.60.-s; 64.60.F-; 64.60.fd

Technologies based on use of supercritical fluid (SCF) are applied in most branches of industry, particularly in oil economy [1]. At the background of traditional methods the use of SCF turned out to be effective due to high solvency and SCF diffusion coefficient. At present two main trends of SCF use are in progress. In first case SCF is used for extraction of necessary substances from different materials, products or wastes of production. In second case SCF is used for realization of chemical reactions.

The aim of the present work is in research of *P-V-T* dependences near critical point of carbon dioxide and calculation of the critical parameters of the state in the oil fractions.

For research experiments were hold at *P-V-T* aggregate of “UGK-4” model equipped with the inspection window making it possible to observe disequilibrium effects in researched region. Scaling of carbon dioxide processing status at the apparatus was carried out at subcritical and overcritical values: $T = 298\text{--}305\text{ K}$ and $P = 1\text{--}10\text{ MPa}$. Hysteresis is observed on isotherms CO₂ i.e. the variation of *P-V* under conditions of increase and decrease of pressure did not coincide. As it is known, a hysteresis is typical to nonlinear processes the state of which is determined by not only current external conditions, but its prehistory as well. For change of system state, definite time is always required, in consequence of which a system reaction falls behind reasons causing it. Hysteresis processes differ by that a lag while deceleration of external conditions change does not decrease. Nonlinear dependences of hysteresis type occurred both at subcritical and overcritical values of state while research of dependence *P-V* for carbon dioxide. From these isotherms *P-V* it follows that quantity of fluid phase at subcritical parameters is much more than at overcritical parameters of CO₂. That is found parameters of state made it possible to change stability of system under subcritical conditions and realize fluid solubility.

Thus, it is determined that at a definite speed of CO₂ pressure increase ensuring process non-equilibrium and its further decrease at temperatures which are lower than critical temperature ($< 304.2\text{ K}$), the quantity of CO₂ fluid phase in system grows many-fold, what is important for effective use of CO₂ as a dissolvent. Under the same

conditions, but at experiment temperatures, which are higher than critical $T (> 304.2\text{ K})$, the quantity of fluid phase considerably decreases, what causes “drying” of gas.

It should be mentioned that nowadays-different oil-producing territories, particularly Apsheron peninsula (Azerbaijan), according to the status of environment approximate to regions of environmental miseries. At those profound changes of environmental components occur: soil and structure of soil covering, ground and subsoil, surface and underground waters and air. The capacity of the system based on CO₂ at critical values to dissolve different substances, particularly hydrocarbons and extract them at decrease of pressure in system has been used by us at assembled aggregate for treatment of oily soil at Scientific-Research Institute Geotechnological Problems of Oil, Gas and Chemistry (Azerbaijan State Oil Academy, Baku).

Carried out experiments and obtained data on extraction of oil and oil products in the system “overcritical fluid of carbon dioxide – oil-producing soil” with use of this method of fluid extraction proves that a this method makes it possible considerably to raise a degree of extraction of oil and oil products from oily soils.

In the process of quality control while extraction of oil products there were measured electrical capacitances of capacitors: empty capacitor, capacitor full of researched mixture (oil + soil) and capacitor full of dry soil, then there was correspondingly determined a dielectric permittivity. According to the level of approximation of dielectric permittivity of oily soil to dielectric permittivity of pure soil, the level of treatment was estimated.

It has been determined that in the result of treatment of oily soil, practically they are completely restored in accordance with established standards on soil composition. Oil extracted in the process of treatment may be used properly, for example, as fuel oil; ecological advancement also occurs; there are created favorable conditions for activity of people living on cleaned territories. On this aggregate oily soil is treated for 95–97 %. The quantity of extracted oil in the result of treatment of soil was 5.0 % from natural soil volume. The quantity of hydrocarbon fraction extracted by CO₂ pressed up to

critical state depends on its content and composition of soil as well as clearness and periodicity of CO₂ gas circulation in extraction-separation system. Critical properties of substances allow determining the important parameters, in particular, oil and its products [2-8]. We have calculated the critical and pseudo critical (pc) parameters of fractions of oil from Sangachal-Deniz deposit. Critical parameters are calculated by different methods. Nakey formula:

$$\lg(1,8 \cdot T_{pc}) = 1,2805 + 0,2985 \lg(\rho_4^{20} \cdot 10^{-3}) + 0,6216 \cdot \lg(1,8 \cdot T_{bp}) \quad (1)$$

where P_{pc} - pseudo critical pressure, MPa; ρ_4^{20} - relative density, g/cm³; T_{bp} - boiling point, K.

Lee - Kesler formula:

$$T_{pc} = 189,833 + 450,6 \cdot \rho_{15}^{15} + (0,4244 + 0,1174 \rho_{15}^{15}) T_{vabp} + \frac{0,1441 + 1,0068 \rho_{15}^{15}}{T_{vabp}} \quad (2)$$

where $\rho_{15}^{15} = 0,212 + 0,9917 \rho_4^{20}$ - relative density, g/cm³; T_{vabp} - volume average boiling point, K.

Kharchenko formula:

$$\lg T_{pc} = 1,10(44 + 0,244988 \rho_4^{20} + 0,65289 \cdot \lg T_{vabp}) \quad (3)$$

Pseudocritical temperatures found by different methods are shown in Table 1

Table 1. Calculated pseudo critical temperatures of oil fractions from Sangachal-Deniz (Azerbaijan)

Temperature of fraction selection, °C	T_{pc} , K – calculated by the formulas		
	(1)	(2)	(3)
85-105	550,15	550,19	912,71
105-140	576,79	577,17	962,67
HK-140	570,89	571,15	950,51
140-180	613,02	613,69	1000,23

Pseudo critical temperatures calculated by different methods differ within the margin of error 4-5%. Lee-Kesler method is the most suitable for these fractions (2). Methods determining the pseudo critical pressures are less accurate than methods determining the pseudo critical temperatures. Pseudo critical pressures of observed fractions are calculated by the following formulas:

Lee-Kesler formula:

$$\ln P_{pc} = \frac{3,3839 - 0,0566}{\rho_{15}^{15}} - \frac{0,436392 + 4,12164}{\rho_{15}^{15}} + \frac{0,213426}{(\rho_{15}^{15})^2} \cdot 10^{-3} T_{bp} + \frac{4,75794 - 11,81952}{\rho_{15}^{15}} + \frac{1,530155}{(\rho_{15}^{15})^2} \cdot 10^{-3} T_{bp} + \frac{2,450548 + 9,900986}{(\rho_{15}^{15})^2} \cdot 10^{-1} \quad (4)$$

To calculate the pseudo critical pressure, we have used the following empirical formula:

$$P_{pc} = 21,531025 \cdot 10^6 (1,8 T_{bp})^a (\rho_{15}^{15})^b \quad (5)$$

where $a = 2,3125$; $b = 2,3201$.

$$P_{pc} = 0,9414 \cdot 10^6 T_{vabp} (-2,017) \cdot \rho_4^{20} \quad (6)$$

Kharchenko formula:

$$P_{pc} = 2,11216 + 0,796456 \cdot \lg \rho_4^{20} + 0,23587 \lg T_{vabp} \quad (7)$$

Pseudo critical pressure values are shown in Table. 2.

Table. 2 The calculated pseudo critical pressures of oil fractions from Sangachal-Deniz deposit (Azerbaijan).

Temperature of fraction selection, °C	P , MPa – calculated by the formulas			
	(4)	(5)	(6)	(7)
85-105	2,47	3,06	4,48	2, 60
105-140	2,31	2,87	4,09	2, 62
HK-140	2,26	2,82	4,10	2, 61
140-180	2,09	2,61	3, 63	2, 64

The values obtained by formula (4) are in good agreement with experimental data of studied oil fractions.

- [1]. *M.M.Asadov, E.E.Ramazanova, A.L.Shabanov* // Azerbaijan oil industry. 2012. No 12. P. 34-41. (in Russian)
- [2]. *N.P.Zhukova, V.I.Bychenka, I.A.Cherepinnikova, Kuzmina S.N.* // Chemistry and Technology of Fuels and Oils. No 4. 1993. P. 29-32. (in Russian)
- [3]. *R.Reid, J.Prausnitz, T.Sherwood* The properties of gases and liquids. M: Chemistry. 1982. 592 p. (in Russian)
- [4]. *C.Bretschneider* The properties of gases and liquids. M.: Chemistry, 1966. 535 p. (in Russian)
- [5]. *S.S. Yarovoy* The calculation methods of physical and chemical properties of hydrocarbons. M.: Chemistry. 1978. 256 p. (in Russian)
- [6]. *S.M.Walas* Phase Equilibria in Chemical Engineering. Boston, MA. Butterworth-Heinemann. 1985. 671p.
- [7]. *M.A.Anisimov, V.A.Rabinovich, V.V.Sychev* Thermodynamics of the critical state of individual substances. M.: Energoizdat. 1990. 190 p. (in Russian)
- [8]. *S.A.Ahmetov, N.A.Gostenova* // Izv. VUZ. Oil and gas. 2005. No 6. P. 92-95. (in Russian)

DIELECTRIC COEFFICIENTS AND CONDUCTIVITY OF TlErTe₂ CRYSTAL IN ALTERNATE ELECTRIC FIELDS

A.M. PASHAEV, S.N. MUSTAFAEVA, E.M. KERIMOVA

G.M.Abdullayev Institute of Physics, Azerbaijan National Academy of Sciences,

Baku, AZ 1143, Azerbaijan,

E-mail: solmust@gmail.com

The electrical properties (loss tangent, real (ϵ') and imaginary (ϵ'') parts of complex dielectric permittivity, and ac conductivity of TlErTe₂ single crystals have been studied in the frequency range $f = 5 \cdot 10^4$ to $3.5 \cdot 10^7$ Hz. The results demonstrate that the dielectric dispersion in the TlErTe₂ crystal has a relaxation nature. The experimental frequency dependence of the dissipation factor $\tan \delta$ for TlErTe₂ single crystal is characterized with a monotonic descending. The hyperbolic decrease of $\tan \delta$ with frequency is evidence of the fact, that conductivity loss becomes the main dielectric loss mechanism at studied frequency range.

At frequencies $f = 2 \cdot 10^5 - 1.8 \cdot 10^7$ Hz the ac conductivity of the TlErTe₂ crystal varies as $f^{0.8}$, characteristic of hopping conduction through localized states near the Fermi level. The Fermi-level density of states ($N_F = 2 \cdot 10^{18} \text{ eV}^{-1} \cdot \text{cm}^{-3}$), the spread of their energies ($\Delta E = 0.05 \text{ eV}$), and the mean hop distance ($R = 174 \text{ \AA}$) and time ($\tau = 0.1 \text{ ns}$) have been estimated. The concentration of deep traps determining the ac-conductivity of TlErTe₂ crystal ($N_t = N_F \times \Delta E$) is 10^{17} cm^{-3} .

Keywords: TlErTe₂ crystal; dielectric permittivity; frequency; ac-conductivity; Fermi-level density of states; the mean hop distance.

PACS: 71.20.-b; 71.20.Eh; 71.20.Nr; 72.15.Rn; 72.30.+q

TlErTe₂ compound belongs to the family of ternary thallium lanthanide chalcogenides, crystallized in the rhombohedral structure of $\alpha - \text{NaFeO}_2$ type [1 – 4]. According to [4] the unit-cell parameters of the TlErTe₂ crystals were determined to be $a = 4.376$; $c = 24.23 \text{ \AA}$. In [4] magnetic properties and crystal field effects in TlErTe₂ compounds were investigated.

The present work was undertaken to study electric and dielectric properties of TlErTe₂ single crystal.

Homogeneous samples were obtained by the method of direct synthesis, i.e. by the reaction between the starting components (Tl, Er, Te) of high purity degree. TlErTe₂ single crystals were grown by the Bridgman method.

TlErTe₂ samples for electrical measurements had the form of planar capacitors. Electrical contacts were made by silver paste. The thickness of the single-crystal TlErTe₂ samples was 0.25 cm. The dielectric properties of the TlGaS₂ single crystals were studied by a resonance technique [5] in the frequency range 5×10^4 to 3.5×10^7 Hz, using a TESLA BM 560 Q-meter. During the measurements, the samples were situated in a shielded chamber. All of the measurements were performed at 300 K in electric fields corresponding to Ohmic current-voltage behavior. The accuracy in determining the sample capacitance and the merit factor ($Q = 1/\tan \delta$) of the measuring circuit was limited by reading errors. The capacitors were calibrated with an accuracy of $\pm 0.1 \text{ pF}$. The reproducibility in the resonance position was $\pm 0.2 \text{ pF}$ in terms of capacitance and ± 1.0 – 1.5 scale divisions in terms of Q . The largest deviations from the average were 3–4 % in ϵ' and 7% in $\tan \delta$.

Figure 1 shows the frequency dependence of relative dielectric permittivity (ϵ') for TlErTe₂. As seen in Fig.1, the permittivity of the crystal exhibit insignificant dispersion: as the frequency is raised from 5×10^4 to 3.5×10^7 Hz, ϵ' decreases from 26.3 to 19. Figure 2 shows the dielectric loss factor $\epsilon'' = \epsilon' \tan \delta$ as a function of frequency for TlErTe₂. In the frequency range studied, ϵ'' varies from 2.6 to 0.46. As the frequency is raised to 3.5×10^7 Hz, ϵ'' decreases by a factor of 5.6; that is, the $\epsilon''(f)$

dispersion curve is characterized by a significant drop over the entire frequency range studied.

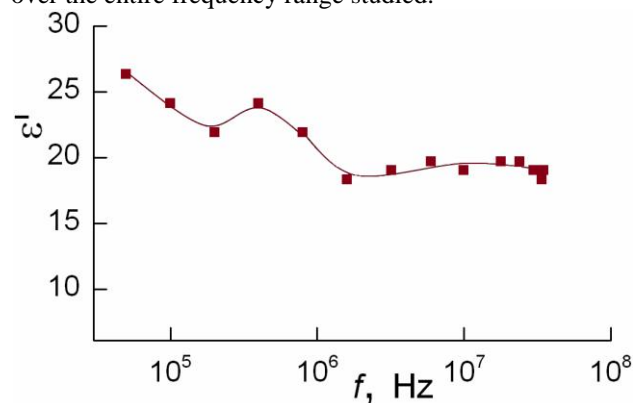


Fig.1. Frequency dispersion of the real part of complex dielectric permittivity of the TlErTe₂ crystal at $T = 300\text{K}$.

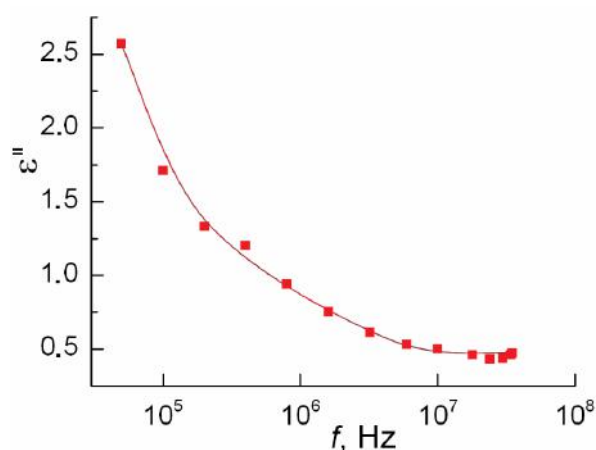


Fig.2. Frequency dependence of the imaginary part of complex dielectric permittivity of the TlErTe₂ crystal.

The experimental frequency dependence of the dissipation factor $\tan \delta$ for TlErTe₂ single crystal is characterized with a monotonic descending (Fig.3). The

hyperbolic decrease of $\tan \delta$ with frequency is evidence of the fact, that conductivity loss becomes the main dielectric loss mechanism [6] at studied frequency range.

Frequency-dependent 300-K ac-conductivity of TlErTe₂ crystal (Fig. 4) follows the relation $\sigma_{ac} \sim f^s$ with $s = 0.3$ at $f = 5 \times 10^4 - 2 \times 10^5$ Hz; $s = 0.8$ at $f = 2 \times 10^5 - 1.8 \times 10^7$ Hz, and $s = 1$ at $f > 1.8 \times 10^7$ Hz.

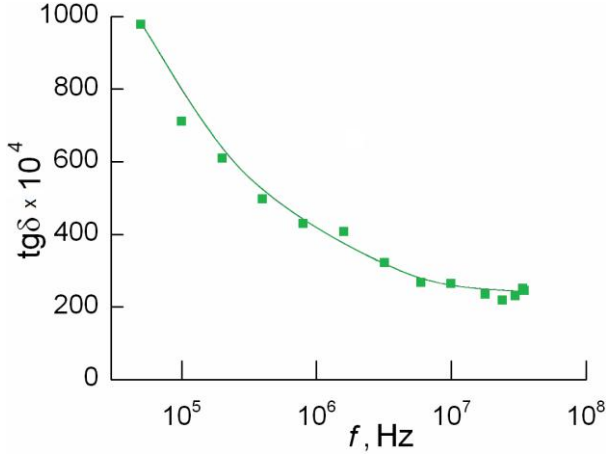


Fig.3. The dissipation factor $\tan \delta$ for TlErTe₂ crystal as a function of frequency.

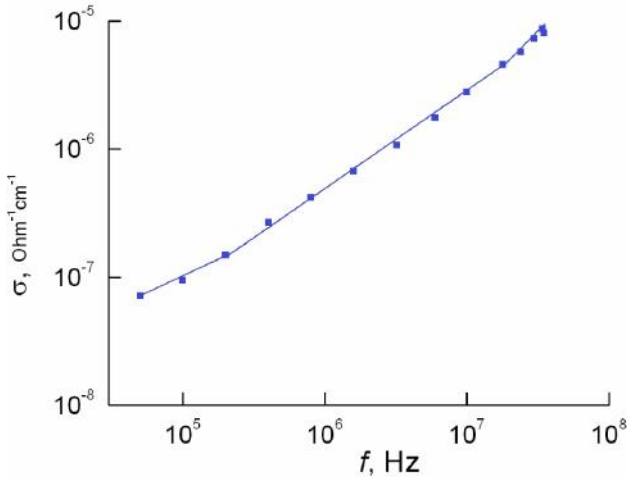


Fig.4. Log – log plot of 300-K ac-conductivity against frequency for the TlErTe₂ crystal.

Conduction-band ac conductivity is known to be mainly frequency-independent up to 10^{10} – 10^{11} Hz. The observed $\sigma_{ac} \sim f^{0.8}$ behavior suggests that the conduction is due to carrier hopping between localized states in the band gap of the material. Such states may be localized near the edges of allowed bands or near the Fermi level [7]. However, under typical experimental conditions, conduction through the states near the Fermi level always prevails over that through the states near band edges. Therefore, the observed $\sigma_{ac} \sim f^{0.8}$ behavior in TlErTe₂

attests to hopping transport through the states localized near the Fermi level [7]

$$\sigma_{ac}(f) = (\pi^3/96) \cdot e^2 k T N_F^2 a^5 f [\ln(v_{ph}/f)]^4, \quad (1)$$

where e is the elementary charge and k is the Boltzmann constant, N_F is density of localized states near the Fermi level, a is the localization length, v_{ph} is the phonon frequency.

According to Eq. (1), ac conductivity varies as $f[\ln(v_{ph}/f)]^4$. Therefore, at frequencies $f \ll v_{ph}$, σ_{ac} is approximately proportional to $f^{0.8}$.

Using Eq (1) and our obtained experimental $\sigma_{ac}(f)$ data, we evaluated the Fermi-level density of states, $N_F = 2 \times 10^{18} \text{ eV}^{-1} \text{ cm}^{-3}$. When calculating N_F , the localization length for the TlErTe₂ was taken as $a = 30 \text{ \AA}$, and $v_{ph} = 10^{12} \text{ Hz}$.

According to the hopping conduction theory, the average ac hopping length is determined from the formula

$$R = (1/2\alpha) \ln(v_{ph}/f) \quad (2)$$

Here, α is the decay constant of the wave function of the localized charge carrier $\Psi \sim e^{-\alpha r}$ ($\alpha = 1/a$).

The value R calculated for TlErTe₂ single crystal using Eq. (2) is 174 \AA . Using this value of R and the formula

$$\tau^{-1} = v_{ph} \exp(-2 \alpha R), \quad (3)$$

we evaluated the mean hop time of charge carriers between localized states in the band gap of TlErTe₂: $\tau = 10^{-7} \text{ s}$. Using the relation [7]

$$\Delta E = 3/(2\pi R^3 N_F) \quad (4)$$

we estimated the energy spread of localized states ΔE near the Fermi level of TlErTe₂ single crystal: $\Delta E = 0.05 \text{ eV}$. The concentration of trapping states responsible for ac-conductivity in TlErTe₂ crystals was calculated according to the formula

$$N_t = N_F \Delta E \quad (5)$$

The N_t value for TlErTe₂ crystal was determined to be 10^{17} cm^{-3} .

Thus, the results of high-frequency dielectric measurements on TlErTe₂ crystals provided an opportunity to determine the mechanisms of dielectric losses and charge transport, and also to evaluate the density of states at the Fermi level; the average time of charge carrier hopping between localized states, average hopping distance, scattering of trap states near the Fermi level and concentration of deep traps.

[1]. M.Duczmal, L.Pawlak Magnetic properties of TlLnS₂ compounds (Ln = Nd, Gd, Dy, Er and Yb). Journal of Alloys and Compounds. 1994. V. 209. N 1-2. P. 271-274.

[2]. M.Duczmal, L.Pawlak Magnetic properties of TlLnS₂ compounds (Ln = Tb, Ho and Tm). Journal of Alloys and Compounds. 1995.V. 219. N 1-2. P.189-192.

- [3]. *M.Duczmal, L.Pawlak* Magnetic and structural characterization of TlLnSe_2 compounds (Ln = Nd to Yb). *Journal of Alloys and Compounds*. 1995. V. 225. N 1-2. P.181-184.
- [4]. *M.Duczmal, L.Pawlak* Magnetic properties and crystal field effects in TlLnX_2 compounds (X = S, Se, Te). *Journal of Alloys and Compounds*. 1997. V. 262-263. P.316-319.
- [5]. *S.N. Mustafaeva* Dielectric properties of $\text{TlGa}_{1-x}\text{Fe}_x\text{Se}_2$ single crystals in alternate electric fields. *Journal of Radioelectronics*. 2008. No 5. P. 1 – 11. (In Russian).
- [6]. *V.V.Pasynkov, V.S.Sorokin* Materials of electron techniques. Moscow. Mir. 1986. 368 p.
- [7]. *N.Mott, E.Davis* Electron processes in noncrystalline materials. Clarendon Press, Oxford, 1971. 472 p.

X-ray PHASE ANALYSIS OF Cu_5SmSe_4

A.S. AMIROV, G. G. GUSEYNOV, T.R. MEHDIYEV

*G.M.Abdullayev Institute of Physics,
Azerbaijan National Academy of Sciences
AZ-1143 Baku, Azerbaijan, H.Javid, 33*

By the method of X-ray phase analysis it is established that the temperature dependence of X-ray diffractograms Cu_5SmSe_4 in first approximation is defined by temperature changes of structural parameters of three polyhedrons: chalcocine, samarium, selenium, moreover the cuprum disposition in polyhedrons is similar to their disposition in cuprum polyhedrons in bornite, at which the one of cuprum atoms is two-valent. The observable minimum on temperature dependence of structural parameters near 400°C is interpreted as structure stabilization Cu_5SmSe_4 and defect disappearance corresponding to Cu_6SmSe_4 compound in which all cuprum atoms are one-valent. The chemical formula of Cu_5SmSe_4 has the form: $2\text{Cu}_2\text{S}-\text{CuSmS}_2$ in which the following valent combinations are possible: $(\text{Cu}^{1+}\text{Sm}^{3+})$ and $(\text{Cu}^{2+}\text{Sm}^{2+})$ corresponding to the cases of samarium introduction into structure in metallic and semiconductor forms and consequently, the appearance of mixed valency effect in given compound.

Keywords: selenides of rare-earth metals, chalcocine, bornite, X-ray phase analysis, mixed valency.

PACs: 63.50.-x, 63.50.Gh, 64.70.Nd

INTRODUCTION

The new physical ideas appeared in the middle of XXth century in the connection with the use of semiconductor materials containing the compounds of rare-earth elements have led to the rapid development of perspective directions in technologies of high-effective energy transformer elements, receivers/radiators, devices and other modern information-logical structures.

The investigations [24] show that rare-earth compound have the significant properties because of the presence of $4f$ -membrane. At compound formation, f -membranes of rare-earth ions aren't overlapped by each other formatting the localized levels which by energy can be situated in semiconductor forbidden band playing the role of "impurity" levels with order concentration 10^{22} cm^{-3} . The uniqueness of this fact is that such big concentration of local impurity levels hasn't been created in any known semiconductors. The first investigations show on the fact that many compounds with rare-earth elements in the dependence on valency state of rare-earth element, can be either metals (when the ion is three-valent) or semiconductors (when ion is two-valent).

The samarium sulfide the properties of which are emphasized not among only rare-earth but semiconductor materials is the one of the brightest representatives of rare-earth semiconductors. It has the lowest pressure value at which the iso-structural phase transition semiconductor-metal is observed (6,5 kbar at 300 K); possibility of transformation of sample surface layer into metal state by the way of polishing; the biggest value of piezo- and tezo-resistive and also thermal-voltaic effects. As it has been established, all these properties are directly connected with the presence of samarium ion transition in the state with intermediate valency ($\text{Sm}^{2+} \rightarrow \text{Sm}^{2.7+}$). Note that analogous transitions are observed in compounds of other rare-earth elements. So for example, the state Ce^{4+} with empty $4f$ -membrane is the stable for cerium besides the usual state Ce^{3+} . As it has been established in first investigations, for $4f$ -electrons of many rare-earth ions, the case of limit localization realizes i.e. the ion electron membranes are atom-like and are characterized by the same quantum numbers as the isolated ion state is.

Nowadays the new rare-earth compounds in which the electron transfers between different configurations of f -membranes characterizing by the different numbers of f -electrons and consequently, by valency. As the f -electron at such transitions has the partially band character, then valency can be fractional value. Thus the phase transition can have the strong electron character; moreover, it can be isomorphous one, i.e. it takes place without lattice symmetry change. Besides pressure and temperature the samarium valency change in the compounds can take place because of composition change and its exchange of other elements with least ion radiuses by its ions. However, effect isn't always achieved, as the structure of these compounds is the main factor influencing on the transition with valency change.

Thus, the investigation actuality of $\text{Cu}_2\text{Se}-\text{Sm}_2\text{Se}_3$ system compounds in which the presence of phase transition with alternative valency is supposed and also allowing the establishment of their use perspectivity in the capacity of the compounds having the high magnetic, photo-sensitive, magneto-photo-sensitive, thermo-electric and other properties, is obvious one.

The results of X-ray investigations of rare-earth semiconductor compound Cu_5SmSe_4 being the one of the stable phases in the system of solid solutions $\text{Cu}_2\text{Se}-\text{Sm}_2\text{Se}_3$ are published in present paper.

Note that state analysis of scientific publications by the given system of solid solutions containing the rare-earth ion, shows the big interest to it from the side of leading scientific centers of Japan, USA, Germany, Russia, Ukraine. The investigations of rare-earth semiconductors in Azerbaijan had been begun in 70th years of XX c. in Institute of Physics of Azerbaijan Academy of Sciences.

SAMPLE PREPARATION

The compound Cu_5SmSe_4 is synthesized from elements Cu (99.99%), Sm (by CMM-1 mark), Se (99.999%) in quartz ampoule at temperature $375-1160^\circ\text{C}$ in vacuum $1.3 \cdot 10^{-3} \text{ Pa}$. The ingot homogenization is carried out at 750°C during 168 hours. According to works [1-2] Cu_5SmSe_4 phase in $\text{Cu}_2\text{Se}-\text{Sm}_2\text{Se}_3$ system forms at heating up to 1048K and incongruently melts at 1353K .

EXPERIMENTAL EQUIPMENT, INVESTIGATION RESULTS AND THEIR DISCUSSION

The experimental results of temperature X-ray diffractometric investigations Cu_5SmSe_4 carried out on X-ray diffractometer D8 ADVANCE (Bruker LTD, Germany) of Institute of Physics of Azerbaijan Academy of Sciences are presented in present work. The additional treatment of X-ray investigation results are carried out by interpolation programs allowing the construction of differential dependences of thermal expansion coefficient.

The powder diffractograms obtained from investigated samples Cu_5SmSe_4 in first approximation correspond to trigonal structure with $P\bar{3} - C_{3i}^1$ space symmetry group. The data of X-ray measurements on this stage of investigations are obtained in the presence of crystal hexagonal installation. The information about some peculiarities of hexagonal installation of trigonal crystals can be found in [3]. The results of structure definition Cu_5SmSe_4 are given below. All results are carried out with delicacy not less 10^{-5} .

Table.1 Temperature dependence of elementary cell parameters Cu_5SmSe_4

T, K	<i>a</i> , Å	<i>c</i> , Å	V,
100	11,4257	8,68014	982,45
150	11,4238	8,67855	981,95
200	11,4298	8,67969	983,11
300	11,443	8,68095	985,52
400	11,4497	8,67903	986,46
700	11,4793	8,69928	993,88

The diffractograms Cu_5SmSe_4 are given on fig.1, the values of elementary cell parameters at temperatures: 100, 150, 200, 300, 400, 700K are given in table 1.

The temperature dependences of parameters «*a*», «*c*» and volume *V* of crystal structure Cu_5SmSe_4 are given on fig. 2-4.

The changes of temperature coefficients of the angles $2\theta = 13.426(a)$; $26.981(b)$; $28.602(c)$; $30.88(d)$; $44.284(e)$; $53.068(f)$ degree of diffraction spectrum Cu_5SmSe_4 in 100 -700K interval are given on fig.5.

The crystal structure CuSmSe_2 ($M^{3+} - \text{Sm}^{3+}$, constructed by data of work [10]) is given on fig.7. The structure component images in the difference on work [10], are given in forms suitable for text understanding of article data. *a* is coordination surrounding in Cu and Sm полиэдрах; *b* is type of cuprum (2), samarium (1) and selenium (3,4) polyhedrons; *c* is structure fragment and disposition of cuprum polyhedron in it $[\text{Cu}_2\text{Se}_6]^{10-}$ and samarium polyhedrons (3), and also the ways of their attachments (1, 2); *d* is layer structure; *e* is elementary fragment; *f* are cuprum polyhedrons and ways of their attachments are shown on the figure.

The dash-diagrams: Cu_5Se_4 , Cu_2Se , SmSe , Cu_{2-x}Se , Cu_5SmSe_4 and diffractogram Cu_5SmSe_4 are given on fig.9-10.

Note that the obtained X-ray data by Cu_5SmSe_4 powders are well agree with published data for isomorphous compounds with Cu_5SmSe_4 : Cu_5GdSe_4 , Cu_5TbSe_4 , Cu_5DySe_4 , Cu_5HoSe_4 , Cu_5ErSe_4 , Cu_5YbSe_4 , Cu_5LuSe_4 .

Nowadays the information about publications of structural investigation results of isomorphous Cu_5SmSe_4 compounds Cu_5GdSe_4 , Cu_5TbSe_4 , Cu_5DySe_4 , Cu_5HoSe_4 , Cu_5ErSe_4 , Cu_5YbSe_4 , Cu_5LuSe_4 have limited and scrappy character [4].

X-RAY PHASE ANALYSIS. THE DISCUSSION OF EXPERIMENTAL INVESTIGATION RESULTS.

The existence of alternative valency effect in compounds SmS , SmSe , CuSmS_2 and etc, is interpreted as result of *Sm* ion position in crystal structure either in position corresponding to its two-valent (semiconductor phase) or corresponding to its three-valent configurations (metal phase) [24].

The peculiarities of «*a*» parameter change of single crystal SmS in temperature interval 100–700K and also filling degrees of multiplet levels of the main therm of Sm^{2+} ion *f*-membrane are investigated in works of colleagues of V.V.Kaminsky group by X-ray diffractometer method. E parameter change

It is established that in samples with expressed thermal-voltaic effect at heating «*a*» parameter change is connected with transition of samarium defect ions into state of mixed valency.

The first electric measurements show on the presence of semiconductor properties of Cu_5SmSe_4 . Note that metallic conduction is the evidence of the fact that samarium is in three-valent state.

For understanding of this situation note that electron state of samarium membranes has the form $1s^2 2s^2 2p^6 3s^2 3p^6 4s^2 3d^{10} 4p^6 5s^2 4d^{10} 5p^6 6s^2 4f^6$. The filling of samarium 4*f*-electron membrane by the half influences on properties of samarium atoms, i.e. each of *f*-orbitals has the one unpaired electron. Sm^{2+} doesn't have electrons on 5*d*-orbitales. Sm^{2+} two-valent ion forms at the breakage from atom of two internal electrons with 6*s*-orbitales. As a result of small radial extension of 4*f*-orbitales, their splitting in crystal field, for example, ligands, insignificantly changes at surrounding (ligand) change. The stability of two-valent state is the consequence of stability conditions of 4*f*-membrane: unfilled, filled by half and totally filled. The transition energy from 4*f*6 state into 4*f* 5(6*H*)5*d*2*g* state is equal to $E_{fd} = 0.18$ eV.

In first approximation from observable dependences of diffractogram spectra it is followed that in considered temperature interval the symmetry space group Cu_5SmSe_4 doesn't change. Though, as it is seen on fig.2-5, in considered temperature interval, the diffraction spectrum maximums shift and consequently the changes of «*a*», «*c*» parameters and elementary cell volume Cu_5SmSe_4 are observed. The further investigations show that temperature changes of elementary cell parameters have the non-linear character, moreover in interval the increase of «*a*» and «*c*» parameters is observed, further, in temperature region 400-550K they decrease and at further temperature growth their increase is observed again. Note that similar changes are observed for example in maximum positions: $2\theta = 13.426$; 26.981 ; 28.602 ; 30.88 ; 44.284 ; 53.068 degree of diffraction spectrum in temperature interval 100-700K (fig.5). It is known that temperature investigations of X-ray diffraction spectra of SmS films [5-6] show on changes of diffraction maximum position [200] with temperature increase connected with

increase of “a” parameter of elementary cell (the given line is connected with Sm position in crystal structure). This effect is interpreted in work [16] as the result of change of the valency and isomorphous phase transitions in rare-earth element compounds. Correspondingly, the interpretation of observable effect in SmS is connected with transition from metal phase into semiconductor, i.e. SmS phase degradation and Sm_3S_4 phase formation. It is established that at transition SmS from semiconductor phase into metal state the anomalous big volume change is observed. The analogous phase transitions are observed in $SmSe$ and $SmTe$. However, in the difference on SmS in which the phase transition into metal state takes place spasmodically at hydrostatic pressure in 6.5kbar, in these compounds the analogous phase transition takes place gradually without change of crystal structure symmetry and pressures by 60 kbar order. It is well known that in case when linear expansion is the linear function from the temperature, it is more obviously that it takes place along crystallographic axis. Such situation explains the obtained non-linear temperature dependences for considered diffraction spectrum maximums. However, the 2θ maximum interpretation as complex ones is possible, i.e. as a result of overlapping of several maximums. Such explanation allows the understanding of observable temperature changes for all diffractogram maximums that evidences about reconstruction of crystal structure Cu_5SmSe_4 .

The temperature dependence explanation of thermal expansion coefficient Cu_5SmSe_4 presents itself the enough complex task though according to phase diagram in

temperature interval from 860 up to 900°C, near formation temperature of Cu_5SmSe_4 , the compound formation Cu_6SmSe_4 and Cu_4SmSe_4 is possible. By other hand, in temperature range up to 550°C according to phase diagram [22] the appearance of other situations connected with both reorientation of cuprum and samarium polyhedrons and changes of bonds in polyhedrons with different temperature coefficients of extensions is quite possible.

In work [8] it is shown that in $Ln-M-Z$ system phase structure (Z is anions of VI $\bar{6}$ subgroup O , S , Se , Te ; Ln is rare-earth elements; M is Cu^{1+} , Zn^{2+} , Cd^{2+} , Al^{3+} , Ga^{3+} , In^{3+} , Si^{4+} , Ge^{4+} and partially for Ag^{1+} , Mg^{2+} , Fe^{2+} , Fe^{3+}) the chalcogenide polyhedrons with small coordinate numbers which are excluded for rare-earth elements, are observed.

It is obvious that cuprum polyhedrons [9] are related to chalcozine structure.

In chalcozine cubic modification sulfur ions (or selenium) form the dense cubic package in which all tetrahedral spaces are occupied by Cu^{1+} . The tetrahedrons have the common edges (each edge belongs to two tetrahedrons) and fill the volume totally. Moreover, cuprum ions being in tetrahedrons form the clusters in which their interaction leads to exchange of $2Cu^{1+} \rightarrow Cu^{2+}$, i.e. structure is defect one $Cu_{2-x}S$. Usually $Cu_8^{1+}Cu^{2+}_2S_5$ instead $Cu_{10}S_5$ on the same volume is on each 10 tetrahedrons.

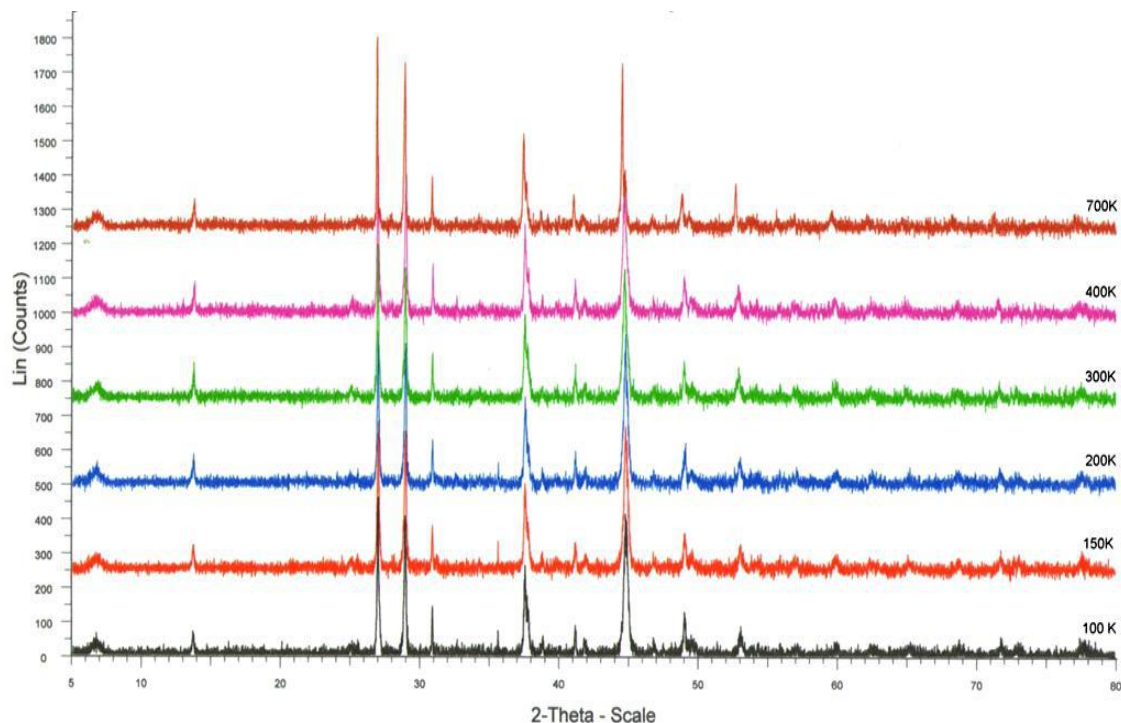


Fig.1. The powder diffractogram Cu_5SmSe_4 obtained at temperatures 100, 150, 200, 300, 400, 700K.

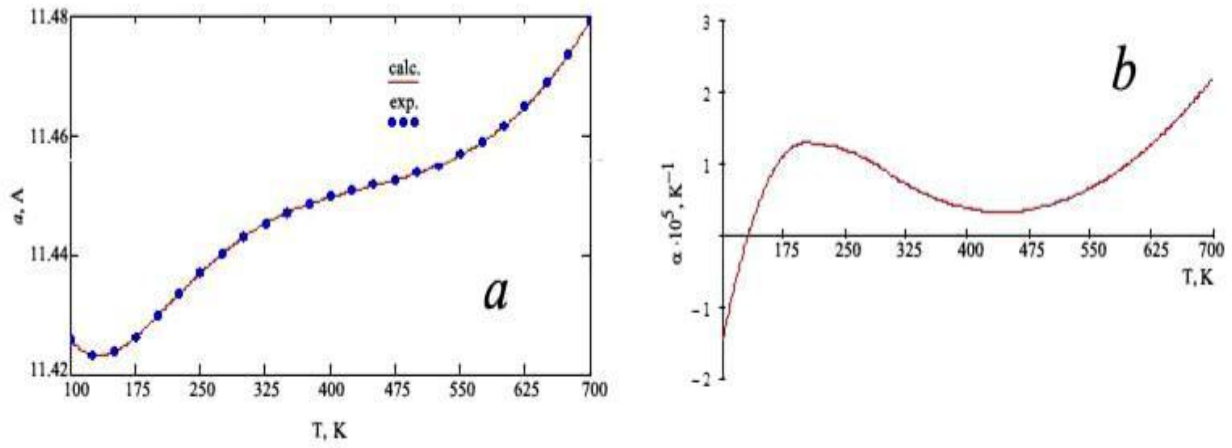


Fig.2 The temperature dependences: (a) of « a » parameter of crystal lattice; (b) of α thermal expansion coefficient.

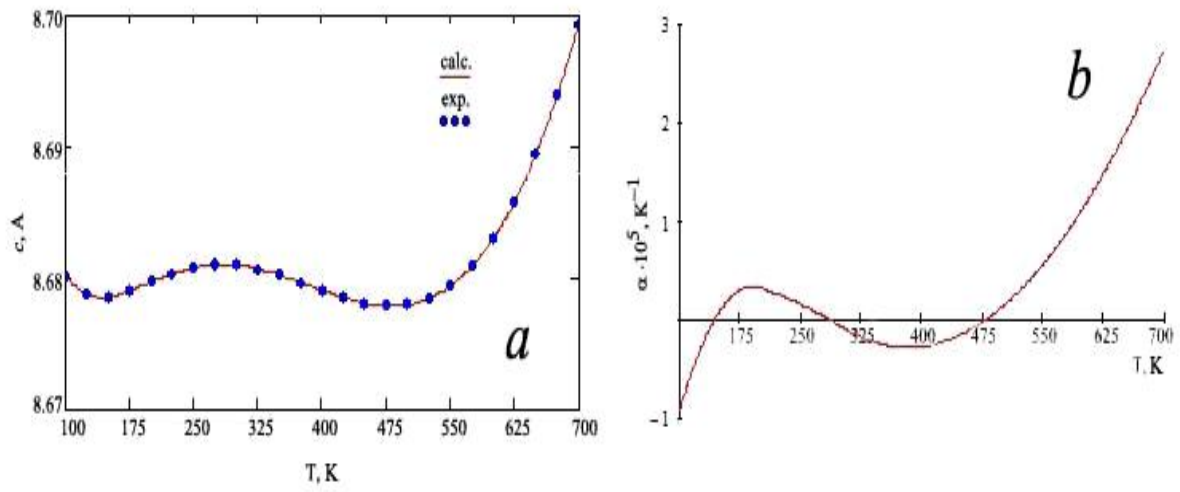


Fig.3 The temperature dependences: (a) of « c » parameter of crystal lattice; (b) of α thermal expansion coefficient.

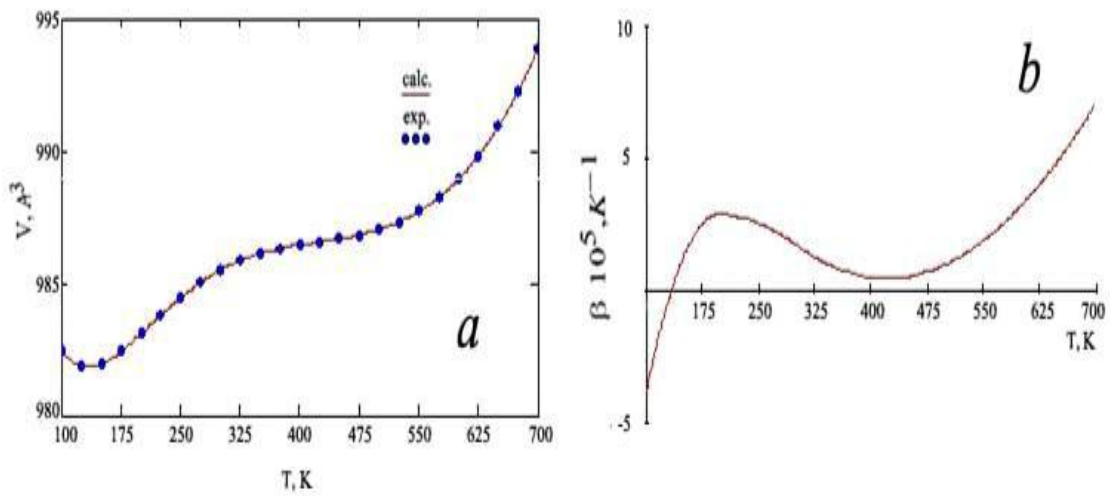


Fig.4 The temperature dependences: (a) of crystal lattice volume « V »; (b) of β thermal volume expansion coefficient

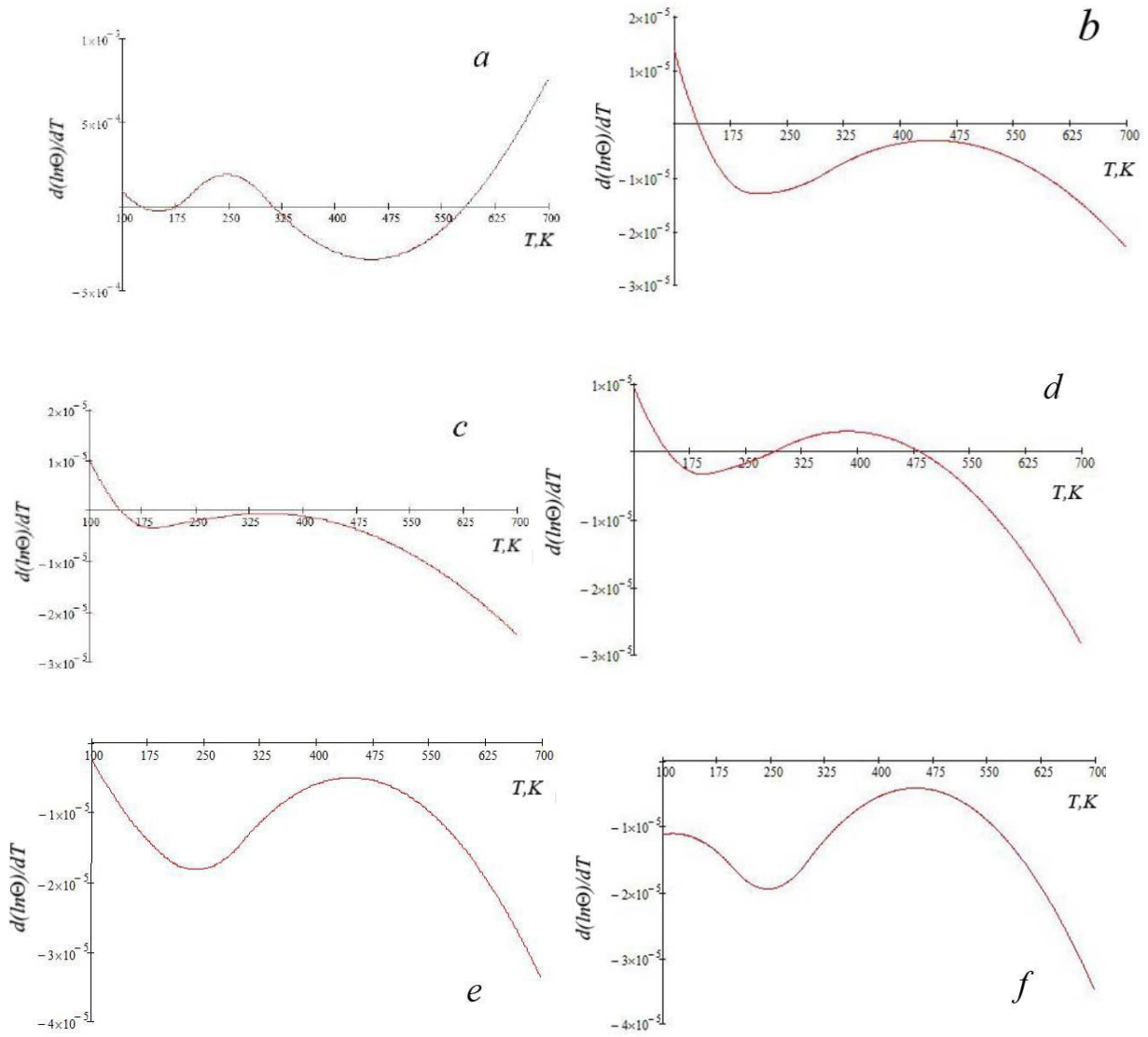


Fig.5 The changes of angle temperature coefficients $2\theta = 13.426(a)$; $26.981(b)$; $28.602(c)$; $30.88(d)$; $44.284(e)$; $53.068(f)$ degree Cu_5SmSe_4 diffraction spectrum in interval 100 -700K.

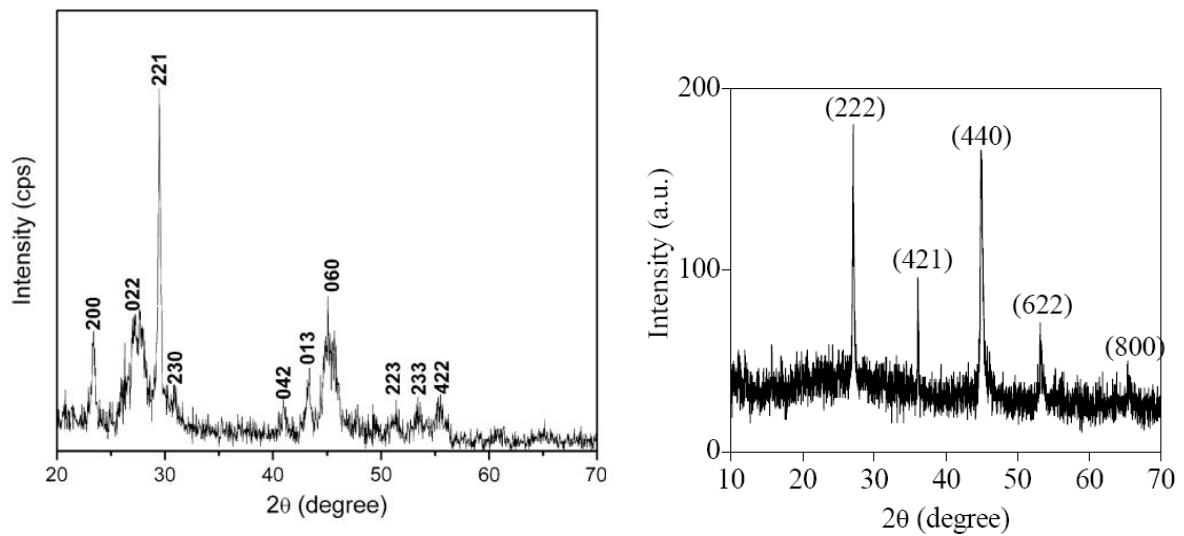


Fig.6 XRD spectra Cu_5Se_4 and cubic phase Cu_7Se_4 at 150°C obtained in works [12-13]

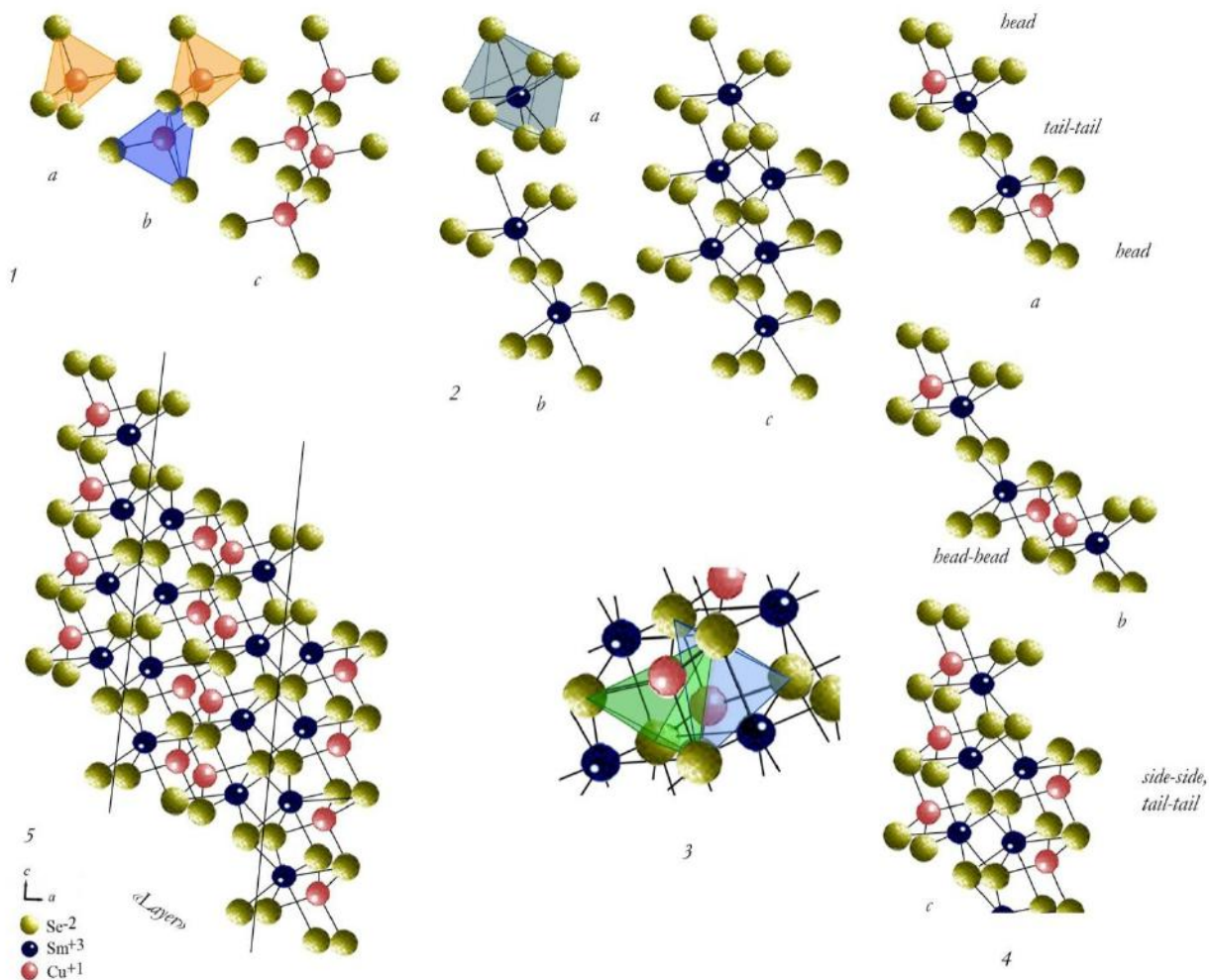


Fig. 7 The crystal structure CuSmSe_2 (M^{3+} - Sm^{3+} constructed by data of works [10,25]): 1-2: a are polyhedrals of Cu and Sm ; b is attachment of polyhedrals of cuprum and samarium; c is structure fragment and position of polyhedrals of cuprum and samarium in it; 3 are selenium (sulfur) polyhedrals and their attachments with cuprum and samarium polyhedrals; 4 (a, b, c) are structure fragment construction; 5 is CuSmSe_2 structure construction, "layer" is emphasized.

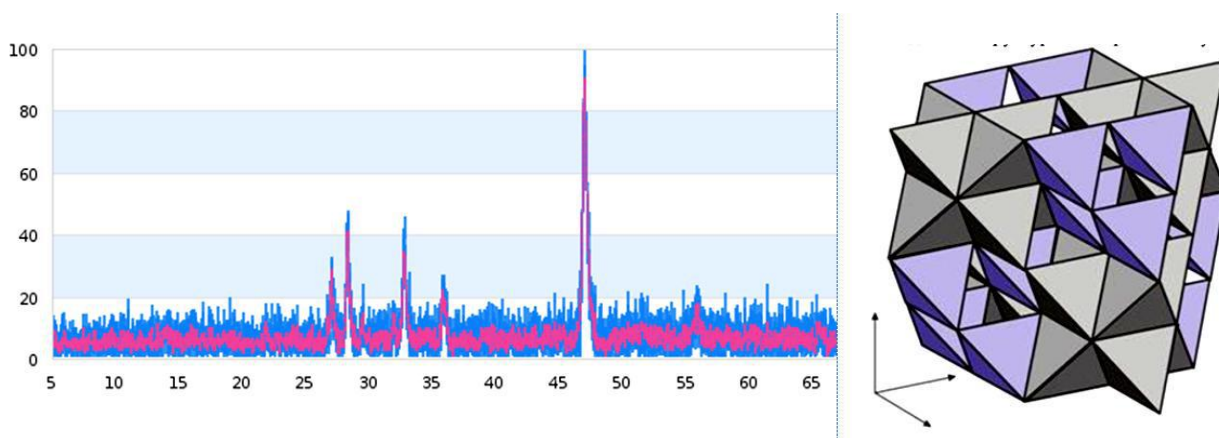


Fig.8 The diffractogram and structure of bornite high-temperature modification with fragments of chalcocine (grey) and chalcocopyrite (lilac) types [13].

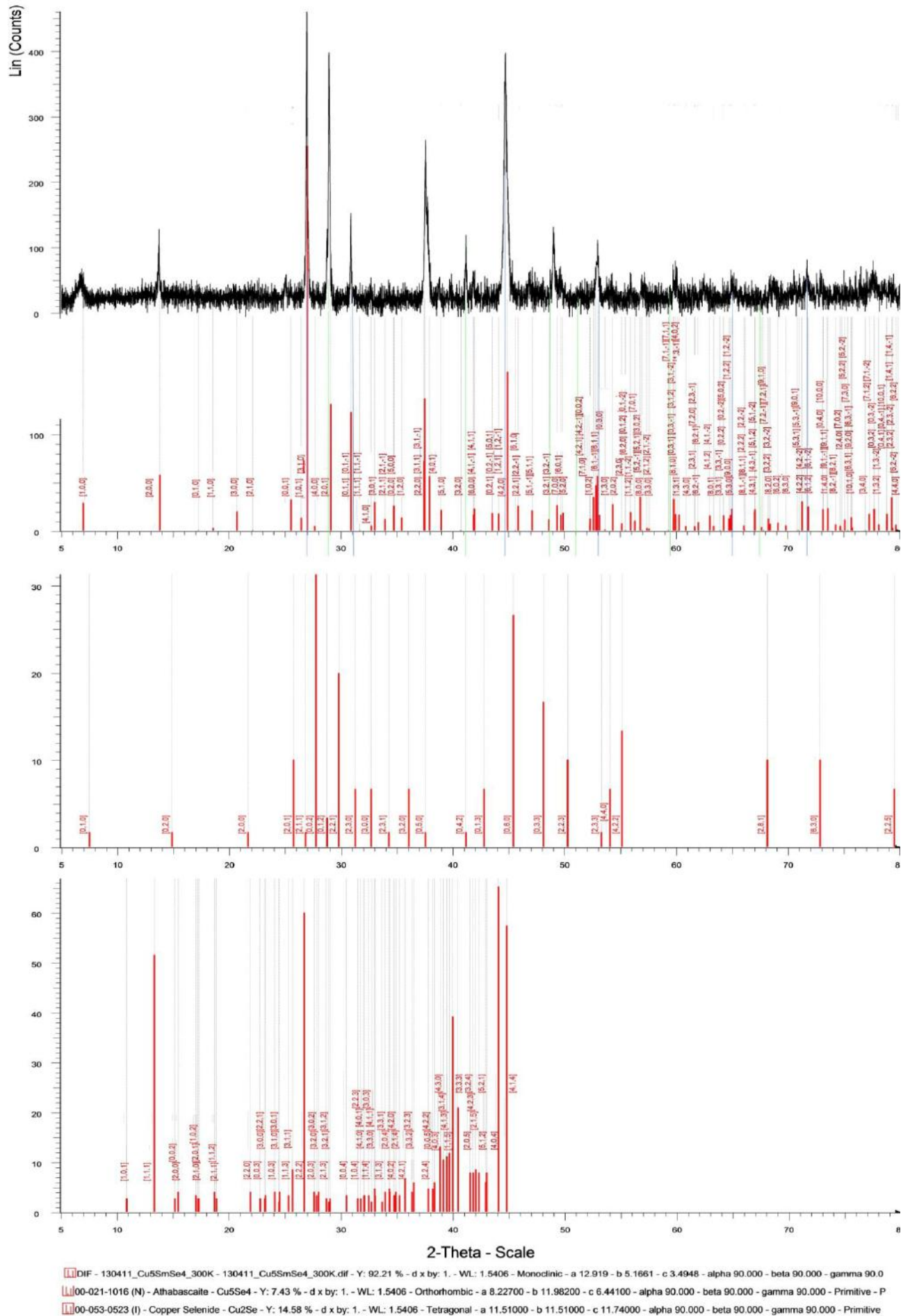


Fig.9 The dash-and-dot diagrams: Cu_5Se_4 , Cu_2Se , Cu_5SmSe_4 and Cu_5SmSe_4 diffractograms

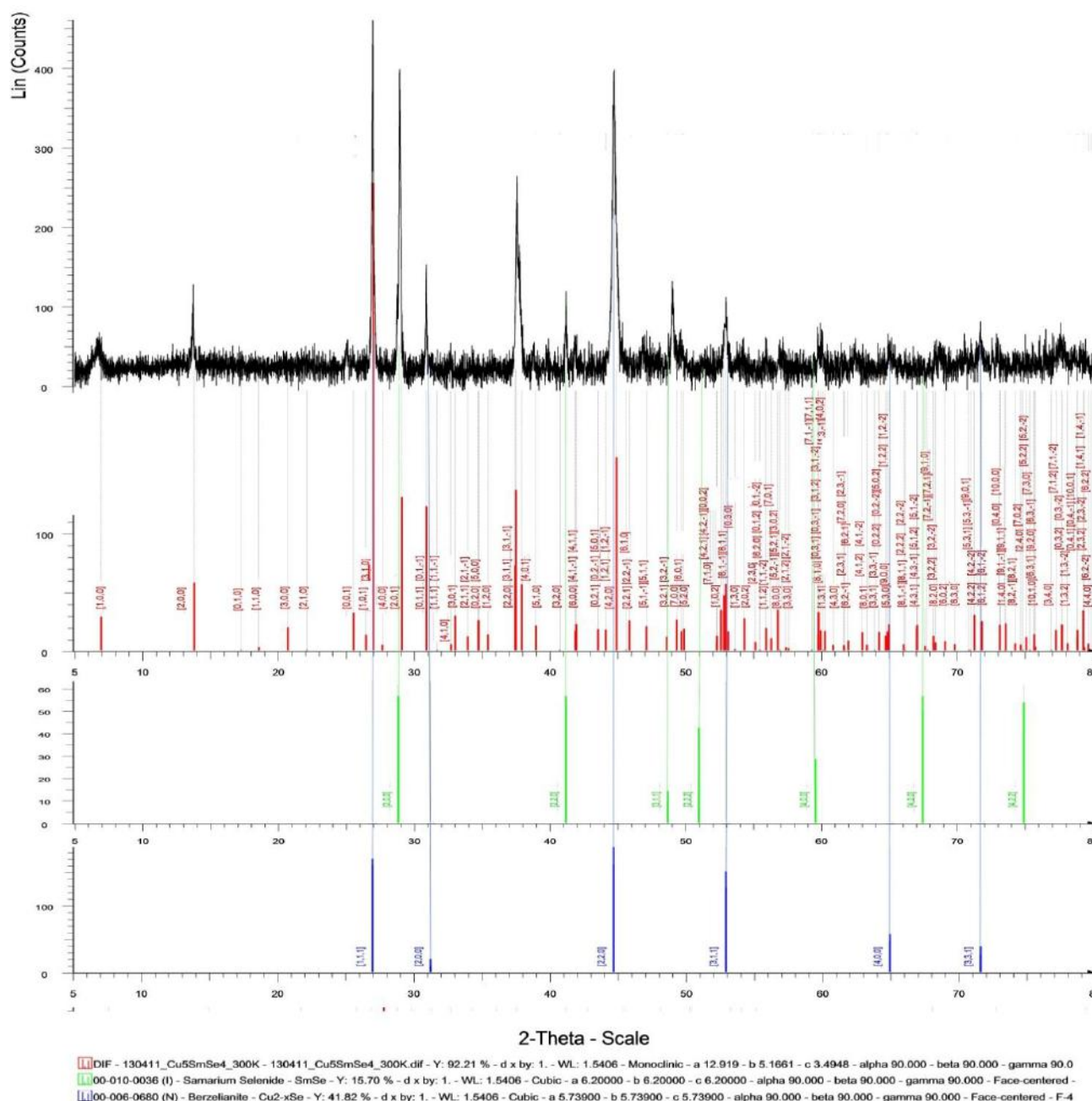


Fig.10 The dash-and-dot diagrams: SmSe , Cu_{2-x}Se , Cu_5SmSe_4 and Cu_5SmSe_4 diffractograms.

This chalcozine modification is stable at temperatures higher 420°C .

At temperatures below 420°C the structural transition into stable phase with dense hexagonal package which is hexachalcozine is observed. The half of Cu^{I+} ion is situated in intervals of closely packed layer, i.e. it has coordinate number 3. The second half stays in centers of tetrahedrons. The hexachalcozine structure is layered one constructed from only triangles CuS_3 touching by edges, that gives it the 16-electron configuration instead normal one consisting of 18 electrons [17]. By other hand, each Cu ion besides three sulfur ions is surrounded on the same distances by three cuprum ions and consequently, the electron lack is partially compensated because of metal bond.

At temperatures lower 103°C the monoclinic modification which is клиноchalcozine becomes stable one. Cu^{I+} ion with coordinate number 3 shifts to triangle side and has the coordinate number (2 + 1). Cu^{I+} ion being in tetrahedral coordination shifts to tetrahedron edge with change of coordinate number with is equal to two.

Thus, the peculiarities of diffractogram changes and consequently, of elementary cell parameters Cu_5SmSe_4 in temperature region up to 700K can be interpreted as a result of phase transformations in cuprum polyhedrons. By other side, such model allows us to explain the similarity of diffraction spectra Cu_5SmSe_4 , Cu_{2-y}Se , Cu_2Se , Cu_5Se_4 (атабаскит) and Cu_7Se_4 (fig. 9-10). For total discussion let's give the short information about these compounds.

The «A» group mineral (Athabascaite) Cu_5Se_4 is related to orthorhombic syngony [11] with parameters of base-centered elementary cell: $a=8.22\text{\AA}$; $b=11.98\text{\AA}$; $c=6.44\text{\AA}$, $V=634.18\text{\AA}^3$, $z=4$, molar mass is 633.5835g/mol . The low-temperature phase has symmetry space group $D_{4h}^{17} - 14/m\bar{m}$ and tetragonal cell parameters: $a=10.40\text{\AA}$, $c=3.93\text{\AA}$. The composition structure is related to cubic one with $a=5.74\text{\AA}$ and space group $O_h^7 - Fd\bar{3}m$ [23]. The XRD spectrum Cu_5Se_4 obtained in work [12] is given on fig.6. The observable Cu_5Se_4 diffractogram maximums correlate by 2θ angle with some diffractogram maximums Cu_5SmSe_4 , however, the symmetry space group of the crystals differ (fig.10). The metastable compound Cu_7Se_4 is related to cubic syngony [12,13]. The maximums of this diffractograms (fig.6) can be corresponded by 2θ angle with several maximums on diffractogram for Cu_5SmSe_4 . Note that at temperature 170°C Cu_7Se_4 compound at the presence of amorphous selenium recrystallize in $CuSe$.

The supposition about samarium introduction into Cu_5Se_4 and Cu_7Se_4 structures doesn't contradict to it [7]. It is obvious that in this case the compound formulae will have the form $Cu_4^{1+}(Cu^{1+}Sm^{3+})Se_4^{-2}$ or $2(Cu_2Se)-(CuSmSe_2)$. The configuration $Cu_4^{1+}(Cu^{2+}Sm^{2+})Se_4^{-2}$ is quite possible.

The results of structural investigation $CuSmSe_2$ the discussion of which will be carried out in further text by [10,25] data are given on fig.7.

Let's consider X-ray data for Cu_5SmSe_4 . First of all this is the difference from $CuSmSe_2$ in symmetry space group. For Cu_5SmSe_4 it is defined as $P\bar{3}$ whereas for $CuSmSe_2$ is $P2_1/c$. For clarification of this situation note that supposition about structure Cu_5SmSe_4 can be chosen in the capacity of analogue of «bornite» mineral [18] the formula of which is usually written in the form of Cu_5FeS_4 . Also note the significant difference which is the construction of electronic membranes of samarium and iron. The some similarity between them is connected with revealing character of two- and three-valent Fe states. The last one is the result of both the participation of d -membrane electron and also the similarity of electron filling of internal valent membranes of Fe and Sm . Note that $5d$ -membrane of samarium is totally free and electron quantity on $4f$ -membrane corresponds to electron quantity on d -membrane of iron.

The bornite lattice presents itself the complex closely packed cubic structure with filled tetrahedral spaces and according to X-ray investigations in bornite crystal structure the one- and two-valent cuprum ions take place the different X-ray positions. All octahedral spaces are free ones. The symmetry class is tetragonally-scalenohedral one. Moreover, the «bornite» chemical formula [13] has the form: $2Cu_2S-CuFeS_2$ ($Cu^{+1,+2}_5Fe^{+2}S_4$) i.e. the four cuprum ions are one valent ones and the fifth ion is two-valent one. The iron ion is also two-valent one. At temperature increase «bornite» passes the series of polymorphous transformations from high-temperature cubic one through metastable and cubic ones to low-temperature orthorhombic phase, moreover metal atoms are ordered and anion package distorts. The polymorphism complexity in bornite is the result of static distribution of cuprum and iron ions in sulfur tetrahedrals.

S atoms situated by motif of dense cubic package in which $3/4$ of tetrahedral positions are filled by Fe^{3+} and Cu^{1+} distributed among 24 positions inside each tetrahedral, are the structure foundation of bornite high-temperature modification ($T>228^\circ\text{C}$). The character of space filling allows us to emphasize the fragments of chalcopryite and chalcocine types (fig.8) alternating in chess order. The coordinate numbers for Fe^{3+} and Cu^{1+} are equal to four. The symmetry of this modification is cubic point group $m(-3)m$, mmm . Note that the similar fragment quantity of chalcopryite and chalcocine types ($4:4$) correspond to bornite elementary cell. From this it is followed that $4 \times Cu_2S$ and $4 \times MeS$ ($Me = Cu, Fe$), i.e. $Me_{12}S_8$ or $Me_6S_4 = (Cu,Fe)_6S_4$ will be included into the cell.

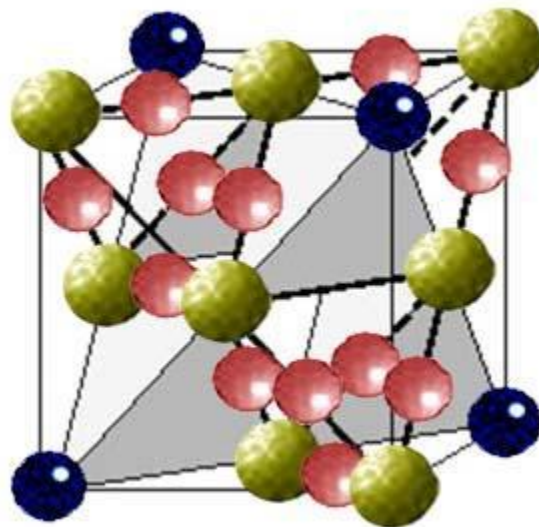


Fig.11 The bornite elementary cell. The balls: blue are Fe ; red are Cu ; yellow are S . The comments in text.

The half of tetrahedral are filled by Fe^{2+} , i.e. $KV_{Fe^{2+}}=4$. These tetrahedral are situated similar to diamond lattice ones in tops of cubic elementary cell, in centers of its edges and in four from eight octants by the tetrahedral (puc.11).

The cuprum fills the second half of tetrahedral but Cu^{1+} ions are situated not in centers but on edges of these tetrahedrals. Moreover, Cu^{1+} each ion is between two tops of tetrahedral on which S^{2-} sulfur ions are situated, i.e. $KV_{Cu^{1+}}=2$ and 6 Cu^{1+} cuprum ions should correspond to each tetrahedral. However, the exchange by scheme $2Cu^{1+} \rightarrow Cu^{2+}$ takes place. Thus, the one edge in tetrahedral stays free one (vacancy) but Cu^{2+} is situated on another one instead of Cu^{1+} (puc.11). The last notes are led us to understanding that as a result of the absence of any reasons of process $2Cu^{1+} \rightarrow Cu^{2+}$, it should led us to appearance of Cu_6FeS_4 and Cu_3FeS_4 compounds (in last compound all Cu are two-valent ones). Making the analogy to Cu_5SmSe_4 compound, the formation of Cu_6SmSe_4 compound is observed on phase diagram in temperature interval from 860 up to 900°C as it is mentioned above. Finally, in bornite $[Cu_5S_4]$ -tetrahedrals are situated on the middle of elementary cell edges and in four residual octants (fig.11) and formulae Cu_5FeS_4 is

decoded by the structure as $\text{Cu}^{+1}_4\text{Cu}^{+2}\text{Fe}^{+2}\text{S}_4$. The structure projection as a whole on plane (001) gives the position of $[\text{FeS}_4]$ - и $[\text{Cu}_5\text{S}_4]$ -tetrahedrals between them (fig.11). It is obvious that structure should be cubic one. But here the vacancy distribution is seen. The obvious connection of the structures of high-temperature bornite and classical chalcopyrite [26] is the association base in relation of bornite structure similarity and Cu_5SmSe_4 . That's why note the some peculiarities of well-known structure of chalcopyrite fragment CuFeS_2 which is characterized by comparatively simple tetragonal lattice close to cubic syngony. The chalcopyrite symmetry space group is $I\bar{4}2d$, $a=5,29\text{\AA}$, $c=10,42\text{\AA}$. The metal-sulfur bond is covalent one. As it is known the chalcopyrite elementary cell consists of from double cell by the height by sphalerite type in which each sulfur ion will be surrounded by four metal ions situated in tetrahedral tops. All tetrahedral are directed by their tops into one side. However, let's note that CuS_4 tetrahedrals are constructed by sp^3 -hybridization type whereas FeS_4 ones are constructed by d^3s -hybridization type. The last one explains Fe isomorphism absence in chalcopyrite with Ga and In. By other hand, the same circumstance explains the absence of Co and Ni analogues, so the increase of d-electron quantity impedes to appearance of tetrahedral coordination. Note also that Cu^{I+} tetrahedral surrounding is possible only in complex compounds in which its one-valency is compensated by electro-positive surrounding. The one more important cuprum property which is Cu^{2+} minimal coordination is equal to three, is shown in [22]. It is observed for example, in coveline moreover, always in Cu^{I+} presence. This coordination also causes the coveline structure lamination in which the layers consisting of triangles Cu^{2+}S and double grids $\text{Cu}_2(\text{S}_2)$ fixed by weak bonds Cu^{I+}S alternate. The discussion of residual existing cuprum coordinates can be found with detail comments in [22].

At $T < 550^\circ\text{C}$ the filling of Cu and Fe by positions in chalcopyrite is ordered one. The ions of Cu^{I+} and Fe^{3+} alternate in chess order by tetrahedral layers. In connection with this fact the crystal parameter by «c» axis duplicates and lattice symmetry increase up to tetragonal one $I\bar{4}2d$. Fe ions are situated on lower and upper edges of tetragonal prisms, by square angles and Cu atom is situated in the center. Cu ions are situated by square angles situated in prism middle and Fe ions are situated in square center. Finally, in second and fourth layers by two ions of Fe and Cu rotated relatively each other on 90° are situated.

At temperatures higher 550°C the position filling of Cu^{I+} and Fe^{3+} is unordered, structure symmetry is $F\bar{4}3m$, and formulae of cubic chalcopyrite can be written in the form $(\text{Cu},\text{Fe})\text{S}$.

At temperatures below 228°C Cu shifting to the one of tetrahedral edges with change of coordinate number Cu^{I+} which becomes equal to three, takes place in bornite structure. This bornite phase has the symmetry $P\bar{4}21c$ and elementary cell parameters are $a=10,94\text{\AA}$; $c=21,88\text{\AA}$. In low-temperature phase the metal ion position in tetrahedral or triangle spaces between sulfur ions is the evidence of anti-fluorite cubic and sphalerite types and vacancy clusters of metal ions in sphalerite cubic. The

two different cubic alternate in the structure led to the mosaic type of vacancy position.

The bornite transition metastable phase in which the one of tetrahedral becomes vacant one and another one with metal ion distributed among four positions of each sulfur tetrahedral, is revealed in temperature interval $170-235^\circ\text{C}$.

The cubic symmetry of metastable phase appears in the result of small domain twinning of rhombohedral symmetry in eight different orientations [18-20]. As it is mentioned in work [20], the sulfur bonding having two: five and seven coordinates, whereas metal ions connected tetrahedrally lies in tops of different tetrahedrals, presents the big interest in bornite structure metastable phase. Finally, that is especially, sulfur d-membrane electrons in bornite structure don't participate in bonds. Note, that in work [21] it is also shown on possible similarity of Cu_5FeS_4 and Cu_5SmSe_4 crystal structures.

According to Cu_5SmSe_4 structure analysis with taking into consideration of above carried out detail discussion of Cu_5Se_4 , Cu_7Se_4 , CuFeS_2 and Cu_5FeSe_4 lets pay attention on peculiarities of CuSmSe_2 structure construction. This compound is related to symmetry group $P2_1/c - C_{2h}^5$, have the elementary cell parameters $a=6,4705(6)\text{\AA}$, $b=7,108(6)\text{\AA}$, $c=6,7812(6)\text{\AA}$, $\beta=98,27(7)^\circ$ in which selenium ions as samarium and cuprum ones take 4e Wyckoff's positions [3,10,25] to which correspond the symmetry operations $x, y, z; \bar{x}, \bar{y}, \bar{z}; \bar{x}, \frac{1}{2} + y, \frac{1}{2} - z; x, \frac{1}{2} - y, \frac{1}{2} + z$. Note the significant differences of symmetry space groups, layer constructions, cuprum polyhedral distortions observable in the structure; attachments of these polyhedrals and etc (see fig.7). The selenium in CuSmSe_2 has two: five and seven coordinates as in chalcopyrite (see fig.7b(3,4)).

The two methods of samarium polyhedral attachments are observed:

- «tail» - «tail» (fig.7,c,1) through end seleniums. The polyhedrals are directed opposite to each other and attach in such way that one of the edges is the common for polyhedrals. The polyhedral total quantity attached in this band is equal to: 4 are samarium ones (2-«tail» - «tail» and 2- «tail» - «side» seleniums) and two opposite directed cuprum polyhedrals;
- «tail» - «side» seleniums (fig.7,c,2), «head» - «side» selenium (side polyhedral is directed to one of polyhedrals)

The cuprum polyhedrals opposite directed relatively each other fix the two samarium polyhedrals in bond «head» - «head», moreover, cuprum polyhedral supporting on side seleniums of samarium polyhedral, is oriented by head to the direction of samarium polyhedral head (see fig.7,e). Note the structure peculiarity; this is sulfur polyhedral presence not containing the metal ions. They carry out the «interlaying» function between polyhedrals of cuprum and samarium moreover the one of the sulfur polyhedral edge is the common one with cuprum polyhedral and one of the edges is the common one with samarium polyhedral.

From this it is followed the obvious statement which is well experimentally defined that temperature dependence of X-ray diffractograms $CuSmSe_2$ will be defined by temperature changes of structural parameters of three above mentioned polyhedrals in first approximation, the properties of which have been above considered by us.

The structure lamination $CuSmSe_2$ (see fig.7) as it is followed from the analysis, is the conditional perception.

In work [10] it is shown on compound structure similarity: $CuSmSe_2$, $CuDySe_2$, $CuNdSe_2$, $CuPrSe_2$.

The diffractogram comparison of bornite (fig.8) and Cu_5SmSe_4 (fig.1,9,10) shows that in angle range 2θ from 25 up to 40° the maximum similar groups are situated. The structure clarification Cu_5SmSe_4 allows us to achieve the well spectrum agreement of its roentgenogram with Cu_5FeSe_4 spectrum and with taking under consideration the investigation results [14] interpret the maximum group (see fig.9-10) situated on diffractogram in angle range 2θ from 25 up to 40° as relating to cuprum selenide polyhedrals. In particular, it means that Cu_5SmSe_4 crystal

structure contains all above mentioned polyhedrals, moreover, cuprum atom position in polyhedrals is similar to their position in cuprum polyhedrals in bornite. The last statement explains the similarity of temperature dependences of diffractograms of bornite and Cu_5SmSe_4 . However, the observable minimum (fig.2-5) near 400C can be connected with Cu_5SmSe_4 structure stabilization and disappearance of possible defects corresponding to Cu_6SmSe_4 compound in which all cuprum atoms are one valent ones.

The chemical formulae Cu_5SmSe_4 have the form $2Cu_2S-CuSmS_2$. Here the following possible combinations are: $(Cu^{1+}Sm^{3+})$ and $(Cu^{2+}Sm^{2+})$ corresponding to cases of samarium introduction into structure in metal and semiconductor forms and consequently, appearance of mixed valency effect in the given compound.

ACKNOWLEDGMENT: This work was supported by the Science Development Foundation under the President of the Republic of Azerbaijan – **Grant №EIF-2012-2(6)-39/01/1.**

- [1]. П.Г.Рустамов, О.М.Алиев, А.В.Эйнулаев, И.П.Алиев Химия редких элементов. Хальколантанаты редких элементов, Москва, Наука, 1989, с.206-208
- [2]. Н.Ю.Прибыльский, Р.С.Гамидов Система $Cu_2Se-Sm_2Se_3$, Журнал неорганической химии, 1983, т.28, №3, с.719-723
- [3]. International Tables for X-ray crystallography, vol.1, N148, p.252, 1969
- [4]. Landolt-Börnstein Database, part of Subvolume E 'Ternary Compounds, Organic Semiconductors' of Volume 41 'Semiconductors' of Landolt-Börnstein - Group III Condensed Matter, (<http://www.springermaterials.com>)
- [5]. П.Е. Тетерин, А.В. Зенкевич, Ю.Ю. Лебединский, О.Е. Парфенов "Исследование структурных и электрофизических свойств тонкопленочных слоев SmS и EuS ", ISBN 978-5-7262-1280-7. Научная Сессия НИЯУ МИФИ - 2010. т. III
- [6]. И.Л.Смирнов, В.С.Оскотский Фазовый переход полупроводник – металл в редкоземельных полупроводниках (монокалькогениды самария), УФН, т.124, вып.2, 1978, с.241-279
- [7]. Д.И.Холмский Проблема промежуточной валентности, УФН, т.129, вып.3, 1979, с.444-485
- [8]. Г.М.Кузьмичева Структурная обусловленность свойств, часть первая: Кристаллохимия халькогенидов редкоземельных элементов, стр.44, Московская государственная Академия тонкой химической технологии им. М.В.Ломоносова, Москва, 2003
- [9]. Банк структурных данных ICSD/RETRIEV 2.1, Gmelin Institute/ FIZ Karlsruhe, 1997, Eliseev A.A., Kuz'micheva G.M., Phase equilibrium and crystal chemistry in rare earth ternary systems with chalcogenide elements. In Handbook of the Physics and Chemistry of Rare Earth edited by K.A.Gschneider, Jr. and L.Eyring, North-Holland, 1990. V13. P.191-282
- [10]. Petra Lauxmann-Melchinger «Synthese und Strukturaufklärung von kupferhaltigen ternären und quaternären Sulfiden der Selten-Erd-Elemente», Institut für Anorganische Chemie der Universität Stuttgart, 2006
- [11]. Amer. Miner., 1971, 56, p.632; 3BMO, 1971, вып. 5, с.617
- [12]. Krishnamoorthy Giribabu, Ranganathan Suresh, Ramadoss Manigandan, Elumalai Thirumal, Arumainathan Stephen, Vengidusamy Narayanan Aqueous based synthesis of Cu_5Se_4 nanosheets and characterization, J Mater Sci: Mater Electron, Springer Science+Business Media New York 2012, 7p.
- [13]. Rakesh K. Sharma, G. Kedarnath, Vimal K. Jain, Amey Wadawale, C. G. S. Pillai, Manoj Nalliath and B. Vishwanadh Copper(I) 2-pyridyl selenolates and tellurolates: Synthesis, structures and their utility as molecular precursors for the preparation of copper chalcogenide nanocrystals and thin films, Electronic Supplementary Material (ESI) for Dalton Transactions. This journal is © The Royal Society of Chemistry, 2011, 68p.
- [14]. I. Mihailova, V. Gerbreder, E. Tamaniš, E. Sledevskis, V. Kolbjonoks Second harmonic generation in selenium-copper structures, Journal of optoelectronics and advanced materials, vol. 11, No. 12, 2009, p. 2083 - 2087
- [15]. В.В. Каминский, Н.В.Шаренкова, Л.Н.Васильев, С.М.Соловьев Исследование температурной зависимости параметра кристаллической решетки SmS , ФТП, 2005, т.47, в.2, с.219-219
- [16]. О.П. Сумбаев Смещение рентгеновских Клиний при изменениях валентности и изоморфных фазовых переходах в редких землях, УФН, февраль 1978, т.124, вып.2, с.281-306

- [17]. *H.B. Белов* Очерки по структурной минералогии, XVI, Минер. сб., Львовский Университет, №10, вып.1, 1965
- [18]. *N. Marimoto* Structures of Two Polymorphic Forms of Cu_5FeSe_4 . *Acta Cryst.*, 17, 351, 1964
- [19]. *Yasuo Kanazawa, Kichiro Koto and Nobuo Morimoto* Bornite (Cu_5FeS_4): stability and crystal structure of the intermediate form, *Canadian Mineralogist*, vol.16, pp.397-404, 1978
- [20]. *P.G.Manning* A study of the bonding properties of sulphur in bornite *The Canadian Mineralogist*, vol. 9, p.85-94, 1967
- [21]. *Yoshio Morita* Molecular beam epitaxial growth of new Cu-Al-(Se,S) compounds blue photoluminescence, *OYO Buturi*, vol.62, pp.143-146, 1993
- [22]. *A.C.Поваренных* Основные черты кристаллохимии минералов меди и серебра, 1966
- [23]. *W. Freyland, A. Goltzene, P. Grosse, G. Harbeke, H. Lehmann, O. Madelung*, University of Marburg, FRG; *W. Richter, C. Schwab, G. Weiser, H. Werheit, W. Zdanowicz, C. Madelung* (Ed.) *Physics of Non-Tetrahedrally Bonded Elements and Binary Compounds I / Physik der nicht-tetraedrisch gebundenen Elemente und binären Verbindungen I Series: Condensed Matter, Subvolume 17e*, p.142, Springer, 1983 - Science - 533 pages
- [24]. Журнал Всесоюзного Химического общества им. Д.И.Менделеева, т.XXVI, №6, 1981 (Номер посвящен редкоземельным элементам)
- [25]. *G.G. Guseinov, A.S. Amirov, I.R. Amiraslanov, Kh.S.Mamedov* Crystall structure of CuSmSe_2 *Dokl. Akad. Nauk Az.SSR*, vol.40, p.62, 1984
- [26]. Неметаллические полезные ископаемые СССР (ред. В.П.Петров). М.: Недра. 1984. 407 с

FERROMAGNETIC METAL/SEMICONDUCTOR CdGeAs₂ DOPED WITH Mn UNDER PRESSURE

A. Yu. MOLLAEV¹, I. K. KAMILOV¹, R. K. ARSLANOV¹,
S. F. MARENKIN² and T.R. ARSLANOV¹

¹*Amirkhanov Institute of Physics,*

Daghestan Scientific Center RAS 367003 Makhachkala, Russia

²*Kurnakov Institute of General and Inorganic Chemistry RAS,
119991 Moscow, Russia*

Here we present a high hydrostatic pressure study of ternary ferromagnetic metal/semiconductor chalcopyrite CdGeAs₂ doped with Mn. In addition, temperature dependencies showed a change in the type of conductivity from semiconductor to metal with increasing manganese content. Observed pressure-induced magnetic phase transitions may be controlled by Mn content in compounds. Also, unusual behavior of Hall resistance under pressure presented.

Keywords: high pressure, magnetic semiconductor

PACS: 62.50.-p, 75.50.Pp, 75.30.Kz

I. INTRODUCTION

Recently, diluted magnetic semiconductors (DMS) are of particular paradigm in condensed matter physics [1], as the ratio between the transport and magnetic properties are still debating the issue extensively. It should be noted that the doping of host semiconductor of DMS with 3d metal – Mn in varying degrees can affect both the properties of the electronic structure, and directly influence the magnetic ordering temperature T_C . For example, in the condition of a high level of Mn doping in the material state is achieved close to their transport characteristics of a metallic conductor [2], resulting in a mean free path of the charge carriers at the Fermi level is less than one nanometer and their states strongly correlated [3]. This behavior is typical for the case of hopping transport for highly disordered semiconductor that makes consequences mechanism by which formed ferromagnetism (FM) in the material. Thus, metal systems can be spin magnetic susceptibility through the valence band, while for the other hopping systems require a method other than the double exchange interaction. [4]

In view of the fact that the DMS exhibit extreme sensitivity to external disturbances, such as doping and the electric field that directly affect the magnetic nature, attracting external pressure in this case can also provide an additional opportunity for manipulation and expansion of fundamental properties. In this paper, on the basis of the measurement ac magnetic susceptibility at high hydrostatic pressure shown in CdGeAs₂:Mn occur magnetic phase transitions induced by high pressure.

II. SAMPLES AND METHOD OF EXPERIMENT

Polycrystalline samples Cd_{1-x}Mn_xGeAs₂ with x.0.06–0.30 were prepared in Kurnakov's Institute of General and Inorganic Chemistry. The bulk Cd_{1-x}Mn_xGeAs₂ crystals were grown with the use of the direct fusion method. The details of the growth process are presented in Ref. [5]. According to the X-ray diffraction data, all the samples were identified as single-phase. However, using the powder XRD method and the high

resolution X'Pert PRO MPD diffractometer, the main phase of crystals is identified as tetragonal chalcopyrite CdGeAs₂ structure with *I*-42d symmetry. In addition to the main phase, the hexagonal and rhombohedral phases of MnAs have been found. The samples were measured by several methods in a Toroid type high-pressure apparatus which was placed in a helical coil having a magnetic field strength of $H < 5$ kOe, with pressure being increased and released in the room temperature region. As an active cell, the teflon capsule of ~80mm³ working volume with 8 lead-in contacts was used. It allowed simultaneous measuring the pressure and the two kinetic parameters. In details the technique of the experiment is described in Refs. [6]

Magnetic susceptibility was calculated from $\chi = (\mu - 1)/4\pi$. Dynamic magnetic permeability μ was derived from the change in the frequency of the resonance circuit where the test sample served as the inductor coil core.

The possibility of using an oscillator based on such a circuit for measuring the dynamic magnetic susceptibility has its advantages both for recording the spectral characteristics, and recording the temperature and field dependences, and also dependences on the applied external pressure. When going through the ferromagnetic ordering and structural transition, its natural frequency ranges from 2 MHz to 20 kHz. The self-excited oscillator frequency was measured with a frequency method. μ was calculated from the equality of the inductance of a toroidal coil having N turns wrapped around the test sample and of the inductance derived from the intrinsic frequency of the oscillation circuit of the selfexcited oscillator, as follows:

$$\mu = t^2 \cdot 10^7 / 8\pi^2 C N^2 h \ln b/a$$

Here, C is the capacitance of the capacitor; t is the oscillation period; a , b , and h are, respectively, the inner radius, outer radius, and height of the toroidal coil. When the effect was poorly pronounced, measurements were taken in the accumulation and averaging modes.

III. RESULTS AND DISCUSSIONS

The temperature dependence of the resistivity are shown in Fig. 1 (a), from Fig. that the conductivity type of the samples varies from semiconductor to $x = 0 \div 0.18$ to the metal with $x = 0.24$ and $x = 0.30$.

Figure 2 (a) - (b) are pressure dependences of the ac magnetic susceptibility with no significant change in temperatures below T_C . At $T = 300$ K for both compounds were observed in the responses of susceptibility $P = 1.6$ GPa for the composition with $x = 0.30$ and $P = 1.7$ GPa for the composition with $x = 0.18$, respectively, indicating the transition to the paramagnetic (PM) state induced by pressure. Higher pressures $P = 4$ GPa observed yet another particular value where the sensitivity is less than the initial one. A slight increase in temperature of about 5-10 K shows a significant shift in the direction of the observed features of low pressures. As was shown in [7],

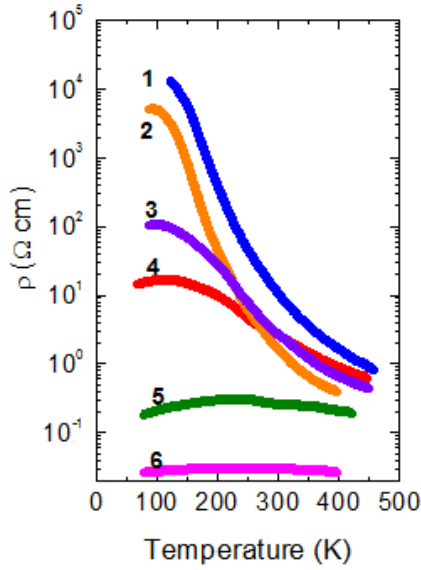


Fig. 1 Temperature dependence of resistivity for Cd_{1-x}Mn_xGeAs₂ with $x = 0 \div 0.30$. Curves 1 - 0, 2 - 0.003, 3 - 0.06, 4 - 0.18, 5 - 0.24, 6 - 0.30, respectively.

$dT_C/dP = (T_C - T_{room})/P_C$ varied between $-14.0 \div -6.8$ K/GPa for compositions with $x = 0.30 - 0.06$, which is in agreement with the observed results.

Next, using the obtained values of the peak of magnetic susceptibility, as well as the values of T_C at atmospheric pressure in Fig. 2 we presented the surface as a function of temperature, pressure and level of doping Mn, illustrating transitions Ferromagnetic (FM) – PM. Thus, it was found that the test samples have the magnetic phase transitions are induced by pressure, depending on the temperature and the Mn content.

In Figure 4 we show the dependence of Hall resistance, measured in a field $H = 5$ kOe at fixed pressure and room temperature. A very unusual behavior was found for samples studied CdGeAs₂ doped with $x=0.24$. With increasing pressure, as expected, an increase in the hysteresis loops of R_S to 3.9 GPa, and a further increase in pressure instilled a typical behavior of the PM. Such an increase of the Hall resistance with increasing pressure may indicate the pressure-induced metamagnetic transition [8].

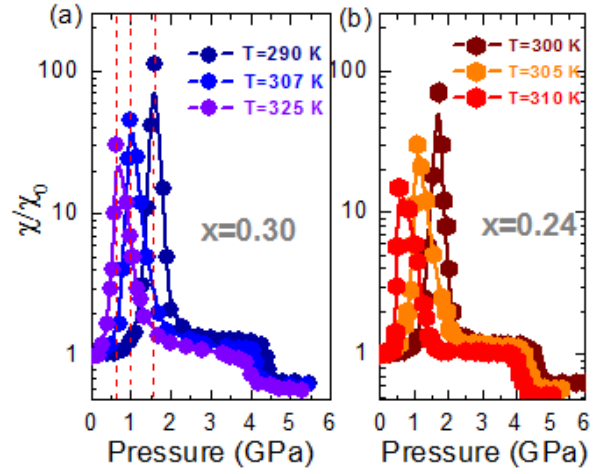


Fig. 2 Pressure dependencies ac magnetic susceptibility measured at various temperatures for CdGeAs₂:Mn with $x = 0.30$ below T_C ($T_C = 350$ K) (a) and $x = 0.24$ ($T_C = 355$ K) (b).

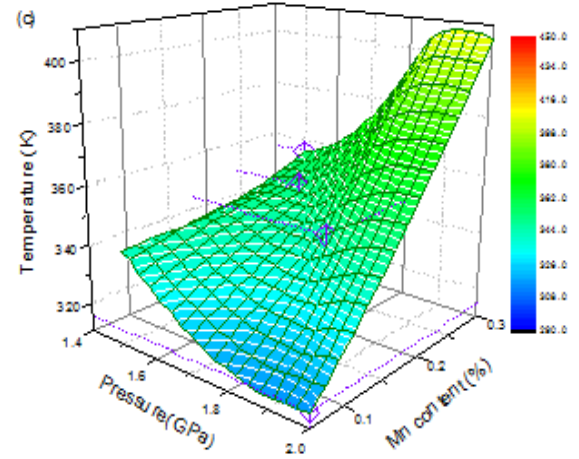


Fig. 3 The dependence of the magnetic ordering temperature of Mn doping level and pressure represented as a surface, which describes the magnetic phase transitions FM-PM. Point – the peak values of magnetic susceptibility, taken from Figure 1.

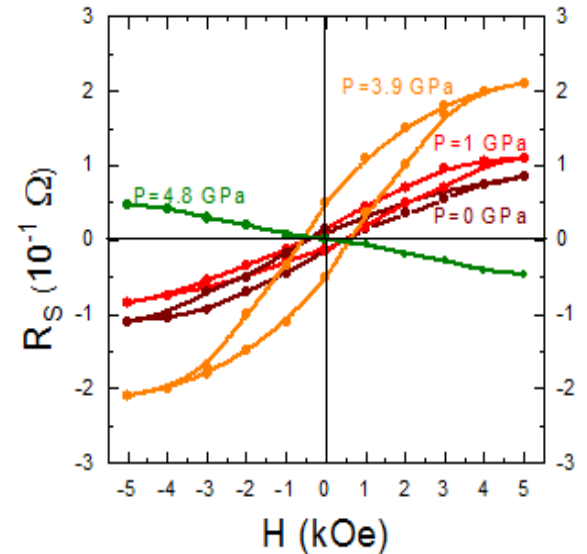


Fig. 4 Dependences for Hall resistance of Cd_{1-x}Mn_xGeAs₂ with $x=0.18$ at fixed values of pressure in magnetic field $H=5$ kOe and room temperature. Curve at $P=4.8$ GPa inverted relative to the Y axis.

In summary, we demonstrated that in all the investigated samples $\text{Cd}_{1-x}\text{Mn}_x\text{GeAs}_2$ ($x=0.06-0.3$), there are observed pressure-induced magnetic transitions which may be controlled by Mn content in compounds. In addition, studies of Hall resistance, shown unusual

increase in the magnetization, which may indicate about metamagnetic behavior under pressure.

This work was supported by the Program of Presidium of RAS No. 2 “Matters at high energy density”, Section 2 “Matters under high static compression”.

-
- [1]. *T. Dietl*, Nature Mater. **9**, 965 (2010).
 - [2]. *Matsukura, F., Ohno, H., Shen, A. & Sugawara, Y.* Phys. Rev. B **57**, R2037 (1998).
 - [3]. *Richardella, A. et al.* Science **327**, 665 (2010).
 - [4]. *Sheu, B. L. et al.* Phys. Rev. Lett. **99**, 227205 (2007).
 - [5]. *S. F. Marenkin, V. M. Novotortsev, K. K. Palkina, S. G. Mikhailov, and V. T. Kalinnikov*, Inorg. Mater. **40**, 93 (2004).
 - [6]. *L.G.Khostantsev, V.N. Slesarev and V.V. Brazhkin*, High Press. Res. **24**, 371 (2004).
 - [7]. *A. Yu. Mollaev, I. K. Kamilov, R. K. Arslanov, T. R. Arslanov, U. Z. Zalibekov et al.* Appl. Phys. Lett. **100**, 202403 (2012).
 - [8]. *A. Yu. Mollaev, I. K. Kamilov, R. K. Arslanov, T. R. Arslanov, U. Z. Zalibekov, V. M. Novotortsev, and S. F. Marenkin*, JETP Lett. **91**, 478 (2010).

ELECTRON ENERGY-LOSS SPECTROSCOPY AND THE ELECTRONIC STRUCTURE OF SOME TERNARY OXIDES: FIRST PRINCIPLE CALCULATIONS

SEVKET SİMSEK, AMİRULLAH M. MAMEDOV, EKMEL OZBAY

Nanotechnology Research Center (NANOTAM), Bilkent University,

Bilkent 06800 Ankara, Turkey

**mamedov@bilkent.edu.tr*

The electronic structures of some ternary oxides are calculated within the density functional theory, and their evolution is analyzed as the crystal-field symmetry changes from cubic to rhombohedral via tetragonal phases. Electronic structure fingerprints that characterize each phase from their electronic spectra are identified. We carried out electron-energy loss spectroscopy experiments by using synchrotron radiation and compared these results to the theoretical spectra calculated within DFT-LDA. The dominant role of the oxygen octahedra in the formation of the energy spectra of ternary oxides was demonstrated.

Keywords: electronic structure, electron energy-loss spectroscopy, ternary oxides

PACs: 71.15.-m; 61-68, 78

1. INTRODUCTION

Over the past decades, electron energy loss (EEL) spectroscopy has developed into a major tool for the characterization of nonlinear structures and electronic structure of materials. The low-loss energy region of the EEL spectrum (<50 eV) can provide information about composition and electronic structure, as well as optical properties [1,2], although it has not found as wide application as the energy-loss near-edge structure. In this low-loss region, interband transitions and plasmon losses are observed. Plasmon losses correspond to a collective oscillation of the valence electrons and their energy is related to the density of valence electrons. Consequently, if the valence electron density changes with the composition, the change in the plasmon energy can be used to measure composition. Some examples of plasmon spectra being used to describe different phases and composition are briefly reviewed in [3].

The plasmons hold a unique position among the quasiparticles of solids because of their special features. The spectra of plasmons are described by the functions $-\text{Im}\epsilon^{-1}$ (volume plasmons) and $-\text{Im}(\epsilon+1)^{-1}$ (surface plasmons). Experimentally, they are determined by measuring the characteristic electron energy loss (EEL) [4-7]. In the general case, the loss function has an intricate form because of the superposition of various effects, among them the excitation of plasmons, interband transitions and metastable excitons.

It is well known that peaks and features in the low-loss spectrum, in addition to the plasmon peak, associated with interband transitions. Interband transitions are an effect lattice, they shift the plasmon energy and can be included via Drude-Lorentz theory [3,7]. However, in order to include interband transitions, we must know where they are expected to occur, that is, we need to have a good understanding of the electronic structure, a rather circular process if one is trying to use the low-loss spectrum, after the zero-loss peak. It is somewhat surprising that there has not been more effort to improve the calculations of the expected plasmon energy.

The aim of this paper is to apply DFT band structure calculations of the electronic structure, dielectric functions, and spectra of plasmons of both types to a wide variety of some ternary oxides in order to explore how well-loss EELS can be predicted.

Our paper is organized as follows. In section 2, we describe the methodology and computational details. In section 3, we describe the computation and theory of EELS. In section 4-5, we illustrate the validity of the formalism by applying methodology and theory (see sections 2 and 3) to nonlinear oxides.

2. COMPUTATIONAL DETAILS

The optical properties of some ternary oxides (ABO_3 , where $A=\text{K, Li, Ba, Sr}$ and $B=\text{Nb, Ta, Ti}$) were theoretically studied by means of first principles calculations in the framework of density functional theory (DFT) [8] and based on the local density approximation (LDA) [9] as implemented in the ABINIT code [10,11]. The self-consistent norm-conserving pseudopotentials are generated using Troullier-Martiens scheme, which for the ABO_3 , include the semicore s and p states of A- and B-atoms [12] which is included in the Perdew-Wang [13] scheme as parameterized by Ceperly and Alder [14]. For the calculations, the wave functions were expanded in plane waves up to a kinetic-energy cutoff of 40 Ha (tetragonal and rhombohedral KNbO_3), 38 Ha (BaTiO_3 , SrTiO_3). The level of accuracy for the Kohn-Sham eigenvalues and eigenvectors is required to calculate the response function. The Brillouin zone was sampled using an $8 \times 8 \times 8$ the Monkhorst-Pack [15] mesh of special k points.

3. THEORY

The EEL spectrum can be described in a dielectric formulation [3,16] by

$$\frac{d^2G}{d\Omega dE} = \frac{1}{\pi^2 a_0 m_0 v^2 n_a} \left(\frac{1}{\theta^2 + \theta_E^2} \right) \text{Im} \left(-\frac{1}{\epsilon(q, E)} \right) \quad (1)$$

Where v is the speed of the incident electron, n_a is the number of atoms per unit volume, and θ_E is the characteristic scattering angle $\theta_E = E/\gamma m v^2$. The term $\text{Im} \left(-\frac{1}{\epsilon} \right)$ is often called the loss-function. Using eq. (1) and a Kramers-Kronig analysis, it possible to obtain the complex dielectric function $\epsilon = \epsilon_1 + i\epsilon_2$ from the low-loss EEL. Optical properties can be calculated from ϵ .

Although loss straightforward than using optical techniques directly, measuring optical properties with EELS offers advantages of better spatial resolution and it extends to higher energies. We can rewrite $Im\left(-\frac{1}{\epsilon}\right)$ as $\frac{\epsilon_2}{\epsilon_1^2 + \epsilon_2^2}$ and the plasmon energy (the maximum of the loss-function) is identified as occurring at the point where ϵ_1 crosses zero with a positive slope ($d\epsilon_1/dE > 0$), and $\epsilon_2 \ll 1$ with a negative slope ($d\epsilon_2/dE < 0$). It follows from eq (1) that, if we want to use an *ab initio* method to calculate the low-loss EELS we must calculate $\epsilon(\omega)$. The dielectric function describes the response of the material to a time-dependent electromagnetic field and the underlying theory is well developed [16].

Table 1. Band gap calculation results of some ABO₃ crystals.

Material s	Phase	Symmetry Class	E _g , eV (indirect)		E _g , eV (direct)
			Theory	Exp.	
KNbO ₃	C	Pm3m	1.538 (R- Γ)	-	2.513 (Γ - Γ)
	T	P4mm	1.538 (R- Γ)	3.30 [28,44]	2.513 (Γ - Γ)
	R	R3m	1.538 (Z- Γ)	-	2.503 (Γ - Γ)
LiNbO ₃	R	R3c	3.390(Z- Γ)	3.63 [39]	3.540 (Γ - Γ)
LiTaO ₃	R	R3c	3.840(Z- Γ)	3.93 [39]	4.110 (Γ - Γ)
KTaO ₃	C	Pm3m	2.158(R- Γ)	3.79 [40,44]	2.987 (Γ - Γ)
BaTiO ₃	C	Pm3m	1.920(R- Γ)	3.05 [44]	2.041 (Γ - Γ)
	T	P4mm	2.145(R- Γ)	3.26 [44]	2.294 (Γ - Γ)
SrTiO ₃	C	Pm3m	1.895(R- Γ)	3.37 [44]	2.230 (Γ - Γ)
	T	I4/mcm	2.2117 (M- Γ)	-	2.361 (Γ - Γ)

Table 2. Theoretical and experimental data of plasmon energies and energy features of $-Im\epsilon^{-1}$ for some ABO₃ ferroelectrics.

Material	Exp E _p , eV	Exp E _s , eV*	Theory E _p , eV	Exp -Im ϵ^{-1}	Theoretical -Im ϵ^{-1}
KNbO ₃ /C	-	-	21.8	-	6.5, 15.0, 22.6, 28.1, 41.5
KNbO ₃ /T	24.0	17.0	22.0	7.1, 14.0, 23.2, 29.5	6.4, 14.9, 22.5, 28.0, 41.0
KNbO ₃ /R	-	-	21.9	-	6.4, 14.9, 22.5, 28.1, 41.4
LiNbO ₃	25.5	18.2	23.2	7.5, 11.0, 13.0, 14.6,	7.65, 8.2, 19.4, 21.0, 21.7, 22.3
LiTaO ₃	25.3	18.0	24.0	16.3, 25.5, 7.1, 11.5, 15.3,	7.95, 16.2, 17.8, 19.3, 21.6, 22.7, 23.9, 24.6
KTaO ₃	20.3	15.0	20.4	7.9, 14.7, 19.8, 21.5, 24.3, 31.2	6.2, 8.3, 11.7, 15.1, 21.3, 22.1, 23.4
BaTiO ₃	24.3	16.8	23.1	7.2, 12.3, 14.2, 19.6,	6.5, 13.7, 21.2, 29.4
SrTiO ₃	29.5	21.0	22.6	23.1, 28.0, 6.1, 7.5, 14.2,	7.82, 9.35, 12.7, 14.1, 17.2, 19.3, 22.4

4. ELECTRONIC STRUCTURE OF THE VALENCE AND CONDUCTION BANDS

In this section, we investigate the evolution of the electronic structure of ABO₃ in the structural and ferroelectric phase transitions in relation with the evolution of the symmetry of the crystal field. Results from VUV reflectivity experiments are reported in the literature for some ABO₃ [17,24-29,32-36]. We furthermore give a comparison of the theoretical band structure of the valence and conduction bands in various phases. Last, we report our results for the theoretical gap, and the gap values determined experimentally. Since ABO₃ ferroelectrics have been widely studied (see Ref. [17-39]) we show in detail only the calculated band structures for KNbO₃ in different phases. For all other calculated compounds we presented the main data in Tables 1-2.

The dispersion of the energy of the valence bands for the cubic (C), tetragonal (T) and rhombohedral (R) phases at the equilibrium lattice parameters are reported in Fig.1-2. The top of valence band is located at R point in cubic and tetragonal phases, and in the Z point in rhombohedral phase. The DOS for all phases show a much higher density of states at and near the top of the valence bands. The valence bandwidth decreases by 1.3 eV between the different crystal fields, from 5.6 eV in the cubic phase to 4.3 eV in the rhombohedral phase. The bandwidth of the tetragonal phase is closer to the width of the cubic phase than to the rhombohedral one.

As we said herein above, the electronic band structure of paraelectric cubic KNbO₃ along the symmetry lines of the cubic Brillouin zone is shown Fig. 1. Let us describe the electronic band structure of the KNbO₃ in more detail. It is clear that the indirect band gap appears between the topmost valence band and at the R point and at the bottom of conduction band at the Γ point. The overall profile of our band structure is qualitatively like the band structure obtained by previous studies [20,21]. It is observed that the conduction band minimum goes from the Γ point through Δ to the X point and always remains nearly flat in agreement with previous studies [28,31]. The calculated indirect band gap (R- Γ) is 1.54 eV while the smallest direct band gap (Γ_V - Γ_C) is 2.51 eV. These calculated values are smaller than the experimental value of 3.1 eV for the indirect gap [29]. The origin of this discrepancy could be the use of DFT, which generally underestimates the band gap in semiconductors and insulators [8,9]. The band with the lowest energy in Fig. 1, lying between -16.0 eV and -17.0 eV, correspond, to a very large extent, to O 2s states. The nine valence bands are between -5.9 eV and Fermi level (zero) are mainly due to the oxygen O 2p states hybridized with Nb 4d states. These nine valence bands are split into triple and double degenerate levels at the Γ point (Γ_{15} , Γ_{25} , Γ_{25}) separated by energies 1.64 eV (Γ_{15} - Γ_{25}), 0.3 eV (Γ_{25} , Γ_{15}), and 1.94 eV (Γ_{15} - Γ_{25}) due to the crystal field and electrostatic interaction between mainly O 2p and Nb 4d orbitals. In the conduction band, the one three double (Γ_{12}) degenerate levels represent Nb 4d t_{2g} and Nb e_g orbitals separated by energy 4.2 eV. The topmost valence bands are the oxygen 2p_x, 2p_y states while the lowest valence bands are formed by hybridization of Nb 4d e_g and O 2p_z states. In the conduction band region, the first

conduction band from about 1.59 eV above the Fermi level to 5.6 eV arises from predominantly Nb t_{2g} states with small O 2p mixing. The bands in the conduction band that are shown in Fig.1 belong to Nb 4d e_g states. Also, some electrons from Nb 4d transform into the valence band and take part in the interaction between Nb and O. This implies that there is hybridization between Nb 4d and O 2p. Conversely, in the conduction band, the DOS of Nb d is much higher than that of O 2p. This implies that there are few O p electrons which transform into the conduction band and hybridize with Nb d electrons. The DOS of Nb-(d) and O-(p) thus show that interaction between Nb and O is covalent. On the other hand, the DOS of K 3p shows a peak around 0.5 eV attributed to the bands around this energy in the band structure. The structures lowest in energy between approx.-17.5 eV and 16.0 eV are shown to be of predominantly O 2s character with some mixing of Nb p states. On the whole, our results are in agreement with the LAPW calculation and MF calculation [31].

The agreement between our DOS and the experimental spectrum is good [17-39]. The dispersion curve of the conduction bands at the theoretical equilibrium lattice parameters are reported in Fig. 1-2. The bottom of the conduction band is found to be at the Γ point for all phases. The first conduction bands are found to have an e_g character at the Γ point in the cubic phase (Fig. 1). At higher energy, conduction bands have a_{1g} or t_{2g} character at the R and Γ points. The gap in the conduction band has a minimum of 1.3 eV at Γ point. The fundamental gap of the single crystal of KNbO_3 has been measured in the cubic and tetragonal phases [25]. More precisely, VUV spectroscopy has been performed in reflectivity in the 1.0-35.0 eV range, and the absorption spectrum has been deduced from a Kramers-Kronig analysis [29]. The band gap obtained from a fit of the low absorption is found to be 2.86 eV. However, EELS experiments a large momentum transfer [30], give a gap value about 2.9 eV. Our fitted value for E_g is 2.45 eV in cubic phase of KNbO_3 .

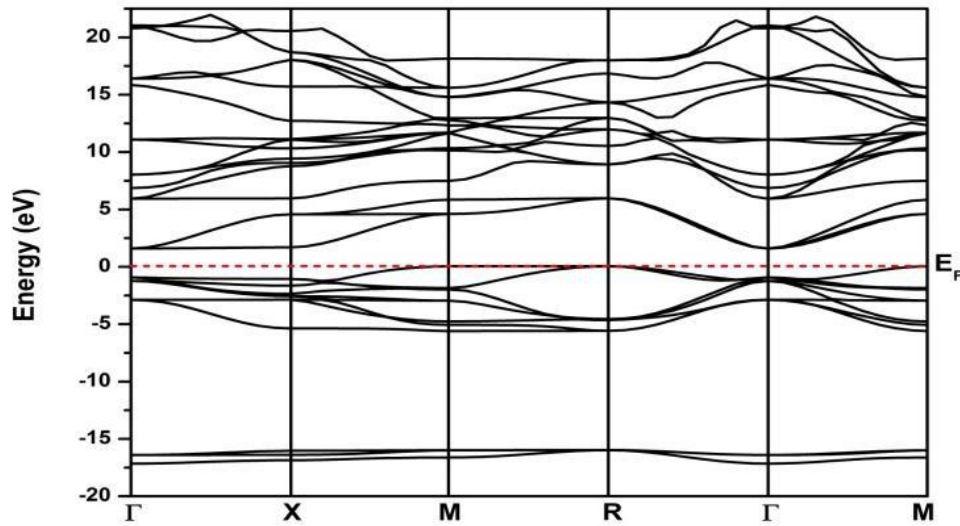


Figure 1. Electronic band structure of cubic KNbO_3 .

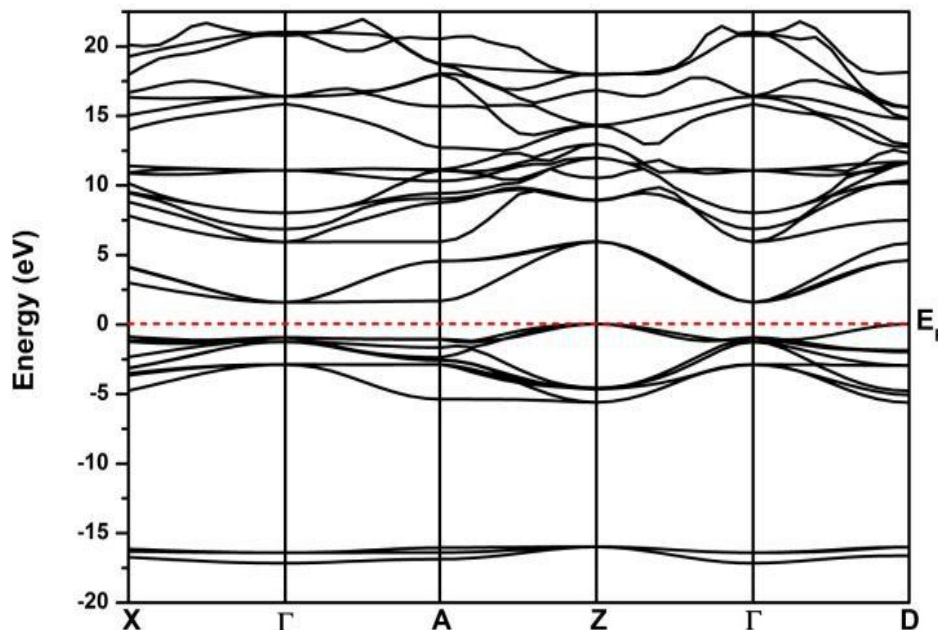


Figure 2. Electronic band structure of rhombohedral KNbO_3 .

We have also calculated the minimum and direct LDA band gap energy at the theoretical lattice parameters (Table 1). Within the accuracy of our calculations, the values of the direct and indirect are within 2.35 eV of each other in all phases except the rhombohedral one, where the minimum gap is 1.5 eV smaller than the first direct gap. Our results are in good agreement with a previous calculation [31] performed at the experimental lattice parameters, with the exception of the rhombohedral phase. The O 2s dispersion curves are reported in Fig.1-2.

As was the case for the B 3s and 3p lines, the O 2s peak position is lower by 0-2.0 eV. However, in contrast to the B 3s and 3p lines, the oxygen 2s band is very sensitive to the oxygen local coordination. We find that, the O 2s band shows a left shoulder at -2.0 eV with respect to the main peak. Second, we see that the oxygen line shape is identical for the cubic and tetragonal structures. In comparison with the experimental results we note that experimentally [17,29] the O 2s band is found to be centered at -17 eV in the tetragonal phase. In contrast, we find our O 2s doublet located at -16.1 eV and -16.4 eV.

5. ELECTRON ENERGY LOSS SPECTROSCOPY

In this section, we first apply the theoretical framework defined in section 3 and report our theoretical EELS spectra. Valance EELS experiments have previously been performed in transmission at a large momentum transfer q (ref [1]) and in reflection (ref [1,24]). In this work, we have performed very low q and VUV reflectivity [17,24-27] experiments and compared them to the theoretical results. The first of all we were calculated in LDA the real (ϵ_1) and imaginary (ϵ_2) parts of dielectric functions for all ABO_3 compounds and then by using eq.(1) were computed $\text{Im}\epsilon^{-1}$ in the energy region up to 30 eV. Three regions can be distinguished. First, we observe that the valence excitation region extends up to 15.0 eV. The form of the structure and the shape of ϵ (ϵ_1 , ϵ_2 and $-\text{Im}\epsilon^{-1}$) for the investigated crystal are determinate by the positions of the critical state density points (see Table 2). The similarity between the ϵ_2 for all modifications of KNbO_3 in the region up to 14.0 eV points to the substantial role of NbO_6 octahedron in the formation of the band structure. This means that the NbO_6 octahedron determines the lowest limit of the conduction band and the upper valence band. These bands are similar for many ABO_3 , since the d-orbitals of the transition metals and the p-orbitals of oxygen, which are joined in each octahedron, make the main contribution to the bands indicated above. The real part of ϵ behaves mainly as a classical oscillator. It vanishes (from positive to negative value) around 5.52, 10.01, 11.88, and 13.48 eV, and correspondingly, ϵ_2 shows maxima of absorption at these frequencies. The real part ϵ vanishes (from negative to positive) at 6.40, 11.29, 12.72, and 14.96 eV (not seen in the figure because of the small broadening). The loss function consequently shows peaks at these energies: 6.50 and 15.00 eV. In the absorption spectrum ϵ_2 the strong absorption below 8.0 eV stems from transitions from the valance band to the e_g states. The absorption band expending beyond 8.5 eV up to 14.0 eV is associated with transitions from the valance band to t_{2g} states in the

conduction band. Second, we see that above 15.0 eV, corresponding to the O 2s and Nb 4p excitations, ϵ_1 also behaves as a classical oscillator: it vanishes (from positive to negative) at 21.30 eV. Peaks are observed in the loss function when ϵ_1 vanishes (from negative to positive) at 22.11 eV. Third, we remark that the region above 22.0 eV cannot be interpreted in terms of classical oscillators. Above 22.0 eV ϵ_1 and ϵ_2 are dominated by linear features, increasing for ϵ_1 and decreasing for ϵ_2 . The corresponding loss function exhibits a broadened peak at 41.3 eV that we assign not to plasmons but to their forms of collective excitations. The plasmons is defined by a vanishing real part of dielectric function and a minimum of the imaginary part, which is not the case for this peak. Such linear behavior for ϵ_1 and ϵ_2 has already been observed in the theoretical EELS of ABO_3 . At higher energies, however, they drastically modify the triple 4p plasmons, both in line shape and peak position. We also find a small anisotropy for the xx and zz directions. The same situation we can observe in ref. [42] and [43-44] for ZrO_2 and TiO_2 . Some of the ABO_3 ferroelectrics that we experimentally investigated had convenient (from the point of view of the apparatus) PT (phase transition) points T_c (KNbO_3 , and others ferroelectrics). This enabled us to carry out a study of the temperature dependences in the PT region on KNbO_3 .

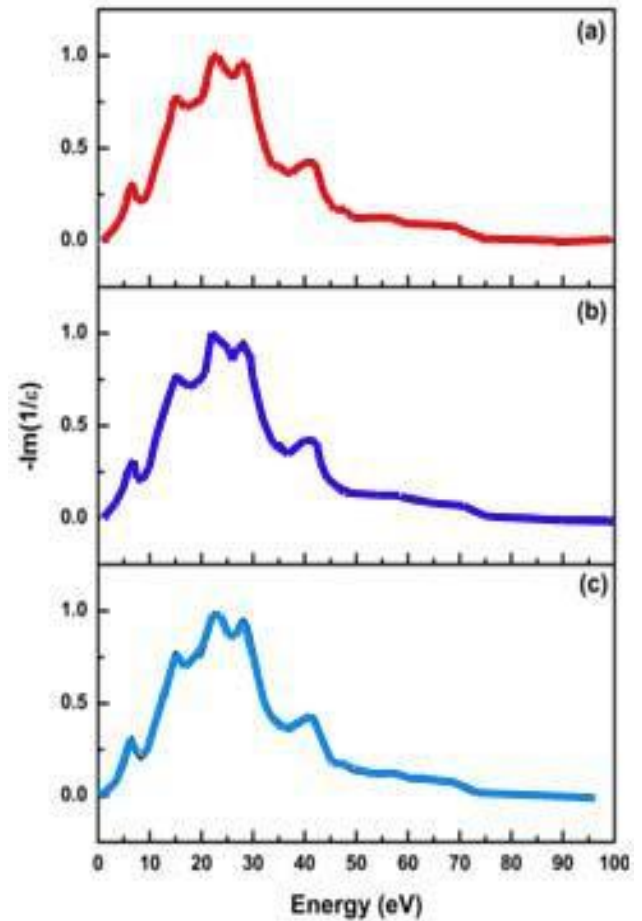


Figure 3. The theoretical electron energy-loss spectra of KNbO_3 in the cubic (a), tetragonal (b) and rhombohedral (c) phases.

The temperature dependences of $-Im\epsilon^{-1}$ constructed by us for a fixed value of the $\hbar\omega = 23.0$ eV demonstrated the anomalous change in $-Im\epsilon^{-1}$ in the region of T_c . Unfortunately, the complexity of the experiments and large volume of calculation work, as well as the difficulties encountered with the stabilization of temperature in the region T_c prevented us from investigating in detail the anomalous behavior of $-Im\epsilon^{-1}$ in $KNbO_3$ in the PT region. We were able to simply report an anomaly in the characteristic loss spectra in the vicinity of T_c . Naturally, such anomalous behavior of $-Im\epsilon^{-1}$ should be associated with ferroelectricity in these crystals. Similar anomalous behavior of the losses was observed by us for $Gd_2(MoO_4)_3$ [45]. Recently, there have been some reports [46] in which an analogous effect was observed in $BaTiO_3$ and in triglycine sulfate.

6. CONCLUSION

In conclusion, we have performed an ab initio study of the electronic structures of some ABO_3 ferroelectric. Within the DFT-LDA framework, we have found it necessary to include the semicore states in the calculations. We have then followed the effect on the electronic structure as the crystal field evolves from cubic to tetragonal structure, to rhombohedral. We have described a fingerprint in the electronic structure of cubic and rhombohedral $KNbO_3$. By using our earlier EELS experimental results on ABO_3 ferroelectrics and the theoretical investigation in the present paper, we find plasmon oscillation energy for the investigated compounds.

- [1]. H. Ibach, D. L. Mills 1982 Electron Energy Loss Spectroscopy and Surface Vibrations (N.Y: Academic Press).
- [2]. V. J. Keast 2005 J. Electron spectr. **143** 97.
- [3]. R. F. Egerton 1996 Electron Energy Loss Spectroscopy in the Electron Microscope (N.Y: Plenum Press).
- [4]. H. Raether 1980 Excitation of Plasmons and Interband Transitions by Electrons (Berlin: Springer-Verlag).
- [5]. P. E. Batson, Elektron Energy Loss Studies in Semiconductors, in: Transmission Electron Energy Loss Spectrometry in Material Science and the EELS. Atlas, 2nd ed. Ch. 10. ed. C.C. Ann Wiley, -VCH Verlag, Weinheim, 2004.
- [6]. C. R. Seabourne, A. J. Scott, R. Brydon, V. Harnchana, S. G. Wang, R.C.C. Ward, C. Wang, A. Kohn 2010 J. Phys: Conf. Ser. **241** 012063.
- [7]. M. Dressel, G. Grüner 2003 Electrodynamics of Solids: Optical Properties of Electrons in Matter (Cambridge: Cambridge University Press).
- [8]. <http://chem.ps.uci.edu/kieron/dft/book/>
- [9]. R. M. Martin 2004 Electronic Structure: Basic Theory and Practical Methods (Cambridge: Cambridge University Press).
- [10]. X. Gonze, J. -M. Beuken, R. Caracas, F. Detraux, M. Fuchs, G.-M. Rignanese, L. Sindic, M. Verstraete, G. Zerah, F. Jollet, M. Torrent, A. Roy, M. Mikami, Ph. Ghosez, J.-Y. Raty, D. C. Allan 2002 Comput. Mater. Sci. **25** 478.
- [11]. X. Conze, B. Amadon, P.-M. Anglade, J.-M. Beuken, F. Bottin, P. Boulanger, F. Bruneval, D. Caliste, R. Caracas, M. Cote, T. Deutsch, L. Genovese, Ph. Ghosez, M. Giantomassi, S. Goedecker, D. R. Hamann, P. Hermet, F. Jollet, G. Jomard, S. Leroux, M. Mancini, S. Mazevet, M. J. T. Oliveira, G. Onida, Y. Pouillon, T. Rangel, G.-M. Rignanese, D. Sangalli, R. Shaltaf, M. Torrent, M. J. Verstraete, G. Zerah, J. W. Zwanziger 2009 Computer Phys. Comm. **180** 2582.
- [12]. N. Troullier, J. L. Martins 1990 Phys.Rev. B **43** 1993.
- [13]. J. P. Perdew, Y. Wang 1992 Phys.Rev. B **45** 243.
- [14]. D. M. Ceperley, B. J. Alder 1980 Phys.Rev.Lett. **45** 566.
- [15]. H. J. Monchorst, J. D. Pack 1976 Phys. Rev. B **13** 5188.
- [16]. M. Fox 2001 Optical Properties of Solids (Oxford: Oxford Unirversity Press).
- [17]. A.M. Mamedov 2004 Ferroelectrics **33** 739.
- [18]. S. Cabuk, H. Akkus, A. M. Mamedov 2007 Physica B **394** 81.
- [19]. S. Cabuk 2010 J. Mod. Phys. B **24** 6277.
- [20]. S. Cabuk 2007 JOAM-Rapid Comm. **1(3)** 100.
- [21]. S. Cabuk, S. Simsek 2010 Phys. Scr. **81** 55703.
- [22]. K.van Benthem, C. Elsasser, R. French 2001 J. Appl. Phys. **90** 6156.
- [23]. Inbar, R. E. Cohen 1996 Phys. Rev. B **53** (3) 1193.
- [24]. A. M. Mamedov 1985 Ferroelectrics Letters **3(4)** 75.
- [25]. A. M. Mamedov 1985 Physica (B+C) **128** (1) 61.
- [26]. A. M. Mamedov 1984 Appl. Phys. A. **34(3)** 189.
- [27]. A. M. Mamedov 1984 Sov. Phys. Sol. State **26(2)** 583.
- [28]. A. M. Mamedov 1983 Izvestia RAS **47** (4) 660.
- [29]. P. Pertosa, F. M. Michel-Calendini 1978 Phys. Rev. B **17(4)** 2011.
- [30]. E. E. Krasovskii, O. V. Krasovskii, W. Schattke 1997 J. Elektron spectr. and Rel. Phen. **83** 121.
- [31]. C. M. I. Okoye 2003 J phys: Cond Matter **15** 5945.
- [32]. S. Kohiki 1998 Phys.Rev. B **57(23)** 14572.
- [33]. L. Douillard, F. Jollet, C. Bellin, M. Gautier, J. P. Duraud 1994 J. Phys. Condens. Matter **6** 5039.
- [34]. Kuepper, A. V. Postrikov, A. Moewes, B. Schkeider, M. Matleueci, H. Hesse, M. Neumann 2004 J. Phys.: Condens. Matter. **16** 8213.
- [35]. S. Cabuk, A. Mamedov 1999 J. Opt. A: Pure Appl. Opt. **1** 424.
- [36]. Tupitsyn, A. Deineka, V. A. Trepakov, L. Jastrabik, S. E. Kapihan 2001 Phys. Rev. B **46** 195111.
- [37]. H. Salehi, N. Shahmasebi, S. M. Hosseini 2003 Eur. Phys. J. B **32** 177.
- [38]. R. Ahuja, O. Eriksson, B. Johansson 2001 J. Appl. Phys. **90(4)** 1854.
- [39]. H. Wang, F. Wu, H. Jiaug 2011 J. Phys. Chem. C **115** 16180.

- [40]. *Y. Shiozaki, E. Nakamura, T. Mitsui* 2002 The Landolt-Bornstein Database (Berlin: Springer New Ser. III/36)
- [41]. *K. Dash, N. Vast, P. Baranek, M.-C. Cheynet, L. Reining* 2004 Phys. Rev. B **70** 245116.
- [42]. *C. Heiliger, F. Heyroth, F. Syrowatka, H. S. Leipner, I. Maznichenko, K. Kokko, W. Hergret, I. Mertig* 2006 Phys. Rev. B **73** 045129.
- [43]. *N. Vast, L. Reining, V. Olevano, P. Schatlshneider, B. Jouffrey* 2002 Phys. Rev. Lett. **88 (3)** 037601.
- [44]. *A. M. Mamedov* 1986 JETP **90** 526.
- [45]. *Large, N. Vmekactha* 1982 Phys. Rev. Lett **49** 1432.

STRUCTURAL, ELECTRONIC, AND OPTICAL PROPERTIES OF Ag_2Se and Ag_2Te COMPOUNDS: A FIRST PRINCIPLES STUDY

H. KOC^{1*}, AMIRULLAH M.MAMEDOV² AND EKMEL OZBAY²

¹ *Department of Physics, Siirt University, 56100 Siirt, Turkey*

² *Nanotechnology Research Center (NANOTAM), Bilkent University,*

06800 Bilkent, Ankara, Turkey

** husnu_01_12@hotmail.com*

We have performed a first principles study of structural, electronic, and optical properties of orthorhombic Ag_2Se and monoclinic Ag_2Te compounds using the density functional theory within the local density approximation. The lattice parameters of these compounds have been obtained. The linear photon-energy dependent dielectric functions and some optical properties such as the energy-loss function, the effective number of valance electrons and the effective optical dielectric constant are calculated. Our structural estimation and some other results are in agreement with the available experimental and theoretical data.

Keywords: structural, electronic, and optical properties of orthorhombic and monoclinic compounds; band structure calculations
PACs:71.15.-m

1. INTRODUCTION.

Ag_2Se and Ag_2Te , the members of silver chalcogenides Ag_2X ($\text{X}=\text{S}$, Se and Te), have unusually large and positive magnetoresistance (MR) for the low-temperature (β) phases. These compounds are non-magnetic [1-3] and are known as very good ionic conductors at room temperature [4,5]. The orthorhombic and monoclinic unit cell of Ag_2Se and Ag_2Te compounds belong to the space group $\text{P2}_1\text{2}_1\text{2}_1$ and $\text{P2}_1/\text{c}$, respectively. These crystals have four Ag_2X_3 ($\text{X}=\text{Se}$, Te) molecules (12 atoms) in their unit cell. Therefore, these compounds have a complex structure with 112 valance electrons per unit cell.

The positions corresponding to the orthorhombic Ag_2Se and monoclinic Ag_2Te have been obtained from experimental data [3]. In the past, some detailed works [3,6-7] have been carried out on the structural and electronic properties of these compounds. Fang et al [3] reported the band structure calculations of (β)- Ag_2Se , (β)- Ag_2Te and (β)- Ag_3AuSe_2 using density functional theory within the local density approximation. Zhang et al [6] calculated the electronic structures of Ag_2Te by using the WIEN2k package. Wang et al [7] performed semiclassical transport simulations based on electronic structures obtained from density functional theory calculations. Harpeness et al [5] prepared the nanocrystals of Ag_2E ($\text{E}=\text{Se}$, Te) using the polyol reduction method under sonochemical irradiation. Ferhat et al [8] synthesized (β)- Ag_2Se using solid state reaction.

As far as we know, the charge density and optical properties have not been considered for Ag_2Se and Ag_2Te so far. Consequently, the main purpose of this work is to provide some additional information to the existing data on the physical properties of Ag_2Se and Ag_2Te by using the ab initio total energy calculations. In the present work, we have investigated the structural, electronic, and photon energy-dependent optical properties of the Ag_2Se and Ag_2Te crystals. The method of calculation is given in Section 2; the results are discussed in Section 3. Finally, the summary and conclusion are given in Section 4.

2. METHOD OF CALCULATION

The calculations were performed using the density functional formalism and local density approximation (LDA) [9] through the Ceperley and Alder functional [10] as parameterized by Perdew and Zunger [11] for the exchange-correlation energy in the SIESTA code [12,13]. This code calculates the total energies and atomic forces using a linear combination of atomic orbitals as the basis set. The basis set is based on the finite range pseudoatomic orbitals (PAOs) of the Sankey-Niklewsky type [14], generalized to include multiple-zeta decays.

The interactions between electrons and core ions are simulated with separable Troullier-Martins [15] norm-conserving pseudopotentials. We have generated atomic pseudopotentials separately for atoms Ag, Se and Te by using the $5s^14d^{10}$, $4s^24p^4$ and $5s^25p^4$ configurations, respectively. The cut-off radii for present atomic pseudopotentials are taken to be 2.52 a.u. for s channels, 2.75 a.u. for p channels, and 2.52 a.u. for the d and f channels of Ag; 1.94 a.u. for s channels, 2.14 a.u. for p channels, 1.94 a.u. for d channels, and 2.49 a.u. for f channels of Se; 3.62 a.u. for s channels, 2.40 a.u. for p channels, and 2.78 a.u. for the d and f channels of Te.

The SIESTA code calculates the self-consistent potential on a grid in real space. The fineness of this grid is determined in terms of an energy cut-off E_c in analogy to the energy cut-off when the basis set involves plane waves. Here by using a double-zeta plus polarization (DZP) orbital basis and the cut-off energies between 100 and 450 Ry with various basis sets, we found an optimal value of around 350 Ry and 400 for Ag_2Se and Ag_2Te , respectively. For the final computations, 320 k-points for Ag_2Se and Ag_2Te were enough to obtain the converged total energies ΔE to about 1 meV/atoms.

It is known that the dielectric function is mainly connected with the electronic response. The dielectric function was calculated in the momentum representation, which requires matrix elements of the momentum \vec{P} between occupied and unoccupied eigenstates. The

imaginary part of the dielectric function, $\varepsilon_2(\omega)$, is given by

$$\varepsilon_2(\omega) = \frac{Ve^2}{2\pi\hbar m^2 \omega^2} \int d^3k \sum_{n,n'} \left| \langle \vec{k}n | \vec{p} | \vec{k}n' \rangle \right|^2 \times x f(\vec{k}n') (1 - f(\vec{k}n)) \delta(E_{\vec{k}n} - E_{\vec{k}n'} - \hbar\omega), \quad (1)$$

where e is the electron charge, m is the electron mass, V is the volume, $|\vec{k}n\rangle$ is a crystal wave function, \vec{p} is the momentum operator, $f(\vec{k}n)$ is the Fermi function, $E_{\vec{k}n}$ is the energy of the electron in the n th state, and $\hbar\omega$ is the energy of the incident photon with \hbar being Planck constant, and ω the photon frequency. The summation over the Brillouin zone (BZ) is the calculation using a linear interpolation on a mesh of uniformly distributed points. Matrix elements, eigenvalues, and eigenvectors are calculated in the irreducible part of the BZ.

As is known, the Kohn-Sham equations determine the ground-state properties. Thus, when the optical response calculations are made, the self-energy effect must be included. Otherwise the unoccupied conduction bands have no physical significance and a band gap problem appears: the absorption starts at too low an energy.

3. RESULTS AND DISCUSSION

3.1 Structural properties

All physical properties are related to the total energy. For instance, the equilibrium lattice constant of a crystal is the lattice constant that minimizes the total energy. If the total energy is calculated, any physical property related to the total energy can be determined. The equilibrium lattice parameters have been computed minimizing the crystal's total energy calculated for the different values of lattice constant by means of Murnaghan's equation of states (EOS)[17]. The lattice constants for Ag_2Se and Ag_2Te compounds are found to be $a=4.317 \text{ \AA}$, $b=7.036 \text{ \AA}$, $c=7.733 \text{ \AA}$ and $a=8.210 \text{ \AA}$, $b=4.408 \text{ \AA}$, $c=8.998 \text{ \AA}$, respectively. The lattice parameters obtained are in a good agreement with the experimental values[3]. In all our calculations, we have used the computed lattice constants.

3.2. Electronic properties

The electronic band structures of Ag_2Se and Ag_2Te compounds have been calculated along the high symmetry directions by using the calculated equilibrium lattice parameters. It can be seen from Fig. 1 that the bottom of the conduction bands overlaps with the top of the valance bands and these exhibit a semimetal character. The present band profiles and the total and partial density of states (DOS and PDOS) agree with the earlier works [3,7]. Band structures of Ag_2Se and Ag_2Te single crystals are compared, band structures of these crystals are highly

resemble one another. Thus, on formation of the band structures of Ag_2Se and Ag_2Te the 5s 4d orbitals of Ag atoms are more dominant than 4s4p and 5s5p orbitals of Se and Te atoms.

From the total and partial density of states (DOS and PDOS) corresponding to the band structures (the position of the Fermi level is at 0 eV) we can see that, the lowest valance bands occur between approximately -14 and -12 eV are dominated by Se 4s and Te 5s states. The other valance bands are essentially dominated by Ag 4d states. The 4p (5p) states of Se (Te) atoms are also contributing to the valance bands, but the values of densities of these states are small compared to Ag 4d states. The energy region just above Fermi energy level is dominated by Ag 5s and 5p. The 4s (5s), 4p (5p), 4d (5d) states of Se (Te) atoms are also contributing to the conduction bands, but the values of densities of these states are so small compared to Ag 5s and 5p states. In view of the quantitative analysis of the overlap extent between the Ag 4d and Se (Te) 4p (5p) states we find that the overlap extent between the Ag 4d and Se (Te) 4p (5p) states are small. For this reason, we can conclude that Ag_2Se and Ag_2Te have a highly ionic character.

The three-dimensional valance charge density distribution of Ag_2Se and Ag_2Te compounds in the plane containing Ag-Se and Ag-Te bonds is illustrated in Fig. 2(a, b). Examination of the nature of chemical bonding, especially the distribution of valance charges between atoms is necessary to explain the overall shape. The overall shape of the charge distributions suggests covalent bonding of Ag-Se and Ag-Te. Ionicity is directly associated with the character of the chemical bond. As can be seen in Fig. 2a and Fig. 2b, the wave-function clearly has a p character on the Se and Te, whereas on the Ag sites the wave-function indicate a pronounced d-like character. The region where the electron density has been enhanced is centered on the Se and Te atoms and is broadly spread between the Se, Te and Ag atoms. This non-directional character of the bonds of Se and Te are compatible with ionic bonding. The charge density distribution of Ag_1 is different from that of Ag_2 . Such a difference can be explained by the existence of metal-metal bonds. We note that the difference of the electro negativity between Ag-Se and Ag-Te appears in the difference of the charge transfer. These imply that the strong covalent interaction exist in the Ag-Se and Ag-Te system. Therefore, the bonds are unusual mixture metallic, covalent, and ionic

3.3. Optical properties

The linear optical properties of Ag_2Se and Ag_2Te are investigated, too. The calculated optical functions are shown in Fig. 3. The calculations neglect all lattice vibrational effects and pertain only to electronic transitions. In order to calculate the optical response, by using the calculated band structure, we have chosen a photon-energy range of 0-25 eV and have seen that a 0-5 eV photon-energy range is sufficient for most optical functions. Thus, we have derived the values of real and imaginary parts of the dielectric function as a function of the photon energy. bondings.

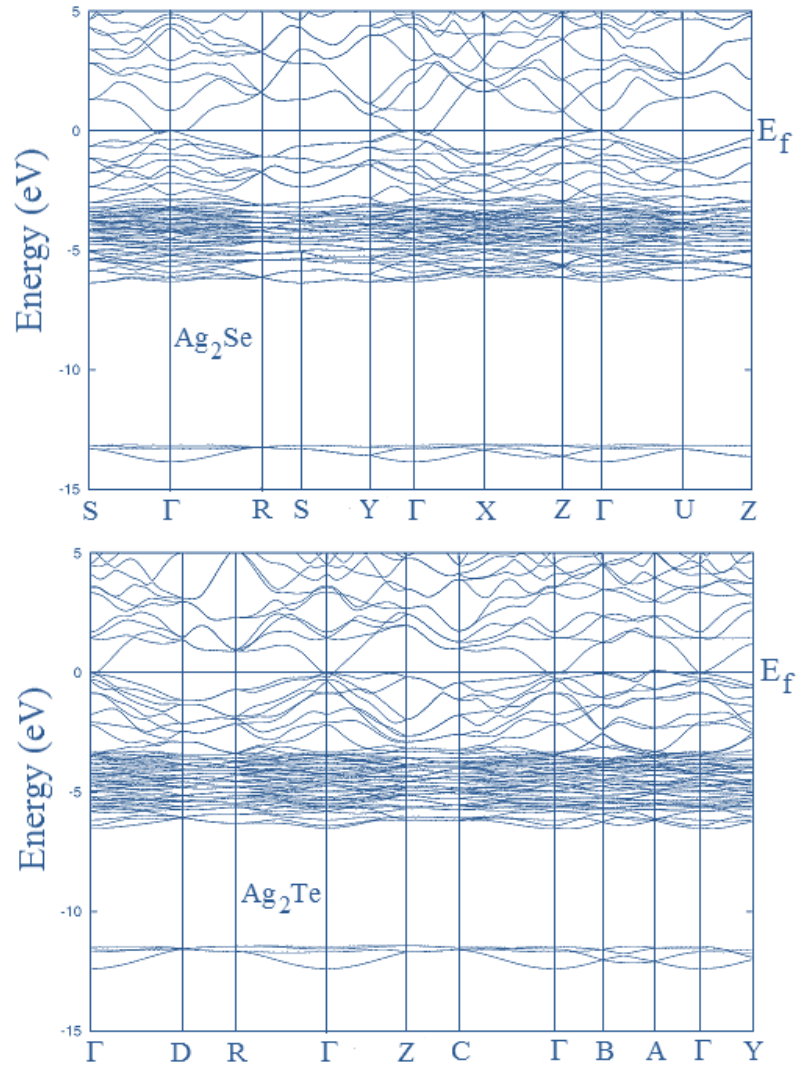


Fig.1. Energy band structure for Ag_2Se and Ag_2Te

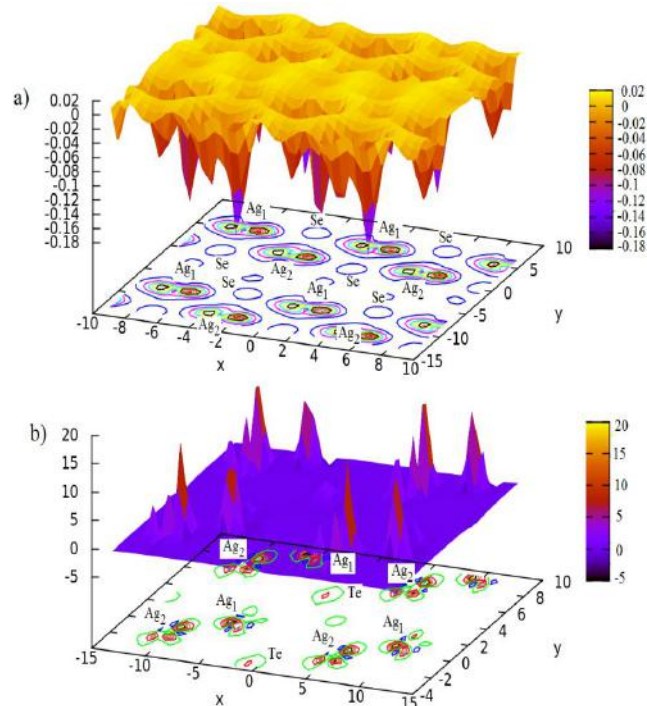


Fig. 2. Charge density distribution of the valence charge of a) Ag_2Se and b) Ag_2Te

We first calculated the real and imaginary parts of the frequency-dependent linear dielectric function and these are shown in Fig. 3. The ϵ_1^x behaves mainly as a classical oscillator. It vanishes (from positive to negative) at about 4.76 eV and 17.28 eV (see Fig. 3), whereas the other function ϵ_1^z is equal to zero at about 5.95 eV and

16.24 eV (see Fig. 3) for Ag_2Se compound. The ϵ_1^x is equal to zero at about 3.10 eV and 17.25 eV (see Fig. 3), whereas the other function ϵ_1^z is equal to zero at about 3.62 eV and 16.21 eV (see Fig. 3) for Ag_2Te compound.

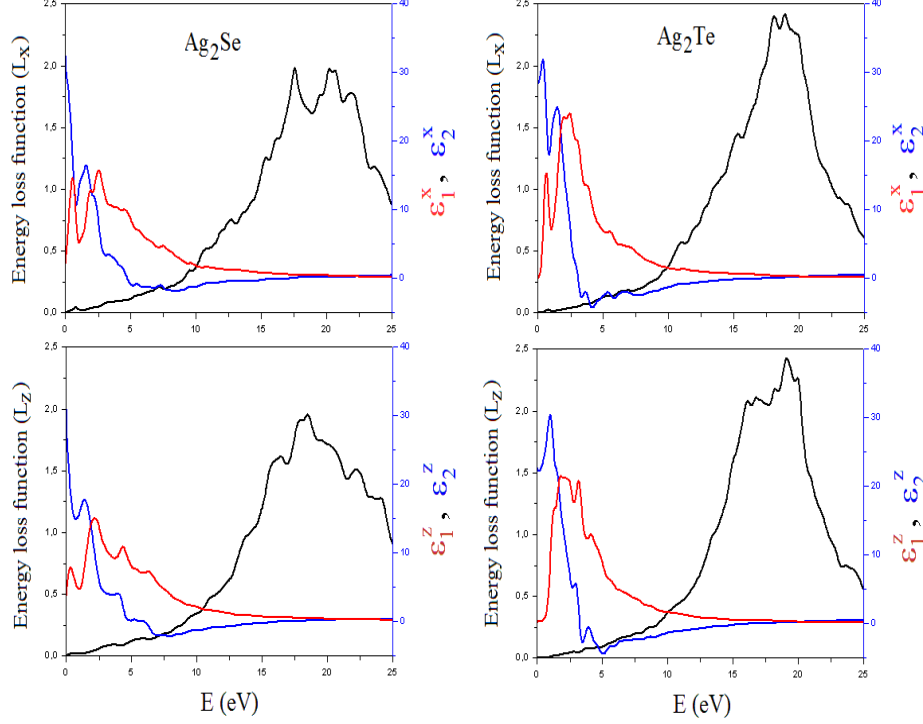


Fig.3. Energy spectra of dielectric function $\epsilon = \epsilon_1 - i\epsilon_2$ and energy-loss function (L) for Ag_2Se and Ag_2Te

The peaks of the ϵ_2^x and ϵ_2^z correspond to the optical transitions from the valence band to the conduction band and are in agreement with the previous results. The maximum peak values of ϵ_2^x and ϵ_2^z for Ag_2Se are around 2.55 eV and 2.18 eV, respectively, whereas the maximum values of ϵ_2^x and ϵ_2^z for Ag_2Te are around 2.42 eV and 1.82 eV, respectively. Spectral dependences of dielectric functions show the similar features for both materials because the electronic configurations of Se ($[\text{Ar}], 3d^{10} 4s^2 4p^3$) and Te ($[\text{Kr}], 4d^{10} 5s^2 5p^4$) are very close to each other. In general, there are various contributions to the dielectric function, but Fig. 3 show only the contribution of the electronic polarizability to the dielectric function. In the range between 0 eV and 5 eV, ϵ_1^z decrease with increasing photon-energy, which is characteristics of an anomalous dispersion. In this energy range, the transitions between occupied and unoccupied states mainly occur between Ag 4d states which can be seen in the DOS (PDOS). The 0-5.0 eV photon energy range is characterized by strong absorption and appreciable reflectivity. The interband transitions at these points, which consist mostly of plasmon excitations, and the scattering probability of volume losses are directly connected with the energy-loss function.[18]

$$L(\omega) = \frac{\epsilon_2}{\epsilon_1^2 + \epsilon_2^2} \quad (2)$$

The calculated energy-loss functions, $L(\omega)$, are also presented in Fig. 3. In this figure, L_x and L_z correspond to the energy-loss functions along the x- and z-directions. The function $L(\omega)$ describes the energy loss of fast electrons traversing the material. The sharp maxima in the energy-loss function are associated with the existence of plasma oscillations[19]. The curves of L_x and L_z in Fig. 3 have a maximum near 17.55 and 18.50 eV for Ag_2Se , respectively and 18.93 and 19.10 eV for Ag_2Te , respectively.

The known sum rules [19] can be used to determine some quantitative parameters, particularly the effective number of the valence electrons per unit cell N_{eff} , as well as the effective optical dielectric constant ϵ_{eff} , which make a contribution to the optical constants of a crystal at the energy E_0 . We recall that

$$N_{\text{eff}}(E) = \frac{2m\epsilon_0}{\pi\hbar^2 e^2 N a} \int_0^\infty \epsilon_2(E) E dE \quad (3)$$

$$\varepsilon_0(E) - 1 = \frac{2}{\pi} \int_0^\infty \varepsilon_2(E') E'^{-1} dE' \quad (4)$$

where N_a is the density of atoms in a crystal, e and m are the charge and mass of the electron, respectively and $N_{\text{eff}}(E_0)$ is the effective number of electrons contributing to optical transitions below an energy of E_0 . The physical meaning of ε_{eff} is quite clear: ε_{eff} is the effective optical dielectric constant governed by the interband transitions in the energy range from zero to E_0 , i.e. by the polarization of the electron shells. The effective number of valence electron per unit cell, N_{eff} , contributing in the interband transitions, reaches saturation value at about 30 eV for both compounds. This means that deep-lying valence orbitals participate in the interband transitions as well.

The effective optical dielectric constant, ε_{eff} , reaches a saturation value at about 7 eV for Ag_2Se and Ag_2Te . This means that the greatest contribution to ε_{eff} arises from interband transitions between 0 and 7 eV.

4. CONCLUSION

In present work, we have made a detailed investigation of the structural, electronic, and frequency-dependent linear optical properties of the Ag_2Se and Ag_2Te compounds using the density functional methods. The results of the structural optimization implemented using the LDA are in good agreement with the experimental results. We have examined photon-energy dependent dielectric functions, some optical properties such as the energy-loss function, the effective number of valence electrons and the effective optical dielectric constant along the x- and z- axes.

-
- | | |
|--|--|
| <p>[1]. R. Xu, A. Hussman, T.F. Rosenbaum, M.L. Saboungi, J.E. Enderby and P.B. Littlewood 1997 Nature 390 57</p> <p>[2]. I.S. Chuprakov and K.H. Dahmen 1998 Appl. Phys. Lett. 72 2165</p> <p>[3]. C.M. Fang, R.A. Groot and G.A. Wiegers 2002 J. Phys. and Chem. of Solid 63 457</p> <p>[4]. D. Grientschnig and W. Sitte 1991 J. Phys. Chem. Solids 52 805</p> <p>[5]. R. Harpeness, O. Palchik, A. Gedanken, V. Dalehik S. Amiel, M.A. Slifkin and A.M. Weiss 2002 Chem. Mater. 14 2094</p> <p>[6]. W. Zhang, R. Yu, W. Feng, Y. Yao, H. Weng, X. Dai and Z. Fang 2011 Phys. Rev. Lett. 106 156808</p> <p>[7]. W. Wang, W. Chu, D. Wang, W. Mao, W. Pan, Y. Guo, Y. Xiong and H. Jin 2011 J. Elect. Mat. 40 624</p> <p>[8]. M. Ferhat and J. Nagao 2000 J. Appl. Phys. 88 813</p> <p>[9]. J.W. Kohn and L.J. Sham 1965 Phys. Rev. 140 A1133</p> <p>[10]. D.M. Ceperley and M.J. Adler 1980 Phys. Rev. Lett. 45 566</p> | <p>[11]. P. Perdew and A. Zunger 1981 Phys. Rev. B 23 5048</p> <p>[12]. P. Ordejón, E. Artacho and J.M. Soler 1996 Phys. Rev. B (Rapid Commun) 53 R10441</p> <p>[13]. J.M. Soler, E. Artacho, J.D. Gale, A. García, J. Junquera, P. Ordejón and D. Sánchez-Portal 2002 J. Phys.: Condens. Matter. 14 2745</p> <p>[14]. O.F. Sankey and D.J. Niklewski 1989 Phys. Rev. B 40 3979</p> <p>[15]. N. Troullier and J.L. Martins 1991 Phys. Rev. B 43 1993</p> <p>[16]. S. Saha and T.P. Sinha 2000 Phys. Rev. B 62 8828</p> <p>[17]. F.D. Murnaghan 1944 Proc Natl Acad Sci U.S.A. 50 244.</p> <p>[18]. M. Fox 2002 Optical Properties of Solids (Oxford University Press, USA)</p> <p>[19]. Z.H. Levine and D.C. Allan 1989 Phys. Rev. Lett. 63 1719</p> <p>[20]. O.V. Kovalev 1965 Representations of the Crystallographic Space Groups. Irreducible Representations Induced Representations and Corepresentations (Amsterdam: Gordon and Breach)</p> |
|--|--|

OPTICAL PHONONS IN ZnGa_2Se_4 and ZnAl_2Se_4 SINGLE CRYSTALS

T.G.KERIMOVA, N.A.ABDULLAYEV, I.A.MAMEDOVA, I.G.NASIBOV, Z.BADALOVA

*G.M.Abdullaev Institute of Physics NAS of Azerbaijan**Baku, AZ-1143, ave.Javid, 33,**E-mail: ktaira@physics.ab.az, taira-kerimova@mail.ru*

Raman spectra of ZnGa_2Se_4 single crystals at various geometries are presented. As a result of analysis of experimental results of Raman scattering spectra of ZnGa_2Se_4 together with data for ZnAl_2Se_4 , conformity between optical phonon frequencies and concrete displacements of atoms in unit cell have been established.

Keywords: Raman scattering, optical phonons, ZnGa_2Se_4 , ZnAl_2Se_4

PACS : 63.20.-e 78.30.-j

1. INTRODUCTION

Semiconducting compounds $\text{A}^2\text{B}_2\text{C}_6$ (A-Zn, Cd; B-In, Ga; C-S, Se, Te), crystallizing in sp.gr. S_4^2 (tiogallate) become crystal chemical analogues of $\text{A}^2\text{B}_4\text{C}_5^2$ (A- Cd; Zn, B- Si, Ge, C-P, As) compounds of chalcopyrite (sp.gr. D_{2d}^{12}) and sphalerite (sp.gr. D_{2d}^{12}) structure.

In fig.1 the crystal lattice of compounds (fig.1a), crystallizing in spatial group S_4^2 , and Brillouin zone of sphalerite, chalcopyrite and tiogallate (fig.1b) are presented. Compounds of space group S_4^2 also as well as chalcopyrites (space group D_{2d}^{12}) crystallize in tetragonal structure and differ from chalcopyrite by the presence of vacancy in cation sublattice. Therefore Brillouin zones of compounds (space group S_4^2) and (space group D_{2d}^{12}) are identical. It is necessary to notice, that Brillouin zone of these compounds in 4 times is less than Brillouin zone of sphalerite and that is why high-symmetrical points on the edge of Brillouin zone of sphalerite are transformed to the centre of Brillouin zone of these compounds. Fall of symmetry of a crystal lattice leads to that, modes active on the edge of Brillouin zone of sphalerite are active in the centre of Brillouin zone of chalcopyrite and tiogallate .

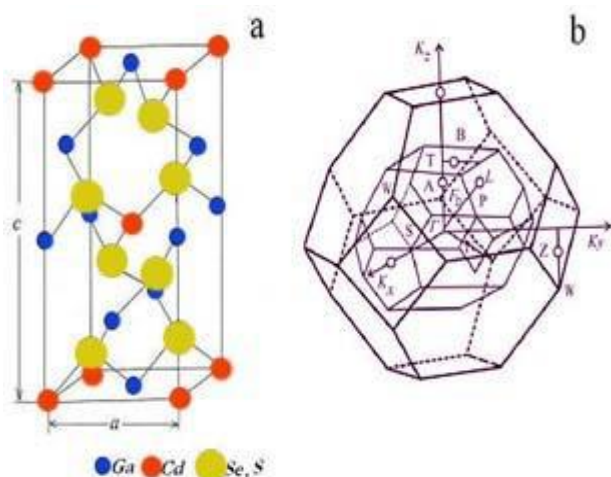


Fig.1 Crystalline lattice (a) of compounds, crystallising in phase group S_4^2 , and Brillouin zone (b) of compounds, crystallising in sphalerite (sp.gr. T_d), and tiogallate (sp.gr. S_4^2) structure

For these compounds birefringence, considerable magnitudes of factor of a nonlinear susceptibility, high

photosensitivity, a bright photoluminescence are characteristic. The special place is occupied with researches of electronic and phonon characteristics of these compounds, both experimentally, and theoretically, as these data are important for an explanation of mechanisms of a thermal capacity, heat conductivity, measurements of band structure, thermodynamical parameters and etc.

Optical phonons in ZnGa_2Se_4 have been investigated in [1,2]. In [1] Raman scattering spectra have been measured in any geometry of experiment. There are disagreements in connect with identification of optical phonons on symmetry types. In [2] spectra of infrared reflection are presented. The measurements have been carried out in the polarization parallel and perpendicular to the tetragonal C axis. It is known that investigation of Raman scattering spectra in various geometries is very important for the full information on optical phonon frequencies.

In the present work the results of Raman scattering spectra investigations in various geometries in ZnGa_2Se_4 are presented. The obtained results are discussed in common with the data of ZnAl_2Se_4 [3].

The aim of the given work is the establishment of the conformity of optical phonon frequencies between the concrete displacement of atoms in the unit cell.

2. GROWTH OF CRYSTALS AND EXPERIMENTAL METHOD

Single crystalline samples ZnGa_2Se_4 were grown by the gas transport reactions. Crystalline iodine was used as a transporter. The grown single crystals had the form of trihedral prisms with the most developed plane $(1\bar{1}2)$, with which the tetragonal axis C makes 37° . Some samples had the form of plates with the plane (001) , i.e. the tetragonal axis was perpendicularly to plane ab . Plates had the sizes $5 \times 4 \times 3 \text{ mm}^3$ from which prepared samples were focused along a and b axes. An axis z is perpendicularly to planes. From the rentgenographic researches the lattice parameters was determined as $a = 5,496 \text{ \AA}$, $c = 10,99 \text{ \AA}$, $c/a = 2$ which is co-ordinated with the data [4].

Raman scattering spectra have been measured on device ДФС-12. As an excitation source the argon laser $5144,6 \text{ \AA}$ was used. As the radiation detector ФЭУ-79, working in a photon account regime was used.

3. DISCUSSION OF RESULTS

Vibrational spectrum in compounds (sp.gr. S_4^2) is described by following irreducible representations

$$\Gamma_{\text{vib}} = 3A(KP) + 6B(IK, KP) + 6E(IK, KP)$$

In Raman scattering spectra 3 modes of A symmetry are active, in infra-red absorption spectra 5 modes of B symmetry resolved in polarization parallel to tetragonal axis C and 5 two-fold degenerated modes of E symmetry in polarization of perpendicular to tetragonal C axis. One mode of B symmetry and two-fold degenerated mode of E symmetry are acoustic.

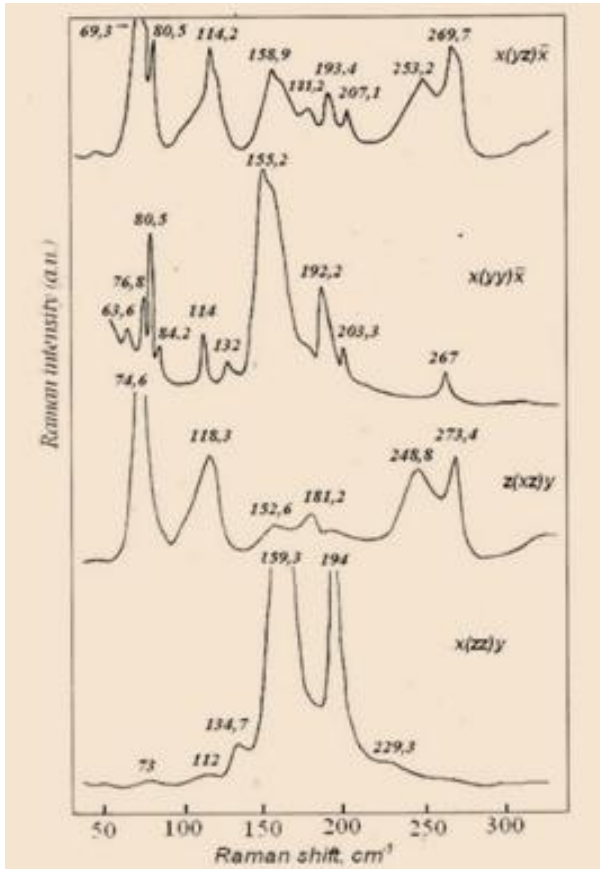


Fig.2 Raman scattering spectra in ZnGa_2Se_4 in various geometries of experiment

In fig.2 Raman scattering spectra of ZnGa_2Se_4 single crystals measured in various geometry of experiment. Identification of observed frequencies of optical phonons have been carried out accordingly to selection rule for according geometries of experiment [5]. The results are presented in table. The optical phonon frequencies for ZnAl_2Se_4 [3] are also presented. For clearing up of a matter that, what optical phonons connect with concrete displacement of atoms in unit cell, it is necessary carrying out the analyses of symmetrized displacement of atoms in the unit cell of compounds, crystallizing in sp.gr. S_4^2 .

In fig.3 symmetrized displacement of atoms in the unit cell of compounds, crystallizing in ph.gr. S_4^2 is presented [6]. It is shown that, A symmetry modes are due to the displacement along a , b and z crystallographic axis. The cation sublattice atoms do not participate in these displacement.

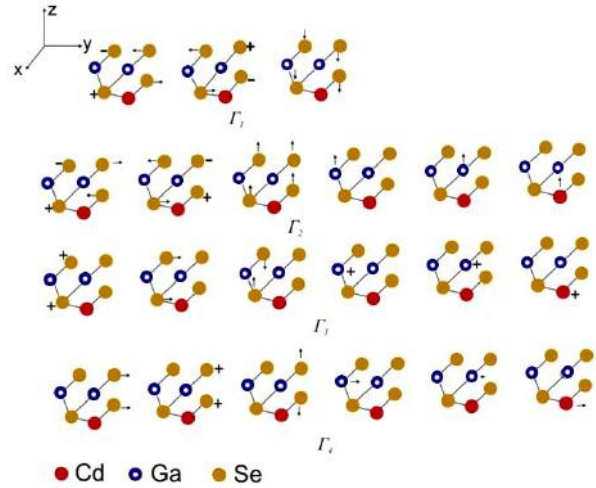


Fig.3. Symmetrized displacement of atoms in unit cell of the compounds crystallising in space group S_4^2 (tiogallate)

Table. The frequencies of optical phonons in ZnGa_2Se_4 и ZnAl_2Se_4 [3]

Symmetry	ZnGa_2Se_4		ZnAl_2Se_4 ω , cm^{-1} [3]
	IR [2] ω , cm^{-1}	Raman shift ω , cm^{-1}	
$B_1(\text{LO})$	278	274	390
$B_2(\text{LO})$	246		348
$B_3(\text{LO})$	200	203	203
$B_4(\text{LO})$	136	130,9	140
$B_5(\text{LO})$	81	84,2	87
$B_1(\text{TO})$	255	267	378
$B_2(\text{TO})$	230	229,3	328
$B_3(\text{TO})$	192	192	193
$B_4(\text{TO})$	126	132	136
$B_5(\text{TO})$	79	80,5	83
$E_1(\text{LO})$	275	273/4	400
$E_2(\text{LO})$	245	248/8	348
$E_3(\text{LO})$	200	203	203
$E_4(\text{LO})$		118	105
$E_5(\text{LO})$	82	80,5	88
$E_1(\text{TO})$	250	253	368
$E_2(\text{TO})$	236	236	336
$E_3(\text{TO})$	190	193,4	193
$E_4(\text{TO})$		114	105
$E_5(\text{TO})$	80	80,5	83
A_1		134/7	
A_2		159/3	
A_3		194	

The analyses of symmetrized displacement of atoms in the unit cell of compounds, crystallizing in sp.gr. S_4^2 [6] show that B and E symmetry modes are caused by in phase displacement of anion sublattice atoms concerning trivalent cations along the crystallographic axis C and in ab plane. In this case considerable dipole moment is created. On the other hand, values of high-frequency modes among the compounds CdGa_2Se_4 [7], ZnGa_2Se_4 , AgGaSe_2 [8], CuGaSe_2 [9] practically do not depend on atoms mass of elements of the first and the second groups of the regular table.

Hence, high-frequency modes are caused by dipole displacement (2Ga-4Se). For confirming of these conclusions in the present work compounds with various trivalent cation sublattice atoms (Ga, Al) are discussed. For comparison in table 1 values of optical phonons for ZnAl_2Se_4 [3] are presented. As it is shown from table 1, values of B_1 , B_2 and E_1 , E_2 high-frequency modes in ZnGa_2Se_4 and ZnAl_2Se_4 considerably differ. The last is connected with distinction of atoms masses of trivalent cations. Values of more low-frequency modes B_3 , B_4 and E_3 , E_4 in ZnAl_2Se_4 coincide with values B_3 , B_4 and E_3 , E_4 modes in ZnGa_2Se_4 . Hence, these modes are caused by dipole displacement (Zn-4Se). Considering, that mass of

Al (27) is less than mass of Zn (67) more than 2 times, it is necessary to assume, that the most low-frequency modes of B_5 and E_5 symmetry are caused by displacement of Al atoms.

4. CONCLUSION

As a result of the analysis of experimental results of spectra of combinational dispersion ZnGa_2Se_4 together with data for ZnAl_2Se_4 conformity between frequencies optical фононов and concrete displacement of atoms in an elementary cell is established.

-
- | | |
|---|--|
| <p>[1]. P.P.Lottici and C.Razzetti Solid State Communications, 46, (1983) 681.</p> <p>[2]. A. Eifler, G. Krauss, V. Riede, V. Krämer, W.Grill Journal of Physics and Chemistry of Solids, 66, (2005) 2052.</p> <p>[3]. A.Eifle, J.-D.Heelhet, G.Lippold, V.Riede, W.Grill, G.Kraub,V.Kramer-Physica B, Condensed Matter,vol.263-264, (1999) p.806-808.</p> <p>[4]. H.Hhan., G.Frank., W.Klinger, A.Stoerger, S.Stoerger Anorg. Allgmaine Chemie, 279, (1955) 241.</p> | <p>[5]. R. Bacewicz, Y.P.Lottici and R.Rozetti. J.Physica C.: Solid.Stat.Phys. 12, (1979) 3603.</p> <p>[6]. T.G.Kerimova Reports AS Azerb.SSR, 35 (1979)33.</p> <p>[7]. T.G.Kerimova, R.X.Nani, E.Yu.Salaev, V.Ya. Shtainshraiber FTT, 21, (1979) 1961.</p> <p>[8]. I.V.Bondar, A.G.Karoza, G.F.Smirnova Phys.Stat.Sol.(b), 84, (1977) K65.</p> <p>[9]. J.P. van der Ziel, A. E. Meixner, H.M. Kasper, and J.A. Ditzenberger Phys.Rev. B 9, (1974) 4286.</p> |
|---|--|

ANALYSIS OF TEMPERATURE DEPENDENCE OF KINETIC COEFFICIENTS OF $\text{Bi}_{0.88}\text{Sb}_{0.12}$ ALLOY

ELTAJ YUZHBAKOV, KHAYALA GASANOVA, BAKIR TAIROV

*G.M.Abdullayev Institute of Physics of
Azerbaijan National Academy of Sciences,
H.Javid pr., 33, Baku, AZ 1143, Azerbaijan
eltaj100@yahoo.com*

On the basis of measured low magnetic field galvanomagnetic coefficients for semiconducting single crystals of $\text{Bi}_{0.88}\text{Sb}_{0.12}$, the main kinetic parameters of the investigated material have been determined in the range of temperatures 77÷300 K.

keywords: Bi-Sb alloys, galvanomagnetic properties, kinetic coefficients of Bi-Sb alloys

PACS: 71.20.Nr, 72.20.My, 72.20.Fr, 73.50.Jt

I. INTRODUCTION

Investigation of solid solutions of $\text{Bi}_{1-x}\text{Sb}_x$ ($x = 0.03 \div 0.2$) displays that those solutions are perspective materials for solid coolers functioning on the basis of galvanomagnetic and thermomagnetic effects [1]. Moreover those materials are of broad interest from the theoretical aspect. Due to the smallness of the characteristic energetic parameters of solid solutions of Bi-Sb, those materials are very sensitive to the external impacts (temperature, pressure, presence of electroactive impurities, defects, etc.). By varying external influence in comparatively small range, it is possible to investigate topology of Fermi surface, various phase transitions, alter the statistics of charge carriers in rather broad range etc. That is why these materials are still being investigated as bulk materials, thin films and nanoscale structures [2-4].

In itself studying the transport phenomena in the system of Bi-Sb represents a powerful tool for investigating energetic zone structure and mechanisms of scattering of charged carriers in these materials. But studying galvanomagnetic and thermomagnetic effects in these materials at intermediate (77K-300K) and high (more than room temperature) temperatures become irreplaceable, because the best powerful methods for investigating energetic zone structure and mechanisms of scattering of charged carriers, as oscillation and resonance methods, are effective only at ultra- and low temperatures.

II. EXPERIMENT

Investigation of temperature dependence of low-field galvanomagnetic coefficients of the alloy of $\text{Bi}_{0.88}\text{Sb}_{0.12}$ at the temperature range of 77÷300 K was carried out in the paper. Single crystals of $\text{Bi}_{0.88}\text{Sb}_{0.12}$ were grown by the method of Chokhralsky in the experimental equipment [5] using solid replenishment. Two types of rectangular samples were cut from the single crystal ingot by electrosparke method; large edges of the first group of samples were parallel to binary axis, but the second group ones were aligned parallel to trigonal axis.

For diminution of influence of parasite thermomagnetic effects on the precision of measurement of isothermal galvanomagnetic coefficients, the measurements were carried out in special module filled with helium. Due to the precautions the temperature gradient between contact points was reduced up to $0.03 \div 0.05$ K. For reducing of thermal leakage over measuring wires and thermocouples

were used thin ones (having diameter less than 0.1 mm). All measuring wires and thermocouples were thermostated. Calculation of the wires' length was carried out according to the work [6]. As known during the measurement of specific resistance of a thermoelectrical specimen an additional error makes its appearance due to the Peltier effect. But using a fast-acting, precious digital voltmeter allows to make this error negligible. The measurement of other galvanomagnetic coefficients was conducted by the high-precious D.C. Potentiometer. In every case the fulfillment of the low-field condition ($\mu\text{B} \ll 1$) were tested, because this varies in the rather broad range depending on temperature and orientation of magnetic field with respect to main crystallographic axes.

The following components of the tensor of electric resistance for the alloy of $\text{Bi}_{0.88}\text{Sb}_{0.12}$ – two components of specific resistance (ρ_{11} and ρ_{33}) and two components of Hall effect (R_{231} and R_{123}) and, five components of magnetoresistance ($\rho_{11,11}$, $\rho_{11,22}$, $\rho_{11,33}$, $\rho_{33,11}$, $\rho_{33,33}$) in low magnetic field – were measured.

From the curve (Fig. 1) of temperature dependence of components of specific resistance (ρ_{11} and ρ_{33}) it is clear that the alloy of $\text{Bi}_{0.88}\text{Sb}_{0.12}$ has semiconducting character up to $\approx 160\text{K}$ and above $\approx 200\text{K}$ it shows metallic character. Furthermore the anisotropy of specific resistance $[(\rho_{33} - \rho_{11})/\rho_{33}]$ is decreasing with temperature, that is opposite to the case of pure Bi and its dilute solutions with antimony. The temperature dependence of the Hall and magnetoresistance coefficients is shown in the figures 2 and 3, correspondingly. From the figure 2 it is clear that both Hall components greatly decrease with temperature. Such decreasing may be caused by increasing of the concentration of charge carriers. However, as the conductance of Bi-Sb alloys is intrinsic at the given temperature range, the changes of Hall coefficients may be related to the alteration of ratio of mobilities of electrons and holes. Therefore, the temperature dependence of Hall coefficients separately cannot quantitatively characterize alteration of the concentration of current carriers and more complicated calculations considering of adopted model of energetic spectra must be conducted.

From the figure 3 it is clear that common features of the temperature dependences of all measured components of magnetoresistance are identical.

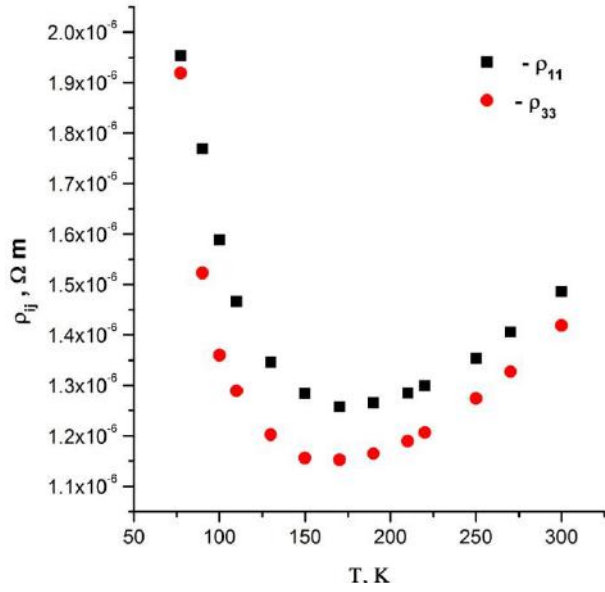


Fig.1. Temperature dependence of of specific resistance (ρ_{11} and ρ_{33}).

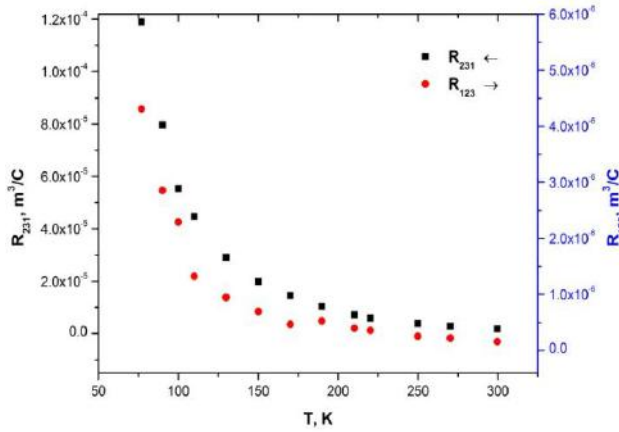


Fig.2. Temperature dependence of the Hall coefficients

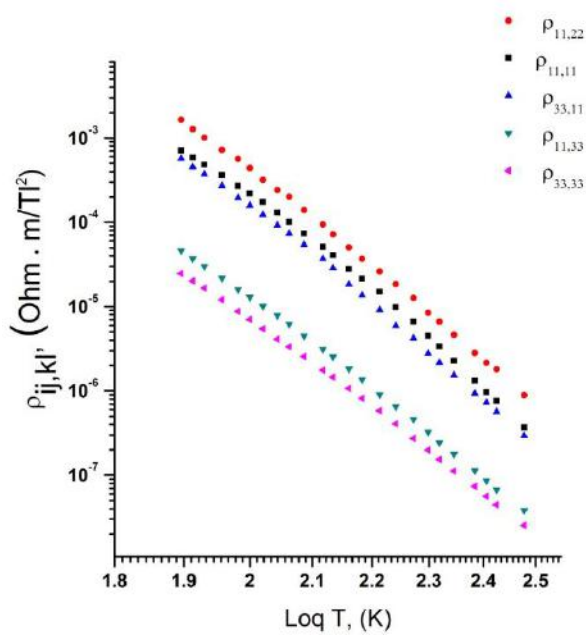


Fig.3. Temperature dependence of the magnetoresistance coefficients.

III. RESULTS AND DISCUSSION

It has been noted that due to the complicated character of zone structure, drastic temperature dependence of energetic gap and effective masses of charge carriers, peculiarities of energetic ellipsoids and mechanisms of scattering it is difficult to determine precisely all kinetic coefficients. So for the description of the features of kinetic parameters of the Bi-Sb alloys it has been proposed some models of energetic zone structure and other approximations. In the frame of adopted model and approximation it is possible to determine carrier densities of electrons N and holes P ; partial mobilities for electrons (μ_1, μ_2, μ_3) and holes (ν_1, ν_2, ν_3), correspondingly; the tilt angle of electronic isoenergetic ellipsoids to the bisectrix axis (φ_e) and etc. For the precious calculation of the kinetic coefficients the temperature dependences of energetic gap ε_g , partial effective masses of electrons and holes m_i^e, m_i^h at the bottom of corresponding energetic minimums must be taken into account. But due to the lack of some of the reliable parameters it is usually simple models for assessment purposes are used.

In our case for estimation the values of some kinetic coefficients it is sufficient to use averaged value of the measured galvanomagnetic coefficients. For this purpose we used the following formulas for specific resistivity, Hall effect and magnetoresistivity, correspondingly [5]:

$$\rho = \frac{1}{3}(2\rho_{11} + \rho_{33}) \quad (1)$$

$$R = \frac{1}{3}(2R_{231} + R_{123}) \quad (2)$$

$$\frac{\delta\rho}{H^2} = \frac{1}{15}(\rho_{1111} + 5\rho_{1122} + 4\rho_{1133} + 4\rho_{3311} + 5\rho_{3333}) \quad (3)$$

The averaged values of those parameters at the temperature range of 77÷300 K are shown in the table 1.

Table 1. The averaged values of the galvanomagnetic coefficients for $\text{Bi}_{0.88}\text{Sb}_{0.12}$ at the temperature range of 77÷300K.

T (K)	ρ (Ωm)	R (m^3/C)	$\delta\rho/H^2$ ($\Omega m/T^2$)
77	1.94E-06	8.08E-05	8.53E-03
90	1.69E-06	5.41E-05	4.05E-03
100	1.51E-06	3.76E-05	2.26E-03
110	1.41E-06	3.04E-05	1.36E-03
130	1.30E-06	1.98E-05	5.07E-04
150	1.24E-06	1.35E-05	2.08E-04
170	1.22E-06	9.91E-06	1.01E-04
190	1.23E-06	7.03E-06	5.23E-05
210	1.25E-06	4.91E-06	2.47E-05
220	1.27E-06	4.08E-06	2.14E-05
250	1.33E-06	2.63E-06	1.06E-05
270	1.38E-06	1.94E-06	6.79E-06
300	1.46E-06	1.24E-06	3.68E-06

From the above mentioned data it is possible to estimate concentration and mobilities for charge carriers. For this purposes the following simple formulas may be used:

$$\frac{1}{\rho} = eN\mu \left(\frac{1+b}{b} \right) \quad (4)$$

$$R = \frac{1}{eN} \left(\frac{1-b}{1+b} \right) \quad (5)$$

$$\frac{\delta\rho}{R^2 H^2} = \frac{b^2}{(b-1)^2} \quad (6)$$

Here N – concentration of electrons; μ and ν are mobilities of electrons and holes, correspondingly; b stands for mobility ratio of electrons to holes, i.e. $(\frac{\mu}{\nu})$.

Of course, these formulas correspond to the case of degeneracy of charge carriers, and $N=P$. More realistic formulas taking into account non degeneracy of charge carriers in our case are available, for example in [7] and include expressions for Hall and magnetoresistance factors (a_r , b_r) too. In our case we suggested that Hall factors for electrons and holes and the mobility ratio of the charge carries vary very slowly with temperature. From the private communication we established that the value of $a_r=1.18$ and $b_r=1.76$ for the given alloy. From the data of table 1 according to the formulas (4-6) there were calculated concentration and mobilities of electrons and holes for $\text{Bi}_{0.88}\text{Sb}_{0.12}$ at the temperature range of

77÷300K. The results of the calculations are depicted in the table 2.

Table 2. The kinetic coefficients for $\text{Bi}_{0.88}\text{Sb}_{0.12}$ at the temperature range of 77÷300 K.

T (K)	N (m^{-3})	μ ($m^2/V\cdot s$)	ν ($m^2/V\cdot s$)
77	3.32E+22	6.93E+01	2.77E+01
90	4.95E+22	5.34E+01	2.14E+01
100	7.12E+22	4.15E+01	1.66E+01
110	8.80E+22	3.61E+01	1.44E+01
130	1.35E+23	2.55E+01	1.02E+01
150	1.98E+23	1.82E+01	7.28E+00
170	2.70E+23	1.35E+01	5.40E+00
190	3.81E+23	9.51E+00	3.81E+00
210	5.46E+23	6.53E+00	2.61E+00
220	6.57E+23	5.36E+00	2.14E+00
250	1.02E+24	3.30E+00	1.32E+00
270	1.38E+24	2.35E+00	9.38E-01
300	2.15E+24	1.42E+00	5.67E-01

In spite of approximateness of some initial conditions the obtained results fairly describe the temperature dependence of the kinetic coefficients. Of course, using more complicated models for energetic zone structure for the given alloy and taking into account temperature dependence of zone parameters would make possible to better analyze rather difficult scattering mechanisms in the BiSb system.

-
- [1]. W.M.Yim, A.Amith Solid State Electronics, 1972, v.15, pp.1141-1165
- [2]. S. Dutta, V. Shubhaa and T.G. Ramesha, Physica B: Condensed Matter, v.405, No 5, (2010), p.1239.
- [3]. D.Choi. A.Balandin, and et.al. Appl. Phys. Lett. 89, (2006), p.1415.
- [4]. S.Dutta, V. Shubha, T.G. Ramesh, Florita D'Sa. Journal of Alloys and Compounds, 467, (2009), p. 305.
- [5]. А.А. Мусаев. Гальваномагнитные эффекты, дисперсия геликоновых волн и рассеяние носителей тока в сплавах Bi-Sb при 77K-300K. – Дисс.канд.физ.-мат. наук. – Баку, 1981
- [6]. Хаст Дж. Приборы для научных исследований, 1970, № 5, с. 8-11
- [7]. Аскеров Б.М. Электронные явления переноса в полупроводниках. Москва: Наука, 1985.

ELLIPSOMETRIC INVESTIGATION OF OPTICAL CONSTANTS OF CASPIAN SEAWATER AND CRUDE OILS FROM DIFFERENT SOURCES

**KHURAMAN KHALILOVA^{A*}, ELDAR MAMMADOV^A,
YEGANE ALIYEVA^A, NAGHI GASIMOV^A, NAZIM MAMEDOV^A**
**Corresponding author: Tel.: (+99412) 5387646; Fax: (+99412) 5372292*

E-mail address: khalilova@physics.ab.az (Kh.Khalilova)

*^a Department of Ellipsometry, G.M.Abdullayev Institute of Physics,
Azerbaijan National Academy of Sciences,
H. Javid ave. 33, Baku AZ-1143, Azerbaijan*

Seawater from different regions of Caspian Sea, as well as seawater-oil system has been accessed by spectroscopic ellipsometry over the 200-1700nm spectral range at room temperature to possibly obtain information that might be useful for the detection and recovery of oil spills. Dielectric function and optical constants have been obtained for each substance depending on oil droplet size and concentration in the oil-water emulsion, oil layer thickness, and oil weathering. Complimentary, X-ray fluorescence of the above substances has been studied and elemental content has been determined.

Key words: Spectroscopic Ellipsometry; Ecology; refractive index; crude oil – seawater emulsion; oil spills

1. INTRODUCTION

Oil spills have been confirmed to have harmful influence on the marine environment. Many research groups reported results of their research on the subject [1]. Oil pollutants turn up in various forms in the marine environment: as aerosols and free molecules in the atmosphere, as layers and emulsions on the water surface, suspensions and dissolved phases in the water column and on the bottom sediments. Among their many impacts, oil pollutants modify electric field of the light above and below the water surface. These modifications are manifested by reflectance of the light passing through an oiled water surface, by changes in light absorption in the seawater column due to the formation of an emulsion, and by the scattering of light by particles of such an emulsion. These processes are determined by interaction of the light with oil-water system.

Dielectric function is the fundamental physical parameter describing the light-matter interaction. Optical characteristics of the oil – seawater system depend on the size distribution of oil droplets, their concentration, and distribution in over the water column. In the case of pollution with fresh crude, the oil undergoes weathering, which alters its properties. In order to get clear understanding of the influence of the oil onto the marine system it is important to study the basic physical processes occurring at the oil-seawater interfaces and emulsions.

Optical techniques have been widely employed in environmental monitoring because they can rapidly scan a wide region. While thick patches of oil can be easily detected and recovered there are problems to be solved with very thin (about micron size) oil layers which are beyond the capabilities of advanced skimming recovery systems and are less investigated. Study of optical properties of thin oil layers on the surface of the seawater is of great interest then.

It has been reported in several studies on oil spillage that day-time-contrast-based detecting of oil spots depends on the thickness of the oil film [2]. Differential heating by sunlight causes oil to rise to a higher temperature than the surrounding water because of its

higher absorption of solar radiation and lower specific heat, giving rise to the commonly observed contrast of native and crude oil covered sea surfaces in day time remote sensing of oil spills. Reversal process occurs when the oil film is thin (micron size) [3]. However, there has been proposed no comprehensive physical model describing this behavior. The film thickness dependent optical properties is of great importance for correct detection of the thin oil layer covered area, as well as estimation of the oil film thickness.

In this work we study of optical parameters and dielectric function of the Azeri crude oil – caspian seawater system depending on oil droplet size and concentration in the oil-water emulsion, oil layer thickness, and oil weathering by Spectroscopic Ellipsometry

2. SAMPLES AND EXPERIMENTAL DETAILS

The samples of seawater is gathered from different coasts of Caspian sea (Fig. 1.). There are samples from Nabran coast-in north, from Absheron peninsula-in center and from Lankaran coast-in South and as crude oils are taken “Neft dashlari”, “Balakhani”. The all samples are measured by spectroscopic ellipsometry from 200 to 1700 nm spectral range in 50, 55, 60, 65, 70 incident angle in open surface configuration.

Spectroscopic ellipsometry is an extremely powerful tool for study of optical parameters and dielectric function of the condensed matter, providing direct information on material-specific constants. It provides extremely precise and accurate determination of optical parameters as opposing to standard transmission/absorption techniques since it probes the polarization state of the light and not the intensity. It is of great importance for analysis in a wide spectral range providing unambiguous separation of contributions from each part of a complex system. Thus, for example, the crude oil contribution to the optical parameters in the visible range can be determined in the oil-seawater system, that is indistinguishable by standard intensity-based techniques [4]. Ellipsometry is often used to determine layer thickness and optical parameters in multilayer structures, atomic interdiffusion in buried

layers, band gap energies in semiconductor structures [5], etc.

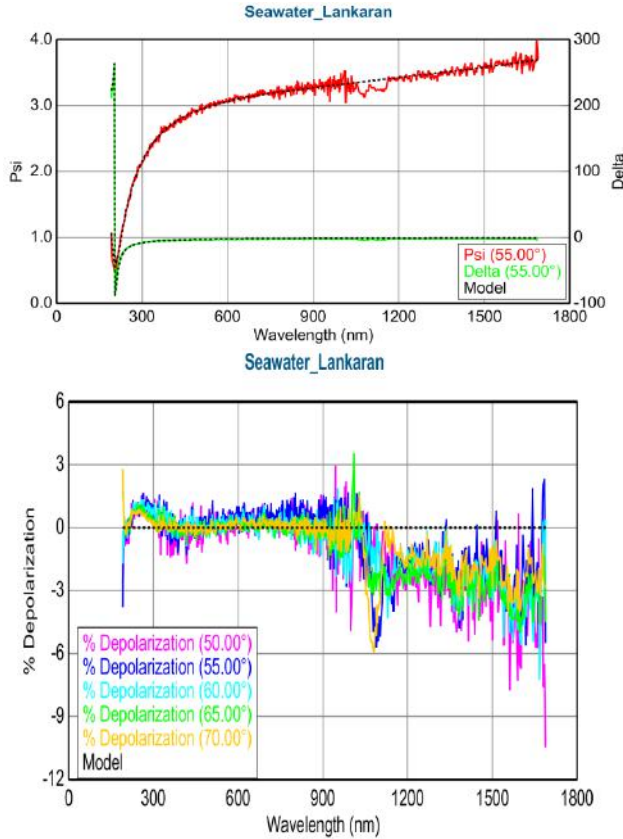


Fig.1. The Ellipsometric parameters of Lankaran seawater and depolarization spectrum of incidence light.

Ellipsometry measures changes in polarization state of the light reflected from the surface of the object under study. These changes are described by two variables ψ and Δ which represent the amplitude ratio and phase shift of the light electric field components in parallel (p) and perpendicular (s) planes with respect to the plane of light incidence. These quantities are given by the ratio of Fresnel coefficients of p - and s -polarizations, r_p and r_s :

$$\rho = \frac{r_p}{r_s} = \tan\psi \cdot \exp(i\Delta)$$

3. RESULTS AND DISCUSSION

The obtained ellipsometric parameters and the depolarization of incident light for seawater shown in Fig.1. As shown from fig. 1. the depolarization of light is near the zero and it's mean that there is not exist backside reflections or any scattering sources and the detected light is reflecting from air-water boundary.

For determination optical constants of samples from experimental parameters optical model is created..The experimental and ellipsometric parameters calculated from optical model is fitted. As shown from fig.1. the calculated and experimental parameters are overlap with each other. The MSE (Mean Square Error) is varies between 1.3-1.5The optical parameters of different seawater samples shown in Fig.2.

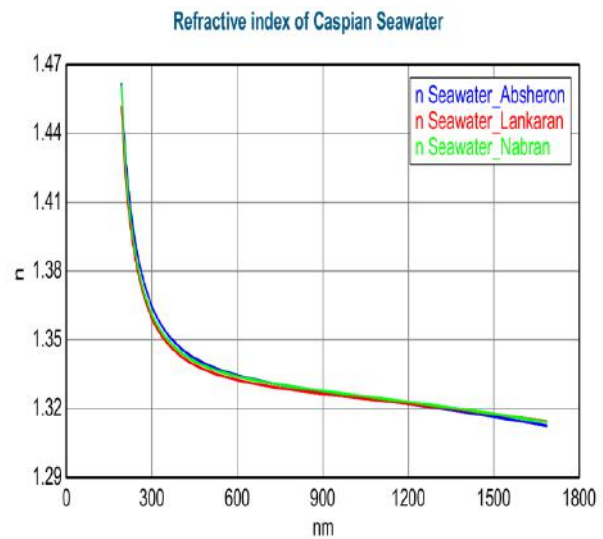


Fig.2. The optical constants of Caspian seawater

Table.1. The elemental analysis of crude oil samples determined by X-Ray Fluorescent (XRF) analysis

Neftin növü	Hidrokarbonlar								
Neft daşları	99.8844 %								
Balaxanı	99.7046 %								
	S								
Neft daşları	0.1194%								
Balaxanı	0.2750 %								
	Mg	Al	Cl	Ca	Ti	V	Mn	Fe	Co
Neft daşları	2 ppm	0 ppm	0 ppm	3 ppm	0.1 ppm	0 ppm	0.3 ppm	6.0 ppm	0.2 ppm
Balaxanı	5 ppm	1 ppm	8 ppm	18 ppm	0.4 ppm	0.7 ppm	0.8 ppm	163.3 ppm	0.6 ppm
	Ni	Zn	Zr	Sn	Ba	Pb	Bi	As	Br
Neft daşları	3.3 ppm	0 ppm	0.7 ppm	1 ppm	0 ppm	0 ppm	0 ppm	0 ppm	0 ppm
Balaxanı	10.1 ppm	0.1 ppm	0.9 ppm	2 ppm	1.4 ppm	0 ppm	0 ppm	0 ppm	0 ppm
	Density								
Neft daşları	0.87								
Balaxanı	0.87								

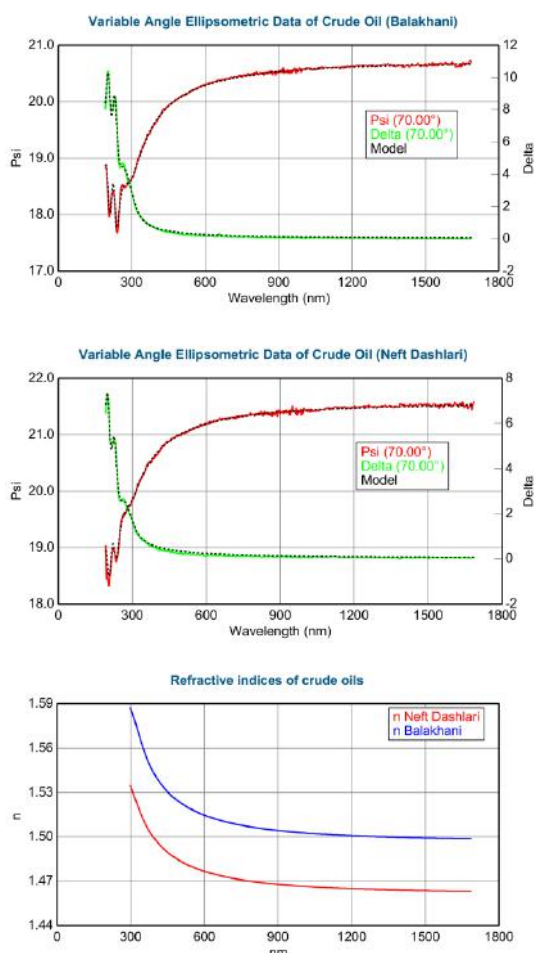


Fig.3. The Ellipsometric parameters and optical constants for crude oil samples

It is evident from the fig. 2. that in 300-600 nm spectral range the refractive index of seawater samples differs from each other very little.

The elemental analysis of crude oil samples determined by X-Ray Fluorescent (XRF) analysis. It is shown under table.1. the oil samples are differs from each other with concentration of hydrocarbons and sulfur.

The crude oil samples are measured by spectroscopic ellipsometry from 200 to 1700 nm spectral range in 50, 55, 60, 65, 70 incident angle in open surface configuration. The ellipsometric parameters and optical constants for crude oil samples are shown in Fig.3. Optical constants of crude oil samples parameterized by using four Gaussian oscillators and calculated ellipsometric parameters fitted with experimental parameters. The MSE (Mean Square Error) value is varies near the 1. It is disclosed that the optical constants of crude oil samples differ significantly as shown from fig.3. This difference show that the interaction between the light electric field and crude oil depending type of oil.

4. CONCLUSIONS

The optical parameters and dielectric function of seawater collected from various coasts of Caspian sea and different type of crude oil samples are determined by Spectroscopic Ellipsometry in the first time.

ACKNOWLEDGMENTS: This work was supported by The State Oil Company of the Azerbaijan Republic (SOCAR)– Grants № SOCAREF2012

- [1]. GESAMP (IMO/FAO/UNESCO/WMO/WHO/IAEA/UN/UNEP Joint Group of Experts on the Scientific Aspects of Marine Pollution), Impact of oil and related chemicals on the marine environment, IMO Rep. Stud. No 50, London, (1993) 180 pp.
- [2]. N. Hurford, The remote sensing of oil slicks, Lodge AE, ed., Wiley, Chichester, UK, (1989)
- [3]. W.-C. Shih, B. Andrews, Modeling of thickness dependent infrared radiance contrast of native and crude oil covered water surfaces, OPTICS EXPRESS **16** 10535-10542 (2008)
- [4]. M. Fingas ed., Oil Spill Science and Technology, Elsevier (2011)
- [5]. H. Fujiwara, Spectroscopic Ellipsometry: Principles and Applications, West Sussex John Wiley & Sons Ltd (2007)

PHYSICAL PROPERTIES OF $(\text{InSb})_{1-x}(\text{HgTe})_x$ SOLID SOLUTIONS

A.R.HAJIYEV, T.B.TAGIYEV

*G.M.Abdullayev Institute of Physics, National Academy of Sciences, Azerbaijan,
H.Javid ave. 33, Baku, Az-1143, Azerbaijan Republic.*

*The Institute of Radiation Problems, National Academy of Sciences, Azerbaijan,
B.Vahabzadeh str. 9, Baku, Az-1143, Azerbaijan Republic.*

t.b.tagiyev@rambler.ru, fax: 539 83 18

In the range of 77-300K the electrical and optical properties of highly-degenerated solid solution $n - (\text{InSb})_{1-x}(\text{HgTe})_x$ up to 5% HgTe have been studied. In particular the optical reflection of electroconductivity, and thermoelectric power have been measured. Effective masses of electron density have been calculated at the Fermi level in two ways: on a minimum in the spectra of optical reflection and from the temperature dependence of thermoelectric power. The results are analyzed on the base of the mechanism for the ionized impurity scattering ($r = 3/2$). It is shown that, both heavy and light holes take part at Γ in optical transitions.

Keywords: transmission, mobility, absorption, relaxation, ionization, effective mass, dielectric constant

PACs: 72.20.My, 71.85.Ce

INTRODUCTION

There have been investigated electric and optical properties of highly degenerate solid solution $n - (\text{InSb})_{1-x}(\text{HgTe})_x$ up to 5% HdTe within 77-300K. Specifically optical reflection, electroconductivity and thermal paver have been measured. There have been estimated effective masses of electron state density at Fermi level by 2 methods: by minimum in spectra of optical reflection and Frau Temperature dependence of thermal power. The results are analyzed on the base of scattering mechanism by ionized impurities ($r=3/2$). It is shown that in optical hansitions at point G as heavy holes as light ones are taken place. First investigations of physico- chemical properties of guise-binary compounds $(\text{InSb})_{1-x}(\text{HgTe})_x$ have been carried out in paper [1] and of some interest is the structure relationship of their specific compounds. It is established that InSb- based solid solutions are formed up to 10mol.% HdTe. The components of the following properties: InSb is the semiconductor crystallizing in cubic crystal system with space group $F4-3m(T_d^2)$ ZnS – typed with lattice parameters $a=6,479[1]$, band gap $E_g = 0,18\text{eV}$. HdTe compound is melted congruently at $T=670^\circ\text{C}$ and crystallizes in cubic crystal system is hardly investigated in literature. In 1984 tlure have been obtained and analyzed $(\text{InSb})_{1-x}(\text{HgTe})_x$ solid solutions up to 20mol.% HdTe in the only paper [1] by Berger and Lyun. In single – phase polycrystalline samples of In Sb-HdTe system there has been studied the diagram of states, differential thermal and X-ray phase analyses up to 20% HdTe have been made out. Within residual beams (7-12 mkm) the optical absorption has been studied. For all obtained samples electric, optical and galvanomagnetic properties have been examined. The materials have been recommended for making epitaxial detectors of infrared radiation (7-12mkm).

EXPERIMENTAL TECHNIQUE

In this paper there have been investigated optical and thermoelectric parameters of InSb-HdTe system samples for the purpose of their using. Samples of $(\text{InSb})_{1-x}(\text{HgTe})_x$ solid solutions up to 5% HdTe are obtained by horizontal zone melting. Samples cut out of ingots to size $0,8 \times 0,5 \times 0,4\text{cm}^3$ undergo mechanical polishing and are processed by polishing etchant.

All samples are of n - type. Concentration of free electrons and their mobility as the functions of composition and temperature have been calculated by Frau Conductivity and Hall coefficient measurements. Measurements of reflection and absorption spectra are conducted on IKS- type spectrometer at temperature over the wavelength range 2,5mkm to 25mkm.

RESULT DISCUSSION

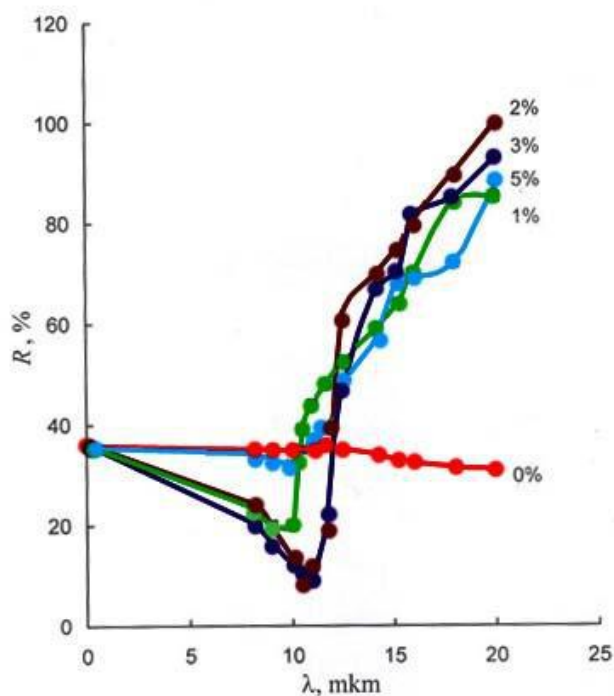


Fig.1. Reflection coefficient of wavelength of $(\text{InSb})_{1-x}(\text{HgTe})_x$ samples.

In fig.1 there has been presented dependence of reflection coefficient R on wavelength. All curves for the reflection coefficient have a pronounced characteristic of minimum appropriate to resonance absorption by free charge carries. By minimum the position of minima λ_{\min} for dissimilar x the effective mass of electrons at Fermi level has been determined [2]. According to [3] in case of highly doped semi-conductive materials when the charge

carrier mobility is high, the approximation $\omega^2 \tau^2 \gg 1$ and $n \gg k^2$ is performed (InSb, HgTe, PbTe). Reflections have a minimum at $R_{\min} = m^*/n\mu$. The less effective mass of carries and the more their concentration and mobility are the less reflection at the frequency ω_{\min} is. As the concentration and mobility of carriers can be determinants rather positively, from the position of reflection the minimum m^* can be estimated by the formula:

$$m^* = \frac{e^2 n}{\epsilon_{\infty} \omega_{\min}} \cdot \frac{1}{(\epsilon_{\infty} - 1)} \quad (1)$$

where ϵ_{∞} is estimated for each composition by method [3] on the assumption of time dependence of electron relaxation in conduction band on energy. Charge carrier concentration is determined from Hall measurements. All samples are highly degenerate with the charge carrier concentration $3,47 \cdot 10^{18} \div 1,1 \cdot 10^{19} \text{ cm}^{-3}$.

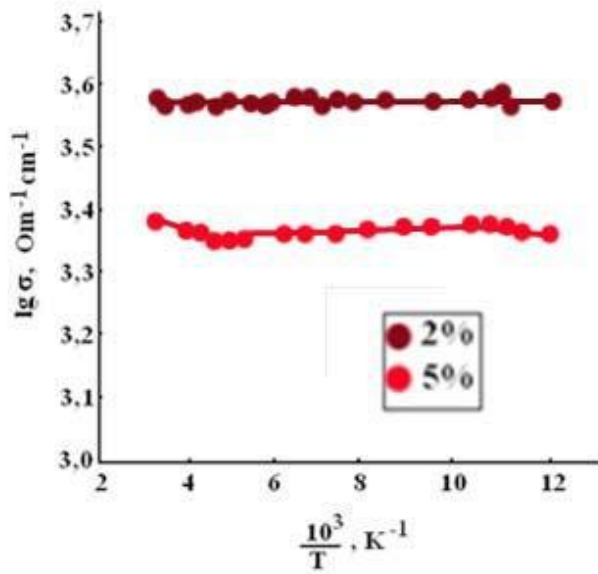


Fig.2. Temperature dependence of electroconductivity

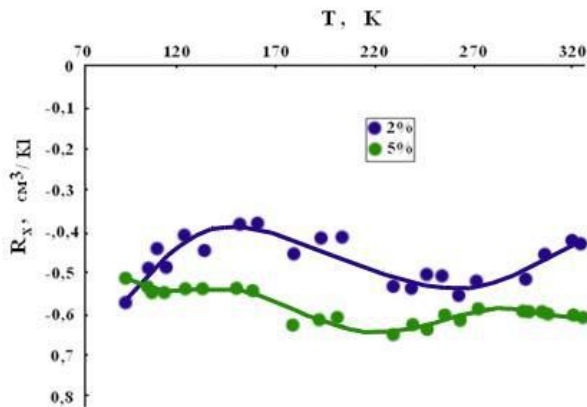


Fig.3. Temperature dependence of Hall constant R_x

Temperature dependences $\alpha(T)$ have a metal behavior (fig.2). Hall constant R_x has a complex dependence (fig. 3), as for all samples the maximum related to surface inverse layer is revealed within $T=120 \div 150 \text{ K}$ [4]. Effective mass m of state density at Fermi level is also defined by measuring thermal paver $\alpha(T)$ from the temperature (fig.4). Experiments on a management from the temperature show that m data

derived from λ_{\min} and $\alpha(T)$ are in agreement in case the charge carrier scattering takes place by ionized impurities ($r=3/2$). According to [3]

$$\alpha = \frac{2\pi^3 k_0 T m^*}{3^3 e h^2 n^3} \left(r + \frac{3}{2} \right) \quad (2)$$

where r is the parameter of scattering. The relationship between m^* and n according to Kane law of dispersion can be given in the form [4]

$$\frac{m^*}{m_c \left(1 - \frac{m^*}{m_c} \right)} = 32,5 \cdot 10^{-32} \frac{E_g}{p^4} + 8,25 \cdot 10^{-30} \frac{n^{\frac{2}{3}}}{p^2} \quad (3)$$

where the matrix element p for InSb and other compounds $A^3 B^6$ is equal to $8,7 \cdot 10^{-8} \text{ eV} \cdot \text{cm}$. In fig.5 there have been presented experimental points spread well on the direct line. Experimental data of m^* on $\alpha(T)$ and plasma reflection (λ_{\min}) are in close agreement.

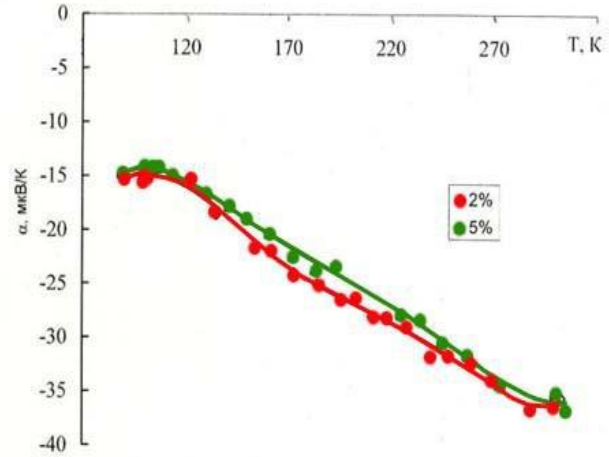


Fig.4. Temperature dependence of $(\text{InSb})_{1-x}(\text{HgTe})_x$ thermal power

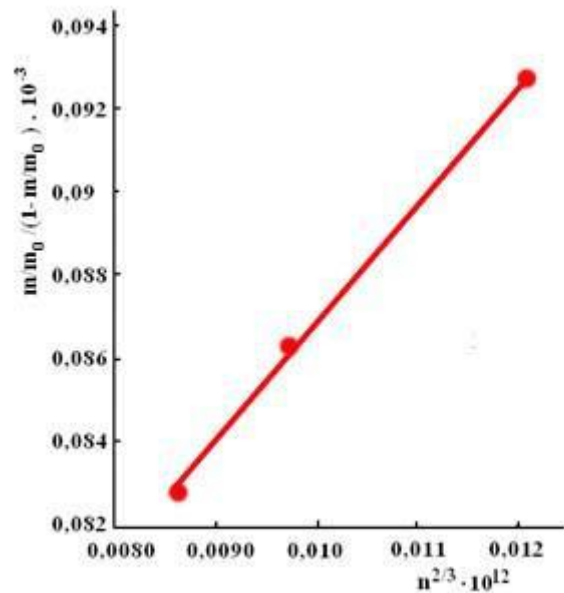


Fig.5. Dependence of electron effective mass at Fermi level on their concentration

X%	m^*/m_0	$n, \text{ cm}^{-3}$	$\mu, \text{ cm}^2/\text{V}\cdot\text{sec}$	$E_g, \text{ eV}$	T, K
0	0,013	$2,97 \cdot 10^{15}$	$4,5 \cdot 10^4$	0,18	300
1	0,083	$3,47 \cdot 10^{18}$	$6 \cdot 10^3$	0,081	300
2	0,086	$6,0 \cdot 10^{18}$	$2,13 \cdot 10^3$	0,090	300
3	0,093	$9,1 \cdot 10^{18}$	$1,5 \cdot 10^3$	0,095	300
5	0,077	$1,1 \cdot 10^{19}$	$1,3 \cdot 10^3$	0,10	300

Magnitude of band gap E_g obtained of the intercept on Y- axis is equal to 0,09eV that is close to experimental data on measuring optical transmission of samples (0,081eV for 1%, 0,10eV for 2%. fig.6).

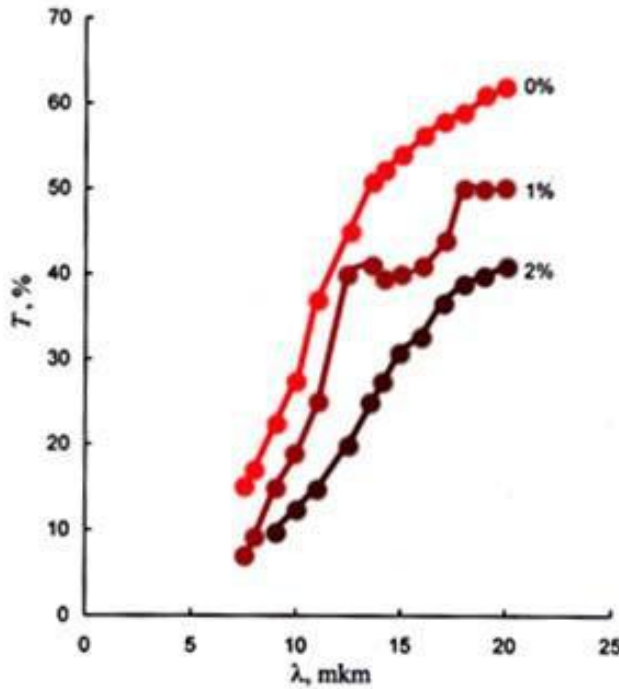


Fig.6. Transmission spectra of $(\text{InSb})_{1-x}(\text{HgTe})_x$ samples 1. - 1%, 2 - 2% HdTe, 3 - 0%InSb.

For one thing, analysis of optical measurements confesses the instability of the theory [5] for all samples, for another, the existence of crossover inter-band transitions and absorption in free charge carriers. In reflection spectrum R of $(\text{InSb})_{1-x}(\text{HgTe})_x$ samples there has been observed a shift of minima (λ_{\min}) with the rise of x to the long-wavelength region (fig.1). The change in the structure of conduction band appears not be taken place but the noticeable change in the valence band is taken place. $E_g = 0,18\text{eV}$ in pure InSb but $E_g = 0,10\text{eV}$ in 1% $(\text{InSb})_{1-x}(\text{HgTe})_x$ solid solutions indicate that such sharp decrease with the rise of x is possible because band of

HdTe. By forming $(\text{InSb})_{1-x}(\text{HgTe})_x$ solid solution due to the interaction of 3 bands at point G (G_8 , G_8 and G_6) the distinct distortion of their curvature, mixing of states and distortion of previous band of heavy holes G_8 downwards have been occurred; as a result at point G there have been mixed two bands: the previous conduction bands G_6 and G_8 . For practical purposes with the rise of x in solid solutions the band of heavy holes closes abruptly in on the conduction band. Thus small dependence m^* on the concentration can be explained by the band convergence and main part of heavy holes in transitions G_6 and G_8 . The band of light holes with highly deformed surface shifts downwards. As it is seen from table the effective masses of charge carriers increase appreciably for samples $(\text{InSb})_{1-x}(\text{HgTe})_x$. It can be related to the fact that with the rise of x the portion of heavy holes increases in the formation of reflection spectrum. At 5% HdTe concentration of free charge carriers $n=1,1 \cdot 10^{19}\text{cm}^{-3}$, effective mass $m^*/m_0 = 0,077$ and the minimum in the spectrum shifts to the short-wavelength region of spectrum ($\lambda_{\min} = 10\text{mkm}$). It can be related to the fact that although the band of heavy holes, their part in the reflection spectrum formation is possible, i.e. to account for physical properties one can use a two band model. The big concentration of charge carriers and presence of heterogeneity in samples brings about the formation of state density tails into the forbidden band. The fact that samples are highly degenerate and R do not depend practically on the temperature, this suggests that the position of Fermi level is in conduction band and attributes optical and electrical properties of samples. The formation of state density tails also points to the heterogeneities of obtained crystals. This reveals the minima in reflection spectra. With the rise of HgTe content in InSb matrix the minima of reflection spectrum become sloping. Heterogeneity in crystals reduces thermal band gap but does not affect on the edges of optical and recombination spectra as in every point the local band gap does not change. Unlike other thermoelectric materials in InSb-HgTe due to small magnitude of dielectric constant ($\epsilon=14$) the formation of state density tails has a strong impact on electric and optical properties of samples. Analysis of experimental data shows that easily producible best samples have been obtained at 1-3% HdTe in InSb. Thus in $(\text{InSb})_{1-x}(\text{HgTe})_x$ solid solutions the band structure compares substantially with InSb structure. Pure samples have a structure of transitions with the part of heavy hole band but in solid solutions they have a structure with the part of light hole band.

[1]. L.I.Berger, S.W.Lin, Quaternary Narrow-Band Semiconductors $(\text{InSb})_x(\text{HgTe})_{1-x}$ for Far-Infrared Detectors. San Diego State Univ. Foundation CA, 31 Aug. 1984.
 [2]. Uhana Yu. I. Optical properties of semiconductors. M.Nuka, 1977.
 [3]. A.A.Kukharsky, V.K.Subashiyev. Studies on determination of effective mass and relaxation

time of carriers in semiconductors light reflection spectra. FTP, 1970, v.4, №2, pp.287-293.
 [4]. M.K.Sharov, Electrical properties of $\text{PbTe}_{1-x}\text{I}_x$ solid solutions investigated reflection method. Perspective materials. 2008, v.2, pp.39-42.
 [5]. E.O.Kane, Band Structure of indium antimonite. J. Phys. and Chem. Solids, 1957, 1, №3, pp.249-261.

CHARACTERIZATION OF ZnO THIN FILMS PREPARED BY MAGNETRON SPUTTERING METHOD

R.H. HAJIMAMMADOV¹, Y.N. ALIYEVA¹, E.A. BAGIYEV¹, N.A. GASIMOV¹,
N.SATO², M.NAKAJIMA², A.H. BAYRAMOV¹

¹ *G.M.Abdullayev Institute of Physics,
Azerbaijan National Academy of Sciences*

² *Chiba Institute of Technology, Japan*

ZnO thin films of about 100 nm thickness were deposited by magnetron sputtering method on glass substrates. The films were characterized by X-Ray Diffraction (XRD), Spectroscopic Ellipsometry (SE), Atomic Force Microscopy (AFM) and Kelvin Probe Force Microscopy (KPFM) methods. Surface morphology and roughness, band gap energy, average particle size and contact potential difference between sample surface and platinum coated cantilever tip were determined.

Keywords: ZnO thin films, magnetron sputtering, spectroscopic ellipsometry, Kelvin probe force microscopy

PACs: 81.15.cd; 68.55.-a; 73.25.-I; 78.20.-e

1. INTRODUCTION

ZnO is one of the most interesting semiconducting materials with band gap energy of 3.3 eV and considered as a potential material for chemical sensor, piezoelectric transducer, electroluminescent device, ultraviolet laser diode, solar cell and other applications [1]. Thin films of ZnO have been studied as the active channel material in thin film transistor development because of n-type semiconductor characteristics and excellent thermal stability and can be well oriented crystalline on various substrates. Normally ZnO films crystallize in hexagonal phase, but non-stable cubic phase also exists. Due to its transparency, optimal electrical and optical properties ZnO films, doped with various impurities can be widely used as a contact electrode in thin film solar cells.

Numerous methods have already been used to deposit ZnO thin films. Magnetron sputtering method has several advantages as compared with the other physical and chemical deposition methods: a low-temperature ion-assisted deposition of metals, semiconductors, insulators, change of deposition rate in wide range (0.1 to 10 nm/s); control further parameters which are important for thin film growth (substrate temperature, plasma density, composition of working gas, ion bombardment of film during deposition) [2]. In this work the preliminary results on the characterization of ZnO films prepared by magnetron sputtering method are given.

2. EXPERIMENTAL

ZnO thin films were deposited on 0.5 mm thick, 2x2 cm size Corning 7059 glass substrates by magnetron sputtering method. Prior to the deposition all of the substrates were chemically cleaned by acid. After chemical cleaning the substrates were rinsed in deionized water in ultrasonic bath and then dried under pure nitrogen flow. The deposition was performed at room temperature of substrate. Deposition rate was 1 Å/sec. All of the measurements were carried out on the "as-prepared" films which were not subjected to thermal annealing, etching and other treatments.

X-ray diffraction (XRD) analyses of the films were carried out in a BRUKER D8 ADVANCE diffractometer. Topography analysis of ZnO thin films was performed with Smart SPM (Tokyo Instruments), ellipsometric data was measured using J.A. Woolam ESM 300 ellipsometer. KPFM measurements were performed in Seiko S300 AFM machine. For KPFM measurements platinum coated cantilevers were used.

3. RESULTS AND DISCUSSIONS

Analysis of XRD patterns shows amorphous structure of as-prepared ZnO thin films. Linear regression analysis of ellipsometric data has given the dielectric function shown in Figure 1. It is seen that dielectric function corresponds to crystalline rather than amorphous case. At the same time X-ray examination has not disclosed crystallinity of ZnO because of deficiency of standard X-ray diffraction method in case of thin films with very small grain sizes. On the other hand, spectroscopic ellipsometry accesses dielectric function of the materials as thin as down to 3-4 Å. This accounts for why X-ray does not show crystalline structure of thin film while SE does. Atomic Force Microscopy images confirm the SE results, apparently showing the average grain size of about 45 nm (Figure 2).

Imaginary part of dielectric function is nothing else but interband electronic density of states. Therefore, a good estimation for energy band gap of the obtained ZnO thin films will be 3.3 eV as shown in Figure 1 by arrow. Thickness of the samples was found from SE measurements to be about 100 nm with surface roughness about 3.5 nm.

In order to determine contact potential difference between ZnO film surface and cantilever tip, Kelvin Probe Force Microscopy technique was used. Figure 3 shows AFM and KPFM images of as-deposited ZnO films. It's found from KPFM results that, potential images of ZnO films are uniform, i.e. contact potential difference between sample surface and platinum coated cantilever tip are not so different in different areas of the surface [3] and is -30 mV (for hollows) and +25 mV (for projections).

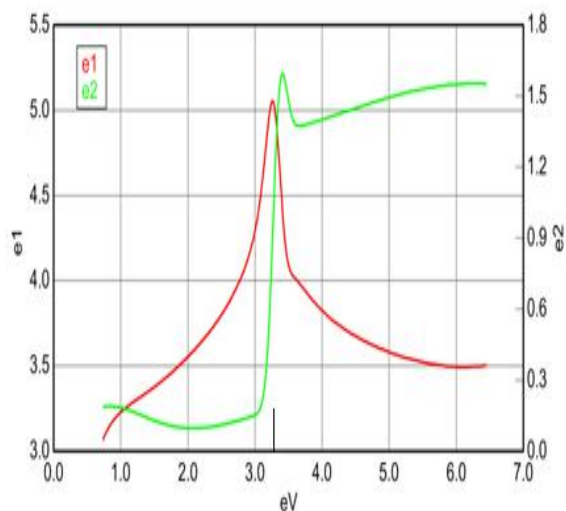


Fig. 1. Real and imaginary parts of dielectric constant for ZnO thin film.

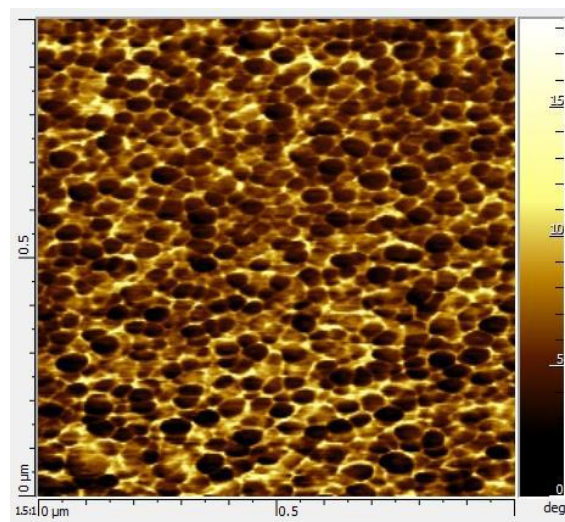
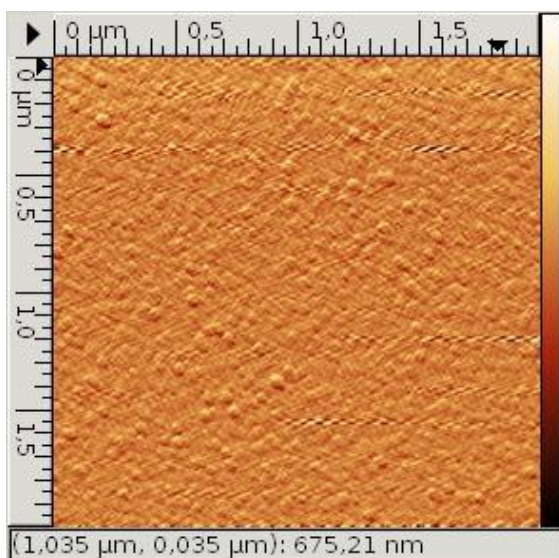
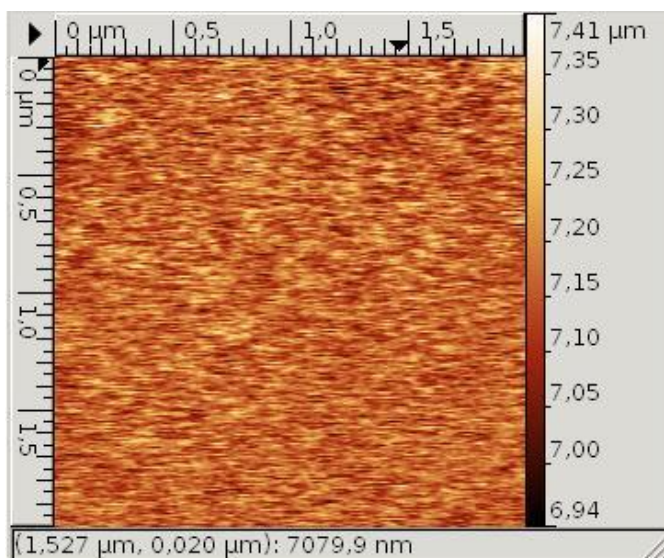


Fig.2 AFM image of ZnO thin film



a)



b)

Fig. 3. AFM (a) and KPFM (b) images of ZnO thin film.

4. CONCLUSION.

ZnO thin films deposited by magnetron sputtering on cold glass substrates has an average grain size of about 45 nm and surface roughness of about 3.5 nm. Energy band gap of ZnO thin films is 3.3 eV, contact potential difference between sample surface and platinum coated cantilever tip is -30mV (for hollows) and +25mV (for projections).

ACKNOWLEDGMENT This work was supported by the Science Development Foundation under President of Azerbaijan Republic under Grant No EIF-2012-2(6)-39/02/1

We would also like to specifically thank Prof.K.Wakita and Prof.N.Mamedov for their fruitful discussions.

[1]. Klaus Ellmer, Andreas Klein, Bernd Rech. Transparent Conductive Zinc Oxide, Basics and applications in Thin Film Solar Cells. Springer 2008

[2]. Sona Flickyngerova, Vladimir Tvarozek, Pavol Gasparik. Zinc Oxide- A Unique Material For Advanced Photovoltaic Solar Cells. J.of Electrical Engineering vol. 61, No 5, 2010, 291-295

- [3]. *Shigetaka Katori, Nobuo Satoh, Masayuki Yahiro, Kei Kobayashi, Hirofumi Yamada, Kazumi Matsushige and Shizuo Fujita.* Surface Potential Measurement of Tris(8-hydroxyquinolino)aluminum and Bis[N-(1-naphthyl)-N-phenyl] benzidine Thin Films Fabricated on Indium–Tin Oxide by Kelvin Probe Force Microscopy. *Jpn. J. Appl. Phys.* 50 (2011) 071601.

X-ray EMISSION OF PULSARS AND PARTICLE ACCELERATION

S.O. TAGIEVA, H.I. NOVBUZOVA

*Academy of Science, Physics Institute,
Baku 370143, Azerbaijan Republic*

The available data on isolated X-ray pulsars, their wind nebulae, and the supernova remnants which are connected to some of these sources are analyzed. It is shown that electric fields of neutron stars tear off charged particles from the surface of neutron star and trigger the acceleration of particles. The charged particles are accelerated mainly in the field of magneto-dipole radiation wave. Power and energy spectra of the charged particles depend on the strength of the magneto-dipole radiation. Therefore, the X-ray radiation is strongly dependent on the rate of rotational energy loss and weakly dependent on the electric field intensity. Coulomb interaction between the charged particles is the main factor for the energy loss and the X-ray spectra of the charged particles.

Key words: Pulsar, PWN, X-ray

INTRODUCTION

The number of isolated X-ray pulsars and the radio pulsars which have been detected in X-ray with characteristic age (τ) up to 10^6 yr located at distances less than 7 kpc from the Sun together with 2 pulsars in Magellanic Clouds is 35 (see Table 1). The so called magnetars (anomalous X-ray pulsars and soft gamma repeaters) and dim radio quiet neutron stars like the isolated young X-ray pulsar 1E 1207.4-5209 are not included in this list as our main aim in this article is to examine the non-thermal synchrotron (power-law) emission of isolated young pulsars with relatively well known ages based on the existing observational data. Also, our list includes only the pulsars which are certainly not accreting sources. In order to exclude thermal emission of pulsars, we will particularly focus our attention on the hard X-ray emission of the pulsars in the 2-10 keV band. On the other hand, we have included the old recycled millisecond pulsars in the list and examined them in detail throughout the text to make comparisons between them and the isolated young pulsars.

Most of the pulsars displayed in Table 1 have been observed in 0.1-2.4 keV band^{1,2} and in 2-10 keV band³ and all the available data have been collected, revised and put together as represented in the table. Among the 35 pulsars, 2 of them are X-ray pulsars from which radio emission has not been observed and they are connected to SNRs (pulsar J1846-0258 to SNR G29.7-0.3 and pulsar J1811-1925 to SNR G11.2-0.3). Radio pulsar J1646-4346 ($d=4.51$ kpc) which is connected to C-type SNR G341.2+0.9 but not observed in X-ray is also included in the list. Other than these sources, we have also included 14 radio pulsars with $\dot{E} > 4 \times 10^{35}$ erg/s, $\dot{P} > 10^{-15}$ s/s and $d \leq 7$ kpc in Table 1. Also, 6 isolated millisecond pulsars from which X-ray radiation have been observed are displayed in Table 1. Our main aims in this work are to analyze the conditions which are necessary for the acceleration of relativistic particles, the X-ray radiation produced in the magnetospheres of pulsars, and the presence or absence of PWNe around these objects.

ANALIZED OBSERVATIONAL DATA

From the observations of the radio and X-ray radiation of neutron stars with power-law spectra (excluding the cooling radiation of neutron stars), there is direct evidence for continuing particle acceleration. Such X-ray radiation have been observed, for example, from pulsars J1856+0113 and J1801-2451 which have PWN and have values of $\dot{E} \sim (4-5) \times 10^{35}$ erg/s and 2.5×10^{36} erg/s,

respectively. On the other hand, old millisecond pulsars J1939+2134 and J1824-2452 with $\dot{E} \sim (1-2) \times 10^{36}$ erg/s also have similar X-ray radiation as the previous pulsars 2, but with smaller luminosity in the 2-10 keV band. As seen in Table 1, these pulsars, beginning from J1856+0113, have values of X-ray radiation 10^{33} , 1.5×10^{33} , 5×10^{32} , and 3.6×10^{33} erg/s, respectively, in the 2-10 keV band 2,3. We have estimated the ratio $(\dot{P} \dot{P})^{1/2} \sim 1/2$ from the dependence of \dot{E} for pulsars J1856+0113, J1801-2451, J1939+2134, and J1824-2452 and we have found the values 9×10^{-7} , 10^{-6} , 7×10^{-9} , and $3 \times 10^{-8} \text{ s}^{-1/2}$, respectively.

In Figure 1, dependence of the X-ray luminosity in 2-10 keV band ($L_{2-10\text{keV}}$) on the value of \dot{E} for the isolated pulsars with comparably hard spectra which are located up to 6 kpc from the Sun together with 2 pulsars in the Magellanic Clouds (see Table 1) is represented. As seen in Figure 1, pulsars J1856+0113 and J1801-2451 have \dot{E} values similar to isolated old millisecond pulsars J1824-2452 and J1939+2134, and their \dot{E} values are more than 300 times greater than their X-ray luminosity in 2-10 keV band. Therefore, the luminosity of the power-law X-ray radiation (which includes the radiation of the relativistic particles in the Coulomb and magnetic fields) mainly depends on the value of \dot{E} .

Since we are interested in the acceleration of particles, we have chosen the pulsars for which $L_{2-10\text{keV}}/L_{0.1-2.4\text{keV}} > 1$, so that, we avoid the errors connected to the interstellar absorption and the radiation related with the cooling of neutron stars. As seen from Table 1, these conditions are not satisfied for the last 4 pulsars with $\log \tau = 9.58-9.86$ which are also displayed in Figure 1. But they are very close to the Sun and very old, therefore they do not create any difficulties. All the young pulsars shown in Figure 1 have not only hard spectra but also have PWNe. As seen from the equations of the best fit

$$L_{2-10\text{keV}} = 1.42 \times 10^8 \dot{E}^{0.63} \quad (1)$$

for the pulsars with $\dot{E} < 10^{35}$ erg/s and $L_{2-10\text{keV}} < 10^{31}$ erg/s and

$$L_{2-10\text{keV}} = 1.86 \times 10^{-37} \dot{E}^{1.92} \quad (2)$$

for the other pulsars with higher $L_{2-10\text{keV}}$ and/or higher \dot{E} , there exist clear relations between \dot{E} and $L_{2-10\text{keV}}$ for which the radiation is related with the accelerated particles.

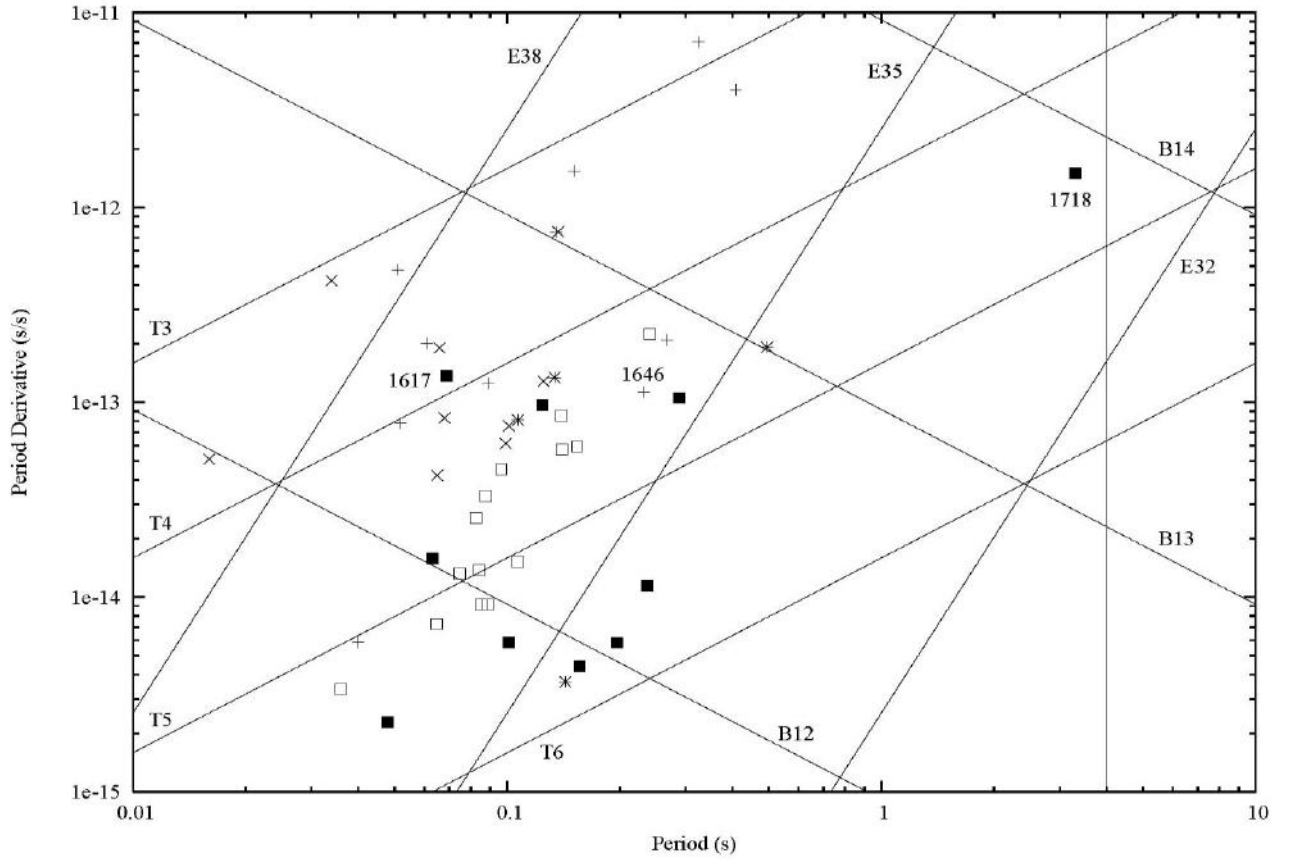


Fig.1

As seen from Figure 1 and expressions (1) and (2), as \dot{E} decreases the X-ray luminosity of pulsars also decreases. So, in order to have the probability to observe X-ray radiation from a pulsar to be high for a fixed value of E_{el} , the rotation period of the pulsar must be short. On the other hand, as seen from Figure 1 and Table 1, the L_x values of the young pulsars which are connected to SNRs are ~ 5 orders of magnitude larger than the L_x values of old ms pulsars and this is also seen from expressions (1) and (2). This must be the result of small number of relativistic particles in the magnetospheres of old ms pulsars

The X-ray luminosity of pulsars together with their PWNe are represented in Table 1. Often, such X-ray luminosity values include both the X-ray radiation coming from the pulsar and the PWN together, because it is difficult to separate the emission of the pulsar from the emission of the PWN. Therefore, the radiation of isolated ms pulsars must be smaller compared to isolated young pulsars for equal values of \dot{E} . This must be true also because of young pulsars having large values of electric field intensity and possibly having smaller masses in some cases. Therefore, it is strange that ms pulsar J1824-2452 has larger luminosity compared to young pulsar J1801-2451 (see Figure 1). On the other hand, their radiation is very hard. Actually, the uncertainties in the luminosity values of these ms pulsars may be large.

Young pulsars have values of electric field intensity about 50 times larger than the values of old ms pulsars, they are hotter and they may also have smaller masses. These facts create conditions for tearing off charged particles more easily from neutron stars. On the other

hand, the magnetic field values of young pulsars are more than 3 orders of magnitude larger (the high magnetic field does not let the particles to escape from the magnetosphere without considerable radiative energy loss). These and the possible existence of large number of charged particles in the magnetospheres and the surroundings of young pulsars must create the best conditions for magneto-braking and Coulomb radiation. Among young pulsars, the small values of X-ray radiation of J0538+2817 and Geminga in 2-10 keV band seem to contradict this natural discussion.

PULSARS IN SUPERNOVA REMNANTS AND PULSAR WIND NEBULAE

Let us now examine the presence or absence of PWN around pulsars and the X-ray radiation. All the pulsars with $\tau < 10^7$ yr represented in Table 1 (except pulsar J0537-6910 in the Magellanic Cloud) are shown on the P- \dot{P} diagram in Figure 1 denoting also the morphological types of the SNRs which some of the pulsars are connected to. If the type of the SNR is C (composite) or F (filled-center), then it means that there is PWN created by the neutron star. In S (shell) type SNRs there is no observed PWN possibly because it is very faint. Other pulsars in Table 1 which are not connected to SNRs and which have $\tau < 10^7$ yr are also displayed in Figure 1. All the pulsars with PWN around them have L_x (2-10 keV) $> 10^{33}$ erg/s (see Table 1). The cooling radiation of these pulsars do not have a considerable role.

X-ray EMISSION OF PULSARS AND PARTICLE ACCELERATION

Table 1 - All 35 radio and X-ray pulsars with detected X-ray radiation in 0.1-2.4 keV and/or in 2-10 keV bands and with $\tau < 10^6$ yr. All 15 pulsars which have $\log \dot{E} > 35.6$ and $\tau < 10^5$ yr. All pulsars which are connected to SNRs (PWNe). Two of these pulsars are in Magellanic Clouds and the others are Galactic pulsars with $d \leq 7$ kpc. In the first column 'G' denotes strong glitch. In column 12 $\beta = 2\Delta\theta/\theta$ (θ : SNR diameter, $\Delta\theta$: angular distance of pulsar from the geometric centre of SNR).

JName	Type	d kpc	P s	P s/s	Log τ	Log B	Log \dot{E}	SNR + l,b	Type	β	Log L_x 0.1-2.4 keV	Log L_x 2-10 keV	n
J1852+0040	X	7	0.1049					G33.6+0.1	S			33.6	
J1846-0258	X	6.7	0.325	7.1E-12	2.859	13.70	36.9	G29.7-0.3	C	~ 0 ²⁰	~ 35.18	35.32	2.65 \pm 0.01
J0534+2200	ROXG	2.0	0.034	4.21E-13	3.10	12.58	38.64	Crab	F	~ 0.19 ²¹	35.98	36.65	2.51
J1513-5908	RXG	4.2	0.151	1.54E-12	3.191	13.19	37.25	G320.4-1.2	C	0.24 ²¹	34.25	35.32	2.839
J1119-6127	RX	7.0	0.408	4.02E-12	3.205	13.61	36.37	G292.2-0.5	C	~ 0 ²²	≤ 32.5	33.42	2.91
J0540-6919	ROX	50	0.051	4.79E-13	3.22	12.70	38.17	N158A	C	~ 0 ²³	36.21	36.93	2.140 \pm 0.009
J1124-5916	RX	6.0	0.135	7.45E-13	3.458	13.01	37.07	G292.0-1.8	C		~ 32.7	34.67	
J1930+1852	RX	7	0.137	7.51E-13	3.462	13.0	37.23	G54.1+0.3	F		~ 34.2		
J0537-6910	X	50	0.016	5.1E-14	3.7	12.6	38.7	N157B	F		~ 36.0	36.11	>6.9?
J1833-1034 ³¹	R	5.5	0.061	2.0E-13	3.7	12.56	37.5	G21.5-0.9	C				
J0205+6449	RX	3.2	0.066	1.9E-13	3.74	12.55	37.42	G130.7+3.1	F		32.38	34.26	
G J1617-5055	RX	6.2	0.069	1.371E-13	3.903	12.40	37.21	332.5,-0.27			34.30	34.59	
J2229+6114	RXG	5.5	0.052	7.8E-14	4.023	12.31	37.34	G106.6+2.9	C	0 ²⁴	33.58	33.69	
G J0835-4510	ROXG	0.40	0.089	1.25E-13	4.05	12.53	36.84	Vela	C	0.29,0.3 ^{21,22}	32.46	33.18	1.4
J1420-6048	RXG	6.1	0.068	8.32E-14	4.113	12.38	37.01	G313.4+0.2?	F	0.2 ²⁵	34.26	34.30	
G J1801-2451	RX	4.5	0.125	1.28E-13	4.19	12.61	36.41	G5.27-0.9	F	~ 0 ²⁶	~ 33.0	33.18	
G J1803-2137	RX	3.5	0.134	1.34E-13	4.197	12.63	36.35	G8.7-0.1	S?	0.7 ²⁷	33.06	32.39	
J1702-4310	R	4.8	0.2405	2.24E-13	4.23	12.88	35.80	343.4,-0.85					
G J1709-4428	RXG	1.8	0.102	9.30E-14	4.241	12.49	36.53	G343.1-2.3?			33.15	32.58	
J1856+0113	RX	2.8	0.267	2.08E-13	4.31	12.88	35.63	G34.7-0.4	C	0.51 ²¹ ,0.6 ²²	≤ 33.0	33.03	
J1048-5832	RXG	2.8	0.124	9.63E-14	4.31	12.54	36.30	287.4,+0.58			≤ 32.11	32.35	
J1016-5857	RX	6	0.107	8.11E-14	4.321	12.48	36.41	G264.3-1.8	S	1 ²⁵ ,1.3 ²⁸	~ 32.6		
G J1826-1334	RX	3.4	0.101	7.55E-14	4.33	12.45	36.45	G18.0-0.7	F		~ 32.7	34.34	
J1811-1925	X	5	0.065	4.22E-14	4.4	12.23	36.78	G11.2-0.3	F	~ 0 ²⁹	32.8	34.54	
J1747-2958	RX	2.0	0.099	6.14E-14	4.41	12.41	36.41	G359.2-0.8?	F		~ 34.0		
G J1730-3350	R	4.24	0.1394	8.51E-14	4.41	12.56	36.09	354.1,+0.09					
J1646-4346	R	6.9	0.232	1.13E-13	4.51	12.71	35.55	G341.2+0.9	C	0.7 ²⁷			
J1837-0604	R	6.2	0.0963	4.52E-14	4.53	12.34	36.30	26.0,+0.27					
J1015-5719	R	4.87	0.1399	5.74E-14	4.59	12.47	35.92	283.1,-0.58					
J1718-3718	RX	4.5	3.3	1.5E-12	4.6	13.9	33.2	349.85,+0.22			33.8	33? ³²	
J2337+6151	RX	2.8	0.495	1.92E-13	4.611	12.99	34.79	G114.3+0.3	S	0.08 ^{21,30}	31.90	31.47	
J1637-4642	R	5.5	0.1540	5.92E-14	4.62	12.50	35.81	337.8,+0.31					
J0940-5428	R	3.8	0.0875	3.29E-14	4.63	12.25	36.29	277.5,-1.29					
J0631+1036	RX	6.6	0.288	1.05E-13	4.639	12.74	35.24	201.2,+0.45				31.90	
J1809-1917	R	3.3	0.0827	2.55E-14	4.71	12.18	36.25	11.1,+0.08					
J1105-6107	RX	7.0	0.063	1.58E-14	4.801	12.01	36.39	290.5,-0.85			~ 33.2	33.55	
J1718-3825	R	3.3	0.0747	1.32E-14	4.95	12.02	36.10	348.9,-0.43					
J1531-5610	R	2.6	0.0842	1.37E-14	4.99	12.05	35.96	323.9,+0.03					
J1952+3252	RXG	2.0	0.040	5.84E-15	5.030	11.69	36.57	G69.0+2.7	C	0.14,0.15 ^{21,22}	33.64	33.07	
J0659+1414	ROX	0.3	0.385	5.50E-14	5.044	12.67	34.58	G201.1+8.7			32.18	30.32	
J0908-4913	R	4.5	0.1068	1.51E-14	5.05	12.12	35.69	270.3,-1.02					
J0855-4644	R	6.4	0.0647	7.26E-15	5.15	11.85	36.03	267.0,-1.0					
G J1833-0827	R	5.67	0.0853	9.17E-15	5.17	11.97	35.77	23.4,+0.06					
J1509-5850	R	2.5	0.0880	9.17E-15	5.19	11.97	35.71	320.0,-0.62					
J1913+1011	R	4.1	0.0359	3.37E-15	5.23	11.56	36.46	44.5,-0.17					
J0117+5914	RX	2.4	0.101	5.85E-15	5.44	11.89	35.34	126.3,-3.46				30.44	
Be J1302-6350	RX	1.3	0.048	2.28E-15	5.52	11.52	35.92	304.2,-1.00			32.95	32.57	
Geminga	X	0.15	0.237	1.14E-14	5.53	12.22	34.53	195.13,+4.27			31.10	29.33	
J1057-5226	RX	1.0	0.197	5.83E-15	5.73	12.04	34.48	286.0,+6.65			33.13	30.08	
G J0958+5413	RX	2	0.156	4.4E-15	5.75	11.92	34.66	148.2,+0.81			31.96	31.75	
J0538+2817	RX	1.5	0.143	3.67E-15	5.79	11.87	34.69	G180.0-1.7?	S	0.41 ³²	32.74	29.31	
J1932+1059	RX	0.2	0.227	1.16E-15	6.49	11.71	33.59	47.38,-3.88			30.07	29.41	
J0826+2637	RX	0.4	0.531	1.71E-15	6.69	11.98	32.65	196.96,+31.74			31.85	29.01	
J0953+0755	RX	0.13	0.253	2.29E-16	7.24	11.39	32.75	228.91,+43.7			29.35	28.62	
J1824-2452	RX	5.1	0.003	1.62E-18	7.48	9.35	36.35	7.8,-5.58			32.2	33.56	
J1939+2134	RX	3.6	0.0015	1.06E-19	8.37	8.61	36.04	57.51,-0.29			< 32.1	32.54	
J2124-3358	RX	0.25	0.005	2.0E-20	9.58	8.51	33.83	10.93,-45.44			30.35	29.58	
J1024-0719	RX	0.35	0.005	1.9E-20	9.64	8.50	33.73	251.7,+40.52			29.48	29.09	
J0030+0451	RX	0.23	0.005	1.0E-20	9.89	8.35	33.53	113.14,-57.61			30.56	29.88	
J1744-1134	RX	0.36	0.004	8.9E-21	9.86	8.29	33.72	14.79,+9.18			29.58	29.25	

Pulsars J1803-2137, J1016-5857, J2337+6151, and J0659+1414, which are connected to S-type SNRs (in the radio band), have been observed to radiate in X-ray band. Pulsars J2337+6151 and J0659+1414 have suitable distance values and positions to observe possible PWNe around them, but \dot{E} and L_x (2-10 keV) values of these pulsars are so small that it is not so likely that PWNe with observable brightness are present around them.

From the analysis of these data, we see that lifetime of the X-ray radiation produced by the relativistic particles in the magnetospheres of neutron stars is

considerably longer than lifetime of PWNe (see Table 1). But there may be one exception, namely pulsar J0538+2817, which is connected to SNR G180.0-1.7 (S147). This SNR is S-type in radio band. Romani & Ng 16 claim evidence for a faint nebula around the pulsar, but in a more recent work 18 no evidence has been found of a PWN and the pulsar has been observed to radiate only thermally. Also, the position and ages of the pulsar and the SNR show that a physical connection between these two sources is dubious and there are no data directly showing evidence for the connection.

CONCLUSIONS

From the analysis of all the available data on isolated X-ray pulsars, their wind nebulae and the SNRs which are connected to some of these sources and also from theoretical considerations, we have found the conclusions below:

1. The electric field intensity (voltage) of neutron stars is not the main physical quantity for the spectra, energy, and intensity of the relativistic particles which produce the X-ray radiation of isolated pulsars and their wind nebulae. The voltage mainly triggers the acceleration of particles. In order to tear off charged particles from the surface of neutron star E_{el} must be large. This process occurs more easily in hot and extended atmospheres. Therefore, the values of mass and age of pulsars also have important roles in the formation of the X-ray radiation.
2. The acceleration of relativistic particles mainly takes place in the field of the magneto-dipole radiation wave. Because of this, the X-ray radiation of pulsars and their wind nebulae

strongly depend on the value of the rate of rotational energy loss which is reflected by the spectra of the magneto-dipole radiation.

3. The high magnetic field and particularly the number density of the charged particles create conditions under which the energy loss of the particles in 0.1-2.4 keV band may surpass the energy received from the magneto-dipole radiation wave for further acceleration. This must be responsible for the steeper X-ray spectra of young pulsars as compared to old ms pulsars.
4. PWN exists only around pulsars with $\dot{E} > 10^{35}$ erg/s and $\tau < 5 \times 10^4$ yr. Also, the X-ray luminosity of pulsars in 2-10 keV band drops down to $\sim 10^{33}$ erg/s at about the same time when the PWN becomes unobservable in both radio and X-ray bands. The lifetime of S-type SNRs exceeds the lifetimes of F-type and C-type SNRs. So, it may be possible that C-type SNRs can show themselves as S-type after some time in their evolution. PWN must be observed around pulsar J1617-5055.

-
- | | |
|---|---|
| <p>[1]. W. Becker and J. Trumper, <i>Astron. Astrophys.</i> 326, 682 (1997).</p> <p>[2]. W. Becker and B. Aschenbach, <i>Proceedings of the 270. WE-Heraeus</i></p> <p>[3]. Seminar on: "Neutron Stars, Pulsars and Supernova Remnants", eds. W. Becker, H. Lesch and J. Trumper, <i>MPE Report</i> 278, p.64 (2002).</p> <p>[4]. A. Possenti, R. Cerutti, M. Colpi and S. Mereghetti, <i>Astron. Astrophys.</i> 387, 993 (2002).</p> <p>[5]. V. M. Lipunov, <i>Astrophysics of Neutron Stars</i>, Springer-Verlag (1992).</p> <p>[6]. A. G. Lyne and F. Graham-Smith, <i>Pulsar Astronomy</i>, Cambridge University Press (2006).</p> <p>[7]. O. H. Guseinov, A. Ankay, S. O. Tagieva, <i>Int. J. Mod. Phys. D</i> 14, 1465 (2005).</p> <p>[8]. O. H. Guseinov, A. Ankay, S. O. Tagieva, <i>Astrophys. Space Sci.</i> 298, 553 (2005).</p> <p>[9]. A. R. Bell, <i>Mon. Not. Roy. Astron. Soc.</i> 182, 147 (1978).</p> <p>[10]. A. R. Bell, <i>Mon. Not. Roy. Astron. Soc.</i> 182, 443 (1978).</p> <p>[11]. G. F. Krymsky, <i>Dokl. Akad. Nauk SSSR</i> 234, 1306 (1977).</p> <p>[12]. A. O. Allakhverdiev, A. I. Asvarov, O. H. Guseinov, F. K. Kasumov, <i>Astrophys. Space Sci.</i> 123, 237 (1986).</p> <p>[13]. G. S. Bisnovatyi-Kogan and B. V. Komberg, <i>Sov. Astron.</i> 18, 217 (1974).</p> <p>[14]. G. S. Bisnovatyi-Kogan and B. V. Komberg, <i>Sov. Astron. Lett.</i> 2, 130 (1976).</p> <p>[15]. ATNF – Australia Telescope National Facility Pulsar Catalogue (2007), http://www.atnf.csiro.au/research/pulsar/psrcat/.</p> <p>[16]. O. H. Guseinov, S. K. Yerli, S. Ozkan, A. Sezer and S. O. Tagieva, <i>Astron. Astrophys. Transac.</i> 23, 357 (2004).</p> <p>[17]. R. W. Romani and C. -Y. Ng, 2003, <i>Astrophys. J.</i>, 585, L41 (2003).</p> | <p>[18]. D. A. Green, 'A Catalogue of Galactic Supernova Remnants (2006 April version)', http://www.mrao.cam.ac.uk/surveys/snrs/.</p> <p>[19]. K. E. McGowan, J. A. Kennea, S. Zane, et al., <i>Astrophys. J.</i> 591, 380 (2003).</p> <p>[20]. O. H. Guseinov, A. Ankay, A. Sezer, S. O. Tagieva, <i>Astron. Astrophys. Transac.</i> 22, 273 (2003).</p> <p>[21]. D. J. Helfand, B. F. Collins and E. V. Gotthelf, <i>Astrophys. J.</i> 582, 783 12 (2003).</p> <p>[22]. D. R. Lorimer, A. G. Lyne and F. Camilo, <i>Astron. Astrophys.</i> 331, 1002 (1998).</p> <p>[23]. A. O. Allakhverdiev, M. A. Alpar, F. Gok and O. H. Guseinov, <i>Turkish J. Phys.</i> 21, 688 (1997).</p> <p>[24]. F. D. Seward, F. R. Jr. Harnden and D. J. Helfand, <i>Astrophys. J.</i> 287, L19 (1984).</p> <p>[25]. R. Kothes, B. Uyaniker and S. Pineault, <i>Astrophys. J.</i> 560, 236 (2001).</p> <p>[26]. R. N. Manchester, J. F. Bell, F. Camilo, et al., <i>Neutron Stars in Supernova Remnants</i>, ASP Conference Series, edited by Patrick O. Slane and Bryan M. Gaensler, 271, p.31 (2002).</p> <p>[27]. S. E. Thorsett, W. F. Brisken and W. M. Goss, <i>Astrophys. J.</i> 573, L111 (2002).</p> <p>[28]. D. A. Frail, W. M. Goss and J. B. Z. Whiteoak, <i>Astrophys. J.</i> 437, 781 (1994).</p> <p>[29]. F. Camilo, J. F. Bell, R. N. Manchester, et al., <i>Astrophys. J.</i> 557, L51 (2001).</p> <p>[30]. V. M. Kaspi, M. E. Roberts, G. Vasisht, E. V. Gotthelf, M. Pivovarov and N. Kawai, <i>Astrophys. J.</i> 560, 371 (2001).</p> <p>[31]. E. Furst, W. Reich and J. H. Seiradakis, <i>Astron. Astrophys.</i> 276, 470 (1993).</p> <p>[32]. Y. Gupta, D. Mitra, D. A. Green and A. Acharyya, <i>astro-ph/0508257</i>.</p> <p>[33]. M. Kramer, A. G. Lyne, G. Hobbs, O. Lohmer, P. Carr, C. Jordan and Wolszczan, <i>Astrophys. J.</i> 593, L31 (2003).</p> |
|---|---|

SAMPLING THE HYDROPHOBIC CLUSTERS OF SILK FIBROIN AT VARIOUS PH VALUES BY ANS FLUORESCENCE.

A.H. AYDEMIROVA, R.L. MAMMADOVA, R.B. ASLANOV, O.K. GASIMOV

G.M. Abdullayev Institute of Physics
of Azerbaijan National Academy of Sciences
AZ1143, 33 H. Javid Avenue, Baku

Silk fibroin produced by silkworm *Bombyx mori* [1] is a fibrous protein. Fibroin has unique properties such as, high tensile strength, biocompatibility, long-term durability and etc. [2-4]. These properties make fibroin very attractive for biomedical applications [5-7]. Wide variety films, composite materials and etc. can be fabricated from fibroin solution. Small additives, such as ethanol, for example, applied in a fabrication procedure can modulate secondary structure and, therefore, many physico-chemical properties of materials obtained from fibroin. Fibroin films have also been formulated for drug delivery [8]. Drug molecules mostly hydrophobic and therefore, interact with biomolecules via hydrophobic interactions. Therefore, identification and characterization of hydrophobic clusters of fibroin are pivotal for many biomedical applications. In this report, we use ANS (8-anilino-1-naphthalenesulfonic acid) molecules to probe hydrophobic clusters of the protein. ANS is a widely utilized fluorescent probe for the characterization of hydrophobicity of proteins. Upon binding to hydrophobic sites of proteins, ANS exhibits enhanced fluorescence intensity and a blue shift of fluorescence emission maxima [9]. These properties of ANS were used to characterize the hydrophobic cluster of fibroin hydrated in solutions with various pH values. Fluorescence spectra of ANS-fibroin complexes hydrated in solutions with various pH values are shown in Figure 1.

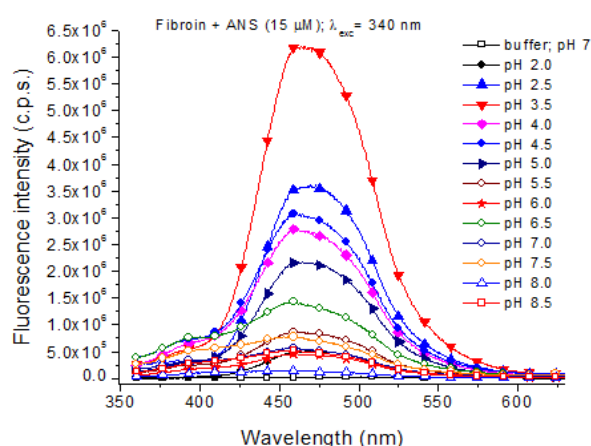


Fig. 1. ANS fluorescence spectra of ANS-fibroin complexes hydrated in solutions with various pH values

As can be seen, ANS fluorescence strongly depends on pH values of solvent. The fluorescence λ_{max} values are in the range of 450nm - 468 nm (Fig. 2). Low pH values shifts fluorescence λ_{max} values toward shorter wavelength. That is in contrast to ANS in buffer in which fluorescence

λ_{max} is about 520 nm. The blue shifted fluorescence of ANS indicates that ANS binds to hydrophobic clusters of fibroin. Decreased pH values make the clusters with higher hydrophobicity available for interaction with ANS molecules.

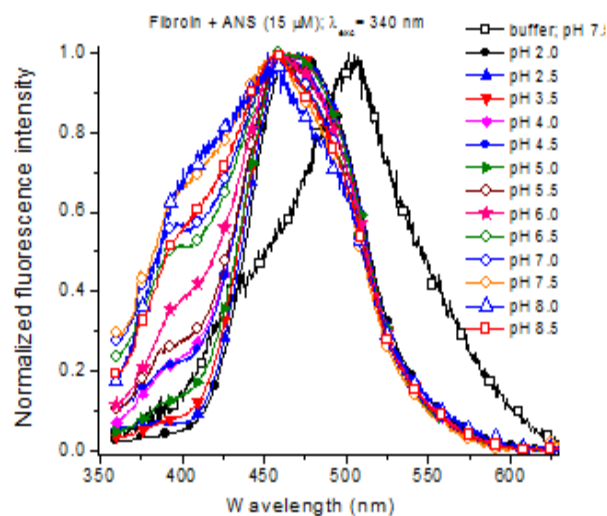


Fig. 2. Normalized ANS fluorescence spectra of ANS-fibroin complexes hydrated in solution with various pH values

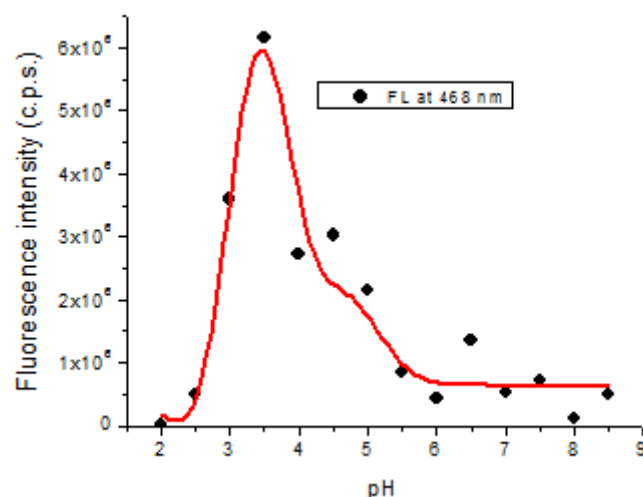


Fig. 3. ANS fluorescence intensities of ANS-fibroin complexes hydrated in solution with various pH values

The fluorescence intensity of ANS in ANS-fibroin complex increases at low pH values reaching to the maximum value around 3.5 (Fig. 3). It indicates that at low pH more hydrophobic clusters become accessible for

ANS molecules. However, diminished values of ANS fluorescence intensity at pH values < 3.5 indicate degradation of the hydrophobic clusters in fibroin.

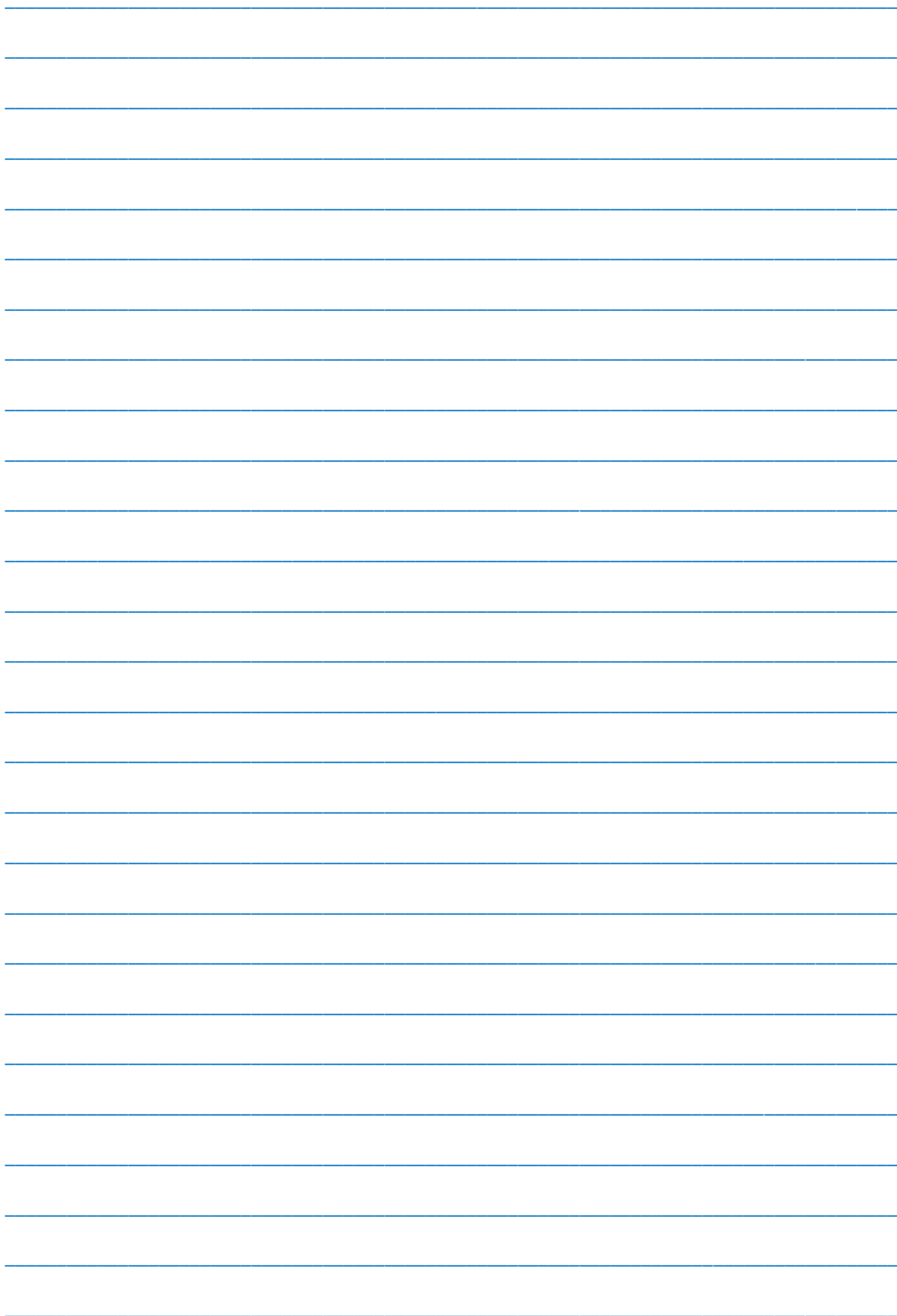
Thus, accessibility of hydrophobic regions of silk fibroin in hydrated state can be manipulated using

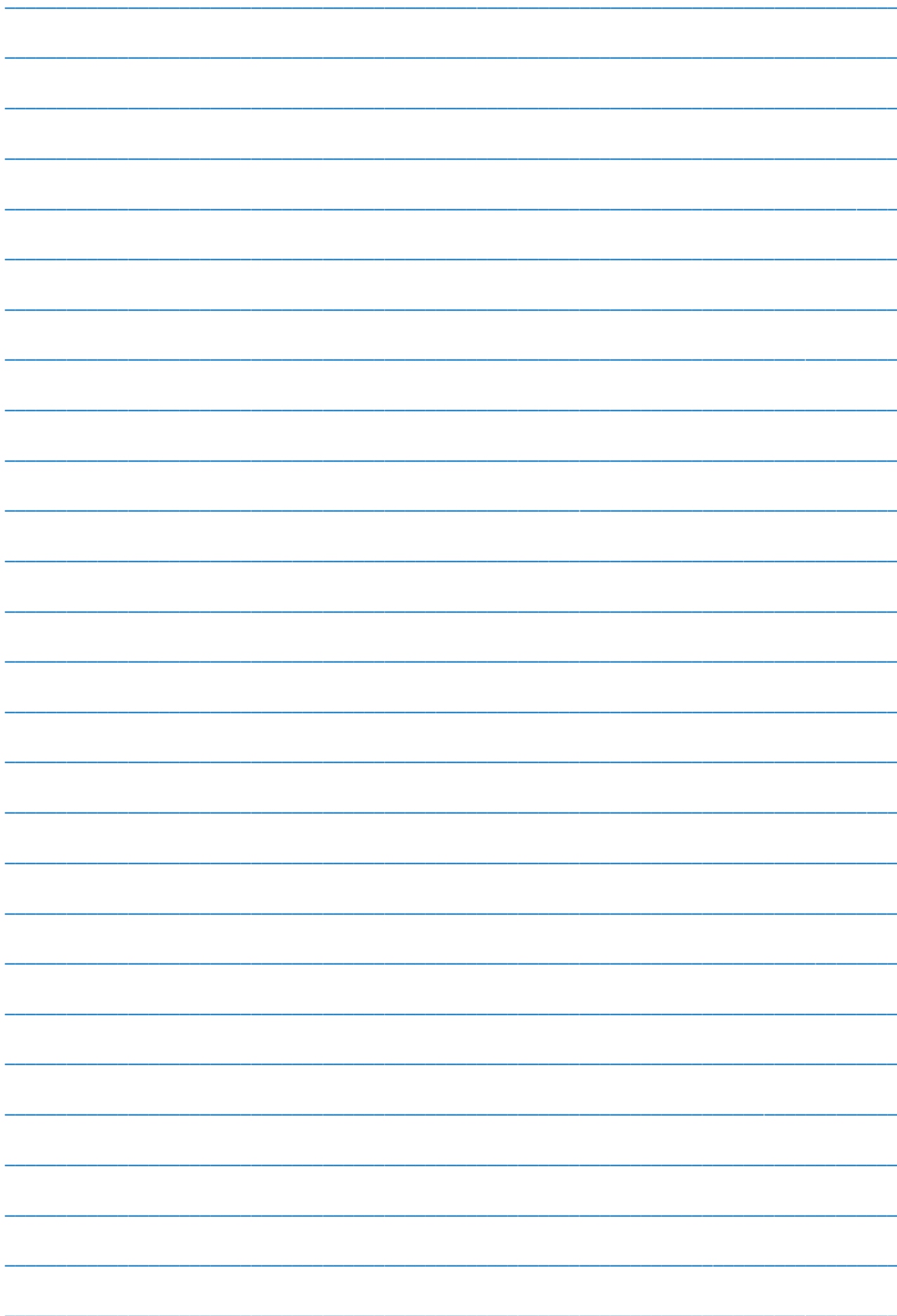
solutions the various pH values. It allows modulate hydrophobic drug binding capacity that is important for biomedical applications of silk fibroin.

-
- [1]. M. Mondal, K. Trivedy and S. N. Kumar, The silk proteins, sericin and fibroin in silkworm, *Bombyx mori* Linn., a review , *Caspian J. Env. Sci.* 2007, 5, 63-76.
 - [2]. G.H. Altman, F. Diaz, C. Jakuba, T. Calabro, R.L. Horan, J. Chen, H. Lu, J. Richmond, D.L. Kaplan, Silk-based biomaterials, *Biomaterials* 24 (3) (2003) 401–416.
 - [3]. R.L. Horan, K. Antle, A.L. Collette, Y. Wang, J. Huang, J.E. Moreau, V. Volloch, D.L. Kaplan, G.H. Altman, In vitro degradation of silk fibroin, *Biomaterials* 26 (17) (2005) 3385–3393.
 - [4]. L. Meinel, S. Hofmann, V. Karageorgiou, C. Kirker-Head, J. McCool, G. Gronowicz, L. Zichner, R. Langer, G. Vunjak-Novakovic, D.L. Kaplan, The inflammatory responses to silk films in vitro and in vivo, *Biomaterials* 26 (2) (2005) 147–155.
 - [5]. S. Hofmann, S. Knecht, R. Langer, D.L. Kaplan, G. Vunjak-Novakovic, H.P. Merkle, L. Meinel, Cartilage-like tissue engineering using silk scaffolds and mesenchymal stem cells, *Tissue Eng.* 12 (10) (2006) 2729–2738.
 - [6]. L. Meinel, O. Betz, R. Fajardo, S. Hofmann, A. Nazarian, E. Cory, M. Hilbe, J. McCool, R. Langer, G. Vunjak-Novakovic, H.P. Merkle, B. Rechenberg, D.L. Kaplan, C. Kirker-Head, Silk based biomaterials to heal critical sized femur defects, *Bone* 39 (4) (2006) 922–931.
 - [7]. C. Kirker-Head, V. Karageorgiou, S. Hofmann, R. Fajardo, O. Betz, H.P. Merkle, M. Hilbe, B. von Rechenberg, J. McCool, L. Abrahamsen, A. Nazarian, E. Cory, M. Curtis, D. Kaplan, L. Meinel, BMP-silk composite matrices heal critically sized femoral defects, *Bone* 41 (2) (2007) 247–255.
 - [8]. E. Wenk, A.J. Wandrey, H. P. Merkle, L. Meinel, Silk fibroin spheres as a platform for controlled drug delivery, *Journal of Controlled Release* 132 (2008) 26–34.
 - [9]. O.K. Gasymov, B.J. Glasgow, ANS fluorescence: Potential to augment the identification of the external binding sites of proteins, *BBA*, 1774 (2007) 403–411

CONTENTS

1.	Deviations from plasma stabilization against the onset of space-charge effect in a gas discharge structure with semiconductor cathode M. Özer, E. Koç and B.G.Salamov	3
2.	The efficient plasma light source on the basis of nanoporous zeolite K. Koseoglu, B.G.Salamov and T.G.Mammadov	7
3.	The charge transport in the nanoporous natural zeolite K. Koseoglu, I. Karaduman, S. Acar and, B.G.Salamov	12
4.	On features of potential distribution in avalanche photodiodes with deeply buried pixels Z.Y.Sadygov, X.I.Abdullayev, F.I.Ahmadov, E.A.Jafarova, A.A.Dovlatov, R.C.Madatov, R.M.Muxtarov, A.Z.Sadygov, N.A.Safarov	17
5.	Synthesis of carbon encapsulated magnetic nanostructures by using Caspian heavy oil S.H.Abdullayeva, N.N.Musayeva, R.B.Jabbarov, A. A. El-Gendy, A. Leonhardt	20
6.	Nanostructure materials and their applications S.H.Abdullayeva, R.B.Jabbarov, N.N.Musayeva	22
7.	Low-temperature study of thermally stimulated currents in layered-structured $Tl_4GaIn_3S_8$ crystals Serdar Delice, Mehmet Isik and Nizami Hasanli	26
8.	Quenching of short circuit current and exciton decay in $CuGaSe_2$ single crystals I.Kasumoglu, I.A.Mamedova	30
9.	Study of effect of annealing on the film structure $Bi_2Te_{2.7}Se_{0.3}<Lu>$ I.T.Mamedova, N.R.Memmedov, N.M.Abdullayev	33
10.	The pressure dependence of the phonon spectra of orthorhombic GeSe and the second order structural phase transition from simple - to base- centered orthorhombic lattice. F.M. Hashimzade, D.A. Huseinova, Z.A. Jahangirli, B.H. Mehdiyev, G.S. Orudzhev	36
11.	P - V - T dependences in the fluid of the carbon dioxide and calculation of oil components properties E.E. Ramazanova, M.M. Asadov, E.N. Aliyev	40
12.	Dielectric coefficients and conductivity of $tlrte_2$ crystal in alternate electric fields A.M. Pashaev, S.N. Mustafaeva, E.M. Kerimova	43
13.	X-ray phase analysis of Cu_5SmSe_4 A.S. Amirov, G.G. Guseynov, T.R. Mehdiyev	46
14.	Ferromagnetic metal/semiconductor $CdGeAs_2$ doped with Mn under pressure A. Yu. Mollaev, I. K. Kamilov, R. K. Arslanov, S. F. Marenkin and T.R. Arslanov	58
15.	Electron energy-loss spectroscopy and the electronic structure of some ternary oxides: first principle calculations Sevket Simsek, Amirullah M. Mamedov, Ekmel Ozbay	61
16.	Structural, electronic, and optical properties of Ag_2Se and Ag_2Te compounds: a first principles study H. Koc, Amirullah M.Mamedov and Ekmel Ozbay	67
17.	Optical phonons in $ZnGa_2Se_4$ and $ZnAl_2Se_4$ single crystals T.G.Kerimova, N.A.Abdullayev, I.A.Mamedova, I.G.Nasibov, Z.Badalova	72
18.	Analysis of temperature dependence of kinetic coefficients of $Bi_{0.88}Sb_{0.12}$ alloy Eltaj Yuzbashov, Khayala Gasanova, Bakir Tairov	75
19.	Ellipsometric investigation of optical constants of Caspian seawater and crude oils from different sources Khuraman Khalilova, Eldar Mammadov, Yegane Aliyeva, Naghi Gasimov, Nazim Mammadov	78
20.	Physical properties of $(InSb)_{1-x}(HgTe)_x$ solid solutions A.R.Hajiyev, T.B.Tagiyev	81
21.	Characterization of ZnO thin films prepared by magnetron sputtering method R.H. Hajimammadov, Y.N. Aliyeva, E.A. Bagiyev, N.A.Gasimov, N.Satoh, M.Nakajima, A.H. Bayramov	84
22.	X-ray emission of pulsars and particle acceleration S.O.Tagieva, H.I.Novruzova	87
23.	Sampling the hydrophobic clusters of silk fibroin at various PH values by <i>ANS</i> fluorescence. A.H. Aydemirova, R.L. Mammadova, R.B. Aslanov, O.K. Gasimov	91







www.physics.gov.az